

University of Louisville

ThinkIR: The University of Louisville's Institutional Repository

Electronic Theses and Dissertations

8-2021

Synthesis, characterization, and catalytic activity of functionalized metal Bis(thiosemicarbazones).

Caleb Aaron Calvary
University of Louisville

Follow this and additional works at: <https://ir.library.louisville.edu/etd>

 Part of the [Inorganic Chemistry Commons](#)

Recommended Citation

Calvary, Caleb Aaron, "Synthesis, characterization, and catalytic activity of functionalized metal Bis(thiosemicarbazones)." (2021). *Electronic Theses and Dissertations*. Paper 3676.
Retrieved from <https://ir.library.louisville.edu/etd/3676>

This Doctoral Dissertation is brought to you for free and open access by ThinkIR: The University of Louisville's Institutional Repository. It has been accepted for inclusion in Electronic Theses and Dissertations by an authorized administrator of ThinkIR: The University of Louisville's Institutional Repository. This title appears here courtesy of the author, who has retained all other copyrights. For more information, please contact thinkir@louisville.edu.

SYNTHESIS, CHARACTERIZATION, AND CATALYTIC ACTIVITY OF
FUNCTIONALIZED METAL BIS(THIOSEMICARBAZONES)

By

Caleb Aaron Calvary

B.S., Marshall University, 2014

M.S., University of Louisville, 2018

A Dissertation

Submitted to the Faculty of the

College of Arts and Sciences of the University of Louisville

in Partial Fulfillment of the Requirements

for the Degree of

Doctor of Philosophy

in Chemistry

Department of Chemistry

University of Louisville

Louisville, KY

August 2021

Copyright 2021 by Caleb Aaron Calvary

All rights reserved

SYNTHESIS, CHARACTERIZATION, AND CATALYTIC ACTIVITY OF
FUNCTIONALIZED METAL BIS(THIOSEMICARBAZONES)

By

Caleb Aaron Calvary

B.S., Marshall University, 2014

M.S., University of Louisville, 2018

A Dissertation Approved on

May 11, 2021

By the following Dissertation Committee

Dr. Craig A. Grapperhaus

Dr. Robert M. Buchanan

Dr. Sachin Handa

Dr. Joshua M. Spurgeon

DEDICATION

To Faye, Nancy, and Eleanor. I would be lost without your guidance.

ACKNOWLEDGEMENT

I would like to thank my advisors, Dr. Craig Grapperhaus and Dr. Robert Buchanan, who took me into their group and allowed my interest in chemistry to flourish. I would also like to thank Dr. Sachin Handa, who always would be willing to converse whenever we would meet in the hallway. In addition, I would like to thank Dr. Josh Spurgeon, whose lab members greatly assisted with experiments vital to all of the papers I published. I would like to thank the National Science Foundation for support as graduate research assistant (CHE-1665136 and CHE-1800245).

I would like to thank Dr. Oleksandr Hietsoi for his invaluable assistance in my research. I would also like to thank Dr. Dillon Hofsommer whose advice and guidance about my projects helped me immensely. I would also like to thank Dr. Mark Mashuta for his help with all of the X-ray crystallography experiments. In addition, I would like to thank Dr. Nick Vishnosky, Kritika Bajaj, Christine Phipps, Peter Armstrong, Sashil Chapagain, Mohan Paudel, and Chinmay Pontis for being more than just lab mates, they were, and will forever be, family. I would also like to acknowledge Dr. Rahul Jain, Dr. Wuyu Zhang, Dr. Andrew Haddad, and Dr. Davinder Kumar for the assistance in getting started in the lab. Further, I would like to acknowledge Dino, Hari, Richard, and Emily who were always there to help me with anything.

I would like to thank Mark and Nancy Calvary for raising me and giving me a great start to my life. Further, I would like to thank Evan, Dustin, and Josh for helping me enjoy the fun side of life. Finally, I would give my undying appreciation to my wife, Dr. Ma. Faye Charmagne Carvajal, without whom I would have never made it this far in both my academic career and my life.

ABSTRACT

SYNTHESIS, CHARACTERIZATION, AND CATALYTIC ACTIVITY OF FUNCTIONALIZED METAL BIS(THIOSEMICARBAZONES)

Caleb Aaron Calvary

May 11, 2021

Bis-(thiosemicarbazones) are a class of ligands that have found a wide range of uses from electrocatalysts to medicinal and diagnostic reagents. These ligands contain a diimine backbone, N_2S_2 chelating core, and pendent amines. In order to further explore this class of ligands, the previously underreported transamination reaction, which exchanges one pendent amine group for another, was utilized to create several derivatives using aliphatic and aromatic amines. The transamination reaction is appealing alternative to making the desired thiosemicarbazide. Further appeals come from the fact that it is a one-pot reaction that gives highly pure products in good yields. Product yields were improved as varying reaction conditions and solvents.

One of these newly transaminated species that contained hindered amine bases were then treated with nickel(II) and copper(II) salts resulting in the corresponding metal complexes. These complexes were then alkylated to create charged pendent frameworks.

Subsequently, both the charged and free base metal complexes were tested for homogeneous HER activity. It was observed that the free base complexes were the most active due to a proposed proton relay mechanism involving the pendent amine groups. The charged species did display an anodic shift in the onset potentials, however they were found to be less active as HER catalysts.

Heterogeneous studies were conducted with NiATSM on p-Si electrode surfaces. Initial films were form by drop casting an acetonitrile solution of NiATSM followed by evaporation. The films were found to peel off after a short period of time during HER studies in 0.5 M H₂SO₄ as the acid source. To stabilize the film, a Nafion solution (5% w/v) was drop casted over the NIATSM film and evaporated in an oven for 15 minutes prior to use in HER studies. With this, there was no drop off in activity of the catalytic film. The photo indued HER studies for NiATSM indicated that it was a viable material with low onset potential needed.

TABLE OF CONTENTS

Acknowledgement	iv
Abstract.....	v
List of Figures.....	x
List of Tables	xiv
Chapter 1 Introduction	1
1.1 Lay Summary	1
1.2 Scope of Dissertation	2
1.3 Bis(thiosemicarbazones)	4
1.4 Electrochemistry	7
1.4.1 Cyclic Voltammetry	7
1.4.2 Overpotential and Turnover Frequency (TOF)	10
1.5 Hydrogen and the Hydrogen Evolution Reaction (HER)	11
Chapter 2 Facile and Efficient Synthesis of C _S -Symmetric Bis(thiosemicarbazones) with Functionalized Pendent Amines	20
2.1 Introduction.....	20
2.2 Results and Discussion	22
2.3 Materials and Methods.....	32
2.3.1 Syntheses of C _S -symmetric Bis(thiosemicarbazones)	33
Chapter 3 Electrochemical Characterization of Pendent Diamine Derivatives of Nickel(II) and Copper (II) Bis(thiosemicarbazones)	39

3.1 Introduction.....	39
3.2 Synthesis and Spectroscopic Analysis	42
3.3 Crystallographic Characterization.....	47
3.4 Electrochemical Studies.....	53
3.4.1 Cyclic Voltammetry	53
3.4.2 Diffusion Studies	56
3.4.3 HER Studies.....	57
3.4.4 Controlled Potential Coulometry Studies	62
3.4.5 Post Coulometry Dip Test.....	65
3.5 Conclusion	67
3.6 Experimental Section	71
3.6.1 Physical Methods.....	71
3.6.2 Electrochemical Methods.....	71
3.6.3 Materials and Methods.....	73
3.6.4 Syntheses.....	74
Chapter 4 Covalent Attachment and Photoelectrochemistry Characterization of Metal (II) Bis(thiosemicarbazone) to Various Surfaces	80
4.1 Introduction.....	80
4.2 Results and Discussion	83
4.3 Conclusions	94
4.4 Materials and Methods	95
4.4.1 NiATSM Catalyst Synthesis and Characterization.....	95

4.4.2 Electrode Preparation.....	96
4.4.3 Photoelectrochemical Measurements.....	97
4.4.4 Materials Characterization	98
4.4.5 Nafion Binding Effect on <i>J-E</i> Behavior Stability	99
4.4.6 Effect of Nafion on the p-Si Performance	100
4.4.7 Elemental Mapping of NiATSM on p-Si.....	100
4.4.8 XPS of NiATSM and Nafion on p-Si	101
4.4.9 Behavior of Electrodeposited Ni on p-Si.....	103
Chapter 5 Concluding Thoughts and Future Directions	104
References	107
Appendices	115
Appendix A. Structural Analysis of Transaminated BTSC Products.....	115
Appendix B. Structural and Spectroscopic Analyses of the Metal BTSC Complexes	129
Appendix C. Determination of Diffusion Coefficient (D_0) for Ni-1	157
Appendix D. Electrochemical Studies and Catalytic Activity Determination of Metal BTSCs	158
Appendix E. Overpotential Determination.....	168
Appendix F. Turnover Frequency Determination.....	169
Appendix G. TON Calculations for Ni-1	171
Appendix H. Photoelectric Characterization of Metal BTSC Attached to Various Surfaces	171
Curriculum Vitae.....	172

LIST OF FIGURES

Figure 1.1 A representative of a BTSC showing the highly interchangeable nature. R1 and R2 represent the backbone moieties. R3 - R6 represent the pendent amine moieties. 5	5
Figure 1.2 General BTSC complexation. 6	6
Figure 1.3 a) Orbital representation of conjugated network in metal BTSCs (excerpt from Vishnosky ¹³). b) Representation of CuATSM x-ray structure showing planarity of metal BTSC core. 7	7
Figure 1.4 A) Illustration of a cyclic voltammogram using IUPAC convention with E_p as the peak potential and I_p as the peak current. B.) Cyclic voltammograms for a) reversible, b) quasi-reversible, and c) irreversible electrochemical processes.. 8	8
Figure 1.5 Structures of the active sites of [NiFe], [FeFe], and Fe-Only hydrogenases found in sulfate-reducing bacteria ([NiFe], [FeFe]) and in methanogenic archaea (Fe-Only). ²⁸ 12	12
Figure 1.6 Depiction of heterogeneous HER catalysis. 13	13
Figure 1.7 Examples of heterolytic (left) and homolytic (right) pathways to hydrogen evolution..... 15	15
Figure 1.8 A sampling of previous HER catalysts. a) Re(PS) ₃ complex studied by the Grapperhaus lab. b) Neutral Aluminum bis(imino)pyridine complex studied by the Berben group. c) “Hangman” nickel porphyrin complex studied by the Nocera group. d) Charged Aluminum bis(pyrazole)pyridine complex studied by the Berben group. 16	16
Figure 2.1 BTSC ligands synthesized using the optimized transamination reaction between molecule 2 and the amines in Table 2.1. 24	24
Figure 2.2 ¹ H NMR Spectrum of 6 in d ₆ -DMSO..... 26	26
Figure 2.3 ¹³ C NMR Spectrum of 6 in d ₆ -DMSO..... 27	27
Figure 2.4 ¹ H NMR Spectrum of 9 in d ₆ -DMSO..... 29	29
Figure 2.5 ¹³ C NMR Spectrum of 9 in d ₆ -DMSO..... 30	30

Figure 2.6 a) Major product of transamination with glycine. b) Dimethylammonium salt of the major product.....	31
Figure 2.7 ¹ H NMR, in <i>d</i> ₆ -DMSO, of the product of the transamination reaction with glycine.....	32
Figure 3.1 ¹ H NMR (400 MHz, <i>d</i> ₆ -DMSO) of 3	44
Figure 3.2 ¹ H NMR (400 MHz, <i>d</i> ₆ -DMSO) of Ni-1	45
Figure 3.3 UV-Vis spectra of a) Ni-1 – Ni-4 and b) Cu-1 – Cu-4	46
Figure 3.4 Low temperature (77 K) EPR spectrum of Cu-3 in DMF. Microwave frequency = 9.603 MHz, <i>g</i> = 2.09, <i>g</i> _⊥ = 2.01, <i>A</i> = 181 G.....	47
Figure 3.5 ORTEP of Ni-1 thermal ellipsoids shown at 50% probability.	50
Figure 3.6 ORTEP view (50% probability ellipsoids) of Cu-1 showing atom labelling for all non-hydrogen atoms in the asymmetric unit.....	53
Figure 3.7 Cyclic voltammograms of Ni-1 – Ni-4 (left) and Cu-1 – Cu-4 (right) in acetonitrile with scan rate of 200 mV/s.	55
Figure 3.8 a) Scan rate dependent CVs of Ni-3 recorded at scan rates of 0.1 (black), 0.2, 0.3, 0.4, and 0.5 V/s (red) in 0.1 M Bu ₄ NPF ₆ /MeCN solution. b) Plot of peak current versus the square root of scan rate.	56
Figure 3.9 a) CVs of 0.3 mM Ni-3 in MeCN solution with 0.1 M Bu ₄ NPF ₆ collected at scan rate of 200 mV/s with 0, 20, 40, 60, 80, 100, 120, 140, 160 μL CH ₃ COOH without acid blanks subtracted and b) with acid blanks subtracted.	58
Figure 3.10 a) CVs of 0.3 mM Cu-3 in MeCN solution with 0.1 M Bu ₄ NPF ₆ collected at scan rate of 200 mV/s with 0, 50, 100, 150 μL CH ₃ COOH without acid blanks subtracted and b) with acid blanks subtracted.....	59
Figure 3.11 CPC of 0.3 mM Ni-1 – Ni-4 in 0.1 M Bu ₄ NPF ₆ /MeCN solutions with 100 mM CH ₃ COOH. The CPC were performed for Ni-1, Ni-2, and Ni-4 at –1.4 V vs Ag/Ag ⁺ and Ni-3 at –1.32 V vs Ag/Ag ⁺ . The charge generated by the acid blanks in the absence of the catalysts were subtracted.....	62
Figure 3.12 Faradaic efficiency of the hydrogen produced during the bulk electrolysis of a) Ni-1 , b) Ni-2 , c) Ni-3 , and d) Ni-4 detected by gas chromatography. The potential was held at -1.4 V vs Ag/Ag ⁺	63

Figure 3.13 CPC of 0.3 mM Cu-1 – Cu-4 and Cu(ATSM) in 0.1 M Bu ₄ NPF ₆ /MeCN solutions with 100 mM CH ₃ COOH. The CPC were performed at –1.5 V vs Ag/Ag ⁺ . The charge generated by the acid blanks in the absence of the catalysts were subtracted.....	64
Figure 3.14 Faradaic efficiencies for hydrogen produced during the bulk electrolysis of a) Cu-1 , b) Cu-2 , c) Cu-3 , and d) Cu-4 detected by gas chromatography. Potential was held at 1.5 V vs Ag/AgCl ⁺	65
Figure 3.15 Post electrolysis dip test on working electrode after CPC of Ni-1 – Ni-4 in a fresh 0.1 M Bu ₄ NPF ₆ /MeCN solution with no acetic acid at scan rate of 0.2 V/s.	66
Figure 3.16 Post electrolysis dip test on working electrode after CPC of Cu-1 – Cu-4 in a fresh 0.1 M Bu ₄ NPF ₆ /MeCN solution with no acetic acid at scan rate of 0.2 V/s.	67
Figure 3.17 Comparison of overpotentials and TOF for M(ATSM) and M-1 – M-4	68
Figure 4.1 a) ¹ H NMR of NiATSM (500 MHz, d ₆ -DMSO): 7.69 (1H, br. s), 2.75 (3H), 1.94 (3H, s). b) Representation of ligand-assisted, metal-centered HER electrocatalysis by NiATSM on p-Si (Nafion not shown).	82
Figure 4.2 Current density vs. potential at (<i>J-E</i>) behavior for electrodes in H ₂ -saturated 1M H ₂ SO ₄ . Dark electrocatalytic behavior for n ⁺ -Si with and without NiATSM and illuminated 1 sun AM15 behavior for p-Si photocathodes with and without NiATSM catalyst.	84
Figure 4.3 Current density vs. potential (<i>J-E</i>) behavior of p-Si/NiATSM without Nafion in 1 M H ₂ SO ₄ under 1 sun AM1.5 illumination, as-deposited performance before and after 1 h at -0.2 V vs. RHE.....	86
Figure 4.4 a) Current density vs. time at -0.2 V vs. RHE under 1 Sun AM1.5 illumination in 1 M H ₂ SO ₄ . b) Calculated vs. measured H ₂ produced by illuminated p-Si/NiATSM/Nafion at -0.2 V vs. RHE in N ₂ -bubbled 1 M H ₂ SO ₄ . SEM images of the p-Si/NiATSM/Nafion electrode c) before and d) after the stability measurement in a). Scale bars correspond to 40 μm and 2 μm for the inset.	86
Figure 4.5 Current density vs. potential (<i>J-E</i>) behavior of p-Si/NiATSM with Nafion in 1 M H ₂ SO ₄ under 1 Sun AM1.5 illumination, as-deposited performance before and after 1 h at -0.2 V vs. RHE.....	87
Figure 4.6 Current density vs. potential (<i>J-E</i>) behavior in 1 M H ₂ SO ₄ under 1 Sun AM1.5 illumination for bare p-Si, p-Si/Nafion, and p-Si/NiATSM/Nafion.	88

Figure 4.7 SEM images (far left) and EDS corresponding elemental maps for Ni (purple), S (red), F (green) and Si (yellow) for p-Si/NiATSM/Nafion before (top panels) and after (bottom panels) 1 h at -0.2 V vs. RHE in 1 M H ₂ SO ₄ under 1 Sun AM1.5 illumination. The scale bar is 20 μm.....	88
Figure 4.8 XPS spectra for the Ni 2p region for various p-Si substrates. Before substrates were measured with as-deposited catalyst, and the After substrate had been exposed to 1 Sun at -0.2 V vs. RHE in 1 M H ₂ SO ₄ for 1 h.....	90
Figure 4.9 XPS spectra for the S 2p region (left panel) and for the Si 2p region (right panel) for various p-Si substrates. Before substrates were measured with as-deposited catalyst, and the After substrate had been exposed to 1 Sun at -0.2 V vs. RHE in 1 M H ₂ SO ₄ for 1 h.	91
Figure 4.10 Current density vs. potential (<i>J-E</i>) behavior of electrodeposited Ni/p-Si electrodes in 1 M H ₂ SO ₄ under 1 Sun AM1.5 illumination as a function of Ni catalyst loading.....	92
Figure 4.11 Current density vs. potential (<i>J-E</i>) behavior for electrodes in H ₂ -saturated 1 M H ₂ SO ₄ . Illuminated 1 Sun AM1.5 photoelectrochemical behavior for p-Si photocathodes with no co-catalyst (black), electrodeposited Ni (blue), NiATSM (red), and Pt (green), as well as a buried junction n ⁺ p-Si with NiATSM (magenta).....	93

LIST OF TABLES

Table 2.1 Aliphatic and Aromatic Amines used in the Transamination Reactions with Molecule 2. Structure of the Products are shown in Figure 2.1.....	23
Table 3.1 Selected Bond Distances (Å) and Angles (deg) for Ni-1 – Ni-4	49
Table 3.2 Crystal Data and Structure Refinement for Ni-1 – Ni-4	51
Table 3.3 Comparison of the M(ATSM) and M-1 – M-4 (M = Cu or Ni) Electrochemical Events. Electrochemical Data of 0.3 mM Complex in 0.1 M Bu ₄ NPF ₆ /MeCN Solution at a Scan Rate of 200 mV/s with Potentials vs Fc ⁺ /Fc ⁰	55
Table 4.1 Photoelectrochemical Energy-conversion Parameters.	84

CHAPTER 1 INTRODUCTION

1.1 Lay Summary

This dissertation describes the development and expansion of a class of organic ligands known as bis(thiosemicarbazones) (BTSCs) and their corresponding metal complexes. Metal BTSC complexes are of interest due to their medical and catalytic applications. For example, some complexes have been utilized as disease imaging agents as well as therapeutics. Additionally, other complexes have been employed as catalysts that help convert protons into hydrogen gas as potential way to store renewable energy. The specific application of an individual metal BTSC complex depends on the variations in the BTSC ligand structure and the identity of the coordinated metal.

The BTSC ligand includes variable groups on the two sides of the molecule, which can be identical to each other (symmetric) or different (asymmetric). The symmetric variants have been thoroughly explored due to their ease of preparation. However, the asymmetric variants are lesser-known due to their more difficult and lengthy preparation. In this dissertation, the transamination reaction was explored for the synthesis of asymmetric BTSCs. In this reaction, a common asymmetric BTSC complex is prepared with one “fixed” group that is unreactive and one “leaving” group that can be displaced when new reagents are added. This reaction, while reported before, required further development to unlock its true potential.

With the ability to prepare a variety of BTSC complexes addressed, the focus of the dissertation shifts to the preparation and application of selected complexes. The first set of complexes were prepared as catalysts. Catalysts are molecules that lower the amount of energy required for a reaction to occur making the process easier and more efficient. The catalyzed reaction of interest in this dissertation is the hydrogen evolution reaction (HER), which generates hydrogen from water or similar sources. Most hydrogen used today is prepared by the decomposition of fossil fuels, which is environmentally unfriendly and unsustainable. The development of catalysts for HER is crucial as hydrogen is an industrially important chemical and it also exhibits potential to store renewable energy. The initial complexes developed in this dissertation were evaluated as electrocatalysts for HER, where electricity was used to drive the reaction. In the last section of this dissertation, the complexes were evaluated as photocatalysts, which use light as the energy source, for the HER.

1.2 Scope of Dissertation

This dissertation describes three studies related to the synthesis, characterization, and application of C_s symmetric BTSCs. The studies include: 1) the synthesis and characterization of nine new BTSC complexes as part of an evaluation of the transamination reaction; 2) eight new metal complexes with BTSC ligands having pendent N,N-dimethylethylenediamine groups that were studied as electrocatalysts for the hydrogen evolution reaction (HER); and 3) re-evaluation of NiATSM as part of a study to immobilize catalysts on surfaces for photocatalytic applications. A comprehensive list of the new compounds synthesized and evaluated are reported in this dissertation.

New ligands and metal complexes developed in these studies were characterized by nuclear magnetic resonance (^1H NMR and ^{13}C NMR), Fourier-transform infrared (FT-IR), and UV-Vis spectroscopies, electrospray ionization mass spectrometry (ESI-MS), elemental analysis, single crystal x-ray crystallography, and cyclic voltammetry. Additionally, copper complexes were characterized by electron paramagnetic resonance (EPR) spectroscopy. NiATSM, which was evaluated as heterogeneous HER catalyst while immobilized on a p-silicon surface, was characterized by additional techniques. These include linear sweep voltammetry (LSV) for complexes deposited on the electrode surface and scanning electron microscopy (SEM).

Chapter 1 of the dissertation provides a lay summary and overview of the dissertation and introduces bis(thiosemicarbazones) and the hydrogen evolution reaction (HER). Chapter 2 covers the exploration of the transamination reaction for the preparation of C_s symmetric BTSCs. In that chapter, the conditions for the optimization of the transamination reaction were investigated. Various functionalized primary amines were subjected to varying conditions for the transamination reaction. Key factors such as solvent and presence of an external base were determined to be crucial to the procurement of high yields and pure products. The chapter details the synthesis and characterization of the resulting transaminated species.

Chapter 3 discusses the synthesis and electrochemical characterization of HER for Ni(II) and Cu(II) BTSC's that contain bases and charged moieties on the pendent. The complexes were designed to evaluate the effect of pendent bases as proton relays, which can increase HER activity. Since the pendent base becomes protonated under the acidic conditions of catalysis, the pendent bases also introduce a charged site that could promote

HER by shifting the onset potential via through space electrostatic interactions. To decouple these two effects, derivatives with non-basic charged sites were prepared by alkylation and the results compared to the basic derivatives.

Chapter 4 covers the non-covalent attachment of a Ni(II) BTSC to a modified silicon electrode, in collaboration with the Spurgeon lab. This was of interest due to the possible photochemical HER properties of the modified electrode. Initially, the dropcast method was used to deposit the Ni(II) BTSC on the surface. However, once subjected to catalytic conditions the film was dislodged by the formation of hydrogen bubbles. This was remedied by the use of Nafion, a cation exchange polymer, to keep the film on the electrode. The dissertation concludes with a summary in Chapter 5 that provides concluding thoughts and possible further directions to the research Chapters 2 – 4.

1.3 Bis(thiosemicarbazones)

Bis(thiosemicarbazones) (BTSCs) are an emerging class of N_2S_2 tetradentate ligands that have a wide array of applications. These ligands are highly stable towards acidic conditions, easy to synthesize using bench top conditions, scalable due to the low cost of the reagents, and highly derivatizable. The main structural components of the BTSC ligands are the diimine backbone, two thiocarbonyl moieties, and a pendent amine groups (Figure 1.1). Due to the interchangeable nature of both the pendent and the backbone, a large library of BTSCs have been synthesized.

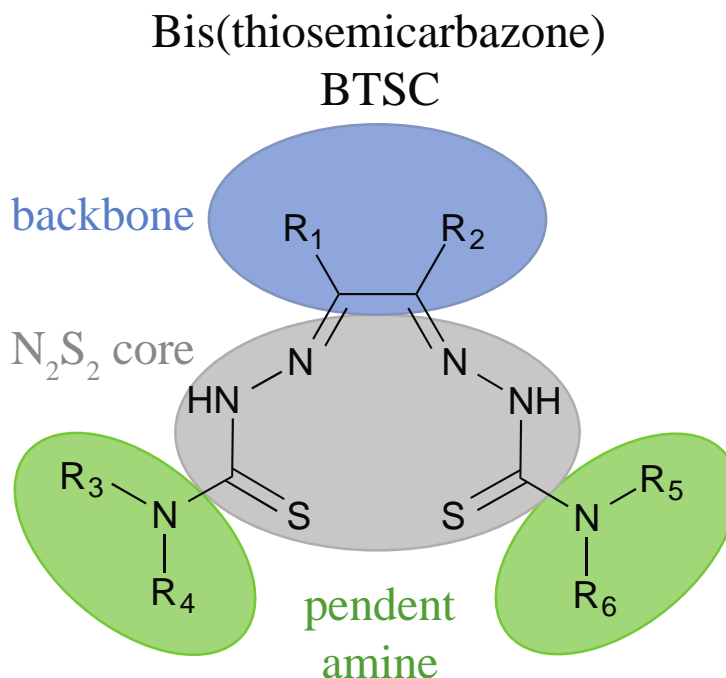


Figure 1.1 A representative of a BTSC showing the highly interchangeable nature. R1 and R2 represent the backbone moieties. R3 - R6 represent the pendent amine moieties.

Deprotonation of hydrazino protons in a BTSC yields a dianionic N_2S_2 ligand with the formal negative charges localized on the two sulfur atoms (Figure 1.2). When BTSC ligands are treated with a metal (II) salt, most commonly a metal (II) acetate, a complex is formed. The coordination environment of these BTSC complexes involve the nitrogen atoms of the diimine backbone bonding into the metal through the lone pairs and the anionic sulfur atoms. The ligand in the resulting complex is highly conjugated with a pi network consisting of alternating single and double bonds and p-type lone pairs on sulfur and the terminal amine nitrogens (Figure 1.3a). As a result, the complexes are often rigorously square planar, as shown for the $Cu(ATSM)$ in Figure 1.3b.¹ The ligand preference for square planar coordination favors the binding of late transition metals, such

as nickel and copper. The extended pi-network also facilitates ligand-centered reactivity with BTSC metal complexes undergo protonation/deprotonation and redox chemistry.

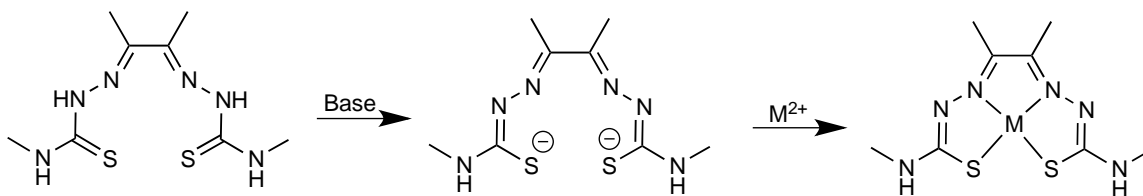


Figure 1.2 General BTSC complexation.

BTSC complexes have gained popularity as imaging agents,²⁻³ therapeutics,⁴⁻⁵ and as active catalysts.⁶⁻⁸ A review, by West *et al.* chronicled the synthetic approaches, characterization, and medicinal uses of Cu(II) BTSCs.⁹ In the review, it was noted that various bis(thiosemicarbazones) acted as anti-cancer, anti-fungal, and anti-viral agents. More recently, Donnelly and co-workers used Cu(II) BTSCs to image amyloid- β plaques that are prevalent in patients diagnosed with Alzheimer's disease.¹⁰ Due to the planarity of the BTSC framework, the complex can easily go through the blood-brain-barrier (BBB). Yet another imaging application is in the area of hypoxia imaging, as seen by Que and co-workers.¹¹ They prepared a fluorinated derivative of a BTSC for PET imaging to study cell hypoxia. Recently, BTSCs containing polyamine pendent groups were shown to selectively target a neuroblastoma cancer cell line.¹²

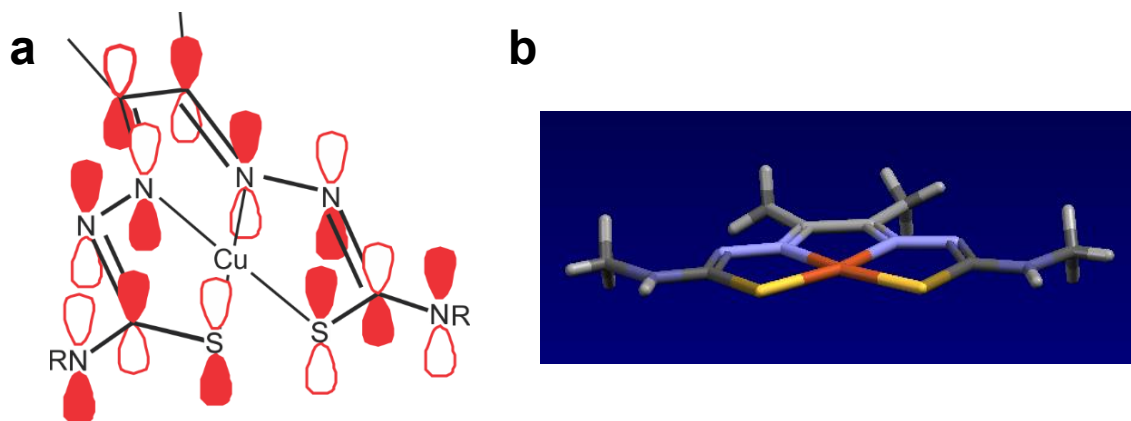


Figure 1.3 a) Orbital representation of conjugated network in metal BTSCs (excerpt from Vishnosky¹³). b) Representation of CuATSM x-ray structure showing planarity of metal BTSC core.

1.4 Electrochemistry

1.4.1 Cyclic Voltammetry

Electron transfer processes are commonly studied using electrochemistry. Electrochemistry provides the connection between the movement of electrons and chemical processes. Cyclic voltammetry (CV) is a technique commonly used to probe the electrochemical processes involved with changes in applied potential. The application of CV in catalysis has been proven to provide a crucial insight into elucidating electron-transfer processes. This involves the measurement of current based on applied potential. This is accomplished by sweeping the potential over a predetermined range and measuring the current (i) as a response to the change in potential. This cyclic sweep is done in both anodic (positive potential) and cathodic (negative potential) directions, at a constant scan rate (v). Peaks in the resulting spectrum indicate the reduction or oxidation potentials of events of the analyte. Furthermore, this also provides information about whether an event

is reversible, quasi-reversible, or irreversible. Figure 1.4 shows a reversible, quasi-reversible, and irreversible CV done in the US convention for plotting.

A three-electrode setup is most commonly used for CV experiments, the working electrode, counter electrode, and reference electrode. The applied potential is measured as the difference between the working and reference electrode whereas the current is measured as the difference in current between the working electrode and the counter electrode. The electrode setup for CVs commonly used in this thesis are glassy carbon for the working electrode, platinum as the counter electrode, and Ag/Ag⁺ as the reference electrode. In addition, ferrocene (Fc/Fc⁺) was added to the cell as an internal standard that allows different CVs to be compared.

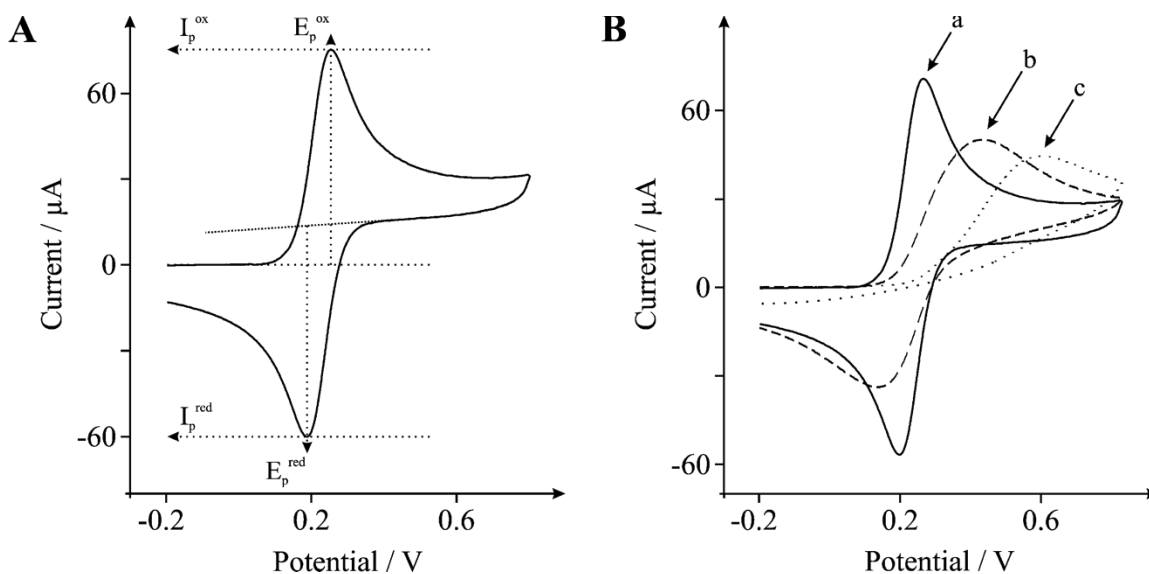


Figure 1.4 A) Illustration of a cyclic voltammogram using IUPAC convention with E_p as the peak potential and I_p as the peak current. B.) Cyclic voltammograms for a) reversible, b) quasi-reversible, and c) irreversible electrochemical processes. Republished with permission of Royal Society of Chemistry from Brownson, D. A.; Kampouris, D. K.; Banks, C. E., *Chemical Society reviews* **2012**, 41 (21), 6944-76¹⁴; permission conveyed through Copyright Clearance Center, Inc.

The solvent in CV experiments must be pure i.e. no contaminants that can interfere with the electrochemical analysis, can solubilize both the analyte and the supporting electrolyte, and has a wide window of redox potential. Acetonitrile was the solvent of choice for all CV experiments. The supporting electrolyte was used to balance any charged species that would interfere with the electrocatalytic measurements. Bu_4NPF_6 is a common supporting electrolyte used for acetonitrile solutions.

From the CV plot of current (i) vs applied potential (V), the reduction and oxidation events as well as the number of electrons involved in the electrochemical processes can be observed. The peak to peak separation (ΔE_p) provides the information of the reversibility of the process. Reversible process entails that the Fc^+ gets reduced to Fc during the negative direction and gets fully oxidized in the positive direction. The peak to peak separation, $\Delta E_p = 57$ mV for reversible processes, as derived from the Nernst equation.

In this system with stagnant solution and presence of supporting electrolyte, the pertinent mode of mass transport from the bulk solution to the electrode surface is through diffusion. The relevant equation that relates the diffusion coefficient with current is the Randles-Sevcik equation (1.1) where F is the Faraday's constant, A is the surface area of the electrode, C is the analyte molar concentration, R is the gas constant, T is the temperature in Kelvin, ν is the scan rate and D is the diffusion coefficient.

$$i_p = 0.4463FAC\sqrt{\frac{F\nu D}{RT}} \quad (1.1)$$

A linear plot of i_p vs the square root of the scan rate (ν) suggests reversible electrochemical process. Deviations in the linearity imply quasi-reversible process or adsorption of the analyte on the electrode surface. Therefore, determination of the diffusion

coefficient is essential prior to catalysis studies to ensure that the analyte is freely diffusing and that heterogeneous catalysis does not occur.¹⁵

1.4.2 Overpotential and Turnover Frequency (TOF)

The ideal electrocatalysts developed for renewable energy applications should be robust, fast and energy efficient.¹⁶ Energy efficiency is highly dependent on overpotential. Overpotential (η) is the amount of energy per Coulomb needed to drive the reaction from equilibrium condition to the catalytic event. Overpotential is influenced by a variety of factors encompassing both catalyst properties and the conditions used. A catalyst property that can affect overpotential is the presence of proton relay. This relay can be introduced by adding basic sites on the ligand, which leads to increased activity by allowing for faster facilitation of the proton to the catalytic core. This usually leads to lower overpotential.¹⁷ Similarly, choice of solvent, choice of acid (an HER specific issue), and metal center has an effect on overpotential as well.

Another important benchmark for catalytic efficiency is the turnover number (TON). TON is the number of moles of product that is generated by one mole of the catalyst until it becomes inactive. To measure this, the catalyst is electrolyzed at a pre-determined potential for a period of time. The charged generated through the solution is recorded and a blank is run at the same potential and for the same amount of time. These values are subtracted from one another and are multiplied by the catalyst concentration to give the final TON. Yet another important benchmark is the turnover frequency (TOF). TOF is a measure how fast a catalyst can turnover product before being rendered inactive. TOF can be measured in different ways depending on the proposed mechanism of the catalyst. TOF

is directly proportional with the overpotential. Determining the overpotential, TON, and TOF for a catalytic process are crucial for measuring the efficiency of a catalyst.

1.5 Hydrogen and the Hydrogen Evolution Reaction (HER)

The increasing demand for energy production is a problem of today's society. Most current projections show that the reserves of petroleum will last 40 years, natural gas 60 years, and coal 150 years.¹⁸ The search for carbon-free alternatives has been underway for decades. Hydrogen is viewed by many as a promising energy source due to a variety of factors—the relative abundance of hydrogen in the universe, the low molecular weight coupled with high energy output, and the only waste product being water. However, problems also arise for the use of hydrogen, mainly the current high cost to produce, store, and transport.¹⁹⁻²¹ Despite these challenges, further research has been conducted into the generation and storage of hydrogen.

An efficient way to produce hydrogen that has been of much interest in the literature is the hydrogen evolution reaction (HER), equation 1.2.^{7-8, 22-26}



HER involves the reduction of two protons into one molecule of hydrogen (H₂) gas. The production and utilization of hydrogen in nature is facilitated by metalloenzymes referred to as hydrogenases. There are three different classifications of hydrogenases based on the metals found in the active site— [NiFe], [FeFe], and Fe-Only (Figure 1.5). The [NiFe] hydrogenase is noted for its ability to generate hydrogen as well as utilizing hydrogen oxidation for generation of other products.²⁷ [FeFe] hydrogenase is noted for its higher activity towards H₂ production than the other two classes of hydrogenases. The notable

features of the active site for this hydrogenase is the dithiolene bridge and pendent amine.²⁷ These moieties are frequently used in the framework for catalysts for HER. Lastly, Fe-Only hydrogenase is the most recent hydrogenase found only in methanogenic archaea. Methanogens have both [Ni-Fe] and Fe-Only hydrogenases. Fe-Only hydrogenase catalyzes one of the reaction steps of the formation of methane from carbon dioxide and H₂.²⁸

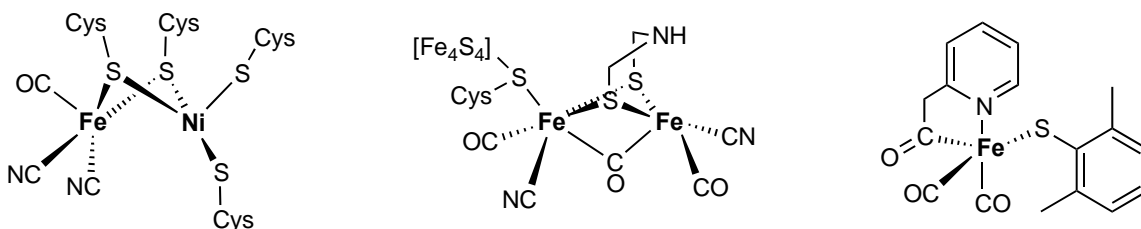


Figure 1.5 Structures of the active sites of [NiFe], [FeFe], and Fe-Only hydrogenases found in sulfate-reducing bacteria ([NiFe], [FeFe]) and in methanogenic archaea (Fe-Only).²⁸

Since the discovery of the hydrogen evolution process in nature, much research has been done to replicate the process in a laboratory setting. Various catalysts have been synthesized, characterized, and tested for hydrogen evolution. Researchers have strived to create catalysts active in similar conditions to the naturally occurring hydrogenases. However, in contrast to the enzymatic process found in vivo, synthetic catalysts for hydrogen evolution are experimentally tested in either heterogeneous or homogeneous conditions.

Heterogeneous catalysis occurs when the substrate and the catalyst are in different phases of matter. Most industrialized catalytic processes are done heterogeneously. A prominent example of heterogeneous catalysis is the steam reforming where solid nickel

catalyst is used to facilitate the oxidation of hydrocarbons with water to produce hydrogen and carbon dioxide. Similarly, the Haber-Bosch process, used to generate ammonia by combining nitrogen and hydrogen, utilizes iron oxides fused on alumina as catalyst. Figure 1.6 shows an example of HER on a heterogeneous catalyst surface. Heterogeneous catalysis is appealing to both academia and industry alike due to the stability of catalysts on the surface as well as the ability to regenerate the catalyst once it becomes inactive through repeated use.

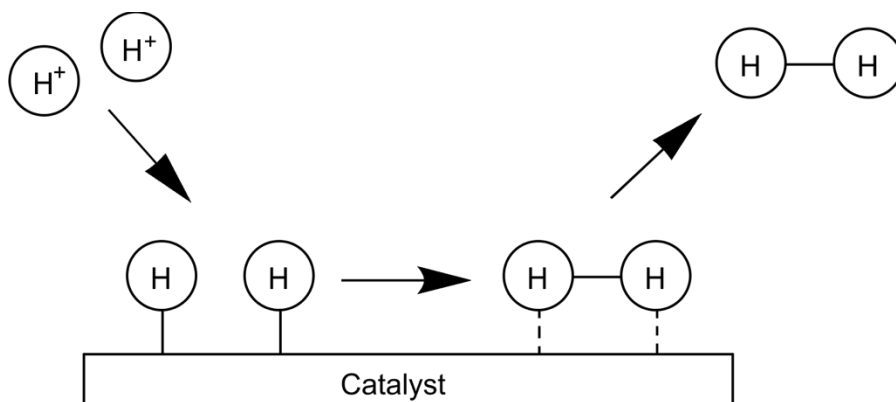


Figure 1.6 Depiction of heterogeneous HER catalysis.

Homogeneous catalysis, in contrast, occurs when the substrate and catalyst are in the same phase of matter, such as when both are dissolved in a solvent. This allows for easier elucidation of the mechanism of the catalyst as the reaction can be evaluated by a variety of physical and spectroscopic techniques.²⁹⁻³⁰ In addition, selectivity of the reaction is easier in a homogeneous reaction. However, homogeneous catalysis has its drawbacks as well. Most solvents, usually organic solvents, used in homogeneous catalysis are too volatile to remain in a liquid phase under temperatures above 100 C°. This limits industrial

applications of this technique due to the need for higher pressures to keep the reaction homogeneous or rapid cooling to avoid a runaway reaction. These problems are avoided on a laboratory scale but need to be considered before scaling up to the industrial level. Furthermore, separation of the product from the reaction mixture can be challenging. All liquid solvents have the capacity to dissolve gases, which means that there will always be a portion of the product to remain in the reaction mixture. Similarly, due to the volatile nature of organic solvents, the vapor could mix with the gaseous product leading to impure product. Despite these drawbacks, homogeneous catalysis is widely studied.

Due to the relative ease of elucidating mechanisms for hydrogen evolution, homogeneous catalysis has been explored in great depth in the literature. Homogeneous hydrogen evolution is traditionally known to occur through two distinct pathways, heterolytic and homolytic (Figure 1.7). When describing mechanisms, electrochemical events are typically denoted as “E” and chemical events, such as a protonation, are typically denoted as “C”. For example, in Figure 1.7 the heterolytic pathway could follow ECEC mechanism or a CEEC mechanism. If the initial electrochemical and chemical events are concerted, it is considered as a proton-coupled electron transfer reaction. The homolytic pathway is considered as an ECC mechanism. Presence of certain metals as well as ligands can favor certain pathways over others.

Heterolytic hydrogen evolution is theorized to occur when the catalyst undergoes an electrochemical reduction and protonation, to yield a hydrogen atom bound species. This can undergo another electrochemical reduction to generate a hydride bound species.

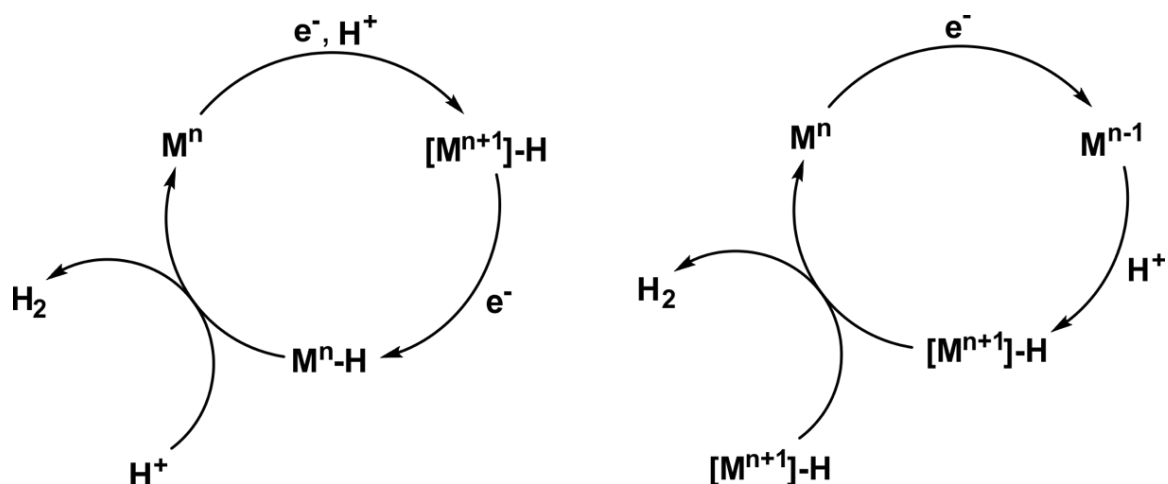


Figure 1.7 Examples of heterolytic (left) and homolytic (right) pathways to hydrogen evolution.

Subsequently, the hydride species will react with free proton to generate dihydrogen and regenerate the catalyst. Conversely, homolytic hydrogen evolution occurs when a catalyst undergoes an electrochemical reduction and protonation to a hydrogen atom bound species. These two hydrogen atom bound species come together and release dihydrogen and regenerate the catalyst. Both of these approaches involve the metal playing the active role in the catalytic process.

Platinum and other platinum group derived catalysts are very efficient hydrogen evolution catalysts. However, the rarity and high cost of this metal has led the search for more sustainable catalysis. Recently, there have been investigations into earth-abundant hydrogen evolution catalysis.^{7-8, 22, 24-26, 31-35} These catalysts employ metals such as copper, nickel, cobalt, aluminum, and zinc to produce hydrogen from acidic sources. These catalysts have also served to shed light on the role of the ligand in the catalysis process.

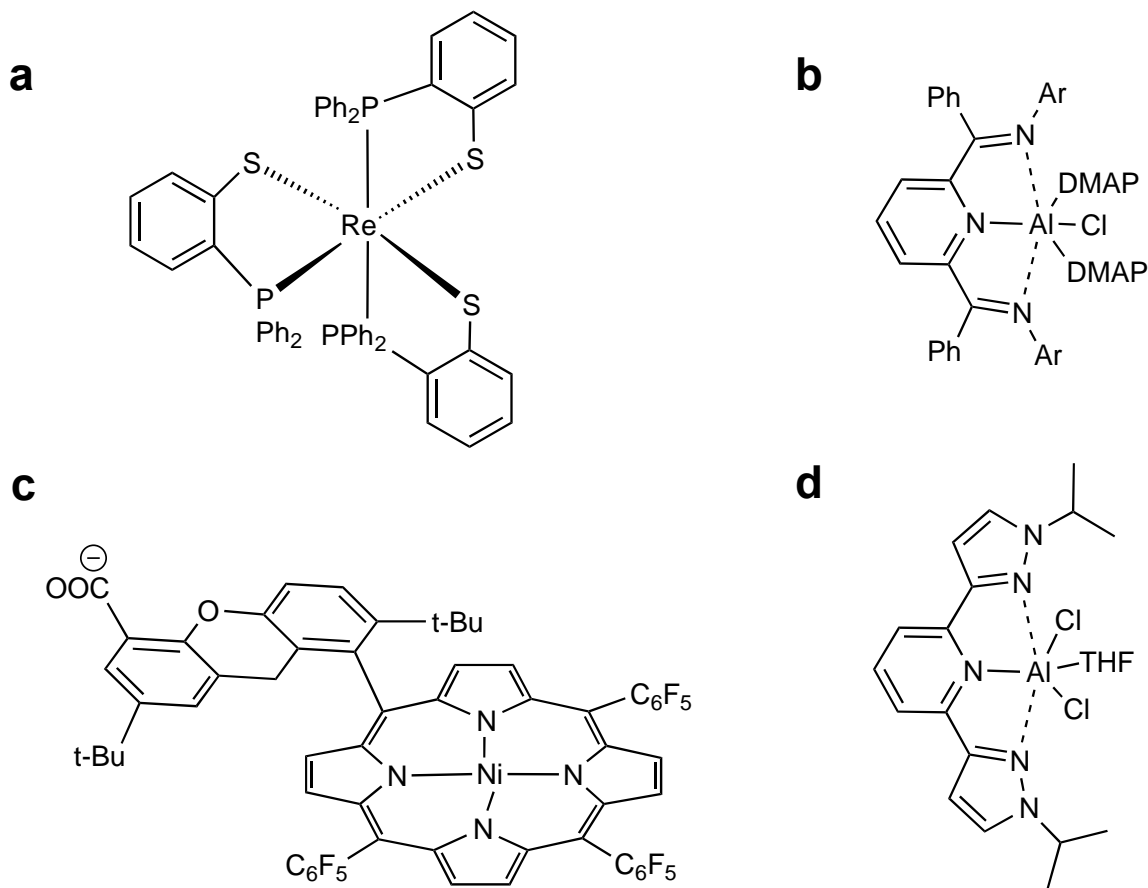


Figure 1.8 A sampling of previous HER catalysts. a) $\text{Re}(\text{PS})_3$ complex studied by the Grapperhaus lab. b) Neutral Aluminum bis(imino)pyridine complex studied by the Berben group. c) “Hangman” nickel porphyrin complex studied by the Nocera group. d) Charged Aluminum bis(pyrazole)pyridine complex studied by the Berben group.

All of the ligands that were used in these catalysts were found to play an active role and assist in the catalysis in some manner. This approach to use a ligand that plays active role in the catalysis, instead of a passive role, is referred to as ligand non-innocence. This is a new and exciting development in the field of hydrogen evolution catalysis.

There are many examples of ligand-assisted HER catalysis in the literature.^{8, 24-26, 31-39} Selected examples are shown in Figure 1.8. The Grapperhaus group has explored rhenium tris(phosphinethiolato) ($\text{Re}(\text{PS})_3$) complex.^{24, 40} This system was previously

explored for its ability to bind ethylene reversibly.⁴⁰ Due to similarities between ethylene and hydrogen, these systems were evaluated for HER. The catalyst was found to have moderate catalytic activity when treated with acetic acid. The kinetic isotope experiments led to two different proposed mechanisms. The result novel concept was that both of these proposed mechanisms involved the generation of a ligand-hydride species instead of a metal hydride. However, recent theoretical study by Brothers, Hall, and Grapperhaus indicate that a metal hydride route is also thermodynamically competent.⁴¹

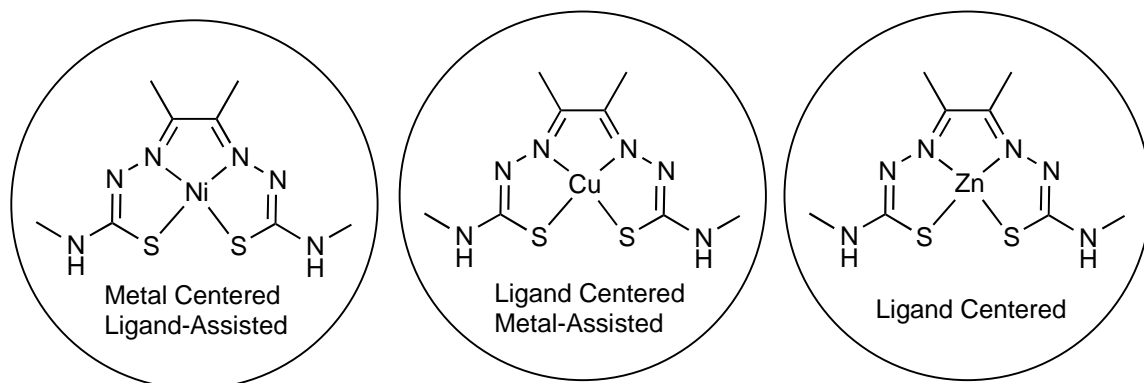
Another HER system that experimentally displays ligand co-operativity is the nickel bis(diphosphine) proton relay catalysts developed by DuBois and Bullock.³⁸⁻³⁹ These catalysts are bio-inspired due to the presence of a pendent amine base found in the [FeFe] hydrogenases. When tested for HER, the catalyst was found to be highly active in both acetonitrile and water. The high activity was attributed to the role of the pendent amine in effectively shuttling protons to the nickel center during catalysis. These experiments demonstrate the high degree of influence that the ligand and its secondary coordination sphere can have on catalysis.

The secondary coordination sphere was also explored by the Nocera group when they tested the HER capabilities of “Hangman” porphyrins.³¹⁻³² These catalysts are notable due to the presence of a carboxylic acid group that hangs over the porphyrin center. In the absence of acid, it was observed two reversible events with an irreversible event in between. When acid was titrated with the catalyst, the irreversible wave displayed catalytic character. Through DFT studies, it was determined that the porphyrin ring was storing the hydride equivalent as a reduced species instead of the metal. This indicated that the bonds

of the ligand could also be used to store electrons and protons for catalysis instead of relying on the metal center to be the sole catalytic site.

The Berben group synthesized and characterized neutral and charged aluminum bis(imino)pyridine complexes for HER.³³⁻³⁴ While both complexes tested were active for HER, it was noted that, despite being similar ligand frameworks, that they went through different mechanisms. Ultimately, this was attributed to the difference in ligand pKa, which indicated that the ability to tune ligand pKa is essential for the ability of a catalyst to generate and store hydride species.

Recently, the Grapperhaus/Buchanan group and others have explored metal BTSC complexes as HER electrocatalysts.^{7, 22, 26, 36, 42-43} Due to the redox activity and multiple basic sites on the ligand, the reaction mechanism can follow a ligand-assisted metal-centered, ligand-centered, or metal-assisted ligand-centered pathway (Scheme 1.1). As noted by Haddad et al.,⁸ the identity of the metal dictates the initial site of protonation and reduction and determines the reaction pathway. For NiATSM, the initial event is ligand-centered reduction followed by ligand-centered protonation. The second reduction occurs at the metal resulting in a transfer of the proton from the ligand to the metal to yield a metal hydride. The reaction follows an ECEC pathway classified as a ligand-assisted metal-centered pathway with a TOF of 5500 s⁻¹ at an overpotential of 0.55 V. In contrast, for CuATSM initial ligand centered protonation is followed by a metal-centered reduction. The next protonation and reduction events occur on the ligand, which is the site of hydrogen evolution. The reaction follows a CECE mechanism classified as metal-assisted ligand-centered with a TOF of 10,000 s⁻¹ at an overpotential of 0.78 V. Finally, for ZnATSM the



Scheme 1.1 The nickel, copper, and zinc form of the ATSM ligand have varying pathways for HER as determined experimentally.

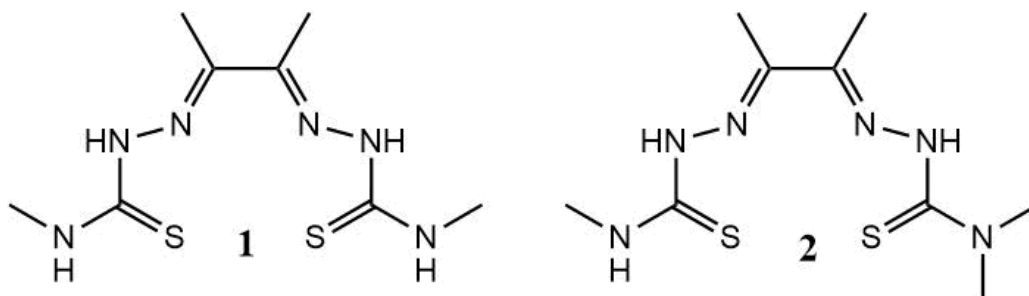
metal is redox inert and all of the protonation and reduction events are ligand-centered. The TOF of ZnATSM is 1170 s^{-1} at an overpotentials of 0.75 V.

In the following chapters of this dissertation, the synthesis of the ATSM ligands were explored. Also, the modification of the ATSM ligand structure were investigated to improve the HER activity of the Cu and Ni BTSC electrocatalysts. Furthermore, in collaboration with the Spurgeon lab, a heterogeneous catalyst was fabricated by attaching the NiATSM complex to p-Si surface. The photocatalytic properties of the NiATSM film reveal the potential application of BTSC complexes for energy storage.

CHAPTER 2 FACILE AND EFFICIENT SYNTHESIS OF C_S -SYMMETRIC
BIS(THIOSEMICARBAZONES) WITH FUNCTIONALIZED PENDENT AMINES

2.1 Introduction

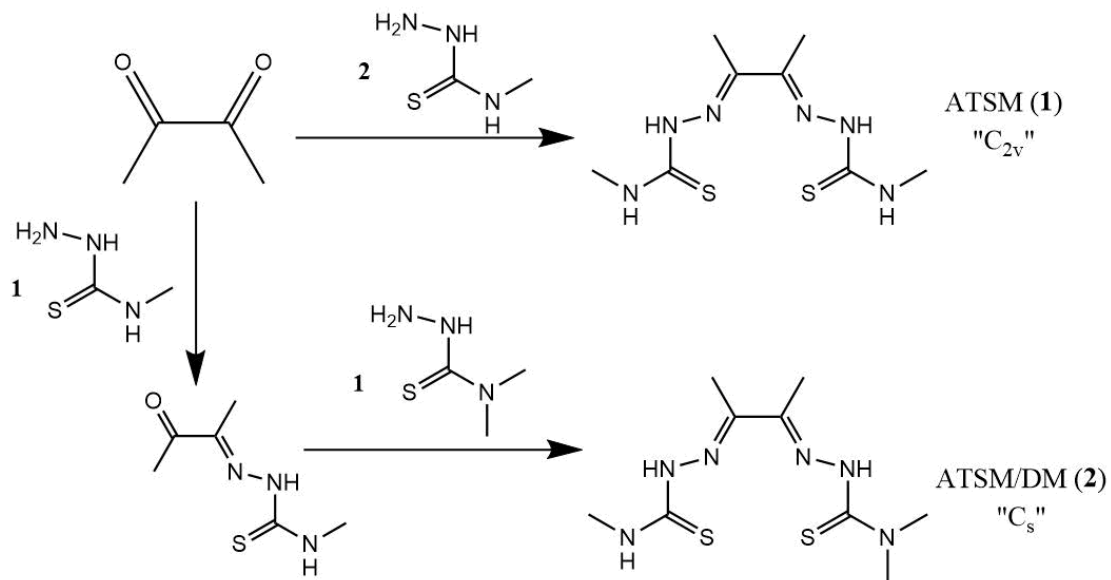
Bis-thiosemicarbazones (BTSCs) are an important class of ligands for the synthesis of transition metal complexes with various applications.¹⁻⁷ Among the most studied BTSCs is diacetyl-2,3-bis(N-methyl-3-thiosemicarbazone) (H_2ATSM , **1**, Scheme 2.1).¹ Deprotonation of **1** yields a dianionic N_2S_2 chelate with non-coordinating, pendent amines. Numerous derivatives of **1** with variation of the pendent methylamine with other amines have previously been reported, including diacetyl-2,3-(N-methylthiosemicarbazone-N'-dimethylthiosemicarbazone) ($ATSM/DM$, **2**, Scheme 2.1).⁸



Scheme 2.1 Structures of H_2ATSM (1) and H_2ATSM/DM (2)

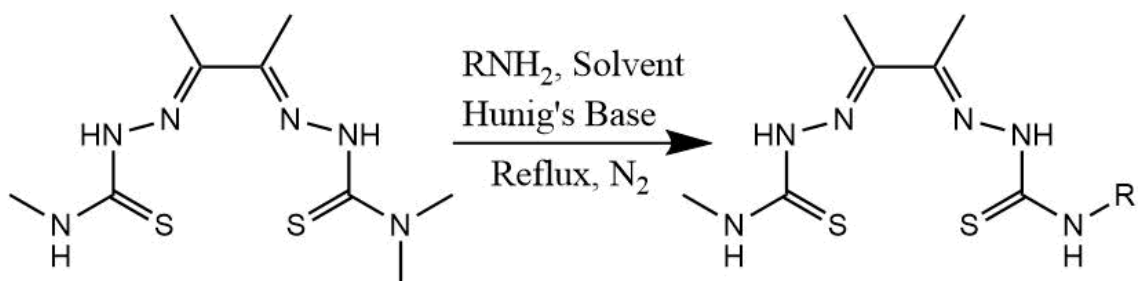
The general synthesis of **1** and its derivatives involves a condensation reaction between 2,3-butanedione and the appropriate thiosemicarbazide(s), many of which are commercially available. As shown in Scheme 2.2, C_{2v} -symmetric BTSCs like **1** can be

prepared in a single step. For C_s -symmetric BTSCs, like **2**, a stepwise approach is required, Scheme 2.2. Using these approaches, a large number of BTSCs have been prepared.^{4,6,8,10} However, the routes are limited by the commercial or synthetic availability of the semithiocarbazide precursor. An alternate route to C_s -symmetric BTSCs involves the transamination of **2**, Scheme 2.3, as first reported by Lin and later improved by Büncic.^{9,11,12} Lin obtained C_s -symmetric BTSCs in 36 – 45% yield upon reaction of pyridyl- and benzylamines with **2** in acetonitrile. Higher yields (50 – 86%) were obtained by Büncic for the transamination of **2** with aromatic aminosulfonic acids in acetonitrile and dimethylformamide. These same reaction conditions were used by Paterson for the transamination of **2** with aminocarboxylic acids (81 – 86%), aminocarbamates (81 – 87%), and polyamines (81 – 89%).^{4,13} A similar approach using Hünig's base for the transamination of **2** with 2,2,2-trifluoroethylamine hydrochloride in DMF yielded 79% of the C_s -symmetric BTSC.⁷



Scheme 2.2 Synthesis of H_2ATSM and H_2ATSM/DM .

In biochemistry, the transamination reaction involves amination and deamination processes to synthesize a new amino acid. In this reaction, the amino group receptors are sp^2 hybridized carbons. This biological process is catalyzed by enzymes known as transaminases with ketoacids, such as α -ketoglutarate, as the amino group receptor. Similarly, synthetic transamination reaction occurs via amination and deamination of an sp^2 hybridized carbon with the assistance of a strong, non-nucleophilic base. The scope of the transamination reaction of **2** through optimization of the synthetic strategy to include synthesis of new H₂ ATSM derivatives with primary amines containing functionalized substituents for further ligand modifications. A variety of “R” groups on the primary amine were investigated, including both aliphatic and aromatic amines, as well as the effect of reagent ratio, reaction solvent, and aromatic ring activation. Isolated products were characterized by ¹H and ¹³C NMR spectroscopy as well as elemental analysis.



Scheme 2.3 Generalized transamination reaction

2.2 Results and Discussion

The transamination reaction of **2** with a series of primary amines was investigated in order to develop the scope of the reaction. This one-pot, synthesis approach was found to be effective using polar aprotic solvents. The choice of this type of solvent was due to

the ability to solubilize the starting amine, to not interfere with the reaction mechanism, and to be easily removable. Acetonitrile and tetrahydrofuran both fulfill these requirements. A summary of the results is provided in Table 2.1 whereas the structures of the products are illustrated in Figure 2.1. Initial reactions were carried out in acetonitrile

Table 2.1 Aliphatic and Aromatic Amines used in the Transamination Reactions with Molecule **2**. Structure of the Products are shown in Figure 2.1.

Aliphatic amines	Conditions*	Yield (%)	Melting point (°C)
C₄H₁₂N₂ (3)	1	14	213.4 – 215.1
C₄H₁₂N₂ (3)	2	87	213.4 – 215.1
C₂H₇NS (4)	2	98	213.6 – 214.3
C₂H₇NO (5)	2	98	234.1 – 234.4
C₄H₉NO₂ • HCl (6)	2	85	236.7 – 240.0
C₄H₁₂N₂ (12)	2	73	n/a
Aromatic amines	Conditions*	Yield (%)	Melting point (°C)
C₆H₇NO (7)	2	62	231.2 – 232.7
C₆H₇NO (7)	3	98	231.2 – 232.7
C₉H₁₃N (8)	2	32	214.5 – 221.1
C₉H₁₃N (8)	3	77	214.5 – 221.1
C₈H₁₂N₂ (9)	3	58	213.1 – 215.5
C₇H₉NO (10)	3	82	219.9 – 220.9
C₆H₆FN (11)	3	79	228.7 – 229.6

*conditions: (1) Reflux 24h under N₂ in MeCN, 1:1 ratio of amine to **2**. (2) Reflux 24h under N₂ in MeCN, 2:1 ratio of amine to **2**. (3) Reflux 24h under N₂ in THF, 2:1 ratio of amine to **2**.

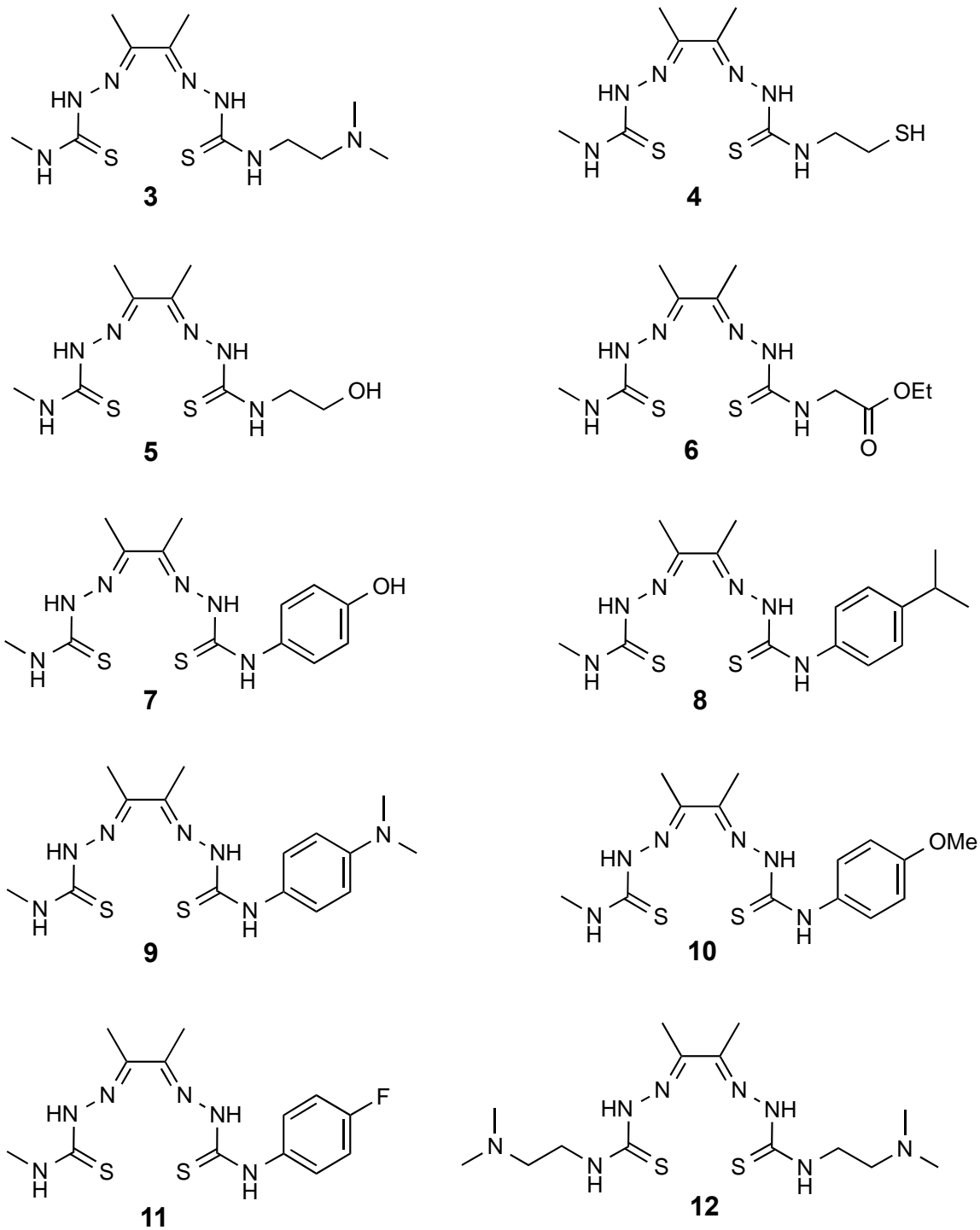
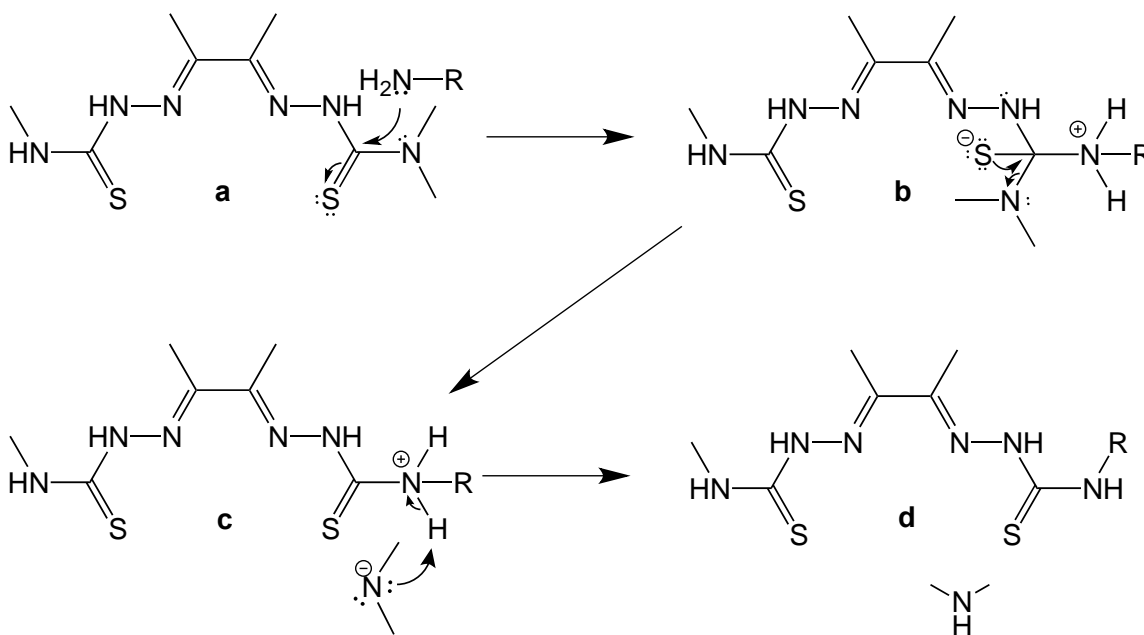


Figure 2.1 BTSC ligands synthesized using the optimized transamination reaction between molecule **2** and the amines in Table 2.1.

with Hünig's base (1.5 eq.) added to the reaction mixture as a weak base to facilitate deprotonation of the proposed intermediate (Scheme 2.3 and 2.4). All reactions were refluxed for 24 hours under an N₂ atmosphere. When a 1:1 ratio of N,N-dimethylethylenediamine to **2** was employed in acetonitrile with 1.5 eq. of Hünig's base (condition 1), the C_s-symmetric BTSC compound **3** was obtained in very poor isolated yield of 14%. Increasing the ratio of the amine to **2** to 2:1 (condition 2) improved the yield of **3** to 87%. Under the same 2:1 conditions of amine to **2** in acetonitrile, isolated yields of 77 – 98% were obtained for the C_s-symmetric BTSCs **4 – 6** when 2-aminoethanethiol, 2-ethanolamine, or ethyl glycinate hydrochloride were employed as the primary amine. The results with aliphatic amines show the transamination reaction is tolerant of thiol, alcohol, ester, and ester functional groups.



Scheme 2.4 Proposed transamination mechanism. a) Primary amine initiates a nucleophilic attack on thione of BTSC then the b) Tetrahedral intermediate is formed and begins to collapse. c) The dimethylamide anion is ejected and in a concerted fashion, abstracts the proton of ammonium leading to d) Transaminated product and dimethylamine byproduct.

In the proposed mechanism (Scheme 2.4) for the transamination reaction, the thiocarbonyl is subjected to a nucleophilic attack by the primary amine. This forms a tetrahedral intermediate which will collapse and eject the dimethyl amide group. The amide is protonated by a hydrogen from the charged intermediate resulting in the formation of the transaminated product. The addition of Hünig's base, as an exogenous base, allows for faster deprotonation of the charged species "c".

Structural information for all new compounds were elucidated using ^1H and ^{13}C NMR. Representative spectra (Figure 2.2 and 2.3) of **6** is shown below. For the ^1H NMR, the most identifying feature of the presented C_s symmetric ligand is the four -NH peaks found at, roughly 10.60, 10.20, 8.60, and 8.30 ppm. The methylene observed at 4.30 ppm is from the transaminated glycine ethyl ester. The well-established ethyl pattern is also observed at 4.10 ppm (-CH₂) and 1.20 ppm (-CH₃). The two overlapping backbone methyl

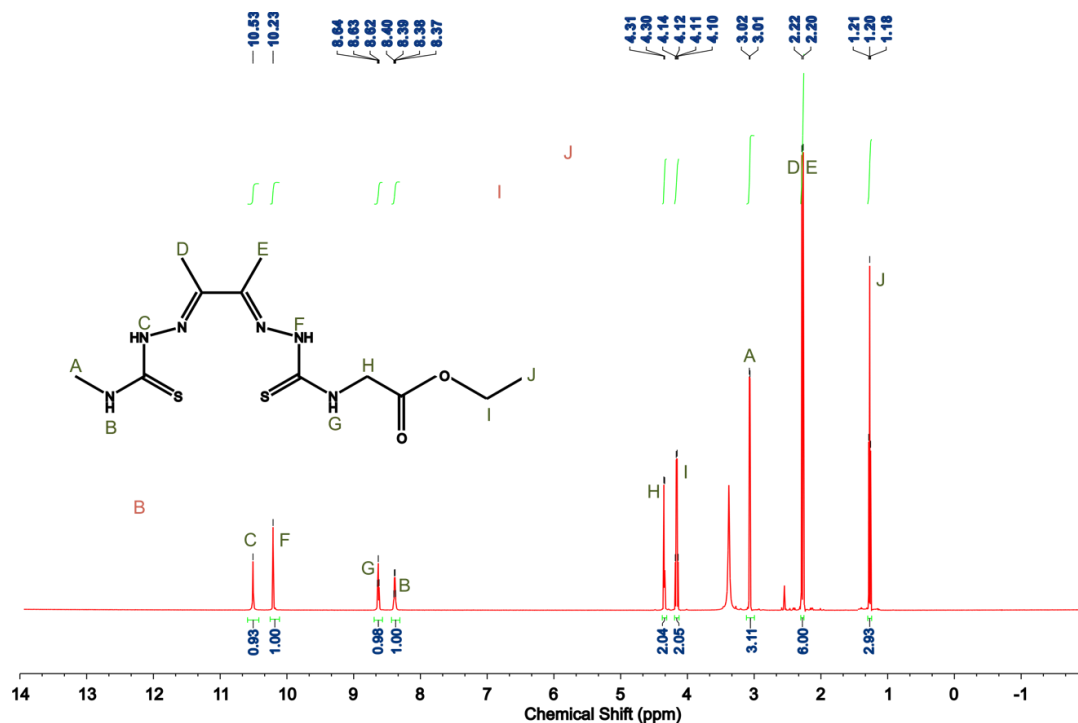


Figure 2.2 ^1H NMR Spectrum of **6** in d_6 -DMSO.

peaks are observed between 2.22 ppm and 2.20 ppm. In addition, the pendent methyl (-CH₃) near 3.01 ppm is a common feature for all spectra.

As for the ¹³C NMR, the pair of thiocarbonyl (-C=S) peaks appear at 179.31 ppm and 178.93 ppm. In addition, there are the pair of imine (-C=N) peaks at 149.21 ppm and 148.14 ppm. These features are found in all of the C_s symmetric bis(thiosemicarbazone) products characterized here. The carbonyl (-C=O) of the transaminated glycine is observed at 169.75 ppm, while the methylene peak is seen at 45.94 ppm and the ethyl ester peak pattern is observed at 60.93 ppm (-CH₂) and 14.59 ppm (-CH₃). The peak at 31.68 ppm corresponds to the pendent methyl group and there is, similar to what is seen in the ¹H NMR, a set of overlapping peaks at 12.33 ppm and 12.11 ppm that correspond to the backbone methyl groups.

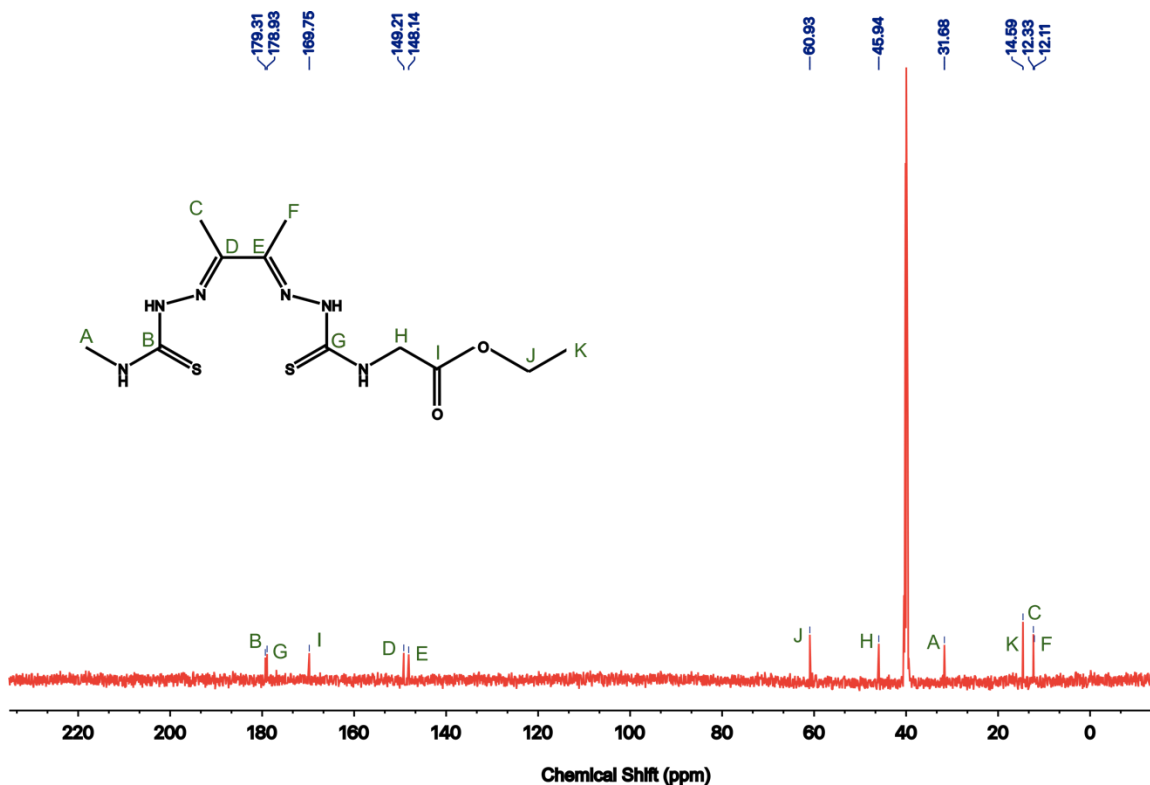


Figure 2.3 ¹³C NMR Spectrum of **6** in d₆-DMSO.

The aromatic amines precursors to **8** and **9**, 4-aminophenol and cumidine, reacted with **2** using the optimized conditions used for aliphatic amines produced a poor to average (62% and 32%, respectively) yield. The lower yields were attributed to the relatively poor solubility of the aromatic amines in acetonitrile as compared with the smaller, more polar aliphatic amines. Improved yields were obtained when the solvent was changed from acetonitrile (condition 2) to tetrahydrofuran (condition 3), which has a dielectric constant of 7.58 compared to 37.5 for acetonitrile. Using a 2:1 ratio of amine to substrate in THF, isolated yields of the C_s-symmetric BTSC compounds **8** and **9** improved to 77 – 98% for the aromatic amines 4-aminophenol and cumidine. This led to the use of THF for 4-anisidine, 4-fluoroaniline, and dimethyl-4-phenylenediamine as well to avoid the low yields. A notable exception to the success of transamination with aromatic amines in THF was the strongly deactivated compound p-nitroaniline, which has a Hammett parameter of +0.778 and is not a strong enough nucleophile to attack the substrate. Attempts to obtain isolable product by increasing the amine to substrate ratio to 4:1 were unsuccessful.

Figures 2.4 and 2.5 are the representative ¹H and ¹³C NMR spectra of the product, **9**. With respect to the ¹H NMR of the backbone methyl peaks (D and E) and the pendent methyl peak (A) are at the same chemical shifts. The N-H on the pendent (B) and the N₂S₂ core (C) of the non-transaminated side are also identical between the spectra of **6** and **9** (Figure 2.2 and 2.4). The difference is that the N-H on the pendent (G) and N₂S₂ core (F) of the transaminated side of the aromatic amine product **9**, have shifted downfield as compared to the aliphatic amine, **6**. This is expected due to the different electronic properties of the aromatic ring versus the aliphatic chain. However, this demonstrates that

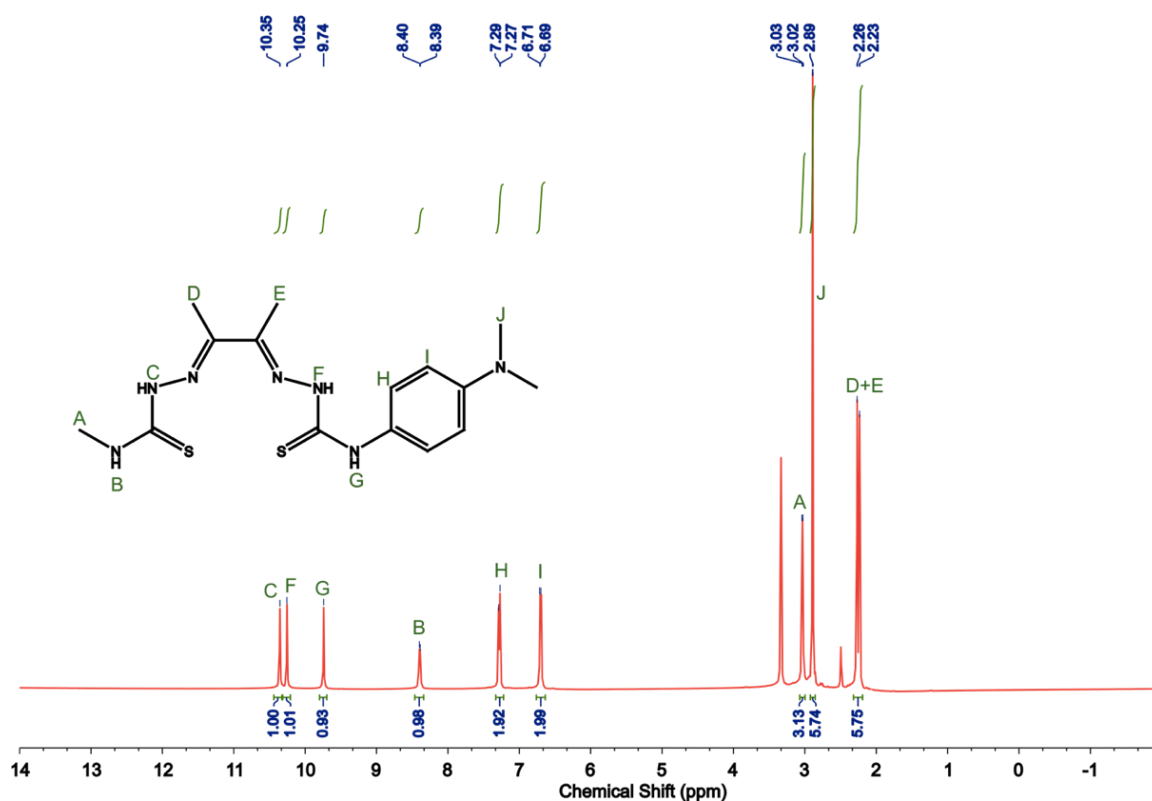


Figure 2.4 ^1H NMR Spectrum of **9** in d_6 -DMSO.

the electronics are not significantly changed between the transamination using aliphatic aliphatic and aromatic groups. Unlike the ^1H NMR, very little change is observed between the ^{13}C NMR spectra of **6** and **9**. This is an even more convincing indication that presence of aliphatic or aromatic pendent amine doesn't drastically affect the electronic structures of the BTSC core or backbone.

The spectral analysis of the aliphatic primary amines containing functional groups such as thiols, alcohols, tertiary amine, and esters have shown the versatility of the transamination reaction. This is due, in part, to their solubility in acetonitrile, unhindered nature, and lack of interference on the mechanism of the reaction. However, when amines, both aliphatic and aromatic, that contained acidic functional groups were tested, charged

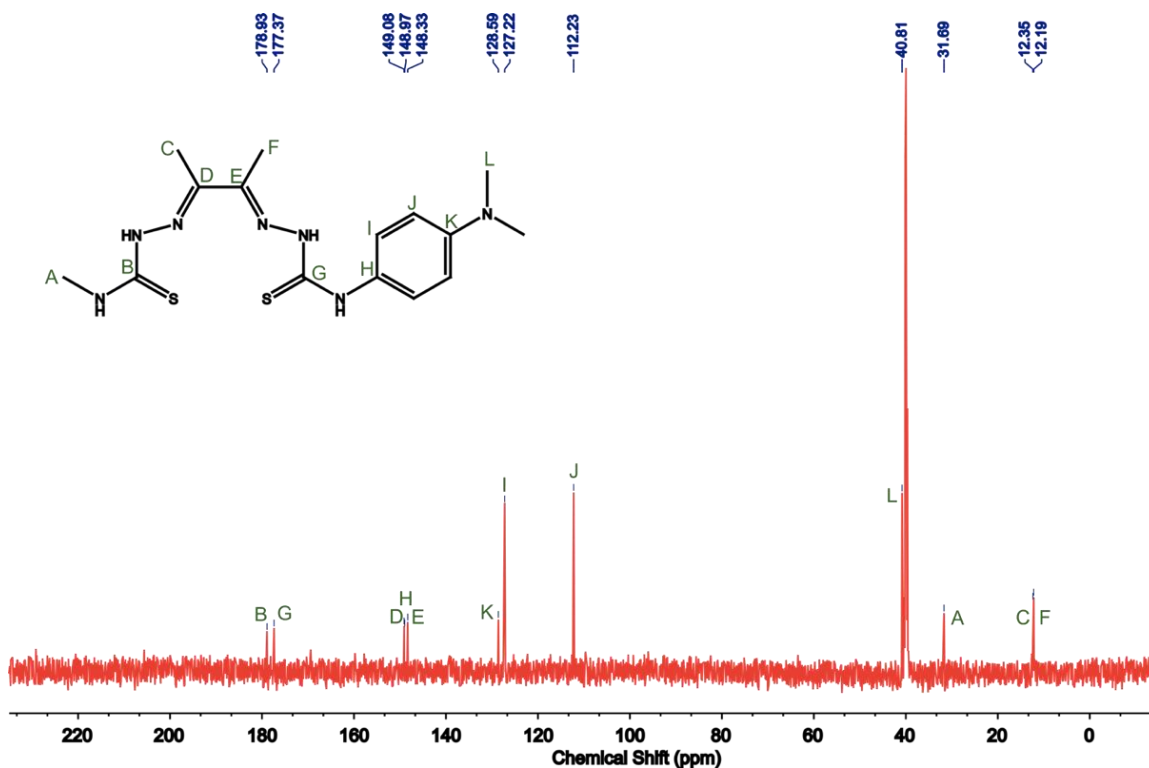


Figure 2.5 ^{13}C NMR Spectrum of **9** in d_6 -DMSO.

side products were observed. For example, when the transamination with glycine was attempted to yield the product in Figure 2.6a. The reaction resulted to a mixture of transamination product and corresponding dimethylammonium salt, Figure 2.6a and Figure 2.6b, respectively. This can be attributed to the capture of the acidic proton of the newly installed glycine by the dimethylamine leaving group.

The ^1H NMR of the resulting product from the transamination of (**2**) with glycine displayed a peak at 2.52 ppm. This peak is attributed to the formation of the dimethylammonium salt as corroborated by the results found by Donnelly et al¹¹ that when aromatic sulfonic acid derivatives were used for transamination, the dimethylammonium salt of the desired product was received. Subsequent washing of the impure product with 0.1 M HCl did not result in protonation of the dimethylamino salt. This was circumvented

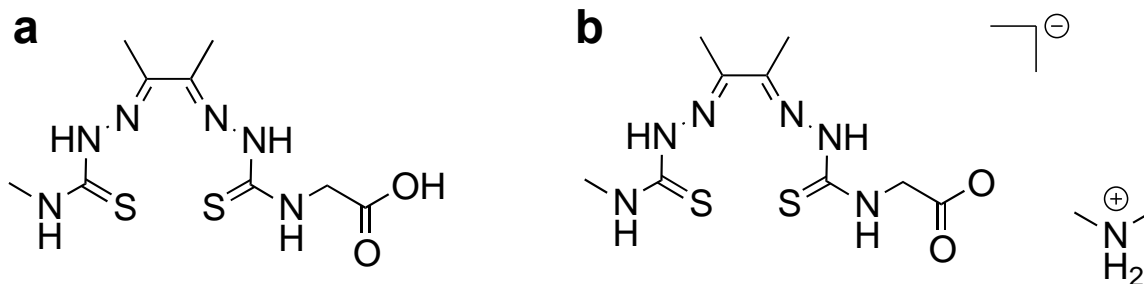


Figure 2.6 a) Major product of transamination with glycine. b) Dimethylammonium salt of the major product.

by using the ethyl ester hydrochloride of glycine. The transamination reaction with taurine, $C_2H_7NSO_3$, was also attempted. The reaction resulted in a mixture of **2** and transaminated product. It can be theorized that the strongly acidic sulfonic acid has protonated the amine of the taurine, creating a zwitterionic species, and that resulting ammonium salt has a high pKa in acetonitrile. In addition, the sulfonate is also strongly electron withdrawing, thereby slowing the reaction down.

The transamination reaction of **2** with a variety of functionalized aliphatic and aromatic primary amines has been explored. Yields are reported for isolated products, which were characterized by 1H and ^{13}C NMR spectroscopy and elemental analysis. Reaction yields for aliphatic amines under optimized conditions are overall good (77%) to excellent (98%) in acetonitrile for primary amines with a variety of other functional groups present. For aromatic amines, good (77%) to excellent (98%) yields were obtained with the substitution of THF as the solvent. The transamination reaction can be considered as an equilibrium process that is dependent on the basicity of the incoming amine relative to the dimethylamine leaving group. However, since the dimethylamine generated in the reaction leaves as a gas the equilibrium shifts towards the products increasing the yield. As such, reaction yields are not strictly dependent on the basicity of the incoming amine. In the

current study, similar reaction yields are obtained for activated and deactivated aromatic amines, but strongly deactivated aromatic amines are unreactive.

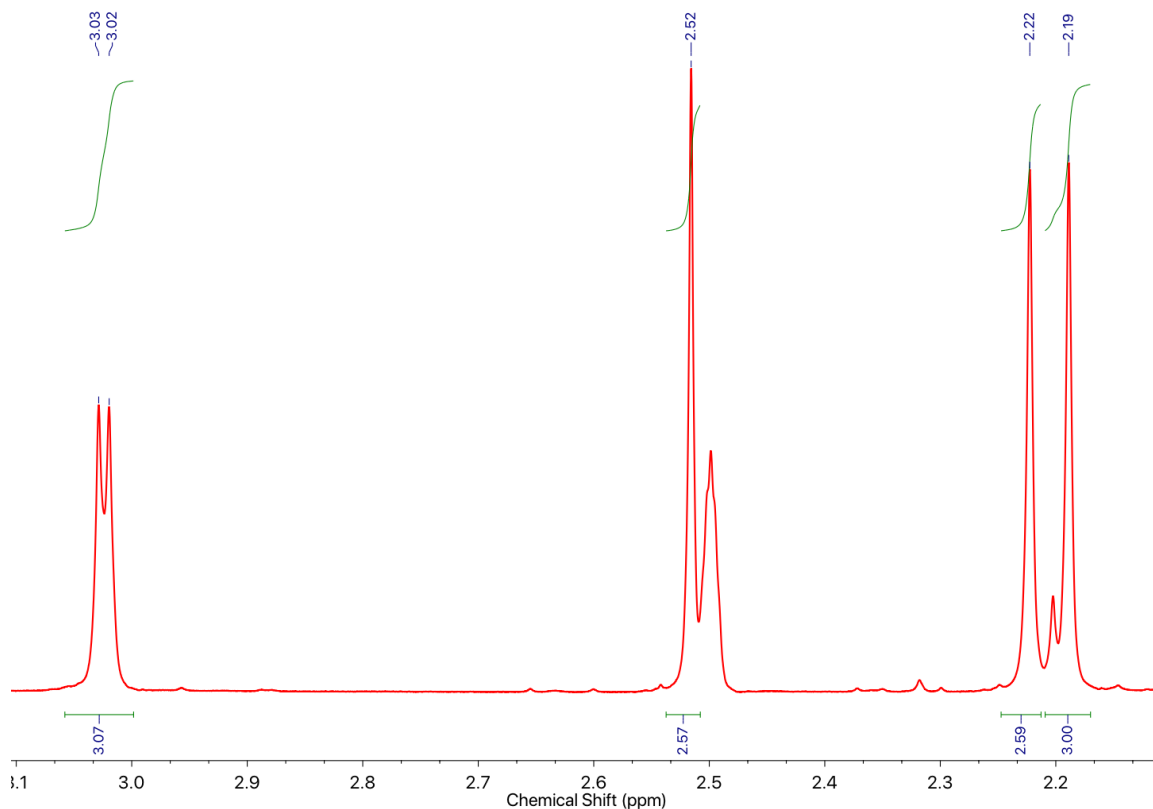


Figure 2.7 ¹H NMR, in d₆-DMSO, of the product of the transamination reaction with glycine.

2.3 Materials and Methods

All reagents were obtained from commercial sources and used as received unless otherwise noted. All solvents were purified with an MBraun solvent purification system prior to use. The BTSC compounds with derivative pendant amines were made according to modified literature methods.^{7,12} All reactions were performed under an inert atmosphere using standard Schlenk techniques. All ¹H and ¹³C MNR were collected on an Agilent 400MR or a Varian *Inova* 500 MHz NMR at the University of Louisville. All elemental

analysis were performed by Midwest Microlab (Indianapolis, IN) and Micro-Analysis Inc. (Wilmington, DE).

2.3.1 Syntheses of C_S-symmetric Bis(thiosemicarbazones)

Diacetyl-N-methyl-N'-(2-(N'',N''-dimethylamino)ethyl)-bis(thiosemicarbazone) (3):

For the reaction, 0.320 mL (3.0 mmol) of N,N-dimethylethylenediamine and 0.41 g (1.5 mmol) of **2** were suspended in 50 mL of acetonitrile. In addition, 0.40 mL (2.3 mmol) Hünig's base was added and the reaction mixture heated to reflux (81 °C) under an N₂ atmosphere for 24 hours. The resulting off-white product was filtered hot and washed with diethyl ether and air dried. Final yield: 87 % (0.41 g). ¹H NMR (400 MHz, *d*₆-DMSO) of *Diacetyl-N-methyl-N'-(2-(N'',N''-dimethylamino)ethyl)-bis(thiosemicarbazone)*: δ (ppm) = 10.23 (br. s, 1H); 8.34 (br. s, 1H); 8.33 (br. s, 1H_b); 3.59 (q, *J* = 7.5 Hz, 2H); 3.34 (s, H₂O); 3.00 (d, *J* = 3.5 Hz, 3H); 3.03 (s, 3H); 2.50 (m, DMSO); 2.42 (t, *J* = 7.5 Hz, 2H); 2.18 (s, 3H); 2.16 (s, 6H_j); 2.14 (s, 3H); 2.07 (s, MeCN) 178.8 (C=S), 178.0 (C=S), 148.4 (C=N), 148.0 (C=N), 57.5 (-CH₂NH-), 45.5 (N(CH₃)₂), 41.9 (-CH₂N(CH₃)₂), 31.6 (CH₃NH-), 12.2 (-CH₃) 11.8 (-CH₃). Anal. Calc. for C₁₁H₂₃N₇S₂·H₂O C, 39.38; H, 7.30; N, 29.22. Found: C, 39.16; H, 7.67; N, 29.10

Diacetyl-N-methyl-N'-(2-mercaptoethyl)-bis(thiosemicarbazone) (4)

For the reaction, 0.23 g (3.0 mmol) of 2-aminoethanethiol and 0.41 g (1.5 mmol) of **2** were suspended in 50 mL of acetonitrile. In addition, 0.40 mL (2.3 mmol) Hünig's base was added and the reaction mixture heated to reflux (81 °C) under an N₂ atmosphere for 24

hours. The resulting off-white product was filtered hot and washed with diethyl ether and air dried. Final yield: 98 % (0.45 g). ¹H NMR (400 MHz, *d*₆-DMSO) of *Diacetyl-N-methyl-N'-(2-mercaptoethyl)-bis(thiosemicarbazone)*: δ (ppm) = 10.32 (br. s, 1H); 10.23 (br. s, 1H); 8.54 (t, *J* = 5.5 Hz, 1H); 8.38 (q, *J* = 4.5 Hz, 1H); 3.89 (br. s, 1H); 3.70 (q, *J* = 8.5 Hz, 2H); 3.01 (d, *J* = 4.5 Hz, 3H); 2.70 (t, *J* = 7.5 Hz, 2H); 2.50 (m, DMSO); 2.21 (s, 3H); 2.20 (s, 3H). ¹³C NMR (125 MHz, *d*₆-DMSO): δ/ppm 178.92, 178.28, 149.19, 148.88, 47.08, 31.67, 23.21, 12.25, 12.12. Anal. Calc. for C₉H₁₈N₆S₃: C, 35.27; H, 5.92; N, 27.42. Found: C, 35.10; H, 5.79; N, 27.26

Diacetyl-N-methyl-N'-(2-hydroxyethyl)-bis(thiosemicarbazone) (**5**)

For the reaction, 0.18 mL (3.0 mmol) of ethanolamine and 0.41 g (1.5 mmol) of **2** were suspended in 50 mL of acetonitrile. In addition, 0.40 mL (2.3 mmol) Hünig's base was added and the reaction mixture heated to reflux (81 °C) under an N₂ atmosphere for 24 hours. The resulting white product was filtered hot and washed with diethyl ether and air dried. Final yield: 98 % (0.43 g). ¹H NMR (400 MHz, *d*₆-DMSO) of *Diacetyl-N-methyl-N'-(2-hydroxyethyl)-bis(thiosemicarbazone)*: δ (ppm) = 10.28 (br. s, 1H); 10.22 (br. s, 1H); 8.35 (q, *J* = 5.0 Hz, 1H); 8.28 (t, *J* = 5.0 Hz, 1H); 7.93 (br. s, 1H); 3.62 (q, *J* = 7.0 Hz, 2H); 3.40 (t, *J* = 7.0 Hz, 2H); 3.01 (d, *J* = 4.5 Hz, 3H); 2.50 (m, DMSO); 2.19 (s, 3H); 2.16 (s, 3H). ¹³C NMR (125 MHz, *d*₇-DMF): δ/ppm 179.52, 178.93, 147.93, 147.40, 60.02, 46.83, 31.20, 11.03, 10.93. Anal. Calc. for C₉H₁₈N₆OS₂: C, 37.22; H, 6.25; N, 28.94. Found: C, 37.15; H, 5.99; N, 28.84

Diacetyl-N-methyl-N'-(2-ethylcarboxymethyl)-bis(thiosemicarbazone) (**6**)

For the reaction, 0.42 g (3.0 mmol) of ethyl glycinate hydrochloride and 0.41 g (1.5 mmol) of **2** were suspended in 50 mL of acetonitrile. In addition, 0.40 mL (2.3 mmol) Hünig's base was added and the reaction mixture heated to reflux (81 °C) under an N₂ atmosphere for 24 hours. The resulting off-white product was filtered hot and washed with diethylether and air dried. Final yield: 85 % (0.42 g). ¹H NMR (500 MHz, DMSO-*d*₆) of *Diacetyl-N-methyl-N'-(2-ethylcarboxymethyl)-bis(thiosemicarbazone)*: δ (ppm) = 10.53 (s, 1H), 10.23 (s, 1H), 8.64 (t, *J* = 5.9 Hz, 1H), 8.39 (q, *J* = 4.6 Hz, 1H), 4.31 (d, *J* = 6.0 Hz, 2H), 4.12 (q, *J* = 7.1 Hz, 2H), 3.02 (d, *J* = 4.6 Hz, 3H), 2.22 (d, *J* = 10.9 Hz, 6H), 1.20 (t, *J* = 7.1 Hz, 3H). ¹³C NMR (125 MHz, DMSO-*d*₆) δ/ppm: 179.31, 178.93, 169.75, 149.21, 148.14, 60.93, 45.94, 31.68, 14.59, 12.33, 12.11. Anal. Calc. for C₁₁H₂₀N₆O₂S₂: C, 39.74; H, 6.06; N, 25.28. Found C, 39.71; H, 5.86; N, 25.13.

Diacetyl-N-methyl-N'-(4-hydroxyphenyl)-bis(thiosemicarbazone) (**7**)

For the reaction, 0.33 g (3.0 mmol) of *p*-aminophenol and 0.41 g (1.5 mmol) of **2** were suspended in 50 mL of ¹H NMR of THF. In addition, 0.40 mL (2.3 mmol) Hünig's base was added and the reaction mixture heated to reflux (65 °C) under an N₂ atmosphere for 24 hours. The resulting light yellow solid product was filtered hot and washed with diethyl ether and air dried. Final yield: 98 % (0.49 g). ¹H NMR (400 MHz) of *Diacetyl-N-methyl-N'-(4-hydroxyphenyl)-bis(thiosemicarbazone)*: δ (ppm) = 10.39 (br. s, 1H); 10.28 (br. s, 1H); 9.78 (s, 1H); 9.41 (s, 1H); 8.42 (br. s, 1H); 7.25 (d, *J* = 8.5 Hz, 2H); 6.75 (d, *J* = 8.5 Hz, 2H); 3.04 (d, *J* = 4.5 Hz, 3H); 2.28 (s, 3H); 2.25 (s, 3H) ¹³C NMR (125 MHz, *d*₆-DMSO) δ (ppm): 178.92 (C=S), 177.59 (C=S), 149.23 (C=N), 148.32 (C=N), 155.71 (C_{Ar}-

O), 130.82 (C_{Ar}-N), 127.91 (C_{Ar}), 115.08 (C_{Ar}), 31.68 (N-CH₃), 12.37 (-CH₃), 12.18 (-CH₃).
Anal. Calc. for C₁₃H₁₈N₆OS₂: C, 46.14; H, 5.36; N, 24.83. Found: C, 45.88; H, 5.35; N, 24.70.

Diacetyl-N-methyl-N'-(4-isopropylphenyl)-bis(thiosemicarbazone) (8)

For the reaction, 0.410 mL (3.0 mmol) of p-isopropylaniline and 0.41 g (1.5 mmol) of **2** were suspended in 50 mL of THF. 0.40 mL (2.3 mmol) Hünig's base was added and the reaction mixture heated to reflux (65 °C) under an N₂ atmosphere for 24 hours. The resulting light yellow solid product was filtered hot and washed with diethyl ether and air dried. Final yield: 77 % (0.42 g) ¹H NMR of *Diacetyl-N-methyl-N'-(4-isopropylphenyl)-bis(thiosemicarbazone)*: δ (ppm) = 10.52 (br. s, 1H); 10.29 (br. s, 1H); 9.88 (s, 1H); 8.41 (s, 1H); 7.46 (d, *J* = 8.0 Hz, 2H); 7.24 (d, *J* = 8.0 Hz, 2H); 3.04 (d, *J* = 4.5 Hz, 3H); 2.91 (m, *J* = 11.2 Hz, 1H); 2.29 (s, 3H); 2.25 (s, 3H); 1.22 (d, *J* = 11.2 Hz, 6H). ¹³C NMR (125 MHz, *d*₆-DMSO): δ/ppm 178.95 (C=S), 177.21 (C=S), 149.54 (C=N), 148.19 (C=N), 146.10 (C_{Ar}-N), 137.13 (C_{Ar}-C), 126.37 (C_{Ar}), 126.01 (C_{Ar}), 33.49 (-CH-(CH₃)₂), 31.69 (N-CH₃), 24.41 (2(-CH₃)), 12.48 (-CH₃), 12.19 (-CH₃). Anal. Calc. for C₁₆H₂₄N₆S₂: C, 52.72; H, 6.64; N, 23.05. Found: C, 52.35; H, 6.62; N, 23.00.

Diacetyl-N-methyl-N'-(4-(N'',N''-dimethylamino)phenyl)-bis(thiosemicarbazone) (9)

0.41 g (3.0 mmol) of p-dimethylphenylenediamine and 0.41 g (1.5 mmol) of **2** were suspended in 50 mL of THF. 0.40 mL (2.3 mmol) Hünig's base was added and the reaction mixture heated to reflux (65 °C) under an N₂ atmosphere for 24 hours. The resulting yellow

product was filtered hot and washed with diethyl ether and air dried. Final yield: 92 % (0.50 g). ¹H NMR (400 MHz, *d*₆-DMSO) of *Diacetyl-N-methyl-N'-(4-(N'',N''-dimethylamino)phenyl)-bis(thiosemicarbazone)*: δ (ppm) = 10.35 (s, 1H); 10.25 (s, 1H); 9.74 (s, 1H); 8.40 (s, 1H); 7.28 (d, *J* = 4.8 Hz, 2H); 6.70 (d, *J* = 4.8 Hz Hz, 2H); 3.03 (d, *J* = 4.5 Hz, 3H); 2.89 (s, 6H), 2.26 (s, 3H); 2.23 (s, 3H). ¹³C NMR (125 MHz, *d*₆-DMSO): δ/ppm 178.93 (C=S), 177.37 (C=S), 149.08 (C=N), 148.97 (C_{Ar}-N), 148.33 (C=N), 128.59 (C_{Ar}-N), 127.22 (C_{Ar}), 112.23 (C_{Ar}), 40.81 ((CH₃)₂), 31.69 (N-CH₃), 12.35 (-CH₃), 12.19 (-CH₃). Anal. Calc. for C₁₅H₂₃N₇S₂: C, 49.29; H, 6.34; N, 26.22. Found: C, 48.92; H, 6.06; N, 26.12

Diacetyl-N-methyl-N'-(4-methoxyphenyl)-bis(thiosemicarbazone) (**10**)

For the reaction, 0.37 g (3.0 mmol) of p-anisidine and 0.41 g (1.5 mmol) of **2** were suspended in 50 mL of THF. In addition, 0.40 mL (2.3 mmol) Hünig's base was added and the reaction mixture heated to reflux (65 °C) under an N₂ atmosphere for 24 hours. The resulting tan-white product was filtered hot and washed with diethyl ether and air dried. Final yield: 82 % (0.43 g). ¹H NMR (400 MHz, *d*₆-DMSO) of *Diacetyl-N-methyl-N'-(4-methoxyphenyl)-bis(thiosemicarbazone)*: δ (ppm) = 10.47 (s, 1H); 10.27 (s, 1H); 9.84 (s, 1H); 8.41 (s, 1H); 7.49 (d, *J* = 6.0 Hz, 2H); 6.92 (d, *J* = 6.0 Hz, 2H); 3.76 (s, 3H); 3.03 (d, *J* = 4.5 Hz, 3H); 2.50 (m, DMSO); 2.28 (s, 3H); 2.25 (s, 3H). ¹³C NMR (125 MHz, *d*₆-DMSO) δ (ppm): ¹³C NMR (125 MHz, *d*₆-DMSO): δ/ppm 178.95 (C=S), 177.21 (C=S), 149.54 (C=N), 148.19 (C=N), 146.10 (C_{Ar}-N), 137.13 (C_{Ar}-C), 126.37 (C_{Ar}), 126.01 (C_{Ar}), 33.49 (-CH-(CH₃)₂), 31.69 (N-CH₃), 24.41 (2(-CH₃)), 12.48 (-CH₃), 12.19 (-CH₃). Anal. Calc. for C₁₄H₂₀N₆OS₂: C, 47.71; H, 5.72; N, 23.83. Found: C, 47.61; H, 5.74; N, 23.83.

Diacetyl-N-methyl-N'-(4-fluorophenyl)-bis(thiosemicarbazone) (11)

0.33 g (3.0 mmol) of p-fluoroaniline and 0.41 g (1.5 mmol) of **2** were suspended in 50 mL of THF. 0.40 mL (2.3 mmol) Hünig's base was added and the reaction mixture heated to reflux (65 °C) under an N₂ atmosphere for 24 hours. The resulting tan-white product was filtered hot and washed with diethyl ether and air dried. Final yield: 79 % (0.40 g). ¹H NMR (400 MHz, *d*₆-DMSO) of *Diacetyl-N-methyl-N'-(4-fluorophenyl)-bis(thiosemicarbazone)*: δ (ppm) = 10.60 (s, 1H); 10.28 (s, 1H); 9.94 (s, 1H); 8.41 (s, 1H); 7.54 (dd, *J* = 5.0 Hz, 2H); 7.20 (t, *J* = 9.0 Hz, 2H); 3.03 (d, *J* = 4.5 Hz, 3H); 2.50 (m, DMSO); 2.29 (s, 3H); 2.25 (s, 3H). ¹³C NMR (125 MHz, *d*₆-DMSO): δ/ppm 178.94 (C=S), 177.68 (C=S), 149.87 (C=N), 148.22 (C=N), 159.19 (C_{Ar}-F), 135.82 (C_{Ar}-N), 128.47 and 128.41 (C_{Ar}), 115.30 and 115.32 (C_{Ar}), 31.69 (N-CH₃), 12.51 (-CH₃), 12.23 (-CH₃). Anal. Calc. for C₁₃H₁₇FN₆S₂: C, 45.87; H, 5.03; N, 24.69. Found: C, 45.51; H, 5.07; N, 24.46

CHAPTER 3 ELECTROCHEMICAL CHARACTERIZATION OF PENDENT
DIAMINE DERIVATIVES OF NICKEL(II) AND COPPER (II)
BIS(THIOSEMICARBAZONES)¹

3.1 Introduction

The metal-centered and ligand-centered reduction potentials of molecular catalysts can be tuned through substituent effects by employing electron-donating or electron-withdrawing groups.⁴⁴⁻⁴⁶ For electrocatalysts, changing the electronic structure directly influences overpotential and the turnover frequency (TOF) of catalysis.⁴⁷⁻⁴⁹ The tuning of electrocatalysts using “through-structure” (electronic, inductive or resonant) and “through-space” (electrostatic and hydrogen bonding) substituent effects was exquisitely demonstrated by Constantin, Robert, and Savéant through a series of groundbreaking studies.^{17, 47, 50-51} The through-structure effects displayed opposing outcomes as factors that

¹ Part of this chapter is republished with permission from Wiley & Sons, Calvary, C. A.; Hietsoi, O.; Strain, J. M.; Mashuta, M. S.; Spurgeon, J. M.; Buchanan, R. M.; Grapperhaus, C. A., Synthesis, Characterization, and HER Activity of Pendant Diamine Derivatives of NiATSM. *Eur. J Inorg. Chem.* **2019**, 33, 3782-3790 and Calvary, C. A.; Hietsoi, O.; Hofsommer, D. T.; Brun, H. C.; Costello, A. M.; Mashuta, M. S.; Spurgeon, J. M.; Buchanan, R. M.; Grapperhaus, C. A., Copper bis(thiosemicarbazone) Complexes with Pendent Polyamines: Effects of Proton Relays and Charged Moieties on Electrocatalytic HER. *Eur. J Inorg. Chem.* **2021**, 3, 267-275.^{7,55}

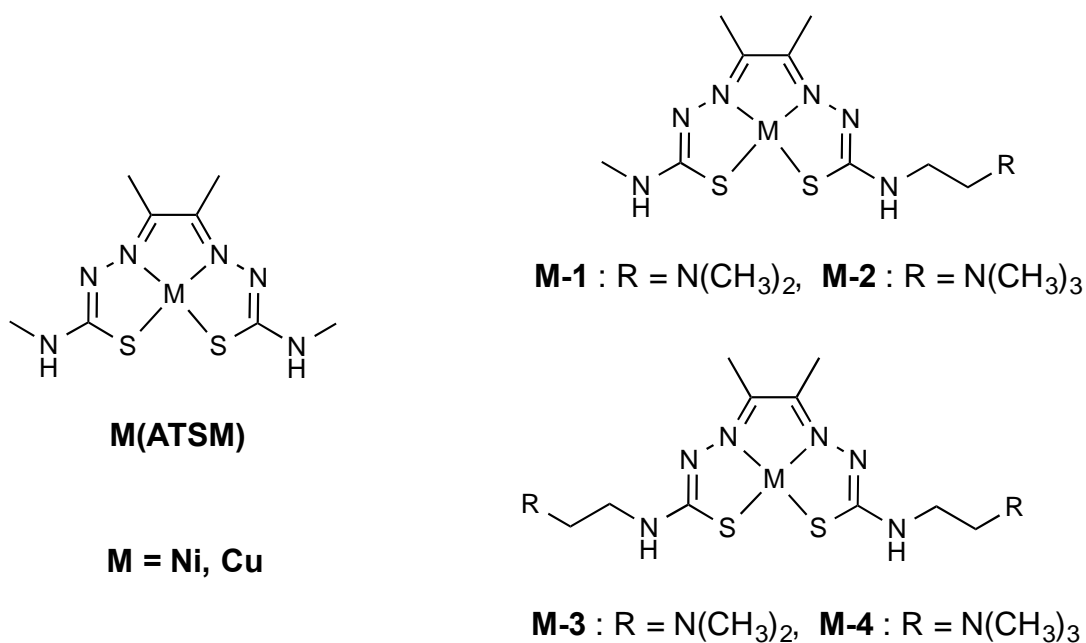
reduced overpotential also decreased turnover TOF and *vice versa*.⁵⁰ This trend is also well documented in electrocatalysts for the hydrogen evolution reaction (HER).²² In contrast, through-space substituent effects provide a means to both lower the overpotential and increase TOF.⁵²

The effect of through-space interactions on electrocatalysis has also been evaluated through the introduction of a secondary coordination sphere.^{17, 22, 53-54} Ligands with bulky groups, fixed charge sites, and hydrogen-bonding proton relay pendants are of growing interest as they may play an important role in generating and stabilizing reactive intermediates during catalysis.^{7, 17} For example, incorporation of charged groups in the second coordination sphere, as part of the ligand framework or as appended groups, have been shown to reduce the reduction potential of the complex via through space interactions.^{7, 52}

Several bis(thiosemicarbazone) (BTSC) metal complexes, including derivatives of diacetyl-bis(N4-methyl-3-thiosemicarbazone) (H₂ATSM), have been evaluated as HER electrocatalysts.^{8, 22, 35-36, 42} The BTSC ligands are non-innocent with HER mechanisms following ligand-assisted metal-centered, ligand-centered, or metal-assisted ligand-centered pathways depending on the identity of the metal. In the ligand-assisted metal-centered pathway, the ligand is involved in the electrochemical and/or chemical events for hydrogen evolution at the metal center.⁴² In the metal-assisted ligand-centered pathway, the metal acts as an electron “reservoir” for the ligand, where the evolution of hydrogen occurs.⁸ Finally, the ligand centered pathway occurs when the metal plays no role in the catalysis, and all electrochemical and chemical events occur on the ligand.²⁶

A ligand-assisted metal-centered pathway is reported for Ni(ATSM) and related complexes.⁴² The ligand serves as an electron reservoir on the pathway to a putative Ni(III)-hydride intermediate. In contrast, Cu(ATSM) follows a ligand-assisted metal-centered pathway in which initial metal-centered reduction is followed by ligand-based protonation and reduction events with evolution of H₂ from the ligand-center.⁸

In this chapter the synthesis, characterization, and HER activity of eight different derivatives of M(ATSM) complexes are described, Scheme 3.1. The new complexes include the addition of a pendent diamine moiety that introduces a second-coordination sphere, which could participate as a proton relay during HER akin to the “Hangman” complexes explored by the Nocera group.³² Since the pendent amine may be protonated under acid saturating conditions during catalysis, this will potentially introduce charge sites that may affect the overpotential of the reaction. To decouple the proton relay and charge effects, methylated derivatives that introduce a fixed charge at a non-basic site were prepared for comparison. This charge is a permanent fixture on the pendent and allows us to delineate the effects of a fixed charge vs. an exchangeable charge. The work described in this chapter has previously been published in a series of publications.^{7, 55}

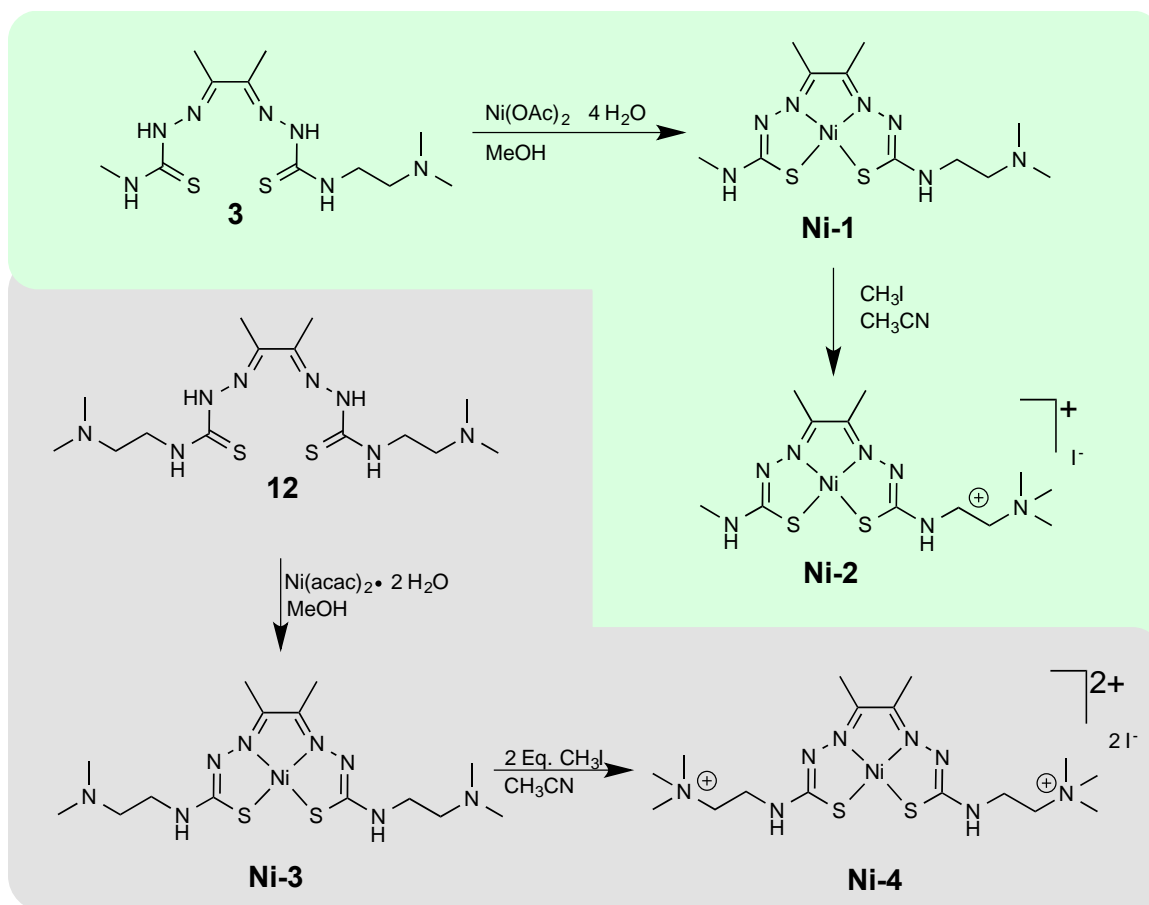


Scheme 3.1 Metal bis(thiosemicarbazone) complexes **M(ATSM)** and **M-1 – M-4**.⁵⁵

3.2 Synthesis and Spectroscopic Analysis

The ligands diacetyl-(N4-dimethylethylenediaminethiosemi-carbazonato)-(N4-methyl-3-thio-semicarbazonato)butane-2,3-diimine) (**3**) and diacetyl-bis(N4-dimethylethylenediamino-3-thiosemicarbazonato)butane-2,3-diimine) (**12**) were prepared via transamination of diacetyl-2,3-N4-methyl-3-thiosemicarbazone-N4-dimethyl-3-thiosemicarbazone (**2**) and diacetyl-2,3-bis-(N4-dimethyl-3-thiosemicarbazone) with *N,N*-dimethylethylenediamine. Synthesis of **3** via a modified pathway, has been previously reported by Cowley and coworkers⁵⁶ whereas synthesis of ligands **3** and **12** via transamination has been described in the previous chapter.⁷

Addition of Ni(OAc)₂ or Cu(OAc)₂ to methanol solutions of **3** yielded **Ni-1** and **Cu-1**, respectively. Similarly, addition of Ni(Acac)₂ or Cu(Acac)₂ to methanol solutions of H₂L² yielded **Ni-3** and **Cu-3**, respectively. Alkylation of the **M-1** derivatives with one



Scheme 3.2 Synthesis of methylated derivatives of **Ni-2** and **Ni-4** from **3** and **12**, respectively.

equivalent of methyl iodide in acetonitrile gave the charged species, **M-2**. Likewise, addition of two equivalents of methyl iodide to the **M-3** complexes in acetonitrile yielded the **M-4** derivatives as shown in Scheme 3.2. The hexafluorophosphate derivative **Cu-2*** was prepared by ion-exchange upon addition of a saturated solution of KPF_6 to **Cu-2** in H_2O resulting in precipitation of the desired product.

The ligands **3** and **12** (Figure 3.1 and Appendix Figure B.1) and complexes **Ni-1** – **Ni-4** (Figure 3.2 and Appendix Figure B.3 –B.6) were characterized by ^1H NMR spectroscopy. The ^1H NMR of **3** displays two sets of overlapping -NH peaks at 10.20 ppm

and 8.33 ppm, one set of methylene protons from the new pendent at 3.58 ppm, methyl protons at 3.00 ppm, another set of methylene protons from the new pendent at 2.43 ppm, the dimethylamino protons at 2.16 ppm, and flanked on both sides by the backbone methyl groups at 2.18 and 2.14 ppm respectively.

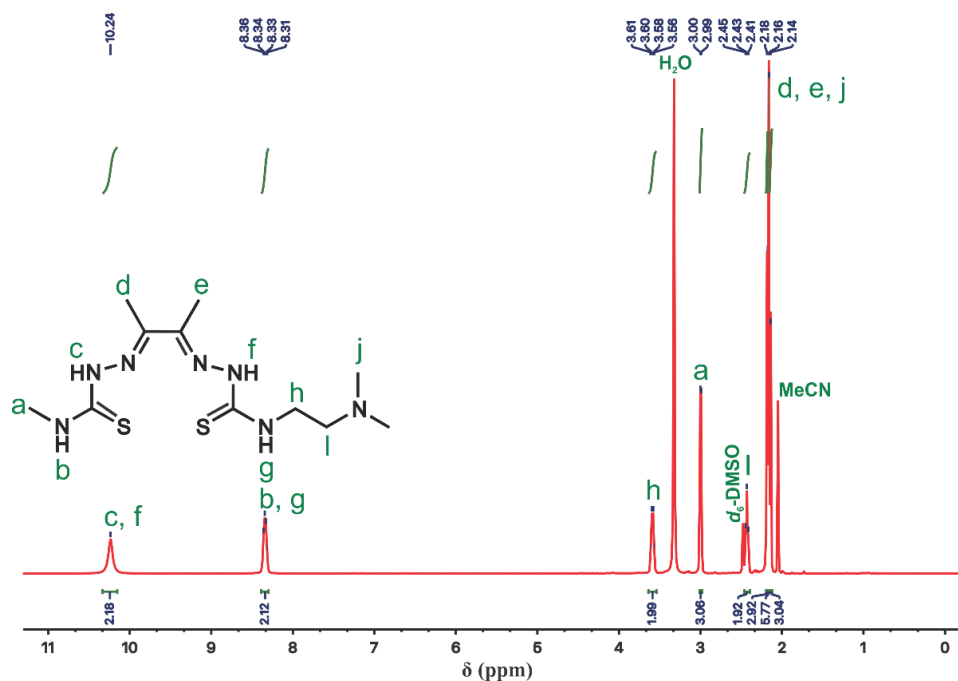


Figure 3.1 ^1H NMR (400 MHz, d_6 -DMSO) of **3**.

Subsequent coordination of nickel results in loss of the hydrazino proton at 10.20 ppm for **3**. Alkylation of **Ni-1** to **Ni-2** causes a large shift of the N-CH₃ signals from 2.13 ppm in **Ni-1** to 3.09 ppm in **Ni-2** with a corresponding increase in integration from 6 to 9 protons. In addition, the methylene protons adjacent to the dimethyl amine undergo a shift from 2.33 to 3.42 ppm. In addition, the infrared spectra of ligands **3** and **12** (Appendix Figure B.11 and Figure B.12) display N-H stretches between 3337 and 3364 cm^{-1} that is lost upon metal complexation (Appendix Figure B.13 – B.16).

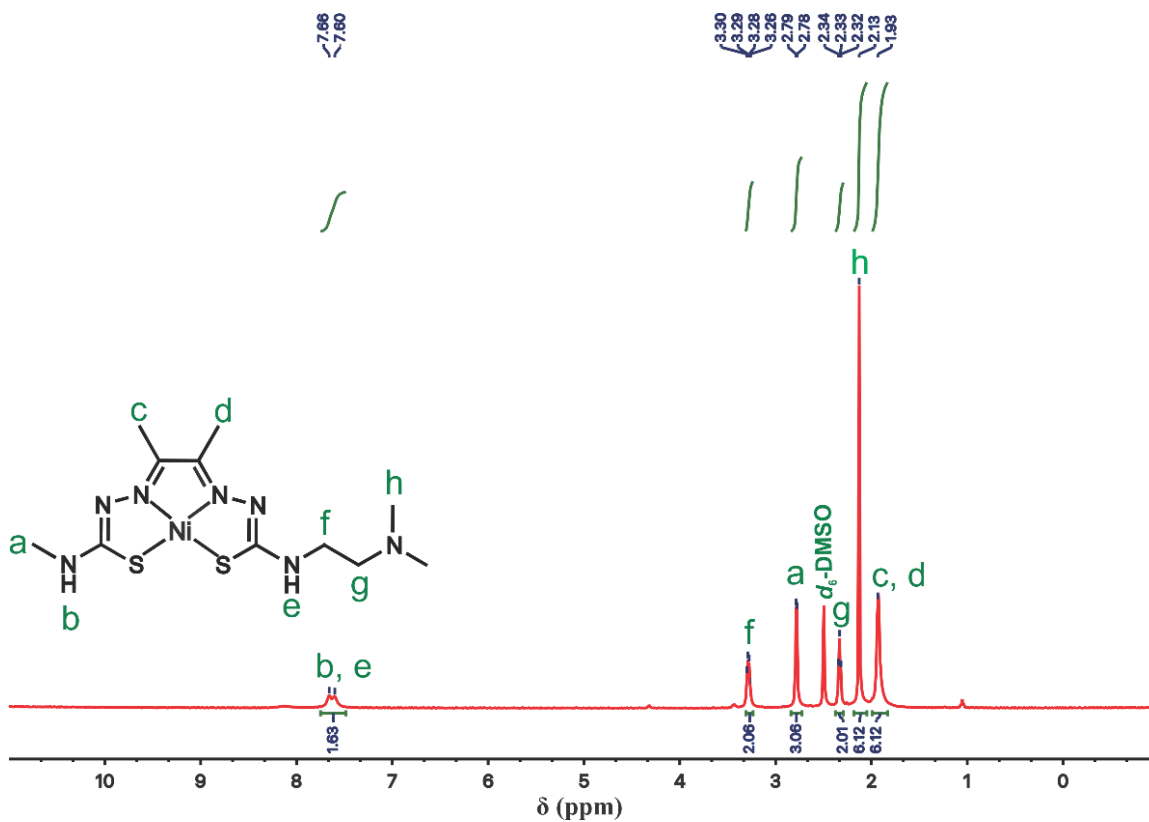


Figure 3.2 ¹H NMR (400 MHz, *d*₆-DMSO) of **Ni-1**.

The electronic spectra of **Ni-1** – **Ni-4** recorded in a 1:1 mixture of acetonitrile/methanol solution display ligand to metal charge transfer bands near 400 nm as seen in Figure 3.3. All four complexes display a more intense ligand to ligand charge transfer bands near 256 nm. Two additional bands are observed in the alkylated species at

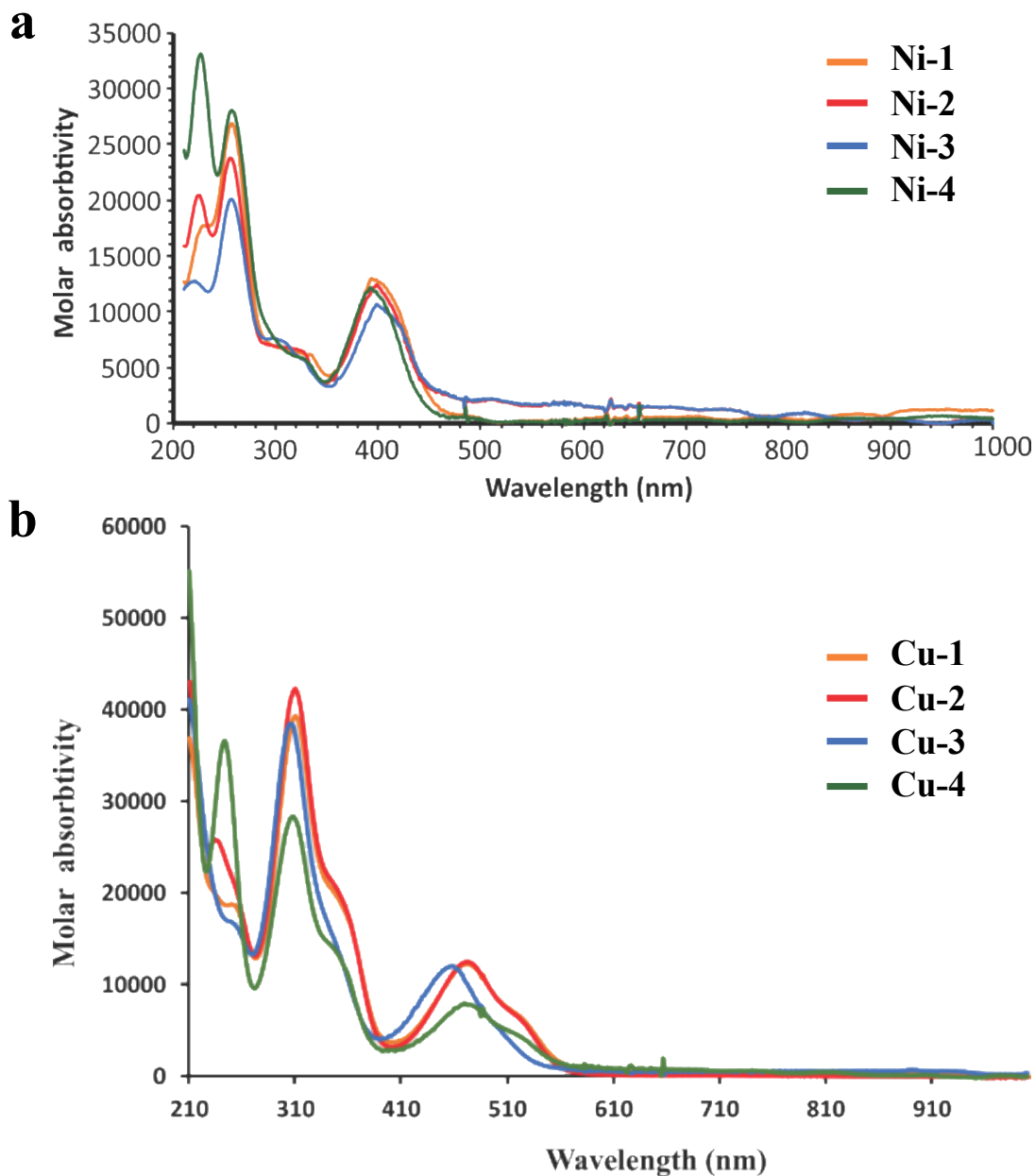


Figure 3.3 UV-Vis spectra of a) Ni-1 – Ni-4 and b) Cu-1 – Cu-4.

223 nm for Ni-2 and 226 nm for Ni-4, which can be attributed to the presence of the non-coordinated iodide counter anions. Similarly, the electronic spectra of Cu-1 – Cu-4 recorded in acetonitrile display ligand to metal charge transfer bands near 460 nm. All four complexes display a more intense ligand to ligand charge transfer bands near 320 nm. Two

additional bands are observed for **Cu-2** and **Cu-4** at 220 nm and 225 nm, respectively, which can be attributed to the presence of the non-coordinated iodide counter anions. For **Cu-2**, metathesis of the iodide with hexafluorophosphate yielded the N-methylated derivative **Cu-2***.

The EPR spectra of **Cu-1** – **Cu-4** in DMF were recorded as frozen solution at 77K. Complexes **Cu-1** ($g_{\parallel} = 2.11$, $g_{\perp} = 2.01$), **Cu-2** ($g_{\parallel} = 2.08$, $g_{\perp} = 2.00$), **Cu-3** ($g_{\parallel} = 2.09$, $g_{\perp} = 2.01$), and **Cu-4** ($g_{\parallel} = 2.09$, $g_{\perp} = 2.01$), display axial spectra with $g_{\parallel} > g_{\perp} > 2$, consistent with square planar Cu(II) and a single unpaired electron located in $d_{x^2-y^2}$. A representative EPR spectrum of **Cu-3** is shown in Figure 3.4 with additional spectra in the Appendix (Figures B.35 – B.37).

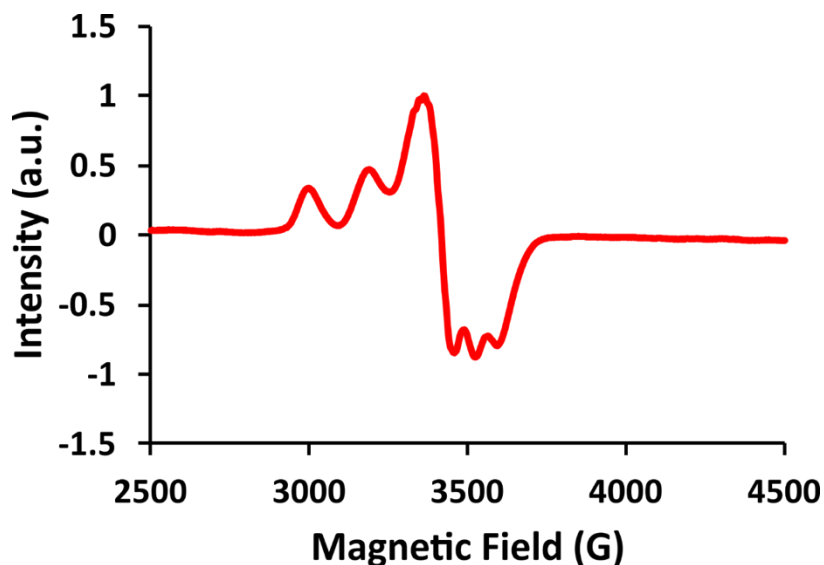


Figure 3.4 Low temperature (77 K) EPR spectrum of **Cu-3** in DMF. Microwave frequency = 9.603 MHz, $g_{\parallel} = 2.09$, $g_{\perp} = 2.01$, $A_{\parallel} = 181$ G.

3.3 Crystallographic Characterization

X-ray quality single crystals of **M-1** – **M-4** were obtained for diffraction studies. **Ni-1** – **Ni-4** all crystallize as discrete, square planar Ni(II) complexes with no solvent molecules in the crystal lattice. Selected bond distances and angles are summarized in

Table 3.1. The core frameworks, ignoring the functional groups of the pendent amines, are rigorously planar. The largest deviation from the best fit plane of the 15 core non-hydrogen atoms in **Ni-1** is ± 0.1437 Å for S1 with a standard deviation of 0.0612 Å. **Ni-2 – Ni-4** have slightly smaller deviations from the best fit plane more similar to NiATSM (± 0.0698 Å for S1 and a standard deviation of 0.0255 Å).

Single crystals of **Ni-1** were obtained by slow diffusion of Et₂O into a MeCN solution of **Ni-1** as orange plates in the orthorhombic space group *Pbca*. The asymmetric unit of **Ni-1** consists of one equivalent of **Ni-1** (Figure 3.5). The Ni center of **Ni-1** occupies an N₂S₂ square plane with Ni–N1, Ni–N3, Ni–S1, and Ni–S2 bond distances of 1.861(2), 1.854(2), 2.1493(8), and 2.1540(8) Å, respectively. The S1–C5, N1–N2, and C1–C2 bond distances of 1.780(3), 1.377(3), and 1.471(4) Å, respectively, are typical of C–S, N–N, and C–C single bonds. The shorter N1–C1 and N2–C5 bond distances of 1.307(4) and 1.317(4) Å, respectively, reveal C=N character. Bond distances and bond angles within the N₂S₂ square plane in **Ni-1** are similar to the parent NiATSM complex. X-ray quality single crystals of **Ni-2** were isolated as dark red-orange needles in the monoclinic space group *C2/c* from an H-shaped tube by slow diffusion of CH₂Cl₂ into a MeCN/MeOH solution of **Ni-2**. The positively charged cation is balanced by two partial (50%) occupancy iodide counter anions. Similar to **Ni-1**, the Ni center of **Ni-2** (Appendix Figure B.17) occupies an N₂S₂ square plane with similar metal-ligand bond distances.

Table 3.1 Selected Bond Distances (Å) and Angles (deg) for **Ni-1 – Ni-4**.

Bond distance	Ni-1	Ni-2	Ni-3^[a]	Ni-4
Ni1-N1	1.861 (2)	1.846 (3)	1.870 (5)	1.864 (2)
Ni1-N3	1.854 (2)	1.860 (3)	1.850 (5)	1.869 (2)
Ni1-S1	2.1493 (8)	2.1562 (12)	2.1569 (18)	2.1710 (7)
Ni1-S2	2.1540 (8)	2.1642 (11)	2.1521(18)	2.1715 (8)
S1–C5	1.780 (3)	1.766 (4)	1.786 (6)	1.769 (3)
S2–C6	1.766 (3)	1.764 (4)	1.763 (6)	1.778 (2)
N1–C1	1.307 (4)	1.317 (5)	1.277 (8)	1.314 (3)
N1–N2	1.377 (3)	1.382 (4)	1.389 (7)	1.388 (3)
N2–C5	1.317 (4)	1.324 (5)	1.283 (8)	1.324 (3)
N3–C2	1.305 (4)	1.301 (5)	1.301 (8)	1.312 (3)
N3–N4	1.375 (3)	1.374 (4)	1.384 (7)	1.387 (3)
N4–C6	1.321 (4)	1.307 (5)	1.326 (8)	1.316 (3)
C1–C2	1.471 (4)	1.481 (6)	1.468 (8)	1.483 (3)
Bond angle	Ni-1	Ni-2	Ni-3^[a]	Ni-4
N3–Ni1–N1	83.87 (11)	83.45 (15)	83.3 (2)	83.63 (9)
N3–Ni1–S1	170.94 (8)	171.07 (10)	170.94 (16)	170.58 (7)
N1–Ni1–S1	87.37 (8)	87.63 (11)	87.66 (17)	87.56 (6)
N3–Ni1–S2	87.47 (8)	87.56 (10)	87.15 (16)	87.24 (7)
N1–Ni1–S2	171.18 (8)	170.68 (11)	170.41 (17)	170.82 (7)
S1–Ni1–S2	101.35(3)	101.37(4)	101.90(7)	101.61(3)

[a] **Ni-3** contains two Ni molecules in the asymmetric unit. The bond distances and angles are for the Ni-1 molecule.

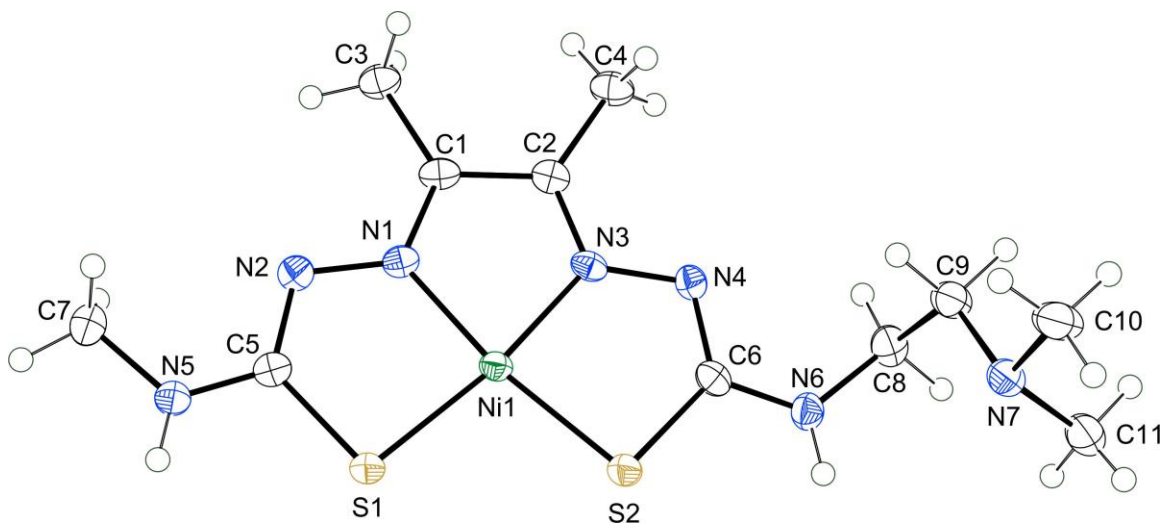


Figure 3.5 ORTEP of **Ni-1** thermal ellipsoids shown at 50% probability.

Ni-3 crystallizes as orange prisms from slow diffusion of Et₂O into a MeCN/MeOH solution of **Ni-3** in the triclinic space group *P*-1. The asymmetric unit of **Ni-3** (Appendix Figure B.18) consists of two crystallographically distinct equivalents of **Ni-3** that differ in the orientation of two pendant diamines. The pendant groups in the **Ni-3** molecule are in an anti-arrangement with respect to the N₂S₂ plane. In the second molecule in the asymmetric unit, the groups are in a syn arrangement and are severely disordered.

Green-brown plate crystals of **Ni-4** in the triclinic space group *P*-1 were obtained using vapor diffusion technique in an H-shaped tube by slow diffusion of Et₂O into a MeCN/MeOH solution of **Ni-4**. The asymmetric unit of **Ni-4** (Appendix Figure B.19) consists of one equivalent of **Ni-4**. The core structure is similar to the other complexes. The pendant diamine groups are in an anti-arrangement with hydrogen bonding from the secondary amines to the iodide counter anions. Crystal data and structure refinement details for **Ni-1** – **Ni-4** are listed in Table 3.2.

Table 3.2 Crystal Data and Structure Refinement for **Ni-1 – Ni-4**.

Identification code	Ni-1	Ni-2	Ni-3	Ni-4
Empirical formula	C ₁₁ H ₂₁ N ₇ NiS ₂	C ₁₂ H ₂₄ IN ₇ NiS ₂	C ₁₄ H _{24.50} N ₈ NiS ₂	C ₁₆ H ₃₄ I ₂ N ₈ NiS ₂
CCDC number	1917418	1917419	1917420	1917421
Formula weight	374.18	516.09	427.75	715.14
Temperature (K)	102(3)	101(1)	102(2)	101.95(10)
Wavelength (Å)	0.71073	0.71073	0.71073	0.71073
Crystal system	Orthorhombic	Monoclinic	Triclinic	Triclinic
Space group	Pbca	C2/c	P ⁻ 1	P ⁻ 1
Unit cell dimensions				
a (Å)	11.7031(4)	13.9471(16)	7.3123(7)	8.8516(9)
b (Å)	15.8057(5)	13.9342(16)	16.3895(14)	9.5977(12)
c (Å)	17.6173(4)	20.699(3)	17.6227(16)	16.172(2)
α (deg)	90	90	70.154(8)	85.494(10)
β (deg)	90	91.826(10)	84.378(8)	78.439(10)
γ (deg)	90	90	89.994(7)	80.176(10)
V (Å ³)	3258.78(17)	4020.6(8)	1975.8(3)	1324.9(3)
Z	8	8	4	2
d _{calcd} (Mg/m ³)	1.525	1.705	1.438	1.793
Absorption coefficient (mm ⁻¹)	1.451	2.717	1.208	3.239
F(000)	1568	2064	898	704
Crystal color, habit	dark orange plate	dark red-orange needle	orange prism	green-brown plate
Crystal size (mm ³)	0.40 × 0.20 × 0.02	0.33 × 0.04 × 0.04	0.38 × 0.08 × 0.04	0.41 × 0.12 × 0.02
θ range for data collection (deg)	3.32 to 27.55	3.47 to 28.12	3.24 to 25.25	3.28 to 30.08
Index ranges	- 15 ≤ h ≤ 15 - 20 ≤ k ≤ 20 - 22 ≤ l ≤ 22	- 18 ≤ h ≤ 18 - 18 ≤ k ≤ 18 - 27 ≤ l ≤ 27	- 8 ≤ h ≤ 8 - 16 ≤ k ≤ 16 - 21 ≤ l ≤ 21	- 12 ≤ h ≤ 12 - 13 ≤ k ≤ 13 - 22 ≤ l ≤ 22
Reflections collected	42277	25351	20780	34415
Independent reflections	3764 [R(int) = 0.0485]	4904 [R(int) = 0.049]	7151 [R(int) = 0.1120]	7776 [R(int) = 0.0455]
Completeness to theta max (%)	99.8	99.7	99.8	99.8
Absorption correction	multi-scan	multi-scan	multi-scan	multi-scan
Max. and min transmission	1.00 and 0.69	1.000 and 0.718	1.000 and 0.877	1.000 and 0.593
Refinement method	full-matrix least-squares on F ²	full-matrix least-squares on F ²	full-matrix least-squares on F ²	full-matrix least-squares on F ²
Data/restraints/parameters	3764 / 0 / 254	4904 / 0 / 233	7151 / 8 / 465	7776 / 0 / 308
Goodness of fit on F ²	1.073	1.074	1.051	1.06
Final R indices [I > 2σ(I)] ^{a,b}	R1 = 0.0441, wR2 = 0.0957	R1 = 0.0423, wR2 = 0.0970	R1 = 0.0739, wR2 = 0.1215	R1 = 0.0281, wR2 = 0.0508
R indices (all data) ^{a,b}	R1 = 0.0647, wR2 = 0.1051	R1 = 0.0571, wR2 = 0.1046	R1 = 0.1335, wR2 = 0.1424	R1 = 0.0402, wR2 = 0.0551
Largest diff. peak and hole (e · Å ⁻³)	0.639 and -0.352	1.621 and -0.439	1.253 and -0.773	1.692 and -0.903

[a] $R1 = \frac{\sum ||F_o| - |F_c||}{\sum |F_o|}$. [b] $wR2 = \{\frac{\sum [w(F_o^2 - F_c^2)^2]}{\sum [w(F_o^2)^2]}\}^{1/2}$, where $w = \frac{q}{\sigma^2(F_o^2)} + (qp)^2 + bp$. GOF = $S = \{\frac{\sum [w(F_o^2 - F_c^2)^2]}{(n - p)}\}^{1/2}$, where n is the number of reflections and p is the number of parameters refined.

X-ray quality single crystals of **Cu-1** – **Cu-3** were obtained by slow evaporation of organic solutions. Crystals of **Cu-4** were twinned and refined as described in the experimental section. Crystal data and structure refinement details for Cu(II) complexes are listed in Appendix Table B.1. All compounds crystallize as discrete, square planar Cu(II) complexes (Figure 3.6, Appendix Figures B.40 – B.42). Complexes **Cu-2** and **Cu-4** contain one water molecule in the crystal lattice. Selected bond distances and angles are summarized in Appendix Table B.2. Overall, complexes **Cu-1** – **Cu-4** are similar to their nickel analogs.

Orange plate single crystals of **Cu-1** were obtained by slow evaporation of a 1:1 MeCN/EtOH solution and crystallizes in the orthorhombic space group *Pbca*. The asymmetric unit consists of one equivalent of **Cu-1** (Figure 3.6). The N₂S₂ coordination environment is square planar, and the Cu–N1, Cu–N3, Cu–S1, and Cu–S2 bond distances are 1.967(2), 1.960(2), 2.2394(7) and 2.2392(8) Å, respectively. The S1–C5, N1–N2 and C1–C2 bond distances of 1.766(3), 1.375(3), and 1.475(4) Å, respectively, are typical of C–S, N–N, and C–C single bonds. The shorter N1–C1 and N2–C5 bond distances of 1.294(3) and 1.323(4) Å, respectively, reveal C=N bond character. In general, the bond distances and bond angles for **Cu-1** are similar to the parent Cu(ATSM) complex. Single crystals of **Cu-2** were isolated as red-brown plates by slow evaporation of 1:1 MeCN/EtOH solution. The complex crystallizes in the monoclinic space group *P21/n*, and the asymmetric unit consists of one molecule of **Cu-2**, an iodide ion and one water molecule of hydration. As observed for **Cu-1**, the CuN₂S₂ unit is square planar and has similar metal-ligand bond distances.

Complex **Cu-3** was isolated as red-brown prisms by vapor diffusion of Et₂O into a MeCN solution. The complex crystallizes in the triclinic space group *P*-1, and the asymmetric unit consists of one molecule of **Cu-3**. Orange needle crystals of **Cu-4** were obtained by slow evaporation of MeCN solution. The complex crystallizes in the triclinic space group *P*-1 containing one cation of **Cu-4**, two iodides and one water of hydration per asymmetric unit. The divalent copper(II) bis(thiosemicarbazone) cation is balanced by two iodide counter anions. The core bond distances and angles are similar to the other complexes. The pendant diamine groups are in an *anti*-arrangement.

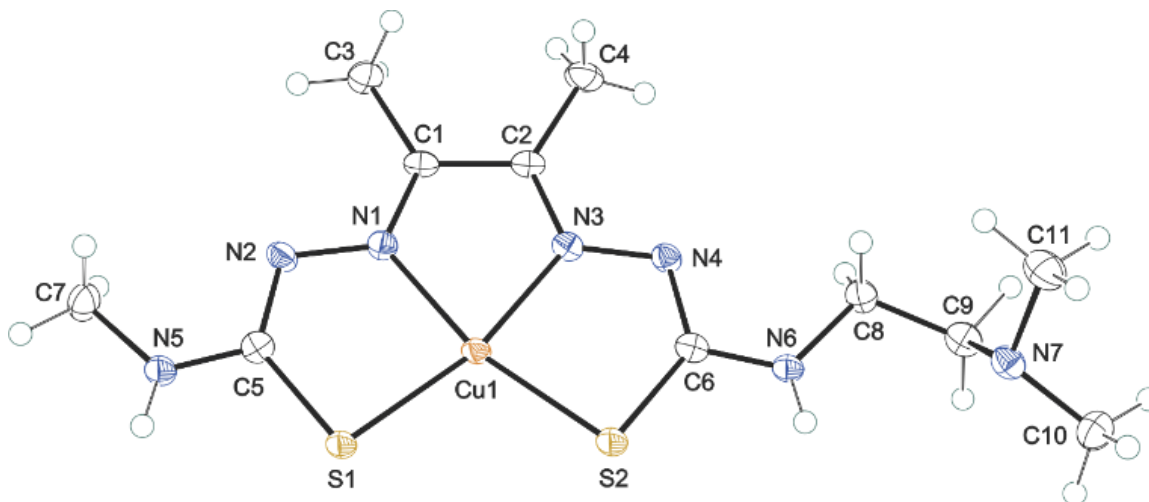


Figure 3.6 ORTEP view (50% probability ellipsoids) of **Cu-1** showing atom labelling for all non-hydrogen atoms in the asymmetric unit.

3.4 Electrochemical Studies

3.4.1 Cyclic Voltammetry

The cyclic voltammograms (CVs) of **Ni-1** – **Ni-4** display two quasi-reversible events in the cathodic region from 0 to -2 V vs Fc⁺/Fc⁰ and an irreversible oxidation event between -1 and -1.3 V that is only observed after scanning through the second reduction

event. Based on the assignments for the NiATSM complex, the first reduction event is attributed to a ligand centered couple, $\text{Ni(II)L}/\text{Ni(II)L}^{\bullet-}$. The second reduction event is metal-centered, $\text{Ni(II)L}^{\bullet-}/\text{Ni(I)L}^{2-}$. The potentials for **Ni-1** and **Ni-3** are similar to those observed for the NiATSM complex indicating the addition of the pendant diamines does not change the core electronic structure. However, the introduction of a fixed charge in the alkylated complexes **Ni-2** and **Ni-4** results in significant anodic shifts. The ligand-centered reduction of the monocation **Ni-2** is shifted by -80 mV compared to **Ni-1** with a similar shift of -90 mV in the metal-centered event. As expected, the shifts are nearly twice as large for the dication **Ni-4**. The ligand-centered and metal-centered events for **Ni-4** shift by -140 mV and -160 mV, respectively, compared to **Ni-3**. The distorted shape of the return peak for the second reduction of **Ni-4** has the appearance of a stripping wave associated with desorption of the doubly reduced, neutral complex.

The cyclic voltammograms (CVs) of **Cu-1**, **Cu-2***, **Cu-3**, and **Cu-4** each display a single quasi-reversible reduction event between 0 to -2 V vs Fc^+/Fc^0 . Based on Cu(ATSM), the reduction event is associated with a metal centered $\text{Cu}^{\text{III/I}}$ couple. The reduction potentials values of -1.10 V and -1.09 V for **Cu-1** and **Cu-3**, respectively, match that of Cu(ATSM) indicating addition of the pendent ethyldimethylamine does not significantly perturb the electronic properties of the $\text{Cu N}_2\text{S}_2$ core. Curiously, **Cu-2** displayed only a 10 mV shift relative to Cu(ATSM), while the reduction potential for **Cu-4** was shifted by 160 mV relative to Cu(ATSM). However, the reduction potential for the hexafluorophosphate derivative, **Cu-2***, showed the expected 60 mV anodic shift suggesting that ion pairing of the cationic metal complex and iodide of **Cu-2** in acetonitrile yields a charge neutral species. To confirm this, a series of conductivity measurements were conducted using

electron impedance spectroscopy (EIS). Complexes **Cu-1** and **Cu-2** have similar conductivity values of 0.054 mS cm^{-1} and 0.052 mS cm^{-1} , respectively, consistent with ion-pairing in the latter. The cyclic voltammograms for **Ni-1** – **Ni-4** and **Cu-1** – **Cu-4** complexes are shown in Figure 3.7 and the comparison summarized in Table 3.3.

Table 3.3 Comparison of the M(ATSM) and **M-1** – **M-4** (M = Cu or Ni) Electrochemical Events. Electrochemical Data of 0.3 mM Complex in 0.1 M $\text{Bu}_4\text{NPF}_6/\text{MeCN}$ Solution at a Scan Rate of 200 mV/s with Potentials vs Fc^+/Fc^0 .

Complex	$\text{Cu}^{\text{II}} E_{1/2}$ (V)	$\text{Ni(II)L}/\text{Ni(II)L}^- E_{1/2}$ (V)	$\text{Ni(II)L}^-/\text{Ni(I)L}^{2-} E_{1/2}$ (V)
M(ATSM)	- 1.10	- 1.72	-2.32
M-1	- 1.10	- 1.72	-2.32
M-2*	- 1.04	- 1.64	- 2.24
M-3	- 1.09	- 1.73	- 2.33
M-4	- 0.94	- 1.57	- 2.18

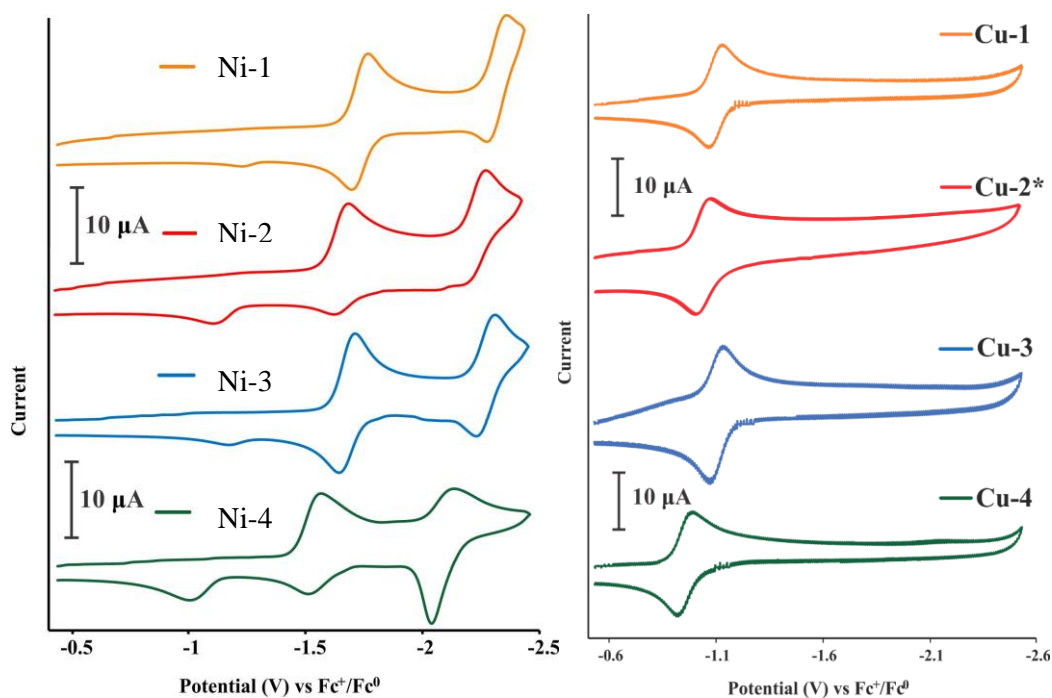


Figure 3.7 Cyclic voltammograms of **Ni-1** – **Ni-4** (left) and **Cu-1** – **Cu-4** (right) in acetonitrile with scan rate of 200 mV/s.

3.4.2 Diffusion Studies

To establish that the reductions are diffusion limited, the CVs of **M-1** – **M-4** in MeCN were recorded over multiple scan rates from 0.1 to 0.5 V/s. Figure 3.8a shows the scan rate dependence of cyclic voltammogram with observed increase in current when the scan rate is increased. The plots of current against the scan rates (Figure 3.8b, Appendix Figure D.1 – Figure D.7) were linear indicating that the complexes are suitable candidates for electrocatalysis.

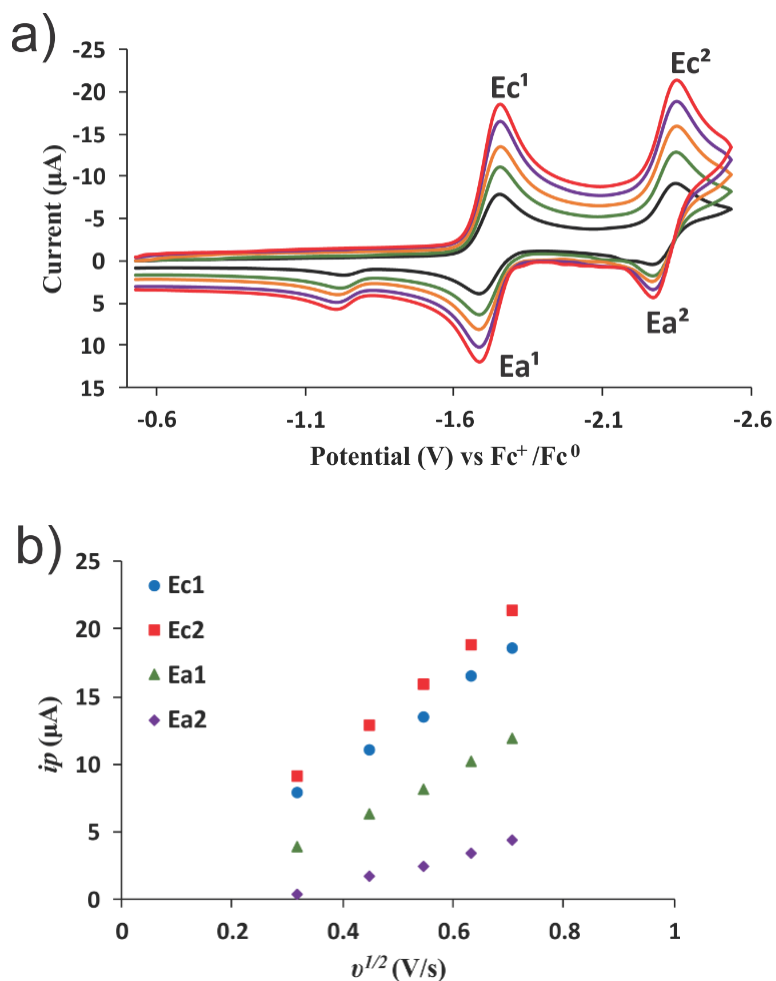


Figure 3.8 a) Scan rate dependent CVs of **Ni-3** recorded at scan rates of 0.1 (black), 0.2, 0.3, 0.4, and 0.5 V/s (red) in 0.1 M Bu₄NPF₆/MeCN solution. b) Plot of peak current versus the square root of scan rate.

The experimentally determined diffusion coefficient (D_0) is $2.34 \times 10^{-5} \text{ cm}^2/\text{s}$ for **Ni-1**, $2.11 \times 10^{-5} \text{ cm}^2/\text{s}$ for **Ni-2**, $2.62 \times 10^{-5} \text{ cm}^2/\text{s}$ for **Ni-3**, and $1.69 \times 10^{-5} \text{ cm}^2/\text{s}$ for **Ni-4**. **Cu-1 – Cu-4** displayed similar diffusion coefficients (D_0) of $1.6 \times 10^{-5} \text{ cm}^2 \text{ s}^{-1}$ for **Cu-1**, $4.2 \times 10^{-5} \text{ cm}^2 \text{ s}^{-1}$ for **Cu-2***, $5.2 \times 10^{-5} \text{ cm}^2 \text{ s}^{-1}$ for **Cu-3**, and $1.6 \times 10^{-5} \text{ cm}^2 \text{ s}^{-1}$ for **Cu-4**. A sample calculation of the diffusion coefficient using Randles – Sevcik equation is provided in Appendix C.

3.4.3 HER Studies

The performance of **M-1 – M-4** as electrocatalysts for the hydrogen evolution reaction (HER) was evaluated in MeCN using glacial acetic acid as a proton source. The addition of CH_3COOH ($\text{p}K_a = 23.51$ in MeCN) to 0.3 mM solutions of **M-1 – M-4** in MeCN containing 0.1 M Bu_4NPF_6 generates catalytic current upon a sweep in the cathodic direction. The catalytic current was corrected by subtracting the CVs of acetic acid in the absence of catalyst (**Ni-1 – Ni-4**: Figure 3.9, Appendix Figure D.8 – Figure D.11, **Cu-1 – Cu-4**: Figure 3.10, Appendix Figure D.12 – Figure D.14). Primarily, the catalytic to peak current ratio (i_{cat}/i_p) increases linearly with the increasing acid concentration until saturation at 100 mM CH_3COOH (**Ni-1 – Ni-4**: Appendix Figure D.15 and **Cu-1 – Cu-4**: Figure D.16). Under acid saturated conditions, the scan rate was increased until the scan rate independent region was observed at 3.0 V/s for **Ni-1**, **Ni-2**, and **Ni-4** and 3.5 V/s for **Ni-3**.

The turnover frequencies (TOF) for **Ni-1 – Ni-4** were determined using *foot-of-the-wave analysis* (FOWA) at a scan rate of 200 mV/s and in the scan rate independent

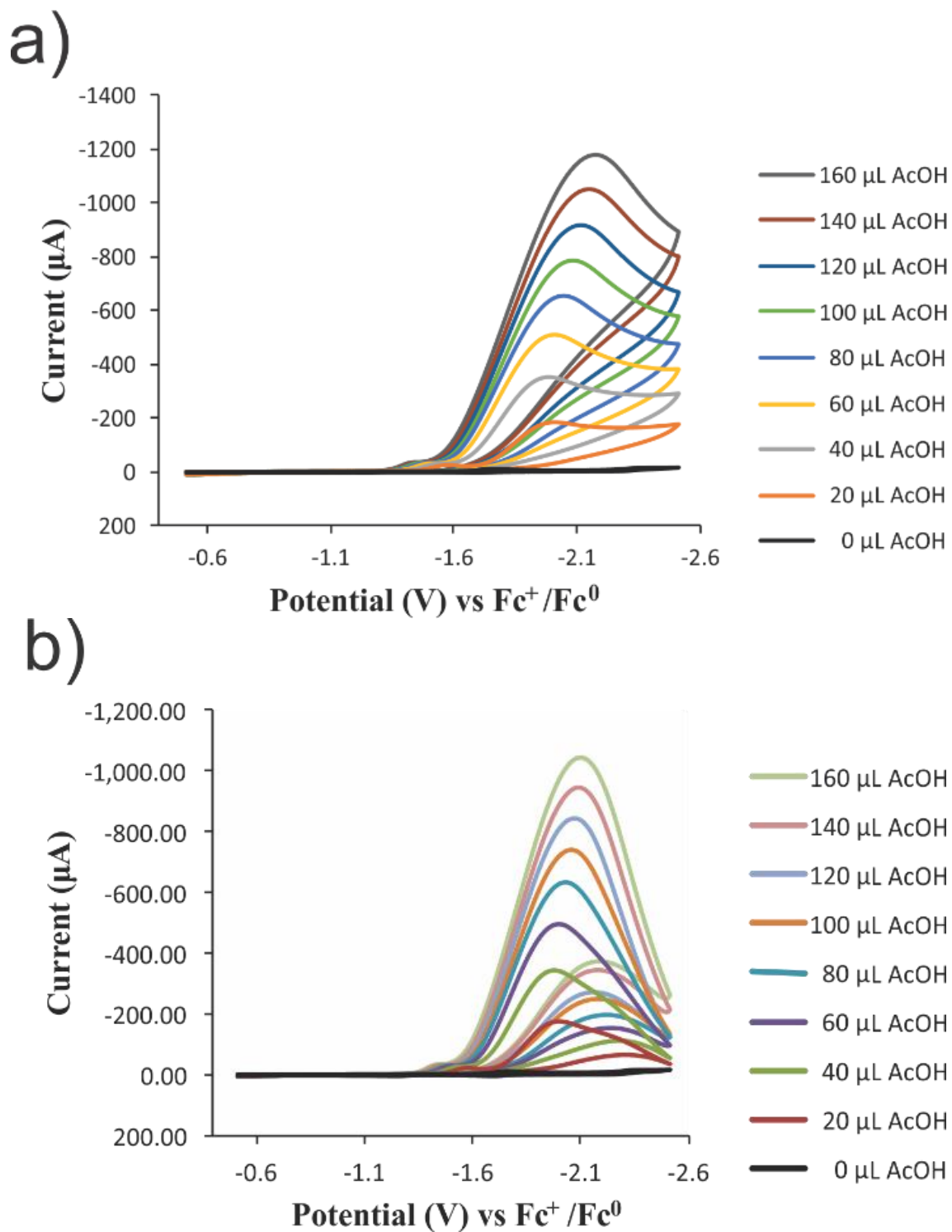


Figure 3.9 a) CVs of 0.3 mM Ni-3 in MeCN solution with 0.1 M Bu₄NPF₆ collected at scan rate of 200 mV/s with 0, 20, 40, 60, 80, 100, 120, 140, 160 µL CH₃COOH without acid blanks subtracted and b) with acid blanks subtracted.

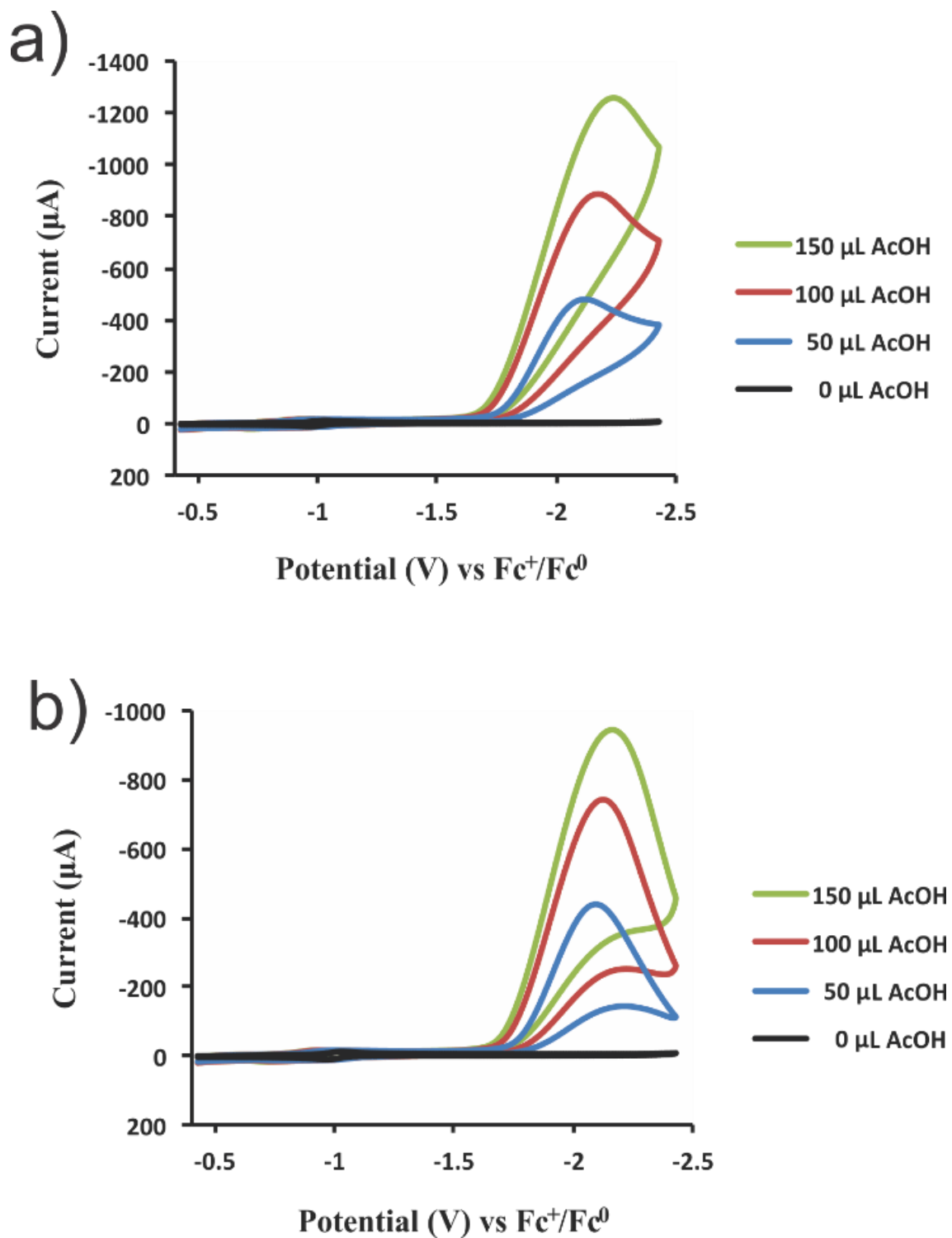


Figure 3.10 a) CVs of 0.3 mM Cu-3 in MeCN solution with 0.1 M Bu₄NPF₆ collected at scan rate of 200 mV/s with 0, 50, 100, 150 µL CH₃COOH without acid blanks subtracted and b) with acid blanks subtracted.

region.^{47,57-58} FOWA allows determination of the TOF, the TOF vs η relationship, and the TOF₀. Normally, factors such as substrate consumption, product inhibition, and deactivation of the catalyst cause high current densities and prevent the expected current plateau from being reached. This is accomplished by looking at the activity where the “S” shape of the CV, where the electrochemical behavior is ideal. Plots of FOWA of **Ni-1** – **Ni-4** and NiATSM can be found in Appendix Figure D.17 – Figure D.21.

For comparison, the activity of the NiATSM complex under identical conditions were re-evaluated. All five complexes exhibit a relatively high TOF with an overpotential (η) below 0.90 V. At a scan rate of 200 mV/s NiATSM, **Ni-2**, and **Ni-4** display similar TOFs at the same overpotential of 0.67 V indicating the presence of the point charge in the second coordination sphere does not significantly affect activity in these complexes. The non-alkylated derivatives **Ni-1** and **Ni-3** display similar TOFs to the NiATSM complex at overpotential values of 0.59 and 0.56 mV, respectively. The 80 to 110 mV shift in overpotential suggests the participation of the pendant amine during catalysis as a proton relay to enhance activity. Under scan rate independent conditions, the overpotential for all 5 compounds increase suggesting intramolecular proton rearrangement is limiting the rate of HER. The overpotential for **Ni-2**, **Ni-4**, and NiATSM shifts to 0.89 V, while the overpotential for **Ni-1** and **Ni-3** remain 40 to 50 mV more accessible.

For **Cu-1** – **Cu-4**, the overpotential was calculated using the methods reported by Fourmond et al.⁵⁹⁻⁶⁰ The turnover frequency (TOF) was calculated from the plateau currents as described for Cu(ATSM).⁸ Although plateau current analysis can only be rigorously applied when S-shaped waves are obtained, they do provide an initial assessment of catalytic activity. Foot-of-the-wave analysis (FOWA) is an alternate method

developed specifically for electrocatalysts that do not operate under pure kinetic conditions. However, FOWA is only appropriate for mechanisms in which the first step involves electron transfer and it is not appropriate for the HER mechanisms that involve an initial proton step, such as Cu(ATSM) and its derivatives. The detailed calculation of overpotential and TOF for Cu complexes are described in Appendix E and Appendix F, respectively.

Relative to Cu(ATSM), the addition of pendent polyamines in **Cu-1** – **Cu-4** were found to reduce the overpotential. A shift of 120-130 mV relative to Cu(ATSM) was observed with values of 0.65 V and 0.66 V for **Cu-1** and **Cu-3**, respectively. For the charged complexes, **Cu-2** and **Cu-4**, calculated overpotential are more accessible than Cu(ATSM) with values of 0.68 V and 0.72 V, respectively. The observed shifts relative to Cu(ATSM) are higher in the neutral derivatives than the charged derivatives. Under acid-saturated catalytic conditions all of the catalysts have charged pendent amines either due to protonation, in the case of **Cu-1** and **Cu-3**, or methylation, in the case of **Cu-2** and **Cu-4**. The introduction of charged pendent amines lowers the overpotential by shifting the reduction potential anodically, although this may be partially offset as the positive charge makes the complex more difficult to protonate, which may retard intramolecular proton rearrangement. In addition to charge effects, the protonated pendent amines in **Cu-1** and **Cu-3** can act as proton relays that facilitate intramolecular proton rearrangement and further lower overpotential.

The TOF values of 10,300 s⁻¹ and 12,000 s⁻¹ for **Cu-1** and **Cu-3**, respectively, are 108 % and 112 % of the value observed for Cu (ATSM). The introduction of pendent

amines as proton relays in **Cu-1** and **Cu-3** improves the TOF. The highest TOF was observed for **Cu-3**, which has two such pendent amines. The introduction of charged pendent amines through methylation decreases TOF. For the charged complexes **Cu-2** and **Cu-4** the TOF values of 9400 s^{-1} and 8700 s^{-1} are 99% and 92% of the Cu(ATSM) TOF.

3.4.4 Controlled Potential Coulometry Studies

The stability of **M-1** – **M-4** as electrocatalysts for HER was evaluated in MeCN by conducting controlled potential coulometry (CPC) experiments over a period of 4 hours. Electrolysis of 0.30 mM MeCN solutions of **Ni-1** – **Ni-4** (Figure 3.11) containing 0.1 M Bu_4NPF_6 , and 100 mM CH_3COOH were performed at a constant potential of $E_{\text{cat}/2}$, defined

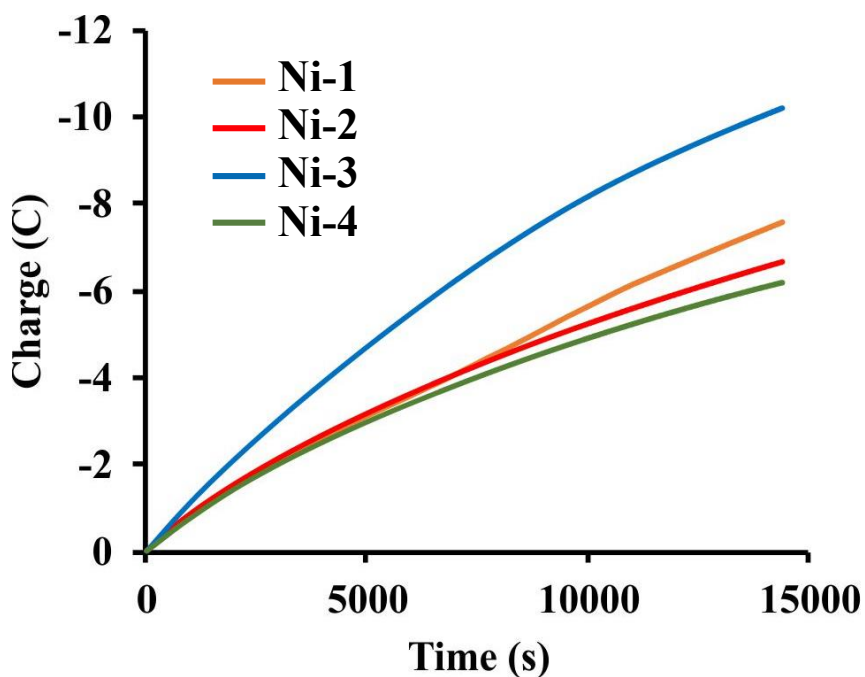


Figure 3.11 CPC of 0.3 mM **Ni-1** – **Ni-4** in 0.1 M $\text{Bu}_4\text{NPF}_6/\text{MeCN}$ solutions with 100 mM CH_3COOH . The CPC were performed for Ni-1, Ni-2, and Ni-4 at -1.4 V vs Ag/Ag^+ and Ni-3 at -1.32 V vs Ag/Ag^+ . The charge generated by the acid blanks in the absence of the catalysts were subtracted.

as the potential required to obtain one-half of the maximum of catalytic current, $i_{cat/2}$, in the CV studies. For **Ni-1**, a total charge (q) of 7.67 C was passed corresponding to 3.97×10^{-5} moles of H_2 produced (n) and a turnover number (TON) of 13. Similar data were obtained for **Ni-2** and **Ni-4**, while **Ni-3** was 50% more active (TON = 18) despite requiring a lower applied potential. Complexes **Ni-1** – **Ni-4** exhibited faradaic efficiencies of approximately 100 % (Figure 3.12).

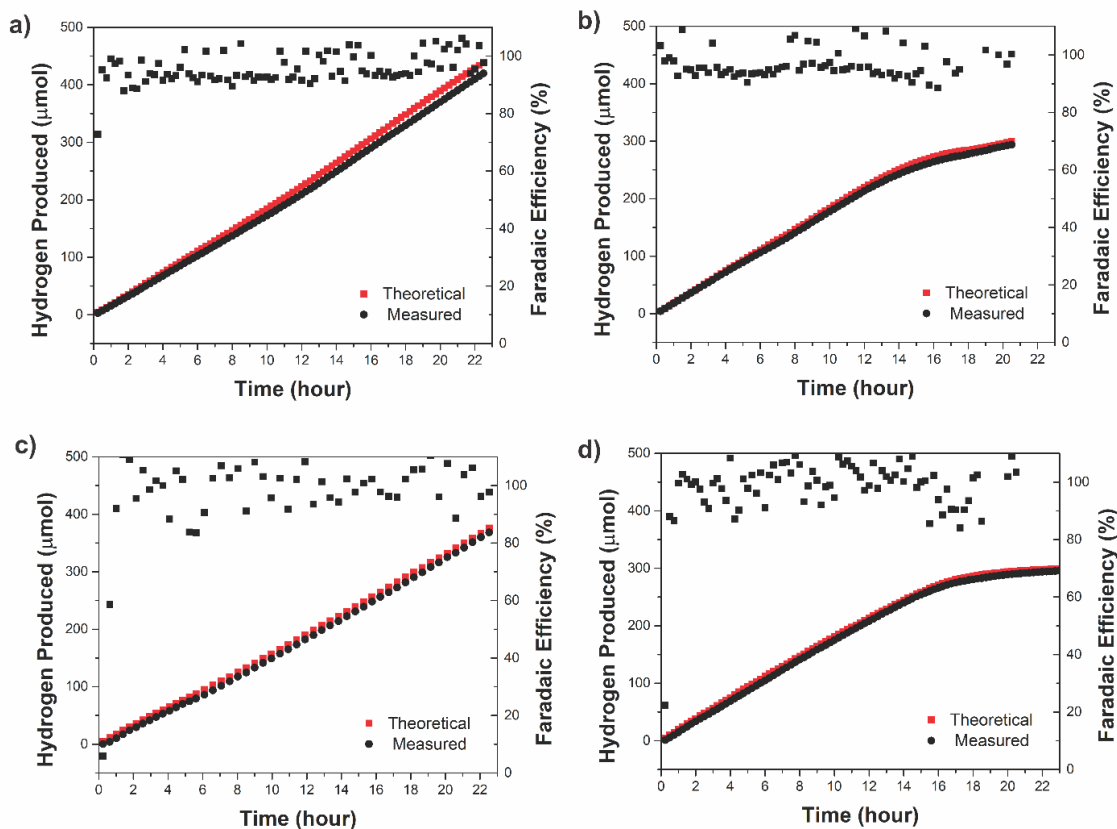


Figure 3.12 Faradaic efficiency of the hydrogen produced during the bulk electrolysis of a) **Ni-1**, b) **Ni-2**, c) **Ni-3**, and d) **Ni-4** detected by gas chromatography. The potential was held at -1.4 V vs Ag/Ag⁺.

The same CPC experiment setup was employed for the Cu complexes. A plot of charge versus time (Figure 3.13) shows a linear dependence over the entire time of the experiment, indicating the catalyst's stability. For **Cu-1**, a total charge (q) of 30.24 C was passed corresponding to 1.56×10^{-4} moles of H_2 produced (n) and 52 turnovers. The greatest activity was displayed by **Cu-3**, which catalyzed 61 turnovers during the time of the electrolysis. The charged derivatives **Cu-2** and **Cu-4** catalyzed 46 and 45 turnovers, respectively, which is similar to the 40 turnovers for Cu(ATSM). All of the complexes exhibited faradaic efficiencies of approximately 100 % (Figure 3.14).

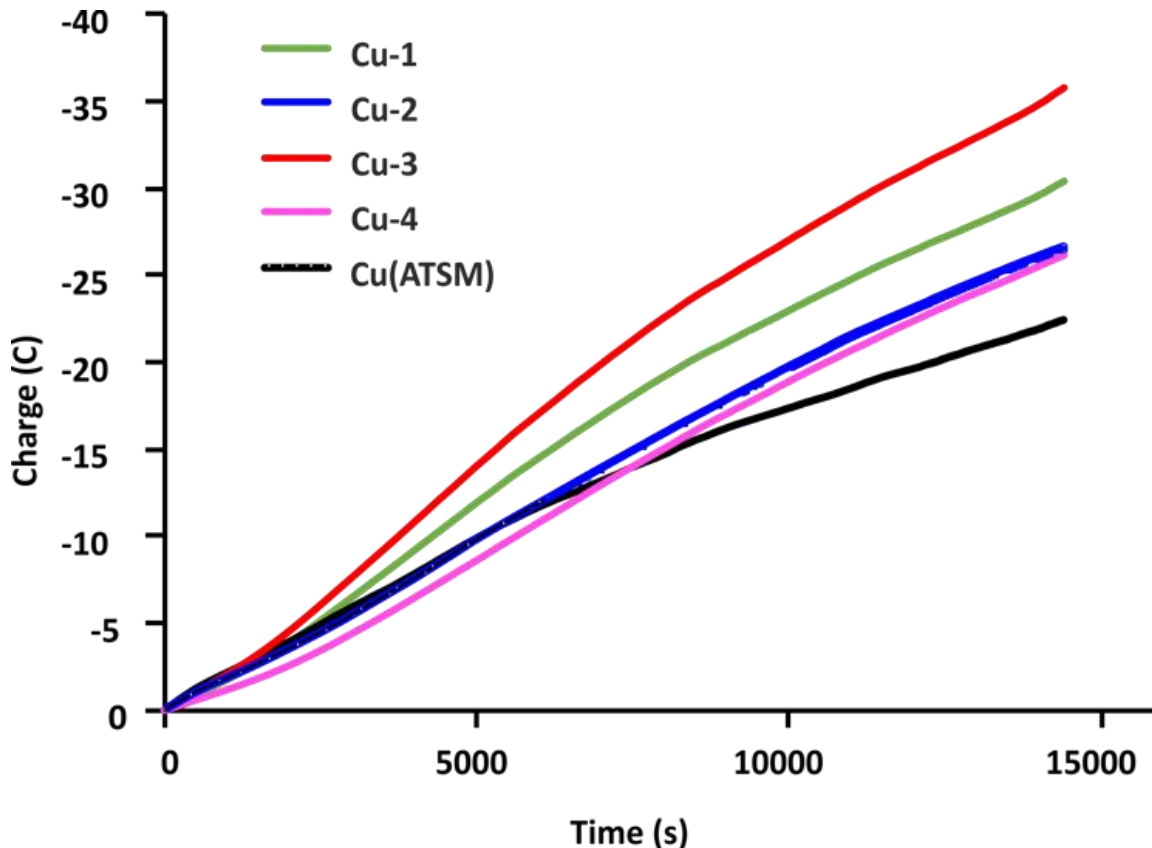


Figure 3.13 CPC of 0.3 mM **Cu-1** – **Cu-4** and Cu(ATSM) in 0.1 M $Bu_4NPF_6/MeCN$ solutions with 100 mM CH_3COOH . The CPC were performed at -1.5 V vs Ag/Ag^+ . The charge generated by the acid blanks in the absence of the catalysts were subtracted.

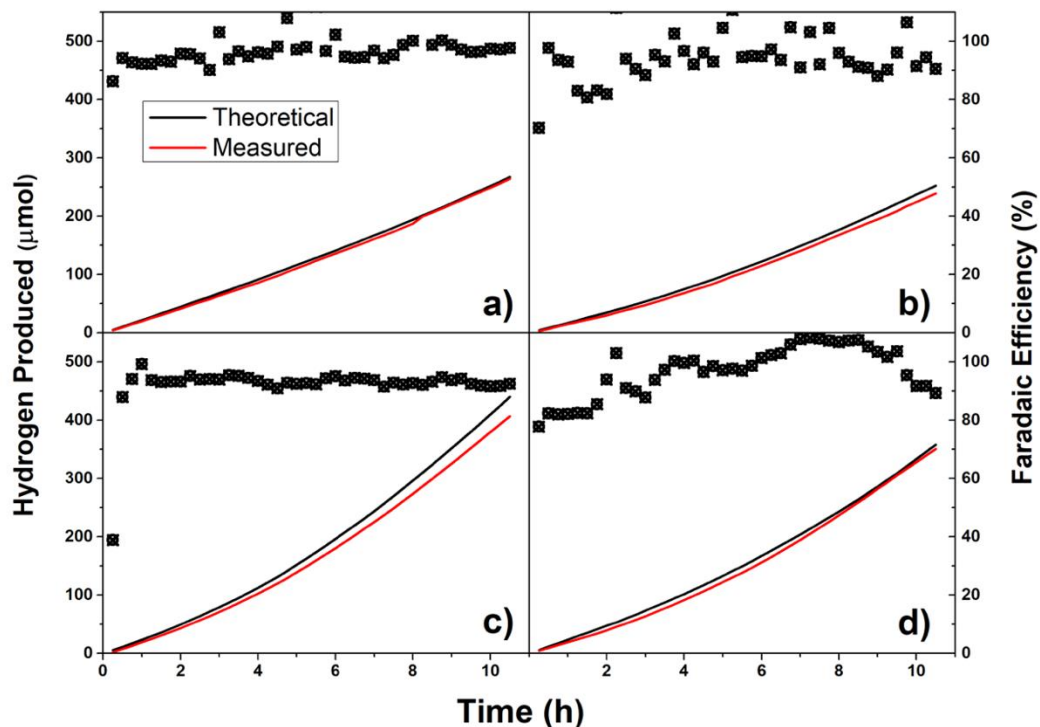


Figure 3.14 Faradaic efficiencies for hydrogen produced during the bulk electrolysis of a) **Cu-1**, b) **Cu-2**, c) **Cu-3**, and d) **Cu-4** detected by gas chromatography. Potential was held at 1.5 V vs Ag/AgCl⁺.

3.4.5 Post Coulometry Dip Test

To confirm that the HER observed is associated with complexes **M-1** – **M-4** in solution and not due to surface adsorbed complex or degradation products, a dip-test was performed following CPC studies. After CPC experiments, the working electrode was removed from solution, washed with DI water without being polished, and immersed into a fresh 0.1 M Bu₄NPF₆/MeCN solution. For all complexes, only background current was observed upon sweeping the potential in the cathodic region, Figure 3.15 and Figure 3.16 for **Ni-1** – **Ni-4** and **Cu-1** – **Cu-4**, respectively. Upon addition of acetic acid, only the acid

blank was observed. This indicates that HER activity is not due to a film of the catalyst or its degradation product absorbed on the electrode surface.

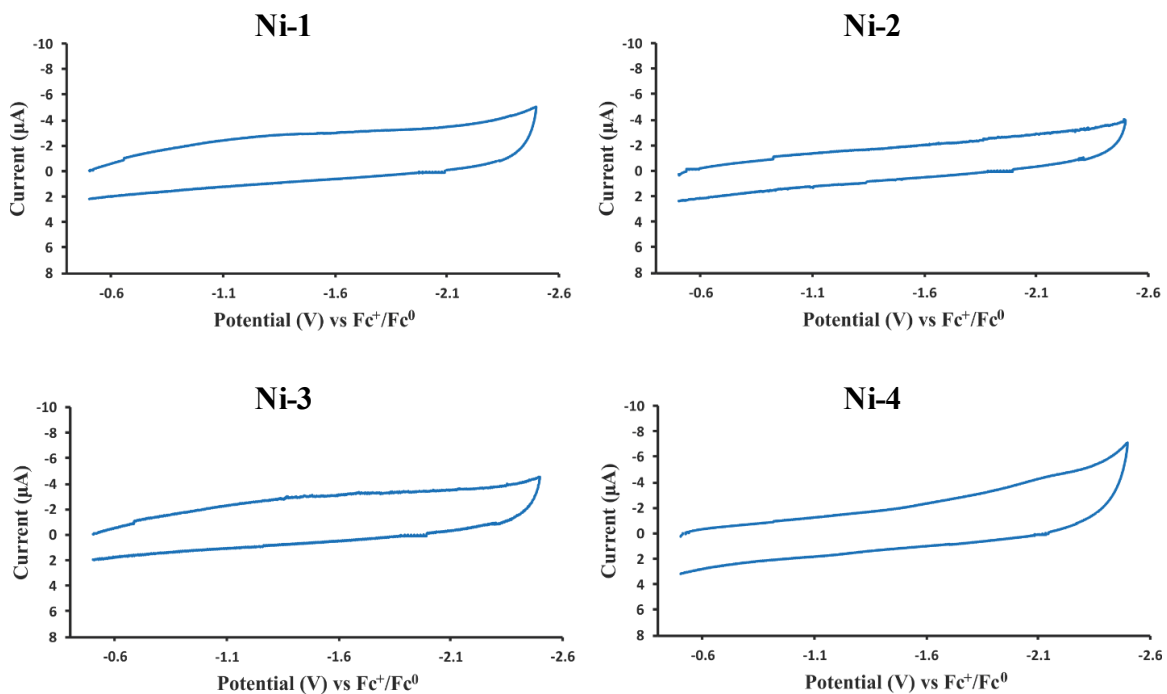


Figure 3.15 Post electrolysis dip test on working electrode after CPC of **Ni-1 – Ni-4** in a fresh 0.1 M Bu₄NPF₆/MeCN solution with no acetic acid at scan rate of 0.2 V/s.

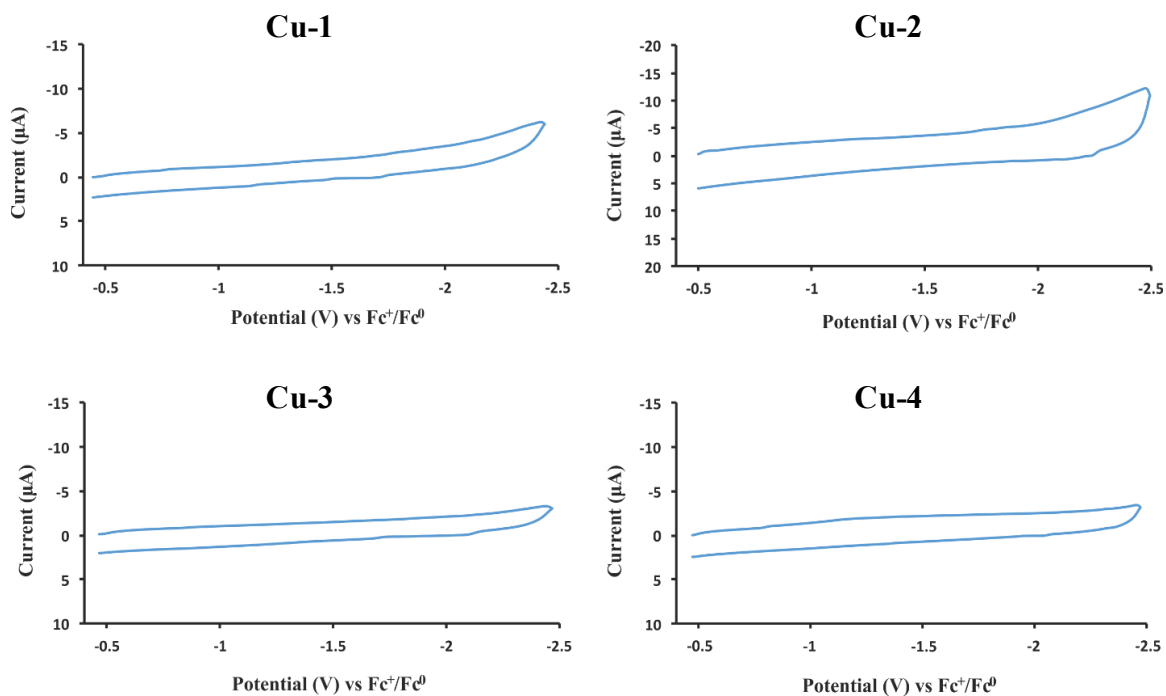


Figure 3.16 Post electrolysis dip test on working electrode after CPC of **Cu-1 – Cu-4** in a fresh 0.1 M Bu₄NPF₆/MeCN solution with no acetic acid at scan rate of 0.2 V/s.

3.5 Conclusion

The HER activity of eight metal BTSC complexes with pendent polyamine groups has been evaluated and compared to their M(ATSM) analogues. Complexes **M-1** and **M-3** contain pendent basic amines, while **M-2** and **M-4** are their quaternary amine derivatives. In the absence of acid substrate, the introduction of the neutral pendent polyamines does not influence the reduction potentials of **M-1** and **M-3**, while the introduction of charged sites in **M-2** and **M-4** shifts the complex reduction potential anodically. However, the effect on HER overpotential is more complicated and metal-dependent. For both sets of catalysts, the catalytic potential ($E_{cat}/2$) does not equal the thermodynamic potential ($E_{1/2}$) and the shifting of overpotential as a function of scan rate indicates intramolecular proton rearrangement is limiting the rate of HER.

Under acid-saturated catalytic conditions, all of the catalysts have charged pendent amines either due to protonation, in the case of **M-1** and **M-3**, or methylation, in the case of **M-2** and **M-4**. The introduction of charged pendent amines may lower the overpotential by shifting the catalyst reduction potential anodically. Alternately, the positive charge could make the catalyst more difficult to protonate, which may retard intramolecular proton rearrangement and increase overpotential. In addition to charge effects, the protonated pendent amines in **M-1** and **M-3** can act as proton relays that facilitate intramolecular proton rearrangement and lower overpotential. The observed metal dependency (Figure 3.17) stems from the differing HER pathways followed by Cu(ATSM) and Ni(ATSM) (Scheme 3.3).

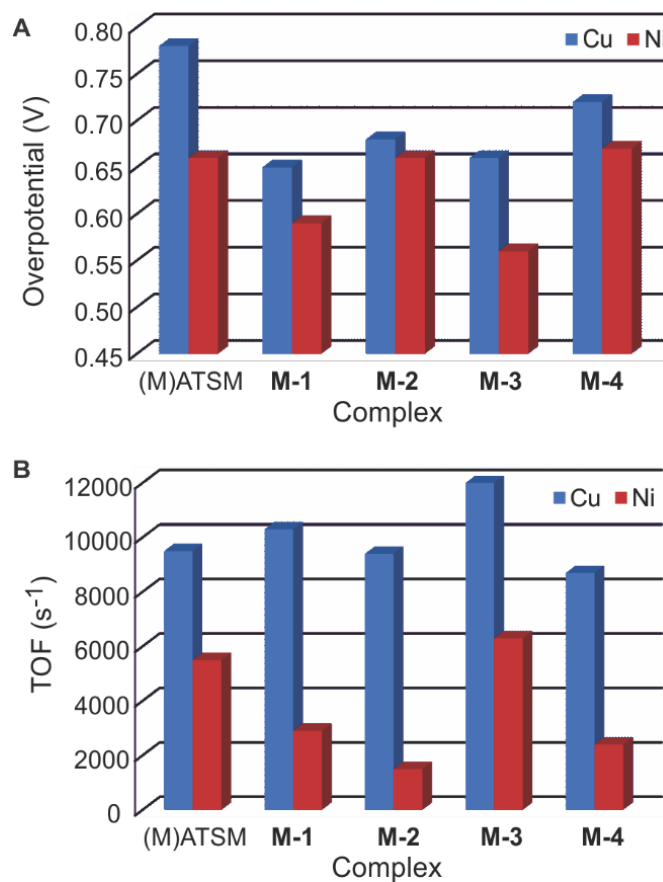
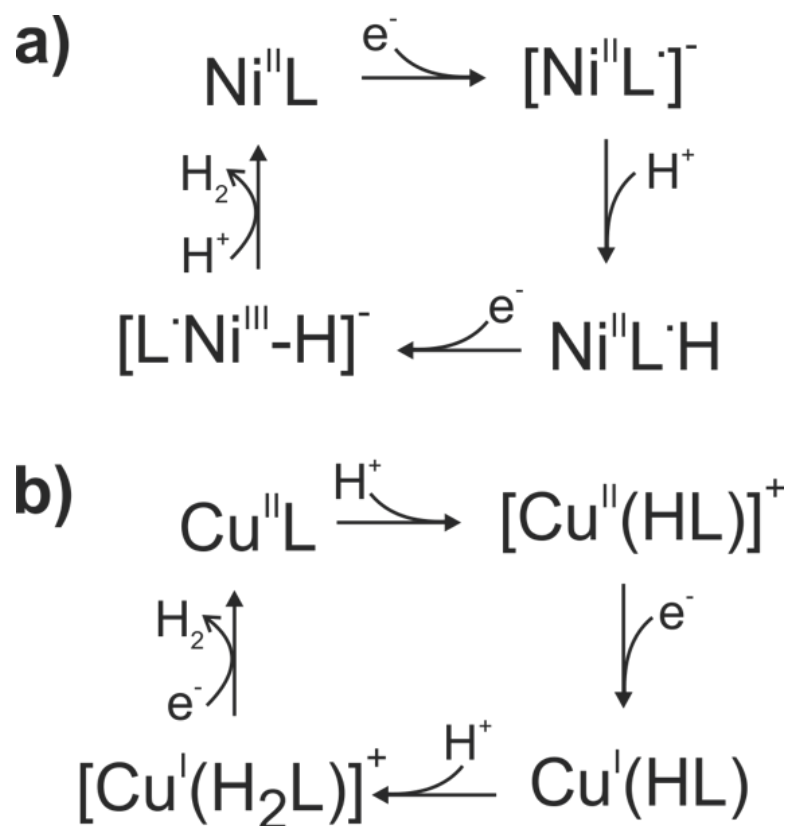


Figure 3.17 Comparison of overpotentials and TOF for M(ATSM) and **M-1 – M-4**.



Scheme 3.3 a) ECEC pathway for Ni(BTSC) catalyzed HER. b) CECE pathway for Cu(BTSC) catalyzed HER.

Ni(ATSM) catalyzes HER through an initial electrochemical step (E), whereas Cu(ATSM) utilizes an initial chemical step (C). The ECEC pathway for Ni(ATSM) alternates between neutral and anionic species. As previously reported, for **Ni-1** – **Ni-4** there are no discernable charge effects as the HER activity of **Ni-2** and **Ni-4** are similar to that of Ni(ATSM). The enhanced activity of **Ni-1** and **Ni-3** results from the ability of the pendent amine to act as a proton relay that lowers the barrier to proton rearrangement.

The CECE path for Cu(ATSM) includes neutral and cationic species. The initial step is protonation. For **Cu-1** – **Cu-4** the data in Figure 3.13 clearly shows a charge effect. The methylated derivatives **Cu-2** and **Cu-4** have a lower HER overpotential than Cu(ATSM) attributed to tuning of the catalyst reduction potential. Notably, the

overpotential for **Cu-2** is lower than **Cu-4** suggesting that the introduction of the second charge site makes protonation and intramolecular proton rearrangement more difficult. In **Cu-1** and **Cu-3** the pendent amine acts as a proton relay enhances proton rearrangement and HER activity.

The effect of the pendent diamine on overpotential is larger at lower scan rates for **Ni-1** – **Ni-4**. The observation that the catalytic potential ($E_{cat/2}$) does not equal the thermodynamic potential ($E_{1/2}$) and the shifting of overpotential as a function of scan rate indicates intramolecular proton rearrangement is limiting the rate of HER. According to the calculated mechanism for NiATSM compound, the most significant proton rearrangement occurs upon the second reduction, which leads to the relocation of the proton from the ligand to the metal (Scheme 3.3a). The enhanced activity of **Ni-1** and **Ni-3** was attributed to the more rapid formation of the Ni-hydride through a proton relay between the pendant diamine and nickel. The effect is more prominent for **Ni-3**, which has two pendant bases. Enhanced HER activity through second coordination sphere effects that promote metal hydride formation has previously been invoked for the “Hangman” porphyrin catalysts.

The effect of proton relays and charged moieties on the electrocatalytic HER activity of copper BTSC complexes is more complex than their nickel analogues. For nickel, the effect was attributed to the presence of pendent relays that lowered HER overpotential by 70 – 100 mV. No evidence of charge effects was observed. For copper, the principal effect of the pendent polyamines is related to charge effects, which lower the HER overpotential by 60 – 100 mV. Notably, increasing the number of charged sites retards the degree of the charge effect, which is attributed to repulsive effects that hinder

protonation. The proton relay effect further decreases overpotential by an additional ~30–60 mV. These results demonstrate the various effects of pendent derivatives to tune the activity of metal BTSC electrocatalysts and their dependence on the reaction pathway.

3.6 Experimental Section

3.6.1 Physical Methods

Elemental analyses were performed by Midwest Microlab, (Indianapolis, IN, USA). ^1H and ^{13}C NMR data were collected on a Varian *Inova* 500 MHz and Varian 400 MHz NMR Spectrometers in commercial deuterated solvents (Aldrich or Cambridge Isotopes). High-resolution electrospray ionization mass spectrometry in the negative ion mode (-ESI) was performed by the Laboratory for Biological Mass Spectrometry at Texas A&M University. Infrared spectra were recorded on a Thermo Nicolet Avatar 360 spectrometer with an ATR attachment (4 cm^{-1} resolution). Electronic absorption spectra were recorded with an Agilent 8453 diode array spectrometer with a 1 cm path length quartz cell.

3.6.2 Electrochemical Methods

Cyclic voltammetry (CV) and controlled potential coulometry (CPC) experiments were performed using a Gamry Interface potentiostat/galvanostat. Overpotential (η) for hydrogen evolution was calculated using the methods reported by Fourmond *et al.* from the theoretical half-wave potential, $E^{T_{1/2}}$, and the experimental potential $E_{\text{cat}/2}$, equation 1.3.⁵⁹

$$\eta = |E_{1/2}^T - E_{cat/2}| \quad (1.3)$$

The value of $E_{cat/2}$ is defined as the potential required to obtain $i_{cat/2}$, one-half of the maximum of catalytic current. The turnover frequency (TOF) for hydrogen evolution was estimated using the *foot-of-the-wave analysis* (FOWA).⁶¹ The CV data were collected using a three-electrode cell comprised of a glassy carbon working electrode, platinum wire counter electrode, and Ag/Ag⁺ reference electrode. Reported potentials are scaled vs. a ferrocenium/ferrocene (Fc⁺/Fc⁰) standard, which was determined using ferrocene as an internal standard. The glassy carbon working electrode was polished by figure-eight motions on a cloth polishing pad in a water-alumina slurry before recording the data. The working and counter electrodes were washed with water, ethanol, isopropanol, acetone, and MeCN, before use. After the washing, the electrodes were sonicated for 15 minutes in the working solvent (MeCN). The three-neck electrochemical cell used for CV studies was washed and dried in an oven overnight before use. In a typical CV experiment, a 0.3 mM solution of the catalyst was prepared in the working solvent (MeCN) containing 0.1 M tetrabutylammonium hexafluorophosphate (Bu₄NPF₆) as supporting electrolyte. The solution was sparged with nitrogen for ~15 minutes and then kept under a nitrogen atmosphere during data collection.

The CPC data were collected using a two-chambered glass electrolysis cell. The working compartment was fitted with a glassy carbon working electrode and Ag/Ag⁺ reference electrode. The auxiliary compartment was fitted with a platinum wire counter electrode. The cell was washed and dried in oven overnight before conducting the experiments. In a typical experiment, the working compartment was loaded with 0.3 mM catalyst, CH₃COOH at saturation conditions, and 0.1 M Bu₄NPF₆ in MeCN solution. The

auxiliary compartment was filled with a 0.1 M $\text{Bu}_4\text{NPF}_6/\text{MeCN}$ solution. Before electrolysis, both compartments were sparged with nitrogen for 15 minutes and then stirred throughout bulk electrolysis experiment. Data were collected at a constant applied potential equal to the potential required for $i_{\text{cat}/2}$ in the CV studies. A control (blank) CPC study was conducted and subtracted from experimental results. Hydrogen gas was measured by gas chromatography (GC, SRI 6810) via online automatic injection (1 mL sample) and a thermal conductivity detector (TCD). Nitrogen (99.99%, Specialty Gases) was used as the carrier gas to enable accurate hydrogen quantification. The gas was injected every 15 minutes and each measured value for faradaic efficiency is representative of the past 15 minutes of electrolysis. In the bulk electrolysis cell itself nitrogen was diffused into the electrolyte at 10 sccm regulated by a mass flow controller (MKS Instruments, Inc.). The electrochemical cell was set up identically as described for all other homogeneous electrochemical experiments except joints were sealed with vacuum grease and a nitrogen outlet line was run from the cell to the GC apparatus. In order to maintain an air-tight seal, the GCE was not rotated. Instead, a magnetic stir was rotated at 360 RPM underneath the GCE to remove hydrogen bubbles from the electrode surface. Theoretical H_2 was determined by counting the coulombs of charge passed, and measured H_2 was determined via GC. The faradaic efficiencies were determined by comparing these values.

3.6.3 Materials and Methods

All reagents were obtained from commercially available sources and used as received unless otherwise noted. Commercial solvents were additionally dried and purified using an MBraun solvent purification system unless otherwise noted. The complexes in this study are air and moisture stable as solids and were handled on the benchtop with no

additional required protection from the atmosphere. Crystal planarity analyses were done using Platon.

3.6.4 Syntheses

All reactions were performed open to air and under ambient conditions unless otherwise indicated.

Ni-1: To a solution of **3** (0.4 g, 1.25 mmol) in MeOH (50 mL) was added Ni(OAc)₂ · 4 H₂O (0.313 g, 1.25 mmol). Formed dark green suspension was heated with stirring for 4 h. The formed dark green solid was filtered and air dried. Yield = 0.383 g (82 %). X-ray quality single crystals were obtained via layering technique by slow diffusion of Et₂O into a MeCN solution of NiL₁. ¹H NMR (400 MHz, *d*₆-DMSO): δ/ppm 7.66 (bs, 1H, NH-C-S), 7.60 (bs, 1H, NH-C=S), 3.28 (q, J_{HH} = 6.0 Hz, 2H, -CH₂NH-), 2.78 (d, J_{HH} = 4.2 Hz, 3H, -CH₃), 2.33 ppm (t, J_{HH} = 6.7 Hz, 2H, CH₂N(CH₃)₂), 2.13 (bs, 6H, -N(CH₃)₂), 1.93-1.92 (bs, 6H, 2 x -CH₃). FT-IR, cm⁻¹: 3274 (br, m, N-H), 2945 (br, w), 1476 (vs, C=N), 1219 (s, thioamide), 942 (w), 771 (w). UV-vis (MeCN/MeOH, 1 : 1): λ_{max}, nm (ε, M⁻¹ cm⁻¹) = 257 (27,000), 393 (13,000). Anal. Calc. for C₁₁H₂₁N₇NiS₂: C, 35.34; H, 5.66; N, 26.24. Found: C, 35.34; H, 5.65; N, 25.99. (-)ESI-MS, m/z calc. for [M-H]⁻, [C₁₁H₂₁N₇NiS₂]-H; 372.0700. Found: 371.9600.

Ni-2: To a suspension of **Ni-1** (0.200 g, 0.534 mmol) in MeCN (25 mL) was added methyl iodide (33.3 μL, 0.534 mmol). The resulting dark green suspension was stirred overnight. Formed dark green solid was filtered and air dried. Yield = 0.212 g (77 %). X-ray quality

single crystals were grown using vapor diffusion technique in an H-shaped tube by slow diffusion of CH₂Cl₂ into a MeCN/MeOH (1 : 1) solution of NiL₁(CH₃)⁺(I)⁻. ¹H NMR (400 MHz, *d*₆-DMSO): δ/ppm 7.96 (bs, 1H, NH–C=S), 7.77 (bs, 1H, NH–C=S), 3.61 (bs, 2H, -CH₂NH-), 3.42 ppm (t, J_{HH} = 5.9 Hz, 2H, CH₂⁺N(CH₃)₃), 3.09 (bs, 9H, -⁺N(CH₃)₃), 2.79 (d, J_{HH} = 3.5 Hz, 3H, -CH₃), 1.96 (bs, 6H, 2 x -CH₃). FT-IR, cm⁻¹: 3218 (br, s, N-H), 2938 (w), 1488 (br, vs, C=N), 1224 (s, thioamide), 964 (m), 922 (m). UV–vis (MeCN/MeOH, 1 : 1): λ_{max}, nm (ε, M⁻¹ cm⁻¹) = 223 (20,000), 256 (24,000), 398 (12,000). Anal. Calc. for C₁₂H₂₄IN₇NiS₂: C, 27.93; H, 4.69; N, 19.00. Found: C, 27.96; H, 4.61; N, 18.96. (-)ESI-MS, m/z calc. for [M-H]⁻, [C₁₂H₂₄IN₇NiS₂]-H; 513.9900, Found: 513.9900.

Ni-3: To a solution of **12** (0.400 g, 1.06 mmol) in MeOH (50 mL) was added Ni(acac)₂ · 2H₂O (0.307 g, 1.06 mmol). Formed dark green solution was heated with stirring for 4 h. A dark green precipitate, formed upon concentration of the solution, was filtered and air dried. Yield = 0.337 g (74 %). X-ray quality single crystals were obtained using layering technique by slow diffusion of Et₂O into a MeCN/MeOH (7 : 3) solution of NiL₂. ¹H NMR (500 MHz, *d*₆-DMSO): δ/ppm 7.61 (bs, 1H, -NH–C=S), 3.27 (q, J_{HH} = 6.2 Hz, 2H, -CH₂NH-), 2.34 (t, J_{HH} = 6.8 Hz, 2H, -CH₂N(CH₃)₂), 2.13 (bs, 6H, -N(CH₃)₂), 1.92 (bs, 3H, -CH₃). FT-IR, cm⁻¹: 3361 (br, m, N-H), 3189 (br, m, N-H), 2937 (br, m), 2767 (br, s), 1404 (vs, C=N), 1230 (s, thioamide), 934 (br, m), 769 (m). UV–vis (MeCN/MeOH, 1 : 1): λ_{max}, nm (ε, M⁻¹ cm⁻¹) = 256 (20,000), 398 (11,000). Anal. Calc. for C₁₄H₃₀N₈NiS₂: C, 38.99; H, 6.54; N, 25.98. Found: C, 38.76; H, 6.40; N, 25.61. (+)ESI-MS, m/z calc. for [M+H]⁺, [C₁₄H₂₈N₈NiS₂]+H: 431.1200. Found: 431.1298.

Ni-4: To a suspension of **Ni-3** (0.200 g, 0.464 mmol) in MeCN (25 mL) was added methyl iodide (57.8 μ L, 0.928 mmol). The resulting dark green suspension was stirred overnight. Formed dark green solid was filtered and air dried. Yield = 0.205 g (62 %). X-ray quality single crystals were grown using vapor diffusion technique in an H-shaped tube by slow diffusion of Et₂O into a MeCN/MeOH (7 : 3) solution of NiL₂(CH₃)₂²⁺(2I)²⁻. ¹H NMR (500 MHz, *d*₆-DMSO): δ /ppm 8.07 (bs, 1H, -NH- C=S), 3.61 (bs, 2H, -CH₂NH-), 3.41 (t, J_{HH} = 6.6 Hz, 2H, -CH₂⁺N(CH₃)₃), 3.08 (bs, 9H, -⁺N(CH₃)₃), 1.97 (bs, 3H, -CH₃). FT-IR, cm⁻¹: 3280 (br, m, N-H), 1410 (vs, C=N), 1227 (s, thioamide), 914 (br, m). UV-vis (MeCN/MeOH, 1 : 1): λ_{max} , nm (ϵ , M⁻¹ cm⁻¹) = 226 (33,000), 256 (28,000), 392 (13,000). Anal. Calc. for C₁₆H₃₄I₂N₈NiS₂ · H₂O: C, 26.21; H, 4.95; N, 15.28. Found: C, 25.84; H, 4.71; N, 15.04. (-)ESI-MS, *m/z* calc. for [M-H]⁻, [C₁₆H₃₄I₂N₈NiS₂]-H; 712.9800. Found: 712.9700.

Synthesis of protonated Ni-3. To a solution of H₂L² (0.400 g, 1.06 mmol) in MeOH (50 mL) was added Ni(OAc)₂ · 4 H₂O (0.263 g, 1.06 mmol). Formed dark green solution was heated for 4 h and concentrated to dryness on a rotary evaporator. A dark green solid was collected and air dried. Yield = 0.310 g (68 %). ¹H NMR (500 MHz, *d*₆-DMSO): δ /ppm 7.61 (bs, 1H, -NH- C=S), 3.27 (q, J_{HH} = 6.2 Hz, 2H, -CH₂NH-), 2.34 (t, J_{HH} = 6.8 Hz, 2H, -CH₂N(CH₃)₂), 2.13 (bs, 6H, -N(CH₃)₂), 1.92 (bs, 3H, -CH₃). FT-IR, cm⁻¹: 3192 (br, m, N-H), 2991, 1473 (vs, C=N), 1221 (s, thioamide), 998 (br, m), 649 (m). Anal. Calc. for

$C_{18}H_{36}N_8NiO_4S_2$: C, 39.21; H, 6.58; N, 20.32. Found: C, 38.69; H, 6.40; N, 20.59. (-)ESI-MS, m/z calc. for $[M-H]^-$, $[C_{14}H_{30}N_8NiS_2]-H$; 429.1200. Found: 429.0800.

Cu-1: To a suspension of **3** (0.2 g, 0.63 mmol) in MeOH (25 mL) was added $Cu(OAc)_2 \cdot H_2O$ (0.126 g, 0.63 mmol). Resulted red-brown suspension was refluxed with stirring overnight. The formed brown precipitate was filtered and air dried. Yield = 0.149 g (62 %). X-ray quality single crystals were obtained by slow evaporation of a MeCN/MeOH/DCM (1 : 1 : 1) solution of CuL_1 . FT-IR, cm^{-1} : 3288 (br, m, N-H), 2947 (br, w), 1395 (vs, C=N), 1217 (s, thioamide), 945 (w), 772 (w). UV-vis (MeCN): λ_{max} , nm (ϵ , $M^{-1} cm^{-1}$) = 324 (39,000), 393 (12,000). Anal. Calc. for $C_{11}H_{21}N_7CuS_2$: C, 34.86; H, 5.58; N, 25.87. Found: C, 34.72; H, 5.39; N, 25.46. +MALDI, m/z calcd for $\{[C_{11}H_{21}N_7CuS_2]-H^+\}$ 379.0700. Found: 379.3300.

Cu-2: To a suspension of **Cu-1** (0.075 g, 0.198 mmol) in MeCN (10 mL) was added methyl iodide (12 μ L, 0.198 mmol). The resulted brown suspension was stirred overnight at room temperature. The formed brown precipitate was filtered and air dried. Yield = 0.066 g (64 %). X-ray quality single crystals were grown by slow evaporation of MeCN solution of $CuL(CH_3)^+(I)^-$. FT-IR, cm^{-1} : 3286 (br, s, N-H), 2946 (w), 139(br, vs, C=N), 1218 (s, thioamide), 1084 (w), 917 (w). UV-vis (MeCN): λ_{max} , nm (ϵ , $M^{-1} cm^{-1}$) = 258 (24,000), 325 (42,000), 472 (12,000). Anal. Calc. for $C_{12}H_{24}IN_7CuS_2 \cdot H_2O$: C, 26.74; H, 4.86; N, 18.19. Found: C, 26.58; H, 4.52; N, 17.92. +MALDI, m/z calcd for $\{[C_{12}H_{24}IN_7CuS_2]-H^+\}$ 393.0800. Found: 393.1500.

Cu-2*: To 20 mL saturated solution of KPF_6 in deionized H_2O a red-brown solution of **Cu-2** (0.060 g, 0.115 mmol) in deionized H_2O was added. Upon addition, **Cu-2*** precipitated as a red-brown solid and was filtered and washed with deionized H_2O (3 x 5 mL) and then air dried. Yield = 0.059 g (95 %). ^{19}F NMR (376 MHz), d_6 -DMSO): δ/ppm -77.39 (d, $J_{\text{FP}} = 706$ Hz). ^{31}P NMR (162 MHz), d_6 -DMSO): δ/ppm -149.07 (h, $J_{\text{PF}} = 706$ Hz).

Cu-3: To a clear solution of **12** (0.200 g, 0.534 mmol) in MeOH (25 mL) was added $\text{Cu}(\text{acac})_2 \cdot \text{H}_2\text{O}$ (0.107 g, 0.534 mmol). Formed red-brown solution was refluxed with stirring for 2 h. The brown precipitate was isolated by addition of diethyl ether, filtered and air dried. Yield = 0.193 g (83 %). X-ray quality single crystals were obtained following the same procedure as in CuL_1 . FT-IR, cm^{-1} : 3336 (br, m, N-H), 2943 (br, m), 2823 (w), 2775 (w), 1415 (vs, C=N), 1215 (s, thioamide), 934 (w), 774 (w). UV-vis (MeCN): λ_{max} , nm (ϵ , $\text{M}^{-1} \text{cm}^{-1}$) = 320 (37,000), 462 (11,000). Anal. Calc. for $\text{C}_{14}\text{H}_{28}\text{N}_8\text{CuS}_2 \cdot 0.75\text{H}_2\text{O}$: C, 37.40; H, 6.63; N, 24.93. Found: C, 37.66; H, 6.42; N, 24.75. +MALDI, m/z calcd for $\{[\text{C}_{14}\text{H}_{28}\text{N}_8\text{CuS}_2]\text{-H}^+\}$ 436.1300. Found: 436.2700.

Cu-4: To a suspension of **Cu-3** (0.100 g, 0.229 mmol) in MeCN (15 mL) was added methyl iodide (28.55 μL , 0.459 mmol). The resulting red-brown suspension was stirred overnight at room temperature. Formed brown precipitate was filtered and air dried. Yield = 0.149 g (90 %). X-ray quality single crystals were obtained following the same procedure as in CuL FT-IR, cm^{-1} : 3272 (br, m, N-H), 1410 (vs, C=N), 1228 (s, thioamide), 914 (br,

m). UV-vis (MeCN): λ_{\max} , nm (ϵ , $M^{-1} \text{ cm}^{-1}$) = 263 (36,000), 318 (28,000), 467 (8,000).

Anal. Calc. for $C_{16}H_{34}I_2N_8CuS_2 \cdot 1.25H_2O$: C, 25.88; H, 4.96; N, 15.09. Found: C, 26.09;

H, 4.64; N, 14.75. +MALDI, m/z calculated for $\{[C_{16}H_{34}I_2N_8CuS_2]-H^+\}$ 233.3532 Found:

233.3874

CHAPTER 4 COVALENT ATTACHMENT AND PHOTOELECTROCHEMISTRY
CHARACTERIZATION OF METAL (II) BIS(THIOSEMICARBAZONE) TO
VARIOUS SURFACES²

4.1 Introduction

Cost-effective, scalable hydrogen production from water-splitting is a grand challenge in the field of clean energy. By coupling the electrolysis to light absorption via artificial photosynthesis, the intermittent energy of sunlight can be captured as H₂ fuel.⁶² While platinum remains the state-of-the-art catalyst for the hydrogen evolution reaction (HER) at the cathode, numerous other catalysts have been studied.⁶³

Molecular catalysts for HER have certain advantages, including low loadings of non-platinum group metal elements, and thus relatively low cost and high abundance. Moreover, the ligand structures can be tailored to tune the active site

² Republished with permission from Royal Society of Chemistry from Gulati, S.; Hietsoi, O.; Calvary, C. A.; Strain, J. M.; Pishgar, S.; Brun, H. C.; Grapperhaus, C. A.; Buchanan, R. M.; Spurgeon, J. M., Photocatalytic hydrogen evolution on Si photocathodes modified with bis(thiosemicarbazonato)nickel(II)/Nafion. *Chem Commun.* **2019**, 55 (64), 9440-9443.⁴³

energetics for activity and selectivity without the constraints imposed by an extended solid lattice in heterogeneous catalysts.⁶⁴⁻⁶⁶ Molecular HER catalysts based on cobalt,⁶⁷⁻⁶⁹ iron,⁷⁰⁻⁷¹ molybdenum,⁷²⁻⁷⁴ and nickel⁷⁵⁻⁷⁷ have been the most common. Molecular nickel complexes are among the most active, such as the well-known DuBois' nickel-bis(diphosphine) catalysts.⁷⁸⁻⁷⁹ More recently, a novel monomeric Ni(II) complex of diacetyl-bis(N-4-methyl-3-thiosemicarbazonato), NiATSM, were explored for its role as a ligand-assisted, metal-centered HER electrocatalyst.³⁷ The structures of bis(thiosemicarbazones) (BTSCs) are easily modified and usually synthesized in high yields from inexpensive organic reagents, making them attractive platforms for the design of new HER electrocatalysts. In addition, BTSC ligands are redox non-innocent and can function as a reservoir for charge with hydrogen evolution at either the metal or the ligand.

There have been a number of studies to leverage molecular HER catalysts for solar H₂ generation by incorporating these structures onto the surface of semiconductor photocathodes.^{65, 80-81} In many cases, the catalyst was immobilized on the semiconductor surface via covalent linking strategies for direct charge transfer between the electrode and catalyst.^{65, 82-83} Covalent attachment is often necessary to prevent catalyst delamination or dissolution in aqueous media but adds processing complexity as well as charge-transfer resistance at the interface. Ideally then, a molecular catalyst could be durably coupled to a photoelectrode with low overpotential in aqueous solution at low or high pH where electrolysis efficiency is maximized. NiATSM co-catalyst with CdS nanorods was recently reported for light-driven hydrogen evolution using monochromatic illumination with a sacrificial

species at moderate pH values.⁸⁴ Building upon these results, that NiATSM can be used to access solar hydrogen generation. Herein, the characterization of the NiATSM catalyst under conditions for practical solar hydrogen generation were reported. Simple catalyst attachment methods were used with p-Si photocathodes in pH 0 aqueous electrolyte to yield robust photoelectrochemical energy-conversion behavior that clearly outperforms an equivalent loading of Ni metal catalyst.

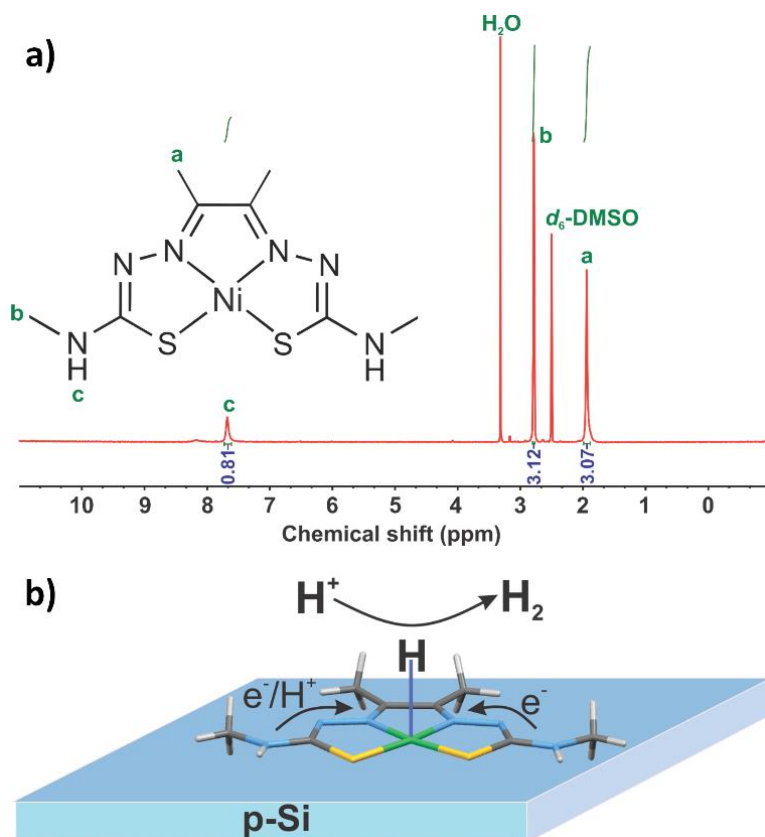


Figure 4.1 a) ^1H NMR of NiATSM (500 MHz, d_6 -DMSO): 7.69 (1H, br. s), 2.75 (3H), 1.94 (3H, s). b) Representation of ligand-assisted, metal-centered HER electrocatalysis by NiATSM on p-Si (Nafion not shown).

The research presented in this chapter was done in collaboration between the Grapperhaus/Buchanan lab in the chemistry department and the Spurgeon lab in the Conn Center. All synthetic work was performed by the Grapperhaus/Buchanan lab.

The inspiration to use Nafion as a binder to the p-Si surfaces was due to previous studies done in the Grapperhaus/Buchanan lab by Wuyu Zhang.⁸⁵ All photochemical measurements and analysis was performed by Saumya Gulati from the Spurgeon lab. The motivation of this work was to demonstrate the viability of ATSM catalysts as a heterogeneous catalyst.

4.2 Results and Discussion

NiATSM was synthesized following previously reported methods^{1, 86} and the complex was characterized by NMR (Figure 4.1), elemental analysis, FT-IR (Appendix Figure H.1a), and UV/vis spectroscopy (Appendix Figure H.1b). NiATSM is known to be a robust HER homogeneous catalyst in organic solutions, and insoluble in 1 M H₂SO₄.^{37, 87} NiATSM was loaded to ~60 nmol cm⁻² onto Si photoelectrodes. In Figure 4.2 shows the photoelectrochemical energy-conversion behavior of NiATSM-coated p-Si photocathodes in 1 M H₂SO₄. Degenerate n⁺-Si electrodes were measured as well to test the behavior of the electrodes in the absence of the photoelectrochemical diode, which instead yields ohmic behavior and permits the measurement of dark electrocatalytic Butler-Volmer HER kinetics on the Si substrate. The onset potential and the potential for each electrode at a standard 10 mA cm⁻² is reported in Table 4.1.

The resulting HER overpotential for the bare n⁺-Si was 860 mV, while 1 Sun-illuminated bare p-Si had a potential of -0.220 V vs. RHE, indicating a typical photovoltage from these electrodes of ~640 mV. With the inclusion of the molecular catalyst layer, the n⁺-Si/NiATSM overpotential decreased to 712 mV, a decrease of

148 mV relative to the bare n⁺-Si. Under illumination, the p-Si/NiATSM potential at 10 mA cm⁻² was -0.080 V vs. RHE. This represents a shift of 140 mV from the

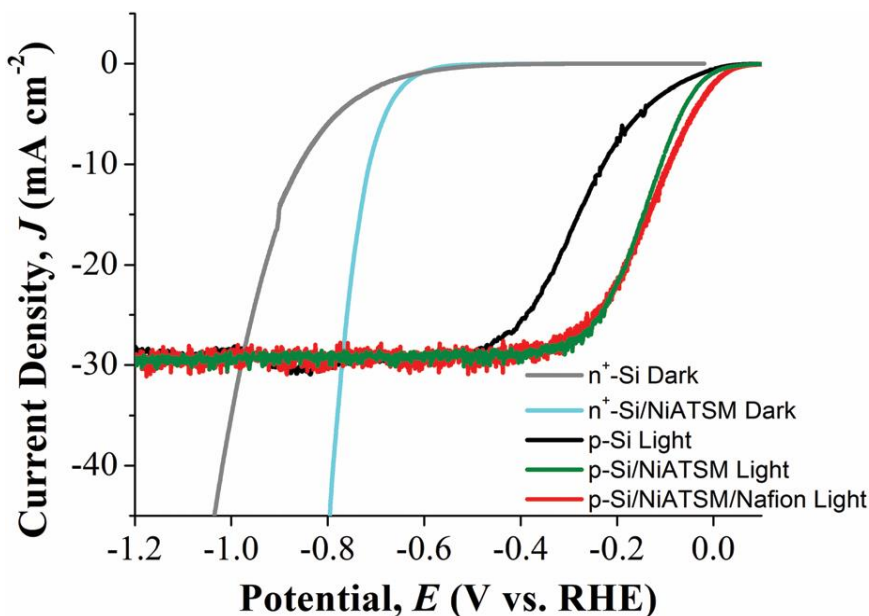


Figure 4.2 Current density vs. potential at (J - E) behavior for electrodes in H₂-saturated 1M H₂SO₄. Dark electrocatalytic behavior for n⁺-Si with and without NiATSM and illuminated 1 sun AM15 behavior for p-Si photocathodes with and without NiATSM catalyst.

Table 4.1 Photoelectrochemical Energy-conversion Parameters.

Electrode	Onset Potential (V vs. RHE)	Potential at 10 mA cm ⁻² (V vs. RHE)
n ⁺ -Si	-0.670	-0.860
n ⁺ -Si / NiATSM	-0.630	-0.712
p-Si	-0.060	-0.220
p-Si/NiATSM	-0.020	-0.080
p-Si/NiATSM/Nafion	0.006	-0.080
p-Si/Ni ^a	-0.024	-0.180
p-Si/Pt ^b	0.124	-0.012

n ⁺ p-Si/NiATSM	0.170	0.025
----------------------------	-------	-------

a Electrodeposited Ni at 60 nmol cm⁻² to match the loading of NiATSM

b Pt deposited by electroless deposition

illuminated bare p-Si and is consistent with the observed catalytic shift on photo-inactive substrates.

The durability of the drop-cast NiATSM catalyst layer was investigated with extended potentiostatic operation under illumination at -0.2 V vs. RHE, a potential with a notable initial difference in current density between p-Si/NiATSM and bare p-Si. The p-Si/NiATSM current density vs. potential (*J-E*) behavior declined after this extended potentiostatic measurement back to the approximate behavior of bare p-Si (Figure 4.3). This response indicates that the molecular catalyst, which is not covalently attached to the Si surface, may be dislodged under extended operation and generation of H₂ bubbles at the surface. To extend the durability, NiATSM was dissolved in a Nafion solution, a cation exchange binder. By casting the NiATSM layer in a dilute Nafion solution as a cation-exchanging binder, the extended current density vs. time performance became stabilized at ~22 mA cm⁻² at -0.2 V vs. RHE over the measured period (Figure. 4.4a), with consistent *J-E* behavior (Figure 4.5).

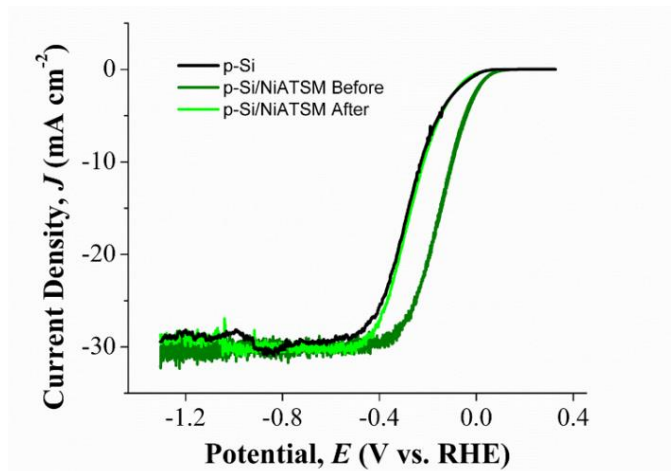


Figure 4.3 Current density vs. potential (J - E) behavior of p-Si/NiATSM without Nafion in 1 M H_2SO_4 under 1 sun AM1.5 illumination, as-deposited performance before and after 1 h at -0.2 V vs. RHE.

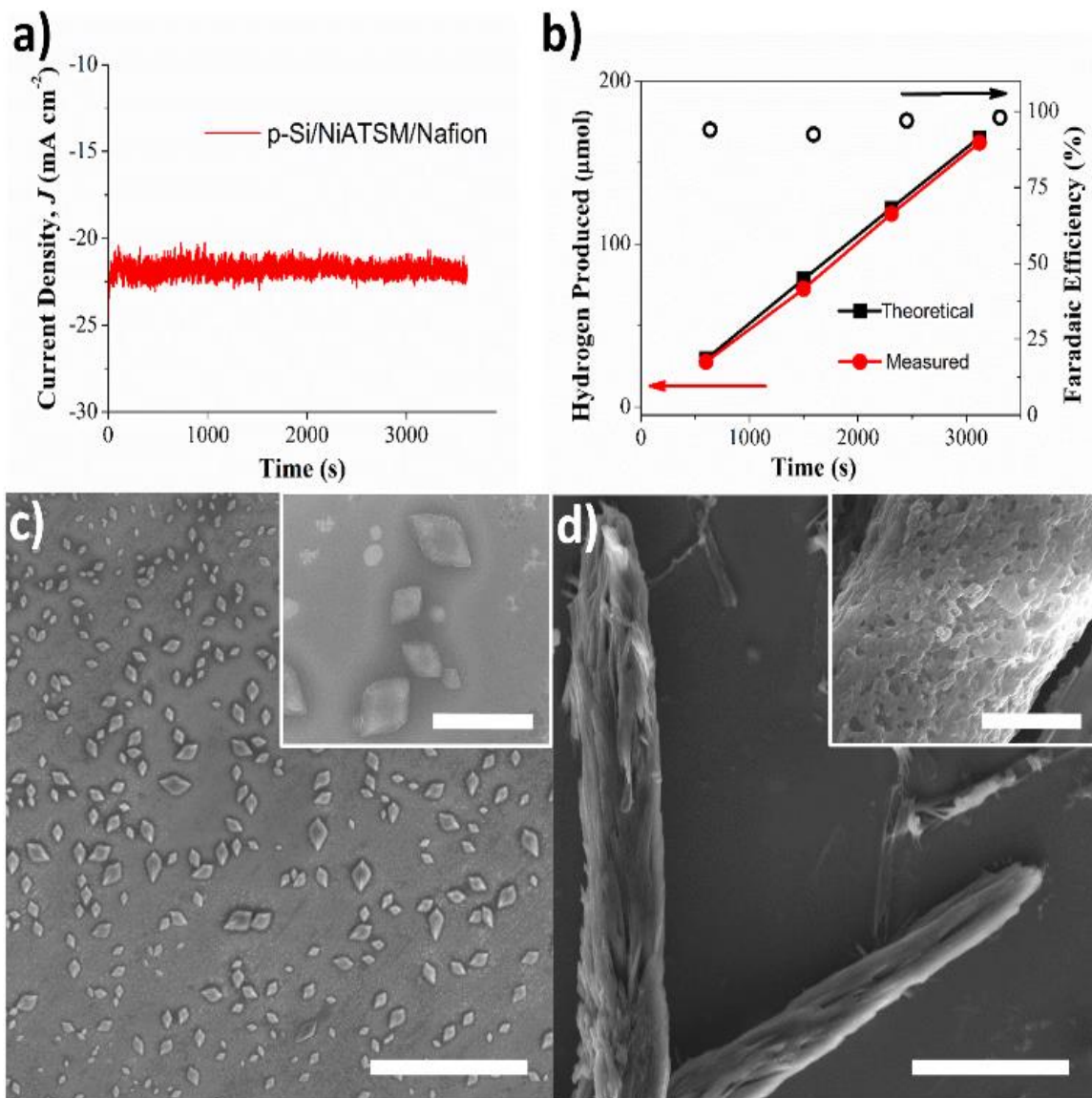


Figure 4.4 a) Current density vs. time at -0.2 V vs. RHE under 1 Sun AM1.5 illumination in 1 M H_2SO_4 . b) Calculated vs. measured H_2 produced by illuminated p-Si/NiATSM/Nafion at -0.2 V vs. RHE in N_2 -bubbled 1 M H_2SO_4 . SEM images of the p-Si/NiATSM/Nafion electrode c) before and d) after the stability measurement in a). Scale bars correspond to $40 \mu\text{m}$ and $2 \mu\text{m}$ for the inset.

Other than promoting adhesion, the Nafion binder had little effect on the initial energy-conversion behavior of the photocathodes (Figure 4.2, Table 4.1, and Figure 4.6). Furthermore, characterization of the H₂ faradaic efficiency by gas

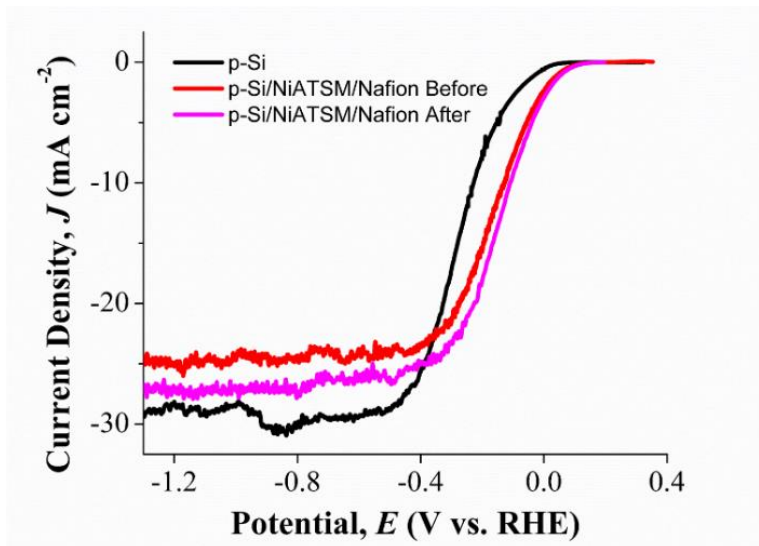


Figure 4.5 Current density vs. potential (J - E) behavior of p-Si/NiATSM with Nafion in 1 M H₂SO₄ under 1 Sun AM1.5 illumination, as-deposited performance before and after 1 h at -0.2 V vs. RHE.

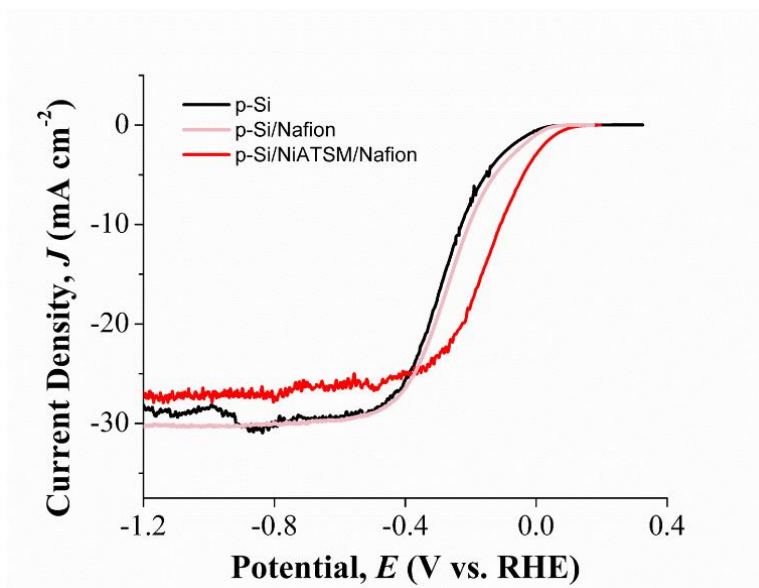
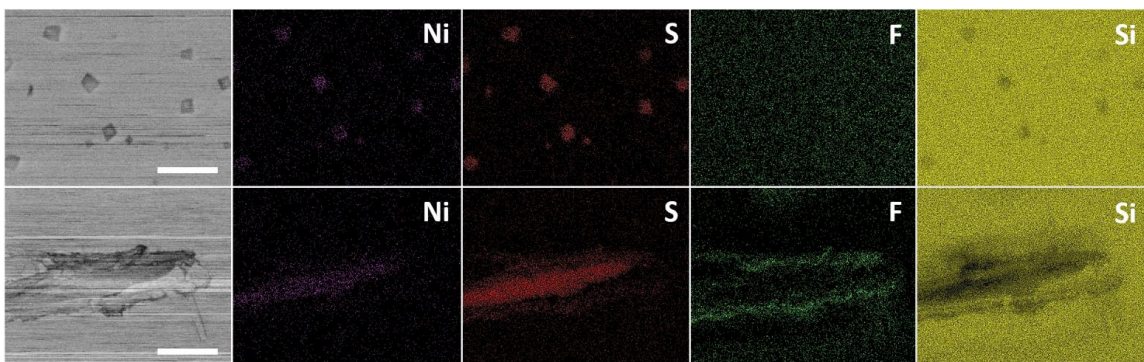


Figure 4.6 Current density vs. potential (J - E) behavior in 1 M H_2SO_4 under 1 Sun AM1.5 illumination for bare p-Si, p-Si/Nafion, and p-Si/NiATSM/Nafion.

chromatography displayed almost total direction of the charge to HER (Figure 4.4b). SEM images of the as-deposited NiATSM/Nafion layer on p-Si show that the catalyst formed 1 – 5 μm crystalline particles in the Nafion film (Figure 4.4c). After extended potentiostatic operation, however, these particles were observed to agglomerate into larger rod-like particles, some as long as $\sim 100 \mu m$ (Figure 4.4d). The structural rearrangement and stacking interactions of NiATSM under cathodic cycling were previously reported and the observed agglomeration here is attributed to similar structural behavior after the passing of significantly more charge.⁸⁷ The elemental composition modeled using energy dispersive X-ray spectroscopy (EDS) mapping showed that the Ni and S of the initial catalyst was confined to this larger agglomerate particle, with Nafion along the rod edges (Figure 4.7). Therefore, the



enhanced stability of the modified photoelectrode may be due to its confinement to the electrode.

Figure 4.7 SEM images (far left) and EDS corresponding elemental maps for Ni (purple), S (red), F (green) and Si (yellow) for p-Si/NiATSM/Nafion before (top panels) and after

(bottom panels) 1 h at -0.2 V vs. RHE in 1 M H₂SO₄ under 1 Sun AM1.5 illumination. The scale bar is 20 μm.

A common challenge for molecular catalysis researchers is to ensure that the observed electrocatalytic activity is attributable to the molecular structure of the ligand-modified metal center rather than direct heterogeneous catalysis of the metal atoms left behind after decomposition of the organic framework. Our previously reported X-ray photoelectron spectroscopy (XPS) data on the Ni 2p and S 2p orbitals of the NiATSM catalyst before and after cathodic current cycling in strongly acidic aqueous electrolyte indicates that the molecular structure does not significantly decompose.⁸⁷ XPS measurements for the NiATSM on p-Si show similar behavior. Though complicated by the presence of the thin Nafion layer, the XPS data indicated that there was no shift in the Ni oxidation state of the catalyst after the 1 h stability measurement (Figure 4.8 and 4.9).

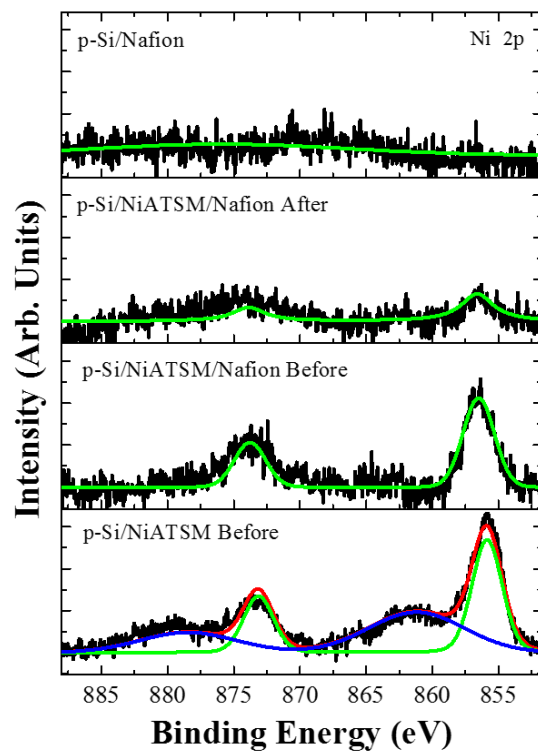


Figure 4.8 XPS spectra for the Ni 2p region for various p-Si substrates. Before substrates were measured with as-deposited catalyst, and the After substrate had been exposed to 1 Sun at -0.2 V vs. RHE in 1 M H₂SO₄ for 1 h.

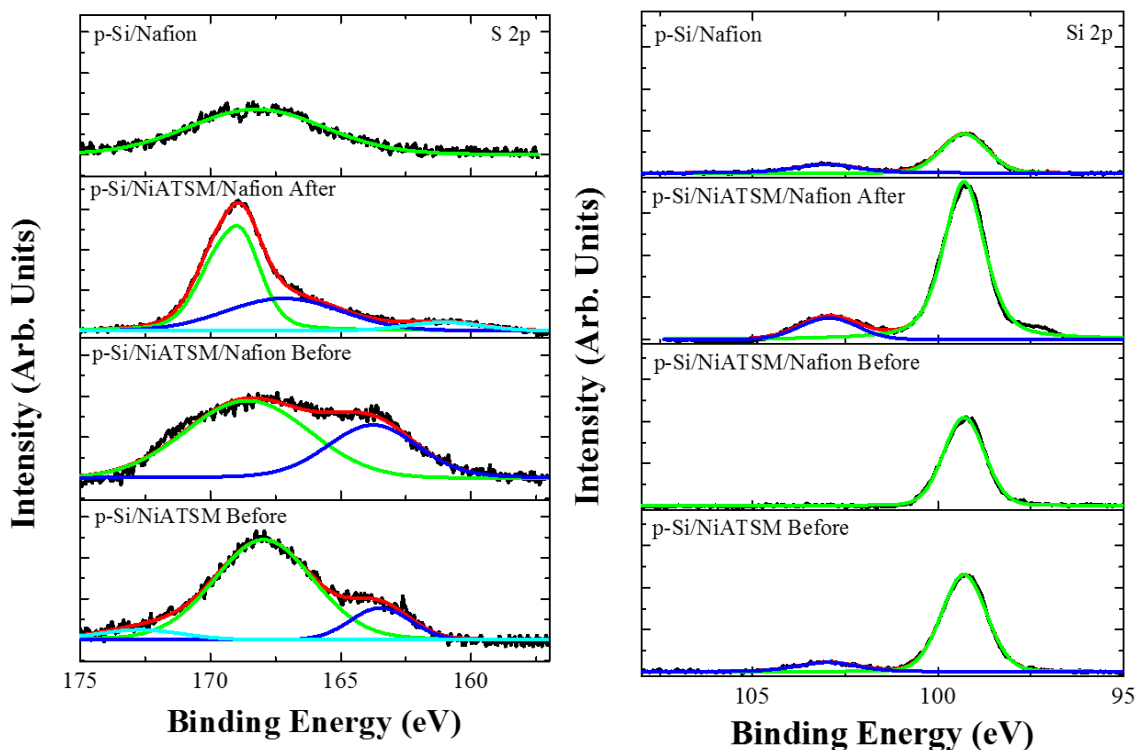


Figure 4.9 XPS spectra for the S 2p region (left panel) and for the Si 2p region (right panel) for various p-Si substrates. Before substrates were measured with as-deposited catalyst, and the After substrate had been exposed to 1 Sun at -0.2 V vs. RHE in 1 M H₂SO₄ for 1 h.

The stability of NiATSM was further tested by measuring p-Si photocathodes with Ni⁰ metal electrodeposited at various loadings. With relatively thick Ni loading (430 nmol cm⁻², corresponding to a 35% decrease in the light-limited photocurrent due to parasitic absorption), the illuminated p-Si/Ni potential at 10 mA cm⁻² was -0.080 V vs. RHE (Figure 4.10). The Ni-metal-catalyzed potential gradually decreased to -0.180 V vs. RHE for a loading of 60 nmol cm⁻², which is the matching loading of Ni atoms calculated to be present in the NiATSM catalyst layer. The photoelectrochemical behavior of p-Si photocathodes for equivalent molar loadings

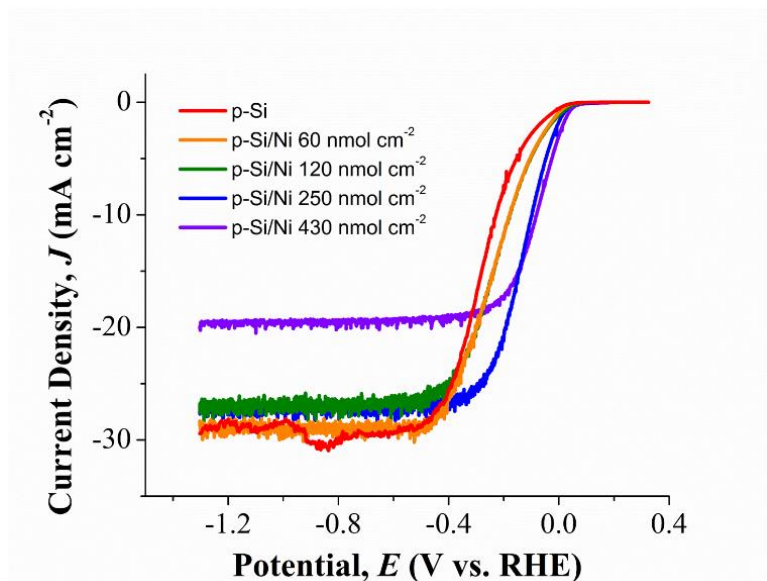


Figure 4.10 Current density vs. potential (J - E) behavior of electrodeposited Ni/p-Si electrodes in 1 M H_2SO_4 under 1 Sun AM1.5 illumination as a function of Ni catalyst loading.

of metallic Ni and NiATSM is shown in Figure 4.11 with a 100 mV improvement in overpotential at 10 mA cm^{-2} for the molecular catalyst relative to the pure metal. The enhanced activity of NiATSM relative to Ni nanoparticles may be attributed to metal-ligand cooperativity during catalysis.⁸⁸ Metal-ligand cooperativity is the concept that the ligand of a complex participates in the catalytic process in conjunction with the metal. This is discussed in more detail in the introduction. In addition to the beneficial contribution of the BTSC ligands to promoting the HER mechanism, the enhancement of the molecular catalyst could be partially attributed to greater access of the electrolyte to each Ni site in the NiATSM molecule compared to the metal Ni deposits.

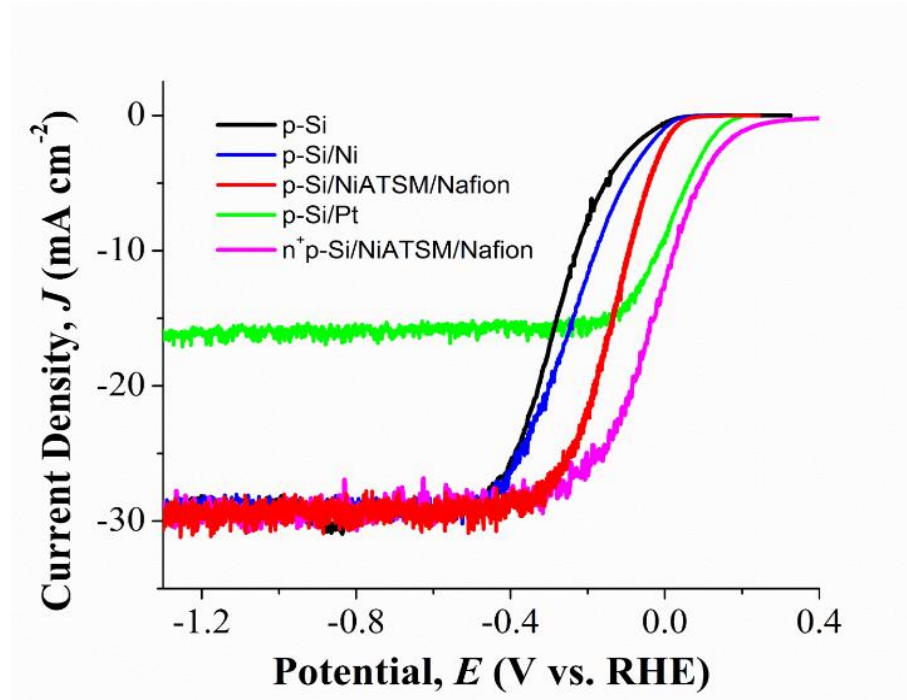


Figure 4.11 Current density vs. potential (J - E) behavior for electrodes in H_2 -saturated 1 M H_2SO_4 . Illuminated 1 Sun AM1.5 photoelectrochemical behavior for p-Si photocathodes with no co-catalyst (black), electrodeposited Ni (blue), NiATSM (red), and Pt (green), as well as a buried junction n^+p -Si with NiATSM (magenta).

The behavior of electrolessly deposited Pt on a p-Si photocathode is also included in Figure 4.11 for a comparison of the NiATSM to the state-of-the-art HER catalyst. As expected, the Pt-catalyzed electrode displayed the more efficient energy-conversion behavior, but it only reduced the overpotential by 68 mV at 10 mA cm^{-2} relative to NiATSM (Table 4.1). Notably, the Pt loading is difficult to control by galvanic displacement and the reduced light-limited current density of the p-Si/Pt curve indicates a significantly heavier catalyst loading in this case as well. Furthermore, forming an n^+p -Si buried homojunction before NiATSM deposition led to even better performance. In this case, a solid-state diode was produced by heavily doping a thin ($\sim 300 \text{ nm}$) n-type emitter layer at the surface before

attachment of the NiATSM for aqueous HER. The 105 mV increase for the buried junction at 10 mA cm⁻² relative to the p-Si/NiATSM/Nafion semiconductor/liquid junction case can be attributed to improved interfacial energetics, increased band bending, and reduced recombination in the p-Si depletion region for a buried junction, as has been demonstrated before for Si photocathodes.⁸⁹ The enhanced HER activity thus comes from the improved photovoltage of the Si buried junction, rather than increased NiATSM activity, and is included to show how Si/NiATSM photocathodes could be improved.

4.3 Conclusions

Molecular NiATSM complex was used as a co-catalyst with planar p-Si for photocathodic hydrogen evolution without covalent surface attachment. The addition of Nafion binder during drop-casting was shown to promote catalyst adhesion and steady potentiostatic operation without degradation of the electrochemical energy-conversion performance. The p-Si/NiATSM/Nafion photocathodes produced H₂ with near unity faradaic efficiency. Moreover, the photoelectrode with Ni molecular catalyst displayed a potential 100 mV more positive than an electrode with an equivalent molar loading of Ni metal, demonstrating the benefit of the BTSC ligands for promoting HER by the ligand-assisted, metal-centered mechanism previously described for NiATSM.³⁷

4.4 Materials and Methods

4.4.1 NiATSM Catalyst Synthesis and Characterization

All reagents were obtained from commercially available sources and used as received unless otherwise noted. Commercial solvents were additionally dried and purified using an MBraun solvent purification system unless otherwise noted. All reactions were performed open to air and under ambient conditions unless otherwise indicated. The diacetyl-bis(N-4-methyl-3-thiosemicarbazone) (H_2ATSM) ligand and the diacetyl-bis(N-4/-methyl-3-thiosemicarazonato)nickel(II) (NiATSM) complex were prepared following previously reported methods.^{1, 86}

The prepared NiATSM complex was characterized by NMR, elemental analysis, FT-IR, and UV/vis spectroscopy. The 1H NMR data were collected on a Varian *Inova* 500 MHz NMR Spectrometer in commercial deuterated solvents (Aldrich or Cambridge Isotopes). The 1H NMR of NiATSM displays characteristic peaks at 1.94 ppm for the backbone methyl protons, at 2.75 ppm for the pendant methyl protons, and at 7.69 ppm for the pendant NH protons. Elemental analyses were performed by Midwest Microlab, (Indianapolis, IN, USA). The purity of NiATSM complex was confirmed by elemental analysis: Anal. Calc. for $C_8H_{14}N_6NiS_2$: C, 30.31; H, 4.45; N, 26.51. Found: C, 30.55; H, 4.35; N, 26.42. Infrared spectra were recorded on a Thermo Nicolet Avatar 360 spectrometer equipped with an ATR attachment (4 cm^{-1} resolution). The infrared spectrum of the H_2ATSM ligand displays two N–H stretches at 3238 and 3357 cm^{-1} . Upon complexation of H_2ATSM with Ni(II) the characteristic hydrazino N–H stretch at 3238 cm^{-1} disappears in the NiATSM spectrum. Electronic UV/vis absorption

spectra were recorded with an Agilent 8453 diode array spectrometer with a 1 cm path length quartz cell. The electronic spectrum of H₂ATSM displays a strong band at 328 nm that upon complexation with Ni(II) is significantly decreased with the appearance of a ligand-to-metal charge-transfer band near 398 nm and a more intense ligand-to-ligand charge-transfer band near 257 nm in the NiATSM spectrum (Appendix Figure H.1a).

4.4.2 Electrode Preparation

Two different types of Si substrate were used in this work. Degenerately doped n⁺-Si(100) (doped with As to a resistivity of 0.001 – 0.005 Ω cm, University Wafer) substrates were used to measure the dark electrocatalytic behavior of the Si semiconductor surface as well as the Si-supported NiATSM electrocatalyst behavior. Photoactive substrates for illuminated hydrogen evolution consisted of p-Si(100) (doped with B to 1 – 10 Ω cm, University Wafer). Before attaching the NiATSM co-catalyst, the Si native oxide layer was removed with a > 10 s dip in 10% HF. To load the catalyst on the electrodes, a 2.0 mM solution of NiATSM in acetonitrile was dropcast on the Si surface to a consistent loading of ~60 nmol cm⁻², followed by 1 min in a vacuum oven at 70 °C. For Nafion-bound NiATSM, each 20 mL of 2 mM solution also contained 25 μL of 5% aqueous Nafion solution (Beantown Chemical) and was further heated in air at 60 °C for 1 min. In the case of electrodeposited Ni metal catalyst on p-Si for comparison, the Si working electrode was placed in nickel electroplating solution (nickel sulfamate and boric acid, Sigma Aldrich) with a Ag/AgCl reference and a fritted Pt counter electrode

and held at -0.5 V vs. RHE under illumination to pass various amounts of charge corresponding to different Ni loadings. To match the molar loading of Ni atoms on the NiATSM/p-Si electrodes with 60 nmol NiATSM cm⁻², a charge of 0.012 C cm⁻² was passed. An ohmic back contact to Si substrates was made using Ga/In eutectic (Alfa Aesar), with the back contact sealed in epoxy. Pt deposition on p-Si was accomplished via a galvanic displacement reaction whereby Si is oxidized (and then etched by HF) and Pt is reduced onto the electrode surface.⁹⁰ The Si wafer was immersed for 2 minutes in an aqueous solution of 0.5 M HF and 2 mM K₂PtCl₆.⁸⁹ The n⁺ p junction was formed on the Si by thermal P diffusion using solid-source CeP₅O₁₄ wafers (Saint-Gobain, PH-900 PDS) at 950 °C for 30 min under N₂ ambient, to yield an n⁺ emitter layer. The room temperature n⁺p-Si was then etched in 10% HF for > 2 min to remove the dopant glass layer, followed by physical abrasion of the wafer edges to eliminate shunting.

4.4.3 Photoelectrochemical Measurements

Current density vs. potential (*J-E*) photoelectrochemical energy-conversion behavior for all electrodes was measured in hydrogen-saturated 1 M H₂SO₄ (pH 0, made with 18 MΩ cm H₂O) under vigorous stirring with active bubbling of H₂ (99.99%, Specialty Gases) at room temperature. The Si electrode was the working electrode in each case, with an Ag/AgCl (saturated KCl) reference electrode (CH instruments, Inc.) along with a Pt gauze counter electrode separated by a glass frit, all in a glass cell with a flat quartz window for illumination. Before each measurement with a Si electrode, the native oxide was removed with a > 10 s dip in

10% HF. A Bio-Logic SP-200 potentiostat was used for all measurements. The results are reported versus the reversible hydrogen electrode (RHE) scale according to $V_{RHE} = V_{Ag/AgCl} + 0.197 + 0.059 \cdot \text{pH}$. Simulated sunlight at an intensity of 100 mW cm^{-2} at normal incidence to the working electrode was generated with a 300 W Xe lamp (Newport 6258) coupled with an AM1.5 global filter (Newport 81094) and calibrated in the electrolyte with a Si photodiode (Thorlabs FDS100-CAL). Cyclic voltammetry measurements of J - E behavior were measured at a scan rate of 20 mV s^{-1} . Reported 1 h stability data was measured potentiostatically at -0.2 V vs. RHE.

Hydrogen quantification and faradaic efficiency determination were measured under potentiostatic conditions at -0.2 V vs. RHE using gas chromatography (GC, SRI 8610). For this measurement, H_2 was not bubbled but instead nitrogen (99.99%, Specialty Gases) was used as the carrier gas to enable accurate hydrogen quantification. The gas outlet from the catholyte was connected to the GC, which used an automatic valve injection (1 mL sample) and a thermal conductivity detector (TCD). Faradaic efficiency was calculated by determining the charge required to produce the measured H_2 concentration and dividing by the total charge passed in the electrolysis during the gas collection period.

4.4.4 Materials Characterization

The electrode surfaces were characterized with scanning electron microscopy (SEM) using a NOVA FEI microscope at an accelerating voltage of $\sim 10 - 15 \text{ kV}$. Energy dispersive X-ray spectroscopy (EDS) mapping measurements were conducted using an FEI Tecnai F20 microscope with an accelerating voltage of 200

kV. Surface elemental analysis was performed using X-ray photoelectron spectroscopy (XPS) with a VG Scientific Multilab 3000 custom-built ultra-high vacuum system with Al-K α radiation. XPSPEAK 4.1 software was used for peak deconvolution and the XPS data analysis.

4.4.5 Nafion Binding Effect on *J-E* Behavior Stability

Although the *J-E* behavior of drop-cast NiATSM on p-Si initially showed a significant positive shift in the potential relative to bare p-Si, this enhancement was not stable under extended operation. After 1 hour of potentiostatic operation at -0.2 V vs. RHE, the photoelectrode *J-E* behavior became indistinguishable from that of bare p-Si. This performance decline was attributed to gradual detachment of the NiATSM catalyst from interfacial agitation during H₂ bubble formation. Thus, a Nafion solution was added to the NiATSM solution to provide an acid-compatible binding layer during drop-casting. The resulting current density vs. potential photoelectrochemical behavior for p-Si/NiATSM/Nafion photoelectrodes became much more stable. The photocurrent response slightly increased after the 1 hour potentiostatic measurement, which may be partially attributable to the beneficial effect of NiATSM molecular catalyst morphology stacking and restructuring as reported in our previous work.⁸⁷

4.4.6 Effect of Nafion on the p-Si Performance

The NiATSM was cast from a dilute solution of Nafion with the cation-exchange selective ionomer used to enhance the binding of the molecular compound to the semiconductor surface while permitting stable performance in acidic media. An equivalent thickness of Nafion film on p-Si in the absence of NiATSM had only a minor effect on the illuminated current density vs. potential behavior. There was a slight positive shift in potential for a Nafion film relative to a bare p-Si photoelectrode. This minor effect could speculatively be attributed to the charged groups in the Nafion sulfonic acid side chains creating a slight dipole at the interface, which contributes to band bending and has been experimentally demonstrated to affect the photoelectrochemical photovoltage.⁹¹ However, initial *J-E* performance curves for p-Si/NiATSM with and without Nafion binder were indistinguishable between multiple electrodes within experimental error.

4.4.7 Elemental Mapping of NiATSM on p-Si

Following extended potentiostatic operation of the p-Si/NiATSM/Nafion photocathodes, the catalyst particles were observed to agglomerate into larger rodlike particle structures. Energy dispersive x-ray spectroscopy (EDS) analysis was performed to map the distribution of the key elements before and after this restructuring. Ni and S, which are primarily present in the NiATSM (S is a minor component in Nafion), are mostly confined to the observed particles even after the agglomeration. Fluorine, F, which is introduced in the polytetrafluoroethylene backbone of the Nafion binder, is initially observed to be uniformly distributed.

However, after particle agglomeration, it was observed to be more concentrated along the edges of the rodlike NiATSM particle. Si, as the underlying substrate, displayed a strong signal everywhere, which was only weakened in the locations of the catalyst particle.

4.4.8 XPS of NiATSM and Nafion on p-Si

Although XPS data for NiATSM after cathodic cycling on glassy carbon substrates in aqueous acidic electrolyte has already shown a steady Ni oxidation state in our previous work,⁸⁷ it was measured and reported again here on p-Si photoelectrodes and in the presence of the Nafion binder. For an as-deposited p-Si/NiATSM without Nafion, a p-Si/Nafion without NiATSM, and p-Si/NiATSM/Nafion before and after 1 h under 1 Sun at -0.2 V vs. RHE in 1 M H₂SO₄, the measured binding energies for the Ni 2p, S 2p, and Si 2p regions. Without Nafion, the as-deposited p-Si/NiATSM shows the same Ni 2p character as previously reported for NiATSM.⁸⁷ When the NiATSM is co-deposited with Nafion binder, the Ni 2p signal was significantly reduced in intensity, which is consistent with a thin surface coating of polymer reducing the signal. The Ni 2p peak intensity was further reduced after operation, consistent with the dispersed catalyst particles concentrating into larger particles and leaving less area of exposed Ni to measure. However, the main Ni 2p peak position at ~856 eV remained unchanged before and after operation, indicating no shift in the oxidation state.

For sulfur, the XPS spectra is more complicated by the presence of the Nafion layer. Nafion polymer owes its cation-selective permeability to the negatively charged groups arising from the clustering of sulfonic acid side chains. Thus, there

are S atoms present throughout the Nafion film, as evidenced by the broad S 2p peak observed for p-Si/Nafion without NiATSM catalyst. For p-Si/NiATSM without Nafion, a sharper S 2p was observed at ~168 eV, which would be attributed to the Ni-adjacent S atoms in NiATSM. When NiATSM is co-deposited with Nafion, the resulting S 2p spectra appears to be a convolution of the broad Nafion S peak and the underlying NiATSM S signal. Interestingly, after the p-Si/NiATSM/Nafion stability measurement, the sharper NiATSM S 2p peak increased in intensity relative to the spectra before photocathodic hydrogen evolution. The nature of this shift is not entirely clear, but we speculate that the NiATSM agglomeration to large rodlike particles during operation leaves more of the NiATSM directly exposed to the x-ray signal, as opposed to the smaller as-deposited NiATSM clusters which have a surface coating of Nafion to interfere with the measurement.

The effect on the underlying Si substrate was also probed with the Si 2p XPS binding energy spectra. After the 1 h stability measurement, the Si peak at 99.6 eV and the SiO₂ peak at 103.4 eV both became more intense relative to the as-deposited substrates. As observed in our SEM measurements after extended potentiostatic operation, the initial smaller microparticles of NiASTM left behind gaps in the Nafion thin film when they migrated and agglomerated into larger particles. We thus attribute the increased Si peak (and Si oxidation) to the underlying Si in these gaps being directly exposed to the x-ray.

4.4.9 Behavior of Electrodeposited Ni on p-Si

Metallic Ni was deposited photoelectrochemically on p-Si for comparison to the performance of photocathodes catalyzed with molecular NiATSM. By controlling the charge passed per electrode area during electrodeposition, well-controlled Ni loadings were achieved. With a single Ni site per NiATSM molecule, a molar loading of Ni of $\sim 60 \text{ nmol cm}^{-2}$ was present as NiATSM catalyst during photoelectrochemical measurements. Thus, 60 nmol cm^{-2} of electrodeposited Ni catalyst was used to directly compare the activity of an equivalent amount of metallic Ni. The low loading of Ni as HER catalyst produced little improvement in the *J-E* behavior of a p-Si photocathode. Progressively higher loadings of Ni managed to reduce the overpotential, with a loading of 430 nmol cm^{-2} reaching 10 mA cm^{-2} at -0.080 V vs. RHE . This potential is comparable to that achieved for p-Si/NiATSM/Nafion photoelectrodes (Table 4.1), however, it required 7.2x as much Ni. Moreover, parasitic light absorption in the catalyst layer became more significant at this loading, leading to a 35% decrease in the light-limited current density.

CHAPTER 5 CONCLUDING THOUGHTS AND FUTURE DIRECTIONS

Transamination is an efficient, one-pot synthesis approach to produce different derivatives of H₂ATSM. Many different functional groups were tested. Most non-acidic functional groups on both aliphatic and aromatic amines gave good isolated yields. However, when acidic functional groups were used either an incomplete reaction or no reaction were observed. In addition, the solvent was changed from acetonitrile to tetrahydrofuran due to low yields for some aromatic amines when acetonitrile was used. The most appealing factor of the transamination reaction was the high yield, high purity, and no further purification needed.

With this current progress in the development of the transamination reaction, there are many opportunities for further exploration. It has been suggested that by using amine-tagged crown ethers as transamination substrates, bigger metal ions can be chelated, which means a larger charged BTSCs (in terms of both size and overall charge of the complex) can be obtained. This can further help shift catalysis, as seen in the studies in chapter three, as a larger charge could result in a larger anodic shift. In addition, the greater charge could lead to an increase in solubility in solvents such as water, that makes it a more appealing catalyst. Another direction for the transamination project is to exploit the usefulness of the thiol (-SH) and alcohol (-OH) transaminated species. These functional groups are of interest due to much

research done for binding of these groups to surfaces, gold in particular. It is postulated that if these transaminated groups were bound to gold nanoparticles, these could be used as targeted delivery systems.

Copper and nickel BTSC complexes that contained hindered alkyamine bases pendants were synthesized, which were subsequently alkylated to produce charged complexes. The free base and charge complexes were then characterized electrochemically. An expected anodic shift was observed in the cases of the charged complexes as compared to the free base complexes. When tested for HER activity, it was revealed that the free base complexes showed the best activity due to the ability of the pendent base to participate in proton relay. The nickel BTSC catalysis was analyzed via foot-of-the-wave analysis (FOWA) while the copper BTSC catalysis was analyzed using plateau current analysis.

There are many avenues to expand this proton relay project. Extending the relay by use of polyamines is a viable option. These polyamine BTSC derivatives have already been reported by Donnelly et al.¹² By extending the relay, the resulting electrochemical proton transfer process may become more facile than a single amine relay. This would lead to an increase in activity as well as an increase in solubility in solvents such as water. Another route to expand this research is to further investigate the potential for anti-cancer activity of these complexes. Initial anti-cancer activity studies on the copper BTSC demonstrated high activity for the double free base complex. This was attributed to the fact that this complex could form discrete dimers which allows for greater delivery of copper to the cancer cells.

The photon induced HER catalysis of NiATSM mounted on p-Si electrodes were explored. For this project, NiATSM was used due the stringent requirements needed for testing, that being high solubility in volatile organic solvents and insoluble to 1 M H₂SO₄. Inspiration was drawn from previous research from the Grapperhaus/Buchanan group and Nafion was suggested as a binding agent to keep the NiATSM film on the surface. When Nafion was used in the preparation of the film, the subsequent photoelectrochemistry study shows no observed loss of activity over time. In addition, the onset potential for film was compared to the platinum standard in the same conditions and proved efficient. This heterogeneous study could be expanded by testing other small molecules to activate. While HER has been very thoroughly explored regarding metal ATSM complexes, not much has been done on other small molecules.

REFERENCES

1. Blower, P. J.; Castle, T. C.; Cowley, A. R.; Dilworth, J. R.; Donnelly, P. S.; Labisbal, E.; Sowrey, F. E.; Teat, S. J.; Went, M. J., Structural trends in copper(II) bis(thiosemicarbazone) radiopharmaceuticals. *Dalton Trans.* **2003**, 0, 4416-4425.
2. Dearling, J. L.; Lewis, J. S.; Mullen, G. E.; Welch, M. J.; Blower, P. J., Copper bis(thiosemicarbazone) complexes as hypoxia imaging agents: structure-activity relationships. *JBIC, J. Biol. Inorg. Chem.* **2002**, 7 (3), 249-259.
3. Bonnitcho, P. D.; Vavere, A. L.; Lewis, J. S.; Dilworth, J. R., In vitro and in vivo evaluation of bifunctional bithiosemicarbazone Cu-64-complexes for the positron emission tomography imaging of hypoxia. *J Med. Chem.* **2008**, 51 (10), 2985-2991.
4. Anjum, R.; Palanimuthu, D.; Kalinowski, D. S.; Lewis, W.; Park, K. C.; Kovacevic, Z.; Khan, I. U.; Richardson, D. R., Synthesis, Characterization, and in Vitro Anticancer Activity of Copper and Zinc Bis(Thiosemicarbazone) Complexes. *Inorg. Chem.* **2019**, 58 (20), 13709-13723.
5. Yu, P.; Deng, J. G.; Cai, J. H.; Zhang, Z. L.; Zhang, J. Z.; Khan, M. H.; Liang, H.; Yang, F., Anticancer and biological properties of a Zn-2,6-diacetylpyridine bis(thiosemicarbazone) complex. *Metallomics* **2019**, 11 (8), 1372-1386.
6. Jiang, W.-X.; Liu, W.-X.; Wang, C.-L.; Zhan, S.-Z.; Wu, S.-P., A bis(thiosemicarbazonato)-copper complex, a new catalyst for electro- and photo-reduction of CO₂ to methanol. *New J Chem.* **2020**, 44 (7), 2721-2726.
7. Calvary, C. A.; Hietsoi, O.; Strain, J. M.; Mashuta, M. S.; Spurgeon, J. M.; Buchanan, R. M.; Grapperhaus, C. A., Synthesis, Characterization, and HER Activity of Pendant Diamine Derivatives of NiATSM. *Eur. J Inorg. Chem.* **2019**, 2019 (33), 3782-3790.
8. Haddad, A. Z.; Cronin, S. P.; Mashuta, M. S.; Buchanan, R. M.; Grapperhaus, C. A., Metal-Assisted Ligand-Centered Electrocatalytic Hydrogen Evolution upon Reduction of a Bis(thiosemicarbazonato)Cu(II) Complex. *Inorg. Chem.* **2017**, 56 (18), 11254-11265.
9. West, D. X.; Liberta, A. E.; Padhye, S. B.; Chikate, R. C.; Sonawane, P. B.; Kumbhar, A. S.; Yerande, R. G., Thiosemicarbazone complexes of copper(II): structural and biological studies. *Coord. Chem. Rev.* **1993**, 123 (1), 49-71.
10. McInnes, L. E.; Noor, A.; Kysenius, K.; Cullinane, C.; Roselt, P.; McLean, C. A.; Chiu, F. C. K.; Powell, A. K.; Crouch, P. J.; White, J. M.; Donnelly, P. S., Potential Diagnostic Imaging of Alzheimer's Disease with Copper-64 Complexes That Bind to Amyloid- β Plaques. *Inorg. Chem.* **2019**, 58 (5), 3382-3395.

11. Xie, D.; King, T. L.; Banerjee, A.; Kohli, V.; Que, E. L., Exploiting Copper Redox for F-19 Magnetic Resonance-Based Detection of Cellular Hypoxia. *J. Am. Chem. Soc.* **2016**, *138*, 2937-2940.
12. Paterson, B. M.; Cullinane, C.; Crouch, P. J.; White, A. R.; Barnham, K. J.; Roselt, P. D.; Noonan, W.; Binns, D.; Hicks, R. J.; Donnelly, P. S., Modification of Biodistribution and Brain Uptake of Copper Bis(thiosemicarbazonato) Complexes by the Incorporation of Amine and Polyamine Functional Groups. *Inorg. Chem.* **2019**, *58* (7), 4540-4552.
13. Vishnosky, N. S. Synthesis, characterization, and evaluation of metal complexes with cancer selective anti-proliferative effects and hydrogen evolution catalytic properties. Doctoral Dissertation, University of Louisville, 2019.
14. Brownson, D. A.; Kampouris, D. K.; Banks, C. E., Graphene electrochemistry: fundamental concepts through to prominent applications. *Chem. Soc. Rev.* **2012**, *41* (21), 6944-76.
15. Elgrishi, N.; Rountree, K. J.; McCarthy, B. D.; Rountree, E. S.; Eisenhart, T. T.; Dempsey, J. L., A Practical Beginner's Guide to Cyclic Voltammetry. *J Chem. Educ.* **2018**, *95* (2), 197-206.
16. Appel, A. M.; Helm, M. L., Determining the Overpotential for a Molecular Electrocatalyst. *ACS Catal.* **2014**, *4* (2), 630-633.
17. Costentin, C.; Robert, M.; Savéant, J.-M.; Tatin, A., Efficient and selective molecular catalyst for the CO₂-to-CO electrochemical conversion in water. *Proc. Natl. Acad. Sci. USA* **2015**, *112* (22), 6882-6886.
18. Midilli, A.; Ay, M.; Dincer, I.; Rosen, M. A., On hydrogen and hydrogen energy strategies: I: current status and needs. *Ren. Sus. Energy Rev.* **2005**, *9* (3), 255-271.
19. Eftekhari, A., Electrocatalysts for hydrogen evolution reaction. *Int. J. Hydrogen Energ.* **2017**, *42* (16), 11053-11077.
20. Csernica, P. M.; McKone, J. R.; Mulzer, C. R.; Dichtel, W. R.; Abruna, H. D.; DiSalvo, F. J., Electrochemical Hydrogen Evolution at Ordered Mo₇Ni₇. *ACS Catal.* **2017**, *7* (5), 3375-3383.
21. Ren, J.; Musyoka, N. M.; Langmi, H. W.; Mathe, M.; Liao, S., Current research trends and perspectives on materials-based hydrogen storage solutions: A critical review. *Int J Hydrogen Energ* **2017**, *42* (1), 289-311.
22. Papadakis, M.; Barrozo, A.; Straistari, T.; Queyriaux, N.; Putri, A.; Fize, J.; Giorgi, M.; Réglie, M.; Massin, J.; Hardré, R.; Orio, M., Ligand-based electronic effects on the electrocatalytic hydrogen production by thiosemicarbazone nickel complexes. *Dalton Trans.* **2020**, *49* (16), 5064-5073.
23. Drosou, M.; Kamatsos, F.; Mitsopoulou, C. A., Recent advances in the mechanisms of the hydrogen evolution reaction by non-innocent sulfur-coordinating metal complexes. *Inorg. Chem. Front.* **2020**, *7* (1), 37-71.
24. Haddad, A. Z.; Kumar, D.; Sampson, K. O.; Matzner, A. M.; Mashuta, M. S.; Grapperhaus, C. A., Proposed Ligand-Centered Electrocatalytic Hydrogen Evolution and

Hydrogen Oxidation at a Noninnocent Mononuclear Metal-Thiolate. *J. Am. Chem. Soc.* **2015**, *137* (29), 9238-9241.

25. Zhang, W. Y.; Haddad, A. Z.; Garabato, B. D.; Kozowski, P. M.; Buchanan, R. M.; Grapperhaus, C. A., Translation of Ligand-Centered Hydrogen Evolution Reaction Activity and Mechanism of a Rhenium-Thiolate from Solution to Modified Electrodes: A Combined Experimental and Density Functional Theory Study. *Inorg. Chem.* **2017**, *56* (4), 2177-2187.

26. Haddad, A. Z.; Garabato, B. D.; Kozowski, P. M.; Buchanan, R. M.; Grapperhaus, C. A., Beyond Metal-Hydrides: Non-Transition-Metal and Metal-Free Ligand-Centered Electrocatalytic Hydrogen Evolution and Hydrogen Oxidation. *J. Am. Chem. Soc.* **2016**, *138*, 7844-7847.

27. Fontecilla-Camps, J. C.; Volbeda, A.; Cavazza, C.; Nicolet, Y., Structure/Function Relationships of [NiFe]- and [FeFe]-Hydrogenases. *Chem Rev.* **2007**, *107* (10), 4273-4303.

28. Lubitz, W.; Ogata, H.; Rudiger, O.; Reijerse, E., Hydrogenases. *Chem Rev* **2014**, *114* (8), 4081-148.

29. Luo, G.-G.; Zhang, H.-L.; Tao, Y.-W.; Wu, Q.-Y.; Tian, D.; Zhang, Q., Recent progress in ligand-centered homogeneous electrocatalysts for hydrogen evolution reaction. *Inorg. Chem. Fronts* **2019**, *6* (2), 343-354.

30. Ackermann, L.; Sortais, J.-B., Homogeneous Catalysis is Up for the Challenge. *ChemCatChem* **2019**, *11* (21), 5158-5159.

31. Roubelakis, M. M.; Bediako, D. K.; Dogutan, D. K.; Nocera, D. G., Proton-coupled electron transfer kinetics for the hydrogen evolution reaction of hangman porphyrins. *Energy Environ. Sci.* **2012**, *5* (7), 7737-7740.

32. Bediako, D. K.; Solis, B. H.; Dogutan, D. K.; Roubelakis, M. M.; Maher, A. G.; Lee, C. H.; Chambers, M. B.; Hammes-Schiffer, S.; Nocera, D. G., Role of pendant proton relays and proton-coupled electron transfer on the hydrogen evolution reaction by nickel hangman porphyrins. *Proc. Natl. Acad. Sci. USA* **2014**, *111*, 15001-15006.

33. Sherbow, T. J.; Fetting, J. C.; Berben, L. A., Control of Ligand pKa Values Tunes the Electrocatalytic Dihydrogen Evolution Mechanism in a Redox-Active Aluminum(III) Complex. *Inorg. Chem.* **2017**, *56* (15), 8651-8660.

34. Thompson, E. J.; Berben, L. A., Electrocatalytic Hydrogen Production by an Aluminum(III) Complex: Ligand-Based Proton and Electron Transfer. *Angew Chem, Int. Ed.* **2015**, *54* (40), 11642-11646.

35. Straistari, T.; Fize, J.; Shova, S.; Réglie, M.; Artero, V.; Orio, M., A Thiosemicarbazone-Nickel(II) Complex as Efficient Electrocatalyst for Hydrogen Evolution. *ChemCatChem* **2017**, *9* (12), 2262-2268.

36. Straistari, T.; Hardré, R.; Fize, J.; Shova, S.; Giorgi, M.; Réglie, M.; Artero, V.; Orio, M., Hydrogen Evolution Reactions Catalyzed by a Bis(thiosemicarbazone) Cobalt Complex: An Experimental and Theoretical Study. *Chem-Eur. J* **2018**, *24* (35), 8779-8786.

37. Jain, R.; Al Mamun, A.; Buchanan, R. M.; Kozłowski, P. M.; Grapperhaus, C. A., Ligand-Assisted Metal-Centered Electrocatalytic Hydrogen Evolution upon Reduction of a Bis(thiosemicarbazonato)Ni(II) Complex. *Inorg. Chem.* **2018**, *57* (21), 13486-13493.
38. Yang, J. Y.; Smith, S. E.; Liu, T.; Dougherty, W. G.; Hoffert, W. A.; Kassel, W. S.; DuBois, M. R.; DuBois, D. L.; Bullock, R. M., Two Pathways for Electrocatalytic Oxidation of Hydrogen by a Nickel Bis(diphosphine) Complex with Pendant Amines in the Second Coordination Sphere. *J. Am. Chem. Soc.* **2013**, *135* (26), 9700-9712.
39. Helm, M. L.; Stewart, M. P.; Bullock, R. M.; DuBois, M. R.; DuBois, D. L., A Synthetic Nickel Electrocatalyst with a Turnover Frequency Above 100,000 s⁻¹ for H₂ Production. *Science* **2011**, *333* (6044), 863.
40. Chauhan, R.; Moreno, M.; Banda, D. M.; Zamborini, F. P.; Grapperhaus, C. A., Chemiresistive metal-stabilized thiyl radical films as highly selective ethylene sensors. *RSC Advances* **2014**, *4* (87), 46787-46790.
41. Tang, H.; Brothers, E. N.; Grapperhaus, C. A.; Hall, M. B., Electrocatalytic Hydrogen Evolution and Oxidation with Rhenium Tris(thiolate) Complexes: A Competition between Rhenium and Sulfur for Electrons and Protons. *ACS Catal.* **2020**, *10* (6), 3778-3789.
42. Jain, R.; Mamun, A. A.; Buchanan, R. M.; Kozłowski, P. M.; Grapperhaus, C. A., Ligand-Assisted Metal-Centered Electrocatalytic Hydrogen Evolution upon Reduction of a Bis(thiosemicarbazonato)Ni(II) Complex. *Inorg. Chem.* **2018**, *57*, 13486-13493.
43. Gulati, S.; Hietsoi, O.; Calvary, C. A.; Strain, J. M.; Pishgar, S.; Brun, H. C.; Grapperhaus, C. A.; Buchanan, R. M.; Spurgeon, J. M., Photocatalytic hydrogen evolution on Si photocathodes modified with bis(thiosemicarbazonato)nickel(II)/Nafion. *Chem Commun.* **2019**, *55* (64), 9440-9443.
44. Palopoli, C.; Ferreyra, J.; Conte-Daban, A.; Richezzi, M.; Foi, A.; Doctorovich, F.; Anxolabéhère-Mallart, E.; Hureau, C.; Signorella, S. R., Insights into Second-Sphere Effects on Redox Potentials, Spectroscopic Properties, and Superoxide Dismutase Activity of Manganese Complexes with Schiff-Base Ligands. *ACS Omega* **2019**, *4* (1), 48-57.
45. Lanznaster, M.; Neves, A.; Bortoluzzi, A. J.; Assumpção, A. M. C.; Vencato, I.; Machado, S. P.; Drechsel, S. M., Electronic Effects of Electron-Donating and -Withdrawing Groups in Model Complexes for Iron-Tyrosine-Containing Metalloenzymes. *Inorg. Chem.* **2006**, *45* (3), 1005-1011.
46. Li, X.-Y.; Sun, Y.-G.; Huo, P.; Shao, M.-Y.; Ji, S.-F.; Zhu, Q.-Y.; Dai, J., Metal centered oxidation or ligand centered oxidation of metal dithiolene? Spectral, electrochemical and structural studies on a nickel-4-pyridine-1,2-dithiolate system. *Phys. Chem. Chem. Phys.* **2013**, *15* (11), 4016-4023.
47. Artero, V.; Saveant, J.-M., Toward the rational benchmarking of homogeneous H₂-evolving catalysts. *Energy Environ. Sci.* **2014**, *7* (11), 3808-3814.
48. Sung, S.; Kumar, D.; Gil-Sepulcre, M.; Nippe, M., Electrocatalytic CO₂ Reduction by Imidazolium-Functionalized Molecular Catalysts. *J. Am. Chem. Soc.* **2017**, *139* (40), 13993-13996.

49. Schmeier, T. J.; Dobereiner, G. E.; Crabtree, R. H.; Hazari, N., Secondary Coordination Sphere Interactions Facilitate the Insertion Step in an Iridium(III) CO₂ Reduction Catalyst. *J. Am. Chem. Soc.* **2011**, *133* (24), 9274-9277.
50. Azcarate, I.; Costentin, C.; Robert, M.; Savéant, J.-M., Dissection of Electronic Substituent Effects in Multielectron–Multistep Molecular Catalysis. Electrochemical CO₂-to-CO Conversion Catalyzed by Iron Porphyrins. *J. Phys. Chem. C* **2016**, *120* (51), 28951-28960.
51. Costentin, C.; Robert, M.; Savéant, J.-M., Current Issues in Molecular Catalysis Illustrated by Iron Porphyrins as Catalysts of the CO₂-to-CO Electrochemical Conversion. *Acc. Chem. Res.* **2015**, *48* (12), 2996-3006.
52. Azcarate, I.; Costentin, C.; Robert, M.; Savéant, J.-M., Through-Space Charge Interaction Substituent Effects in Molecular Catalysis Leading to the Design of the Most Efficient Catalyst of CO₂-to-CO Electrochemical Conversion. *J. Am. Chem. Soc.* **2016**, *138* (51), 16639-16644.
53. Reath, A. H.; Ziller, J. W.; Tsay, C.; Ryan, A. J.; Yang, J. Y., Redox Potential and Electronic Structure Effects of Proximal Nonredox Active Cations in Cobalt Schiff Base Complexes. *Inorg. Chem.* **2017**, *56*, 3713-3718.
54. Kang, K.; Fuller, J.; Reath, A. H.; Ziller, J. W.; Alexandrova, A. N.; Yang, J. Y., Installation of internal electric fields by non-redox active cations in transition metal complexes. *Chem Sci.* **2019**, *10* (43), 10135-10142.
55. Calvary, C. A.; Hietsoi, O.; Hofsommer, D. T.; Brun, H. C.; Costello, A. M.; Mashuta, M. S.; Spurgeon, J. M.; Buchanan, R. M.; Grapperhaus, C. A., Copper bis(thiosemicarbazone) Complexes with Pendent Polyamines: Effects of Proton Relays and Charged Moieties on Electrocatalytic HER. *Eur. J Inorg. Chem.* **2021**, *2021* (3), 267-275.
56. Cowley, A. R.; Dilworth, J. R.; Donnelly, P. S.; Heslop, J. M.; Ratcliffe, S. J., Bifunctional chelators for copper radiopharmaceuticals: the synthesis of [Cu(ATSM)-amino acid] and [Cu(ATSM)-octreotide] conjugates. *Dalton Trans.* **2007**, *0*, 209-217.
57. Costentin, C.; Savéant, J.-M., Multielectron, Multistep Molecular Catalysis of Electrochemical Reactions: Benchmarking of Homogeneous Catalysts. *ChemElectroChem* **2014**, *1* (7), 1226-1236.
58. DiRisio, R. J.; Armstrong, J. E.; Frank, M. A.; Lake, W. R.; McNamara, W. R., Cobalt Schiff-base complexes for electrocatalytic hydrogen generation. *Dalton Trans.* **2017**, *46* (31), 10418-10425.
59. Fourmond, V.; Jacques, P.-A.; Fontecave, M.; Artero, V., H₂ Evolution and Molecular Electrocatalysts: Determination of Overpotentials and Effect of Homoconjugation. *Inorg. Chem.* **2010**, *49* (22), 10338-10347.
60. Fourmond, V.; Jacques, P.-A.; Fontecave, M.; Artero, V., Correction to H₂ Evolution and Molecular Electrocatalysts: Determination of Overpotentials and Effect of Homoconjugation. *Inorg. Chem.* **2015**, *54* (2), 704-704.
61. Costentin, C.; Drouet, S.; Robert, M.; Savéant, J.-M., Turnover Numbers, Turnover Frequencies, and Overpotential in Molecular Catalysis of Electrochemical Reactions.

- Cyclic Voltammetry and Preparative-Scale Electrolysis. *J. Am. Chem. Soc.* **2012**, *134* (27), 11235-11242.
62. Lewis, N. S.; Nocera, D. G., Powering the planet: Chemical challenges in solar energy utilization. *Proc Natl. Acad. Sci. USA* **2006**, *103* (43), 15729-15735.
63. McCrory, C. C. L.; Jung, S.; Ferrer, I. M.; Chatman, S. M.; Peters, J. C.; Jaramillo, T. F., Benchmarking Hydrogen Evolving Reaction and Oxygen Evolving Reaction Electrocatalysts for Solar Water Splitting Devices. *J. Am. Chem. Soc.* **2015**, *137* (13), 4347-4357.
64. Minh, T. D. N.; Ranjbari, A.; Catala, L.; Brisset, F.; Millet, P.; Aukauloo, A., Implementing molecular catalysts for hydrogen production in proton exchange membrane water electrolyzers. *Coord. Chem. Rev.* **2012**, *256* (21-22), 2435-2444.
65. Queyriaux, N.; Kaeffer, N.; Morozan, A.; Chavarot-Kerlidou, M.; Artero, V., Molecular cathode and photocathode materials for hydrogen evolution in photoelectrochemical devices. *J Photoch. Photobio. C* **2015**, *25*, 90-105.
66. Brimblecombe, R.; Dismukes, G. C.; Swiegers, G. F.; Spiccia, L., Molecular water-oxidation catalysts for photoelectrochemical cells. *Dalton Trans.* **2009**, (43), 9374-9384.
67. Zhao, F.; Zhang, J.; Abe, T.; Wohrle, D.; Kaneko, M., Electrocatalytic proton reduction by phthalocyanine cobalt derivatives incorporated in poly(4-vinylpyridine-co-styrene) film. *J Mol. Catal. A-Chem* **1999**, *145* (1-2), 245-256.
68. Deponti, E.; Luisa, A.; Natali, M.; Iengo, E.; Scandola, F., Photoinduced hydrogen evolution by a pentapyridine cobalt complex: elucidating some mechanistic aspects. *Dalton Trans.* **2014**, *43* (43), 16345-16353.
69. Peng, Q. X.; Xue, D.; Yang, L. F.; Zhan, S. Z., A coordinatively saturated cobalt complex as a new kind catalyst for efficient electro- and photo-catalytic hydrogen production in purely aqueous media. *Int. J. Hydrogen Energ.* **2017**, *42* (26), 16428-16435.
70. Ibrahim, S. K.; Liu, X. M.; Tard, C.; Pickett, C. J., Electropolymeric materials incorporating subsite structures related to iron-only hydrogenase: active ester functionalised poly(pyrroles) for covalent binding of {2Fe3S}-carbonyl/cyanide assemblies. *Chem Commun.* **2007**, (15), 1535-1537.
71. Lv, H. J.; Ruberu, T. P. A.; Fleischauer, V. E.; Brennessel, W. W.; Neidig, M. L.; Eisenberg, R., Catalytic Light-Driven Generation of Hydrogen from Water by Iron Dithiolene Complexes. *J. Am. Chem. Soc.* **2016**, *138* (36), 11654-11663.
72. Hou, Y. D.; Abrams, B. L.; Vesborg, P. C. K.; Bjorketun, M. E.; Herbst, K.; Bech, L.; Setti, A. M.; Damsgaard, C. D.; Pedersen, T.; Hansen, O.; Rossmeisl, J.; Dahl, S.; Norskov, J. K.; Chorkendorff, I., Bioinspired molecular co-catalysts bonded to a silicon photocathode for solar hydrogen evolution. *Nat Mater.* **2011**, *10* (6), 434-438.
73. Seger, B.; Herbst, K.; Pedersen, T.; Abrams, B.; Vesborg, P. C. K.; Hansen, O.; Chorkendorff, I., Mo3S4 Clusters as an Effective H₂ Evolution Catalyst on Protected Si Photocathodes. *J. Electrochem. Soc.* **2014**, *161* (12), H722-H724.

74. Webster, L. R.; Ibrahim, S. K.; Wright, J. A.; Pickett, C. J., Solar Fuels: Visible-Light-Driven Generation of Dihydrogen at p-Type Silicon Electrocatalysed by Molybdenum Hydrides. *Chem. Eur. J.* **2012**, *18* (37), 11798-11803.
75. Le Goff, A.; Artero, V.; Jusselme, B.; Tran, P. D.; Guillet, N.; Metaye, R.; Fihri, A.; Palacin, S.; Fontecave, M., From Hydrogenases to Noble Metal-Free Catalytic Nanomaterials for H₂ Production and Uptake. *Science* **2009**, *326* (5958), 1384-1387.
76. Pool, D. H.; DuBois, D. L., Ni((P2N2Ar)-N-Ph)₂(NCMe) BF₄ (2) as an electrocatalyst for H₂ production: (P2N2Ar)-N-Ph=1,5-(di(4-(thiophene-3-yl) phenyl)-3,7-diphenyl-1,5-diaza-3,7-diphosphacyclooctane). *J. Organomet. Chem.* **2009**, *694* (17), 2858-2865.
77. Wise, C. F.; Liu, D.; Mayer, K. J.; Crossland, P. M.; Hartley, C. L.; McNamara, W. R., A nickel complex of a conjugated bis-dithiocarbazate Schiff base for the photocatalytic production of hydrogen. *Dalton Trans.* **2015**, *44* (32), 14265-14271.
78. Artero, V.; Saveant, J. M., Toward the rational benchmarking of homogeneous H₂-evolving catalysts. *Energy Environ. Sci.* **2014**, *7* (11), 3808-3814.
79. DuBois, D. L., Development of Molecular Electrocatalysts for Energy Storage. *Inorg. Chem.* **2014**, *53* (8), 3935-3960.
80. Hartley, C. L.; DiRisio, R. J.; Screen, M. E.; Mayer, K. J.; McNamara, W. R., Iron Polypyridyl Complexes for Photocatalytic Hydrogen Generation. *Inorg. Chem.* **2016**, *55* (17), 8865-8870.
81. McNamara, W. R.; Han, Z. J.; Yin, C. J.; Brennessel, W. W.; Holland, P. L.; Eisenberg, R., Cobalt-dithiolene complexes for the photocatalytic and electrocatalytic reduction of protons in aqueous solutions. *Proc. Natl. Acad. Sci. USA* **2012**, *109* (39), 15594-15599.
82. Krawicz, A.; Yang, J. H.; Anzenberg, E.; Yano, J.; Sharp, I. D.; Moore, G. F., Photofunctional Construct That Interfaces Molecular Cobalt-Based Catalysts for H₂ Production to a Visible-Light-Absorbing Semiconductor. *J. Am. Chem. Soc.* **2013**, *135* (32), 11861-11868.
83. Seo, J.; Pekarek, R. T.; Rose, M. J., Photoelectrochemical operation of a surface-bound, nickel-phosphine H₂ evolution catalyst on p-Si(111): a molecular semiconductor\catalyst construct. *Chem Commun.* **2015**, *51* (68), 13264-13267.
84. Jiang, W. X.; Xie, Z. L.; Zhan, S. Z., A photocatalytic system with a bis(thiosemicarbazonato)-nickel over CdS nanorods for hydrogen evolution from water under visible light. *Inorg. Chem. Commun.* **2019**, *102*, 5-9.
85. Zhang, W. Y. Heterogenization of complexes with redox active ligands for hydrogen evolution reaction. Doctoral Dissertation, University of Louisville, 2017.
86. Betts, H. M.; Barnard, P. J.; Bayly, S. R.; Dilworth, J. R.; Gee, A. D.; Holland, J. P., Controlled Axial Coordination: Solid-Phase Synthesis and Purification of Metallo-Radiopharmaceuticals. *Angew Chem, Int. Ed.* **2008**, *47* (44), 8416-8419.
87. Gupta, A. J.; Vishnosky, N. S.; Hietsoi, O.; Losovyj, Y.; Strain, J.; Spurgeon, J.; Mashuta, M. S.; Jain, R.; Buchanan, R. M.; Gupta, G.; Grapperhaus, C. A., Effect of

Stacking Interactions on the Translation of Structurally Related Bis(thiosemicarbazonato)nickel(II) HER Catalysts to Modified Electrode Surfaces. *Inorg. Chem.* **2019**, *58* (18), 12025-12039.

88. Wodrich, M. D.; Hu, X. L., Natural inspirations for metal-ligand cooperative catalysis. *Nat Rev Chem* **2018**, *2* (1).

89. Boettcher, S. W.; Warren, E. L.; Putnam, M. C.; Santori, E. A.; Turner-Evans, D.; Kelzenberg, M. D.; Walter, M. G.; McKone, J. R.; Brunschwig, B. S.; Atwater, H. A.; Lewis, N. S., Photoelectrochemical Hydrogen Evolution Using Si Microwire Arrays. *J. Am. Chem. Soc.* **2011**, *133* (5), 1216-1219.

90. Lombardi, I.; Marchionna, S.; Zangari, G.; Pizzini, S., Effect of Pt particle size and distribution on photoelectrochemical hydrogen evolution by p-Si photocathodes. *Langmuir* **2007**, *23* (24), 12413-12420.

91. Gleason-Rohrer, D. C.; Brunschwig, B. S.; Lewis, N. S., Measurement of the Band Bending and Surface Dipole at Chemically Functionalized Si(111)/Vacuum Interfaces. *J Phys. Chem. C* **2013**, *117* (35), 18031-18042.

92. Kütt, A.; Leito, I.; Kaljurand, I.; Sooväli, L.; Vlasov, V. M.; Yagupolskii, L. M.; Koppel, I. A., A Comprehensive Self-Consistent Spectrophotometric Acidity Scale of Neutral Brønsted Acids in Acetonitrile. *J Org. Chem.* **2006**, *71* (7), 2829-2838.

93. Bard, J. A., Faulkner, R. L., *Electrochemical Methods: Fundamentals and Applications*. 2nd ed.; Wiley: Somerset, New Jersey, **2001**.

94. Wilson, A. D.; Newell, R. H.; McNevin, M. J.; Muckerman, J. T.; DuBois, M. R.; DuBois, D. L., Hydrogen oxidation and production using nickel-based molecular catalysts with positioned proton relays. *J. Am. Chem. Soc.* **2006**, *128* (1), 358-366.

95. Appel, A. M.; DuBois, D. L.; DuBois, M. R., Molybdenum-sulfur dimers as electrocatalysts for the production of hydrogen at low overpotentials. *J. Am. Chem. Soc.* **2005**, *127* (36), 12717-12726.

96. Lee, K. J.; Elgrishi, N.; Kandemir, B.; Dempsey, J. L., Electrochemical and spectroscopic methods for evaluating molecular electrocatalysts. *Nat. Rev. Chem.* **2017**, *1* (5), 0039.

APPENDICES

Appendix A. Structural Analysis of Transaminated BTSC Products

Diacetyl-N-methyl-N'-(2-(N'',N''-dimethylamino)ethyl)-bis(thiosemicarbazone) (**3**)

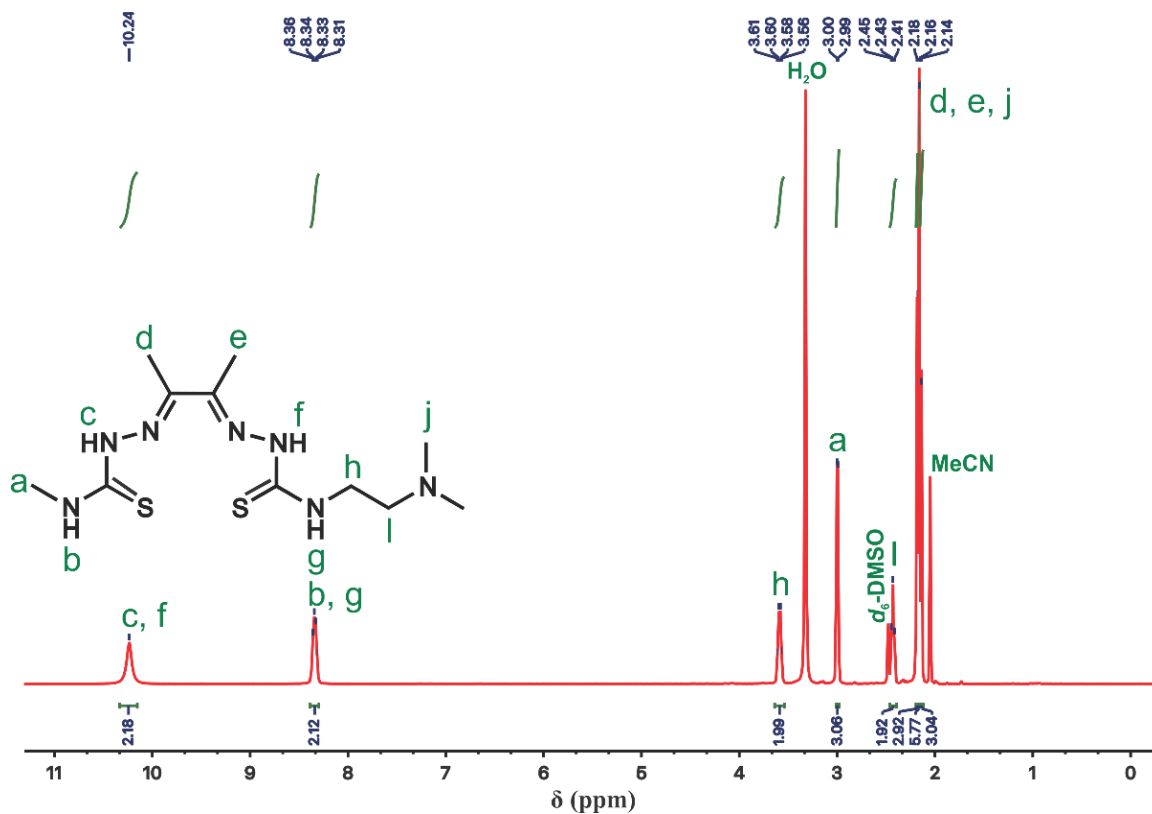


Figure A.1. ¹H NMR (400 MHz, *d*₆-DMSO) of **3**: δ/ppm 10.2 (bs, 2H, -NH-N=C-), 8.33 (q, 2H *J*_{HH} = 4 Hz, 7.5 Hz, -NH-C=S), 3.58 (q, 2H, *J*_{HH} = 7.5 Hz, 8.3 Hz, -CH₂NH-), 3.00 (t, *J*_{HH} = 4 Hz, 3H, NH-CH₃), 2.43 (t, 2H, *J*_{HH} = 8.3 Hz, -CH₂N(CH₃)₃), 2.18 (s, 3H, -CH₃), 2.16 (s, 6H, -N(CH₃)₂), 2.14 (s, 3H, -CH₃).

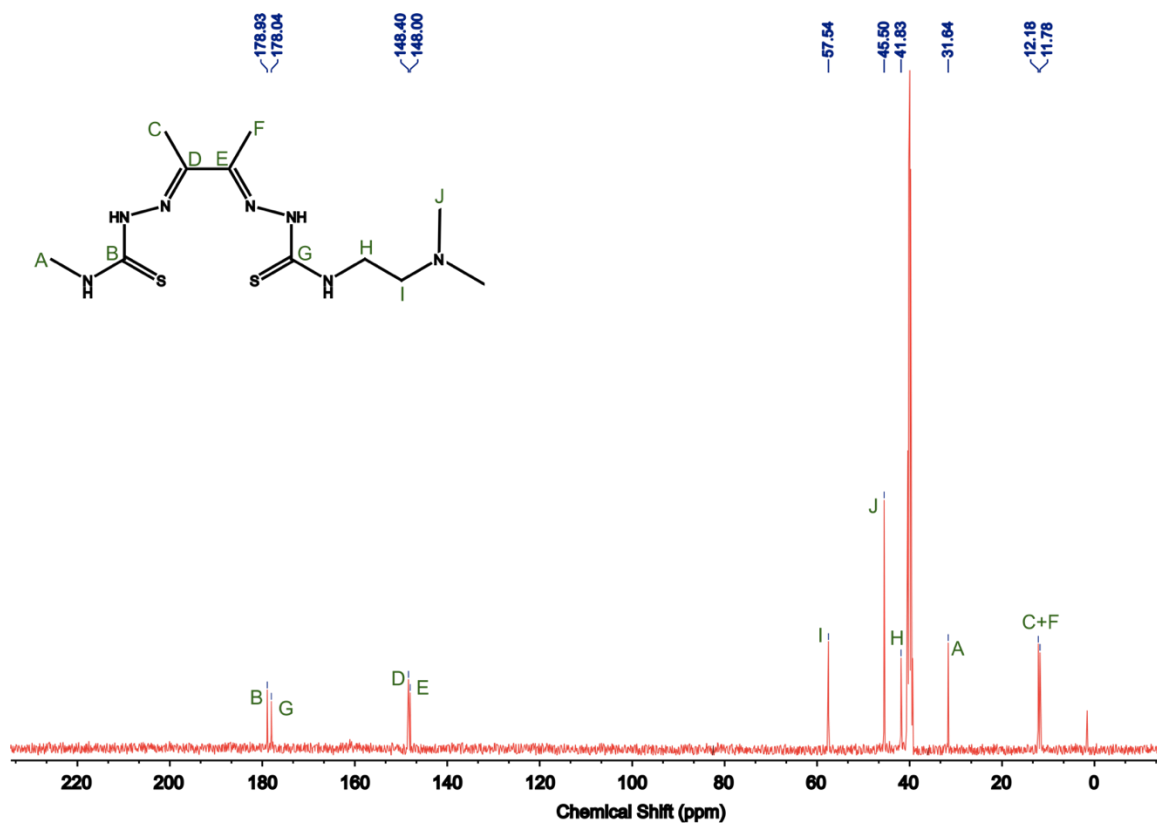


Figure A.2. ¹³C NMR of Diacetyl-N-methyl-N'-(2-(N,N'-dimethylamino)ethyl)-bis(thiosemicarbazone) (3). (100 MHz, *d*₆-DMSO) of H₂L¹: δ/ppm 178.8 (C=S), 178.0 (C=S), 148.4 (C=N), 148.0 (C=N), 57.5 (-CH₂NH-), 45.5 (N(CH₃)₂), 41.9 (-CH₂N(CH₃)₂), 31.6 (CH₃NH-), 12.2 (-CH₃) 11.8 (-CH₃). C, 41.61; H, 7.30; N, 30.88. Found: C, 39.16; H, 6.67; N, 29.1

Diacetyl-N-methyl-N'-(2-mercaptoethyl)-bis(thiosemicarbazone) (**4**)



Figure A.3. ¹H NMR of Diacetyl-N-methyl-N'-(2-mercaptoethyl)-bis(thiosemicarbazone) (**4**). δ (ppm) = 10.32 (br. s, 1H_c); 10.23 (br. s, 1H_f); 8.54 (t, $J = 5.5$ Hz, 1H_g); 8.38 (q, $J = 4.5$ Hz, 1H_b); 3.89 (br. s, 1H_j); 3.70 (q, $J = 8.5$ Hz, 2H_i); 3.34 (s, H₂O); 3.01 (d, $J = 4.5$ Hz, 3H_a); 2.70 (t, $J = 7.5$ Hz, 2H_h); 2.50 (m, DMSO); 2.21 (s, 3H_d); 2.20 (s, 3H_e); 2.07 (s, MeCN)

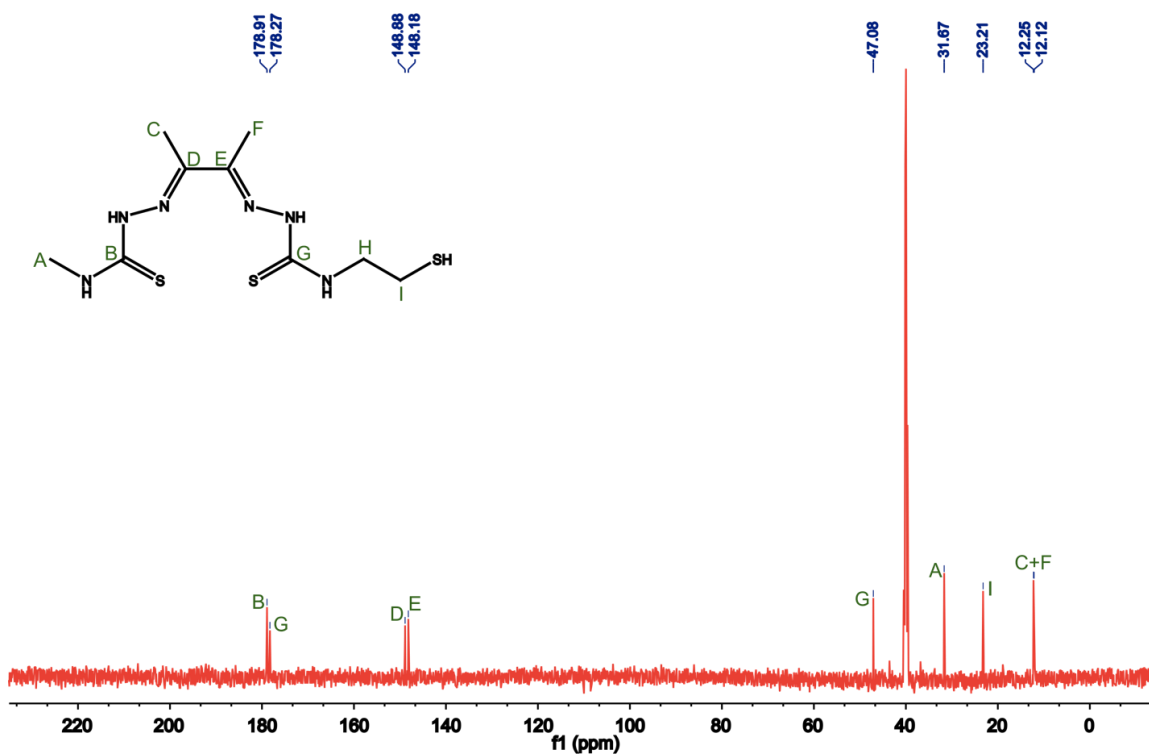


Figure A.4. ¹³C NMR of Diacetyl-N-methyl-N'-(2-mercaptoethyl)-bis(thiosemicarbazone) (**4**). ¹³C NMR (125 MHz, *d*₆-DMSO): δ/ppm 178.92 (C=S), 178.28 (C=S), 149.19 (C=N), 148.88 (C=N), 47.08 (NH-CH₂-), 31.67 (N-CH₃), 23.21 (HS-CH₂), 12.25 (-CH₃), 12.12 (-CH₃). Anal. Calc. for C₉H₁₈N₆S₃: C, 35.27; H, 5.92; N, 27.42. Found: C, 35.10; H, 5.79; N, 27.26

Diacetyl-N-methyl-N'-(2-hydroxyethyl)-bis(thiosemicarbazone) (5)

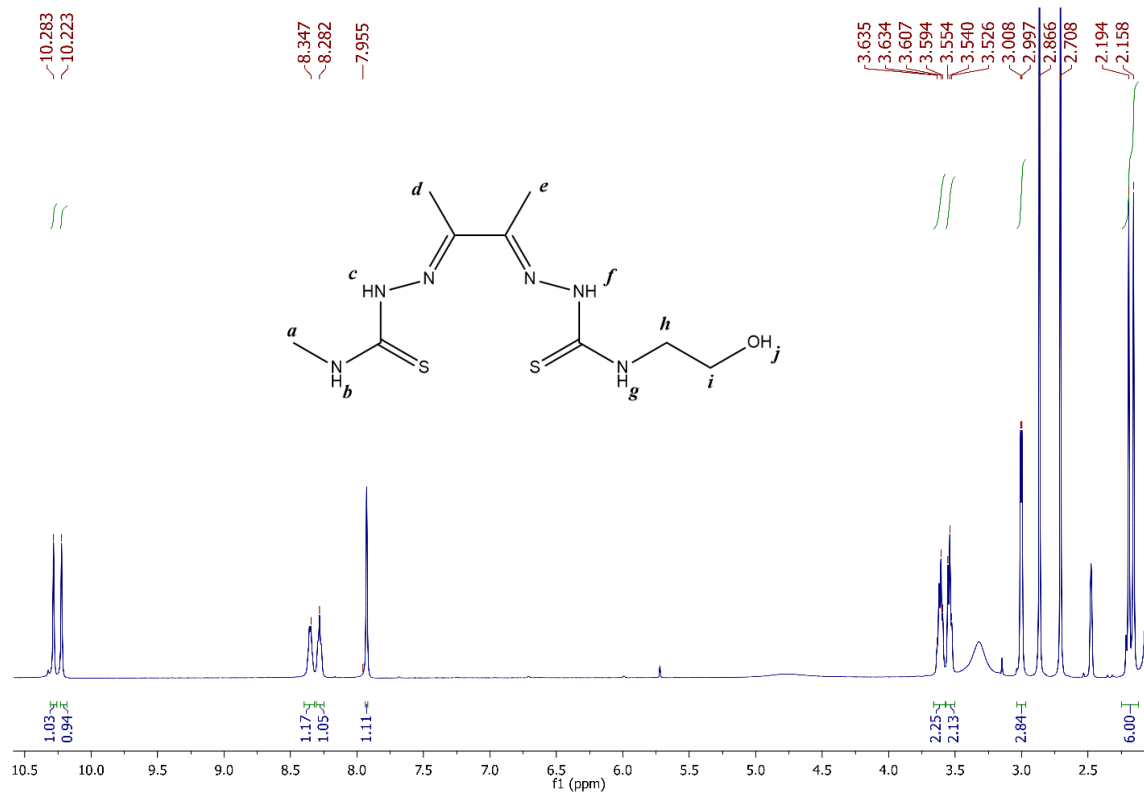


Figure A.5. ¹H NMR of Diacetyl-N-methyl-N'-(2-hydroxyethyl)-bis(thiosemicarbazone) (5): δ (ppm) = 10.28 (br. s, 1H_c); 10.22 (br. s, 1H_f); 8.35 (q, J = 5.0 Hz, 1H_b); 8.28 (t, J = 5.0 Hz, 1H_g); 7.93 (br. s, 1H_j); 3.62 (q, J = 7.0 Hz, 2H_h); 3.40 (t, J = 7.0 Hz, 2H_i); 3.34 (s, H₂O); 3.01 (d, J = 4.5 Hz, 3H_a); 2.87, 2.71 (m, Hunig's Base); 2.50 (m, DMSO); 2.19 (s, 3H_d); 2.16 (s, 3H_e)

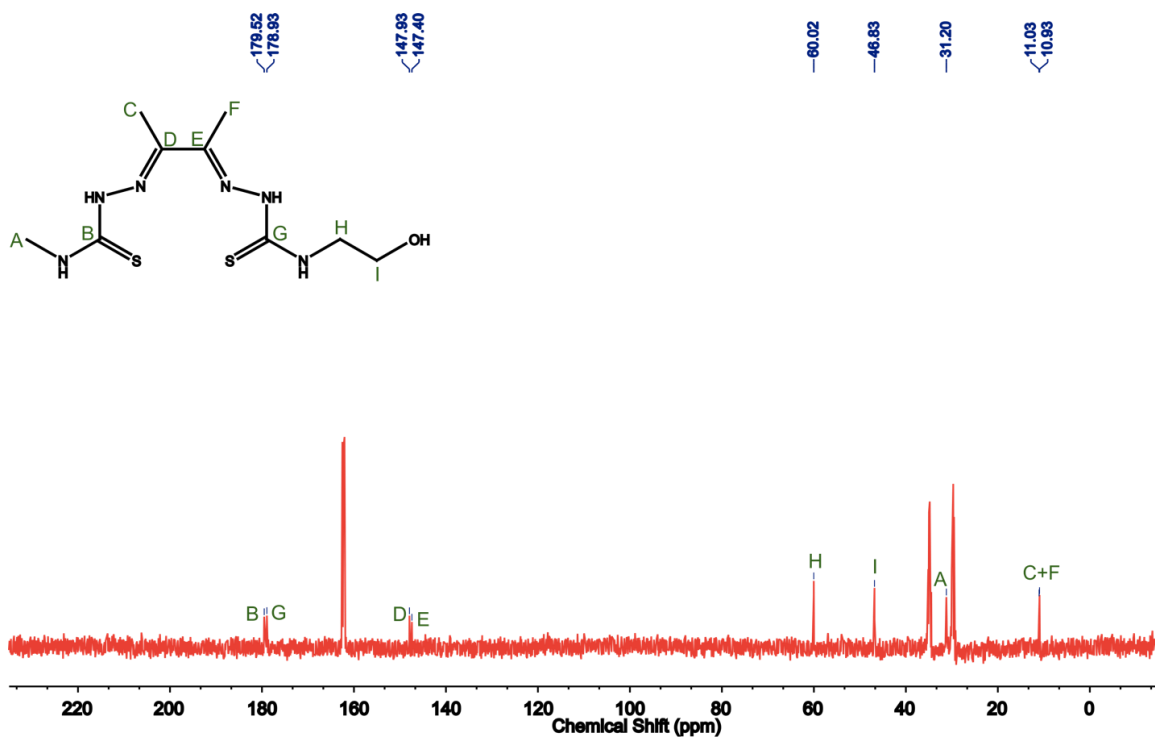


Figure A.6. ^{13}C NMR of Diacetyl-N-methyl-N'-(2-hydroxyethyl)-bis(thiosemicarbazone) (5): ^{13}C NMR (125 MHz, d_7 -DMF): δ /ppm 179.52 (C=S), 178.93 (C=S), 147.93 (C=N), 147.40 (C=N), 60.02 (-CH₂OH), 46.83 (NH-CH₂-), 31.20 (N-CH₃), 11.03 (-CH₃), 10.93 (-CH₃). Anal. Calc. for C₉H₁₈N₆OS₂: C, 37.22; H, 6.25; N, 28.94. Found: C, 37.15; H, 5.99; N, 28.84

Diacetyl-N-methyl-N'-(4-hydroxyphenyl)-bis(thiosemicarbazone) (7)

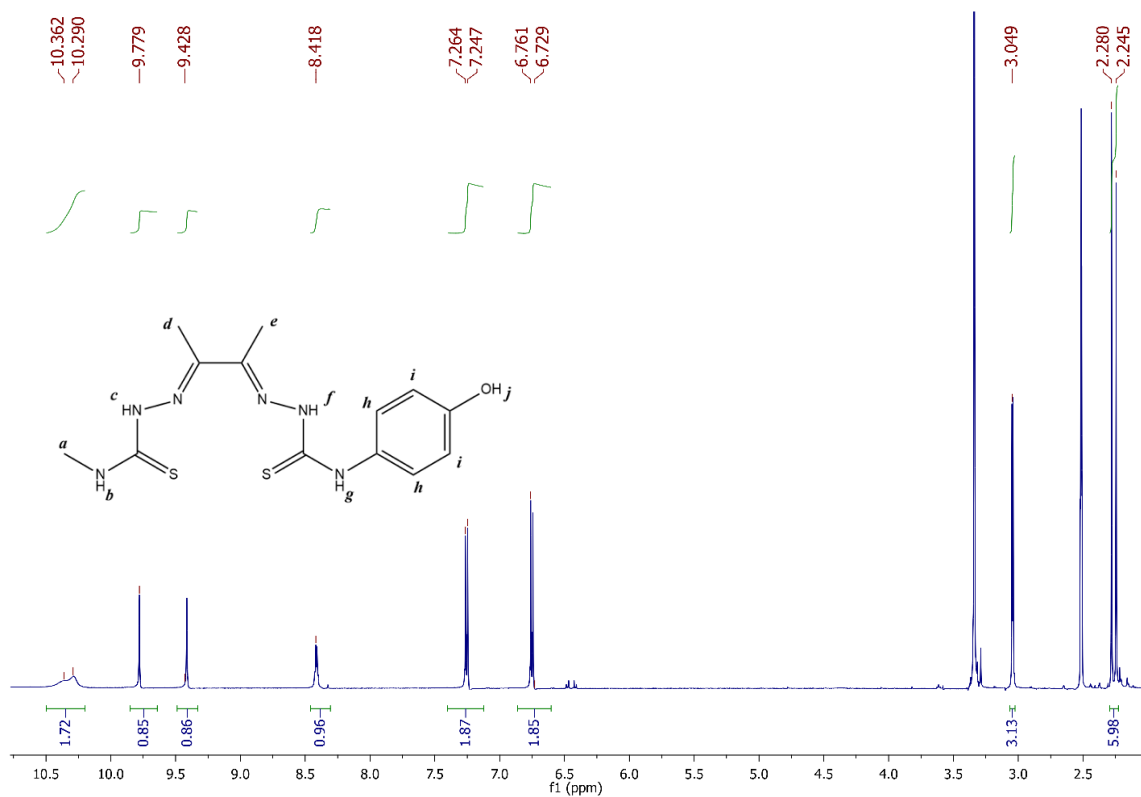


Figure A.7. ¹H NMR of Diacetyl-N-methyl-N'-(4-hydroxyphenyl)-bis(thiosemicarbazone) (**7**): δ (ppm) = 10.39 (br. s, 1H_c); 10.28 (br. s, 1H_f); 9.78 (s, 1H_g); 9.41 (s, 1H_b); 8.42 (br. s, 1H_j); 7.25 (d, $J = 8.5$ Hz, 2H_i); 6.75 (d, $J = 8.5$ Hz, 2H_h); 3.34 (s, H₂O); 3.04 (d, $J = 4.5$ Hz, 3H_a); 2.50 (m, DMSO); 2.28 (s, 3H_d); 2.25 (s, 3H_e)

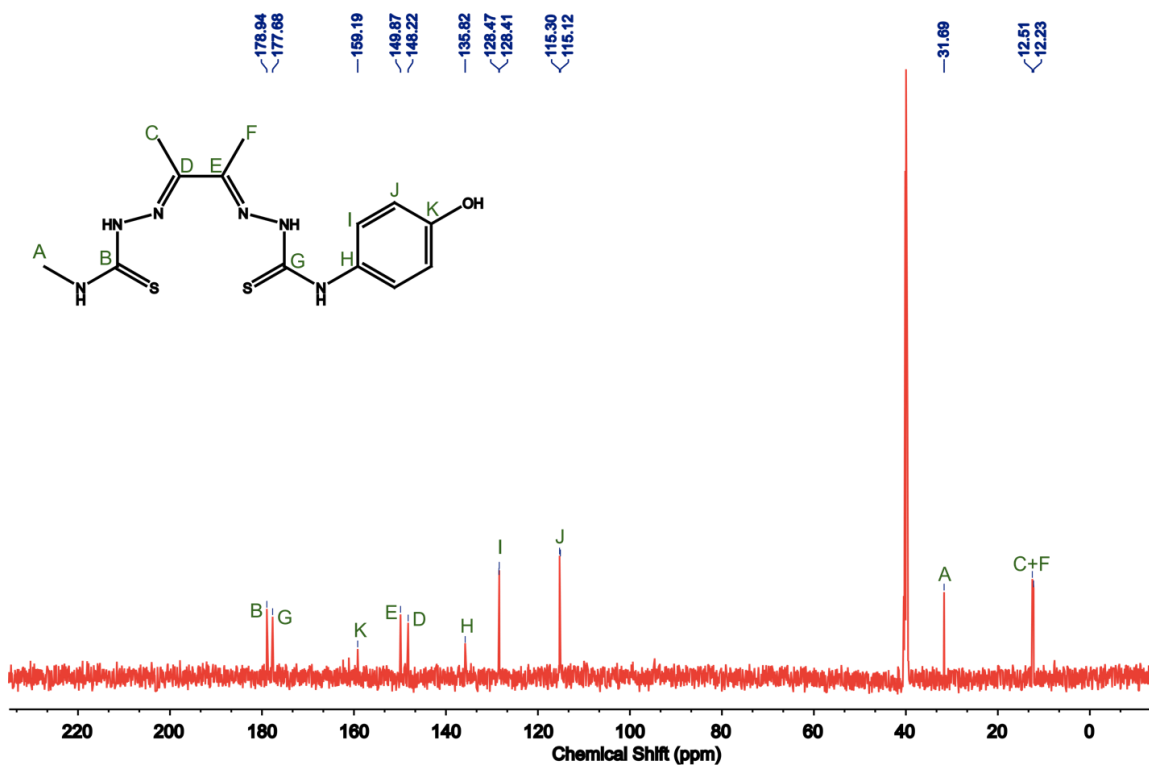


Figure A.8. ^{13}C NMR of Diacetyl-N-methyl-N'-(4-hydroxyphenyl)-bis(thiosemicarbazone) (**7**): ^{13}C NMR (125 MHz, d_6 -DMSO): δ /ppm 178.92 (C=S), 177.59 (C=S), 149.23 (C=N), 148.32 (C=N), 155.71 ($\text{C}_{\text{Ar-O}}$), 130.82 ($\text{C}_{\text{Ar-N}}$), 127.91 (C_{Ar}), 115.08 (C_{Ar}), 31.68 (N- CH_3), 12.37 ($-\text{CH}_3$), 12.18 ($-\text{CH}_3$). Anal. Calc. for $\text{C}_{13}\text{H}_{18}\text{N}_6\text{O}_2\text{S}_2$: C, 46.14; H, 5.36; N, 24.83. Found: C, 45.38; H, 5.35; N, 23.70

Diacetyl-N-methyl-N'-(4-isopropylphenyl)-bis(thiosemicarbazone) (8)

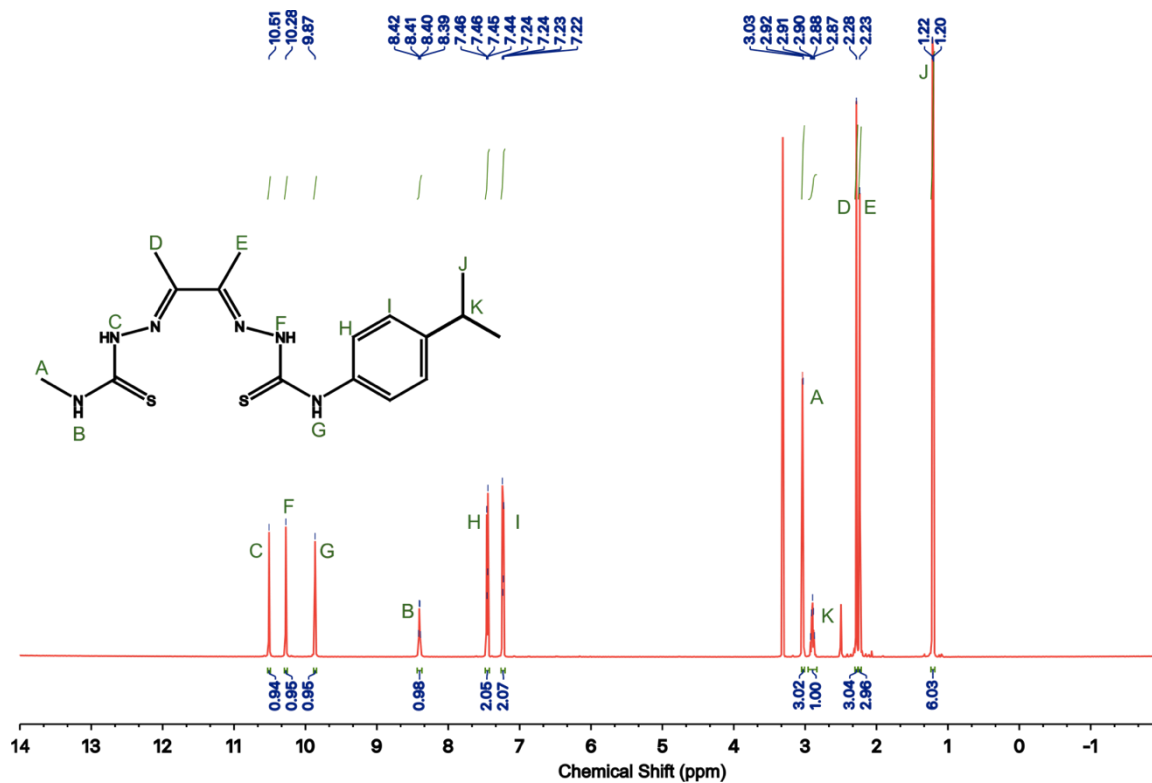


Figure A.9. ¹H NMR of Diacetyl-N-methyl-N'-(4-isopropylphenyl)-bis(thiosemicarbazone) (**8**): δ (ppm) 10.52 (br. s, 1H); 10.29 (br. s, 1H); 9.88 (s, 1H); 8.41 (s, 1H); 7.46 (d, $J = 8.0$ Hz, 2H); 7.24 (d, $J = 8.0$ Hz, 2H); 3.04 (d, $J = 4.5$ Hz, 3H); 2.91 (m, $J = 11.2$ Hz, 1H); 2.29 (s, 3H); 2.25 (s, 3H); 1.22 (d, $J = 11.2$ Hz, 6H)

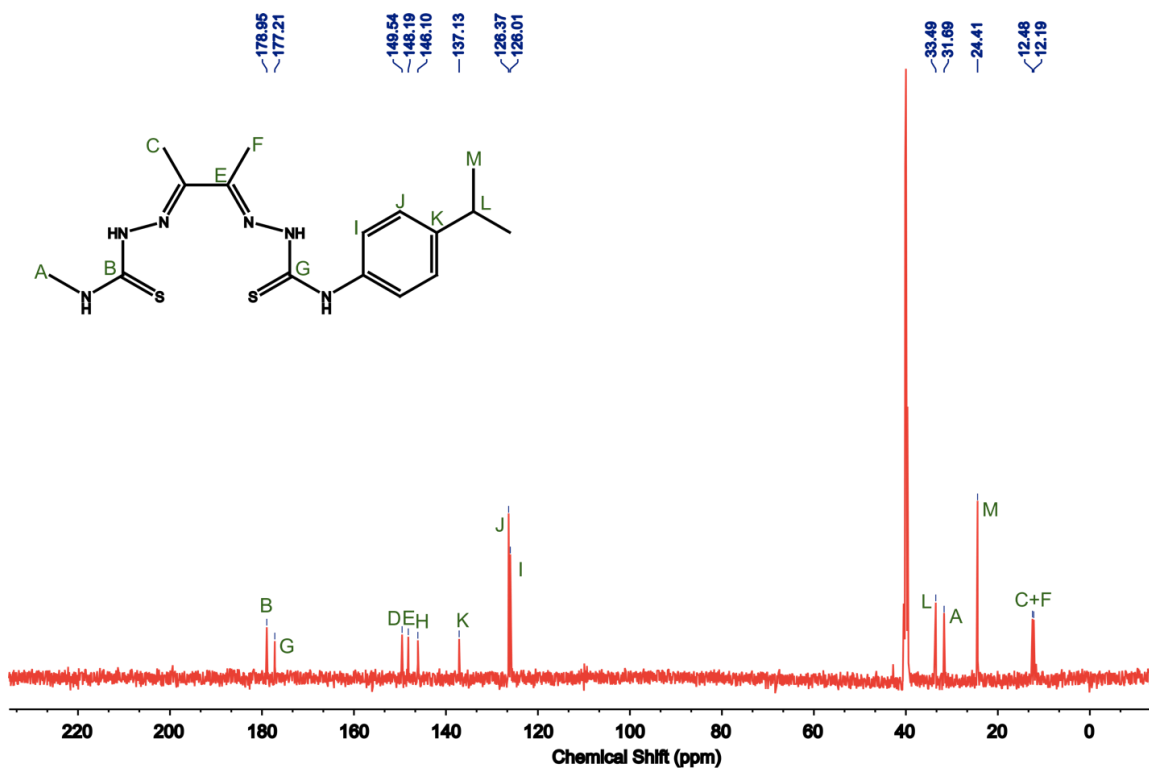


Figure A.10. ¹³C NMR of Diacetyl-N-methyl-N'-(4-isopropylphenyl)-bis(thiosemicarbazone) (**8**): ¹³C NMR (125 MHz, *d*₆-DMSO): δ/ppm 178.95 (C=S), 177.21 (C=S), 149.54 (C=N), 148.19 (C=N), 146.10 (C_{Ar}-N), 137.13 (C_{Ar}-C), 126.37 (C_{Ar}), 126.01 (C_{Ar}), 33.49 (-CH-(CH₃)₂), 31.69 (N-CH₃), 24.41 (2(-CH₃)), 12.48 (-CH₃), 12.19 (-CH₃). Anal. Calc. for C₁₆H₂₄N₆S₂: C, 52.72; H, 6.64; N, 23.05. Found: C, 50.32; H, 6.62; N, 23.88

Diacetyl-N-methyl-N'-(4-methoxyphenyl)-bis(thiosemicarbazone) (9)

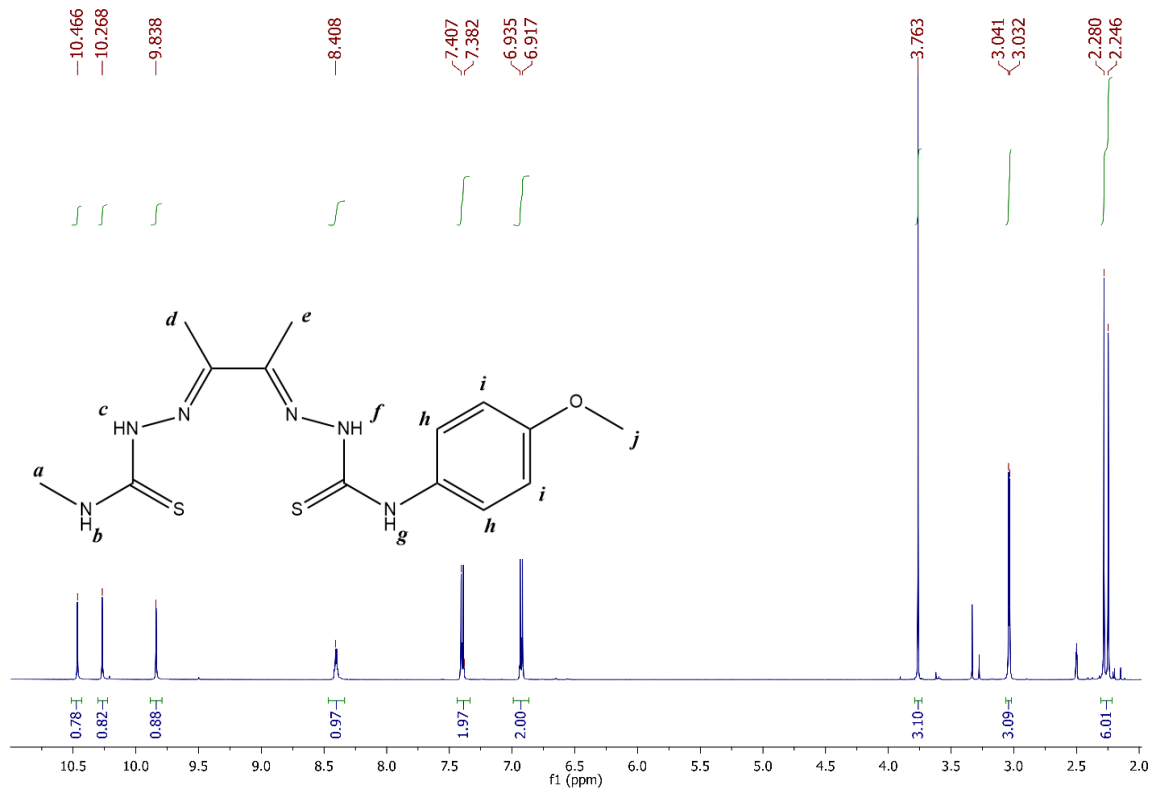


Figure A.11. ¹H NMR of Diacetyl-N-methyl-N'-(4-methoxyphenyl)-bis(thiosemicarbazone) (10): δ (ppm) = 10.47 (s, 1H_c); 10.27 (s, 1H_f); 9.84 (s, 1H_g); 8.41 (s, 1H_b); 7.49 (d, J = 6.0 Hz, 2H_i); 6.92 (d, J = 6.0 Hz, 2H_h); 3.76 (s, 3H_j); 3.34 (s, H₂O); 3.03 (d, J = 4.5 Hz, 3H_a); 2.50 (m, DMSO); 2.28 (s, 3H_d); 2.25 (s, 3H_e)

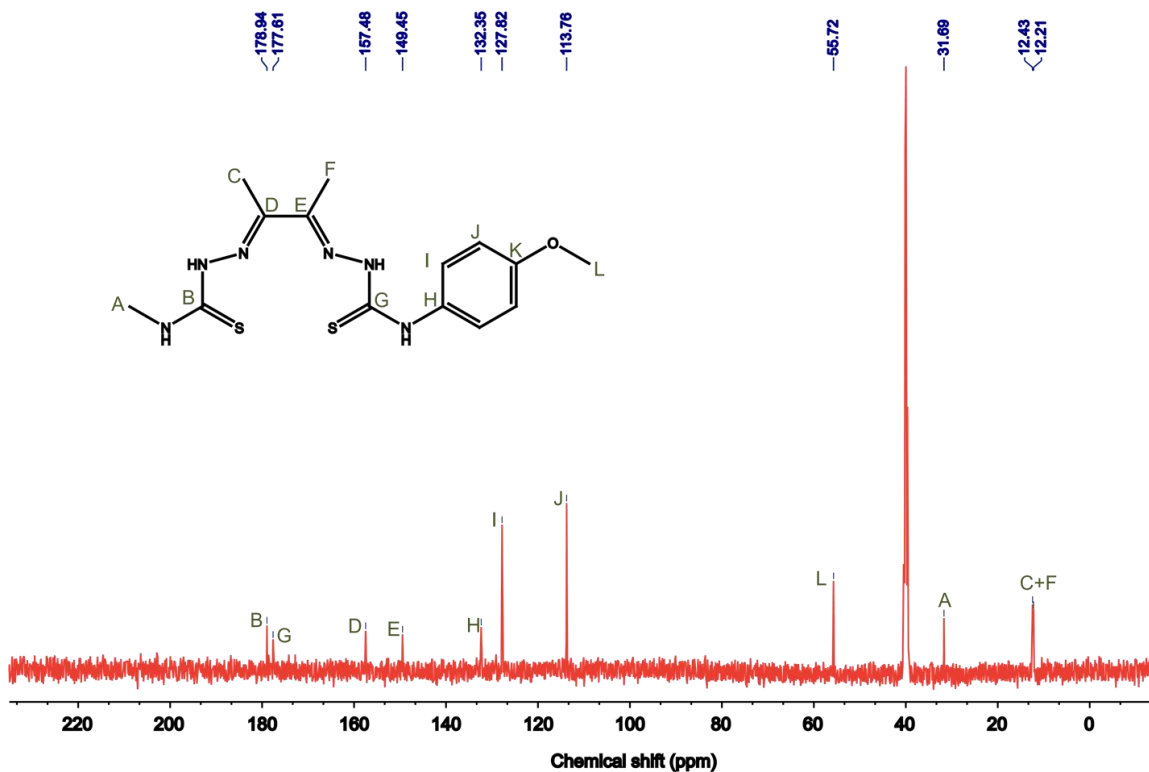


Figure A.12. ^{13}C NMR of Diacetyl-N-methyl-N'-(4-methoxyphenyl)-bis(thiosemicarbazone) (**10**): ^{13}C NMR (125 MHz, d_6 -DMSO): δ /ppm 178.94 (C=S), 177.61 (C=S), 157.48 (C=N), 149.45 (C=N), 148.35 ($\text{C}_{\text{Ar}}\text{-O}$), 132.35 ($\text{C}_{\text{Ar}}\text{-N}$), 127.82 (C_{Ar}), 113.76 (C_{Ar}), 57.5 ($-\text{CH}_2\text{NH}-$), 55.72 ($\text{O}-\text{CH}_3$), 31.69 ($\text{N}-\text{CH}_3$), 12.43 ($-\text{CH}_3$), 12.21 ($-\text{CH}_3$). Anal. Calc. for $\text{C}_{14}\text{H}_{20}\text{N}_6\text{OS}_2$: C, 47.71; H, 5.72; N, 23.83. Found: C, 47.61; H, 5.74; N, 23.83

Diacetyl-N-methyl-N'-(4-fluorophenyl)-bis(thiosemicarbazone) (11)

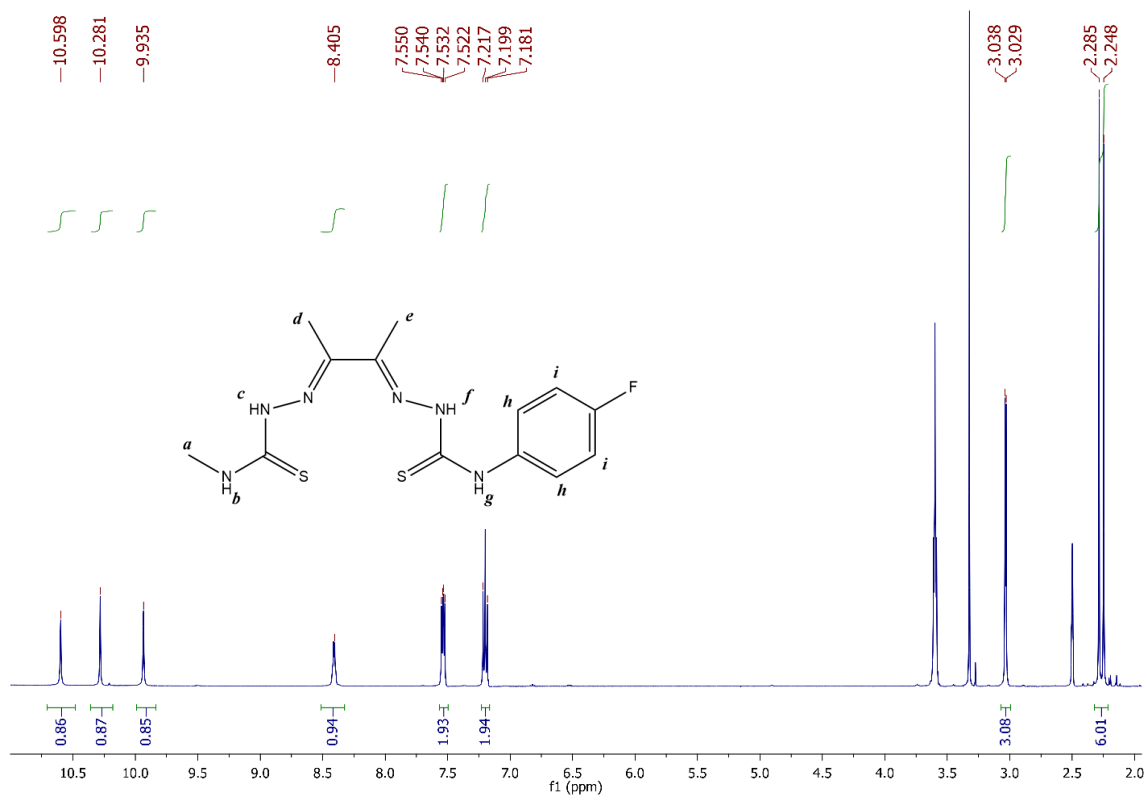


Figure A.13. ¹H NMR of Diacetyl-N-methyl-N'-(4-fluorophenyl)-bis(thiosemicarbazone) (**11**): δ (ppm) = 10.60 (s, 1H_c); 10.28 (s, 1H_f); 9.94 (s, 1H_g); 8.41 (s, 1H_b); 7.54 (dd, J = 5.0 Hz, 2H_h); 7.20 (t, J = 9.0 Hz, 2H_i); 3.60 (t, THF); 3.34 (s, H₂O); 3.03 (d, J = 4.5 Hz, 3H_a); 2.50 (m, DMSO); 2.29 (s, 3H_d); 2.25 (s, 3H_e)

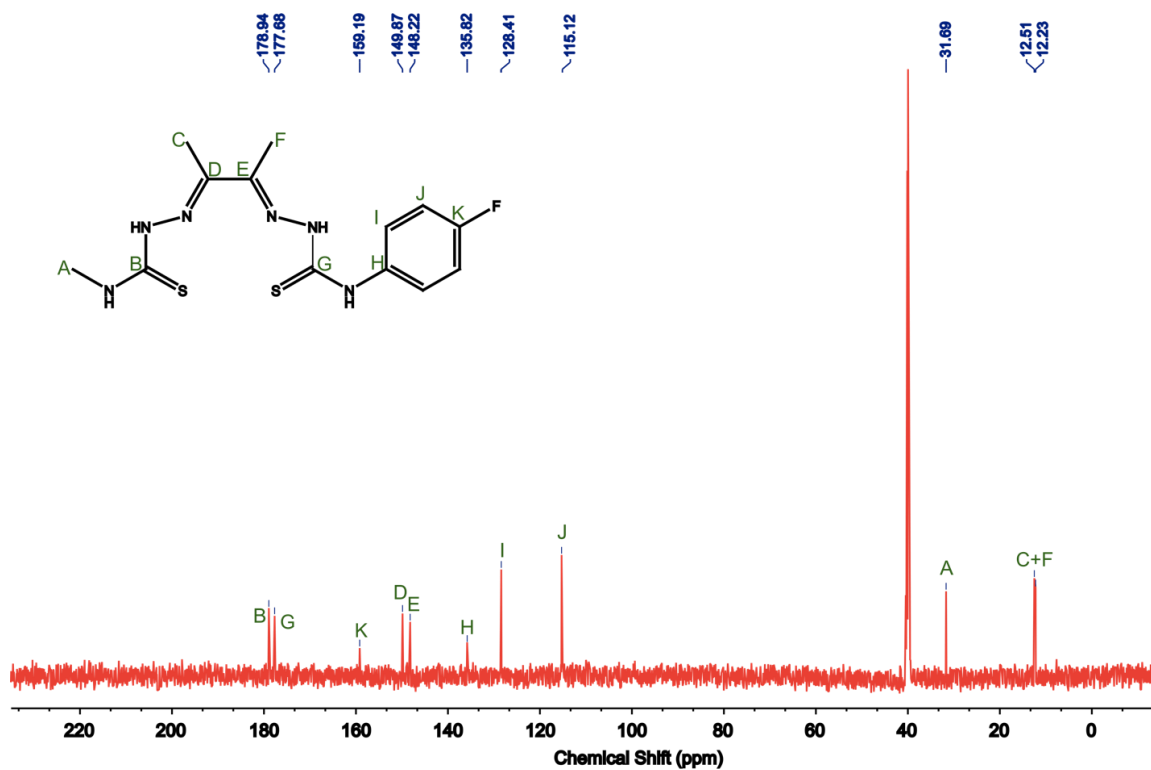


Figure A.14. ¹³C NMR of Diacetyl-N-methyl-N'-(4-fluorophenyl)-bis(thiosemicarbazone) (**11**): ¹³C NMR (125 MHz, *d*₆-DMSO): δ/ppm 178.94 (C=S), 177.68 (C=S), 149.87 (C=N), 148.22 (C=N), 159.19 (C_{Ar}-F), 135.82 (C_{Ar}-N), 128.47 and 128.41 (C_{Ar}), 115.30 and 115.32 (C_{Ar}), 31.69 (N-CH₃), 12.51 (-CH₃), 12.23 (-CH₃). Anal. Calc. for C₁₃H₁₇FN₆S₂: C, 45.87; H, 5.03; N, 24.69. Found: C, 45.51; H, 5.07; N, 24.46

Appendix B. Structural and Spectroscopic Analyses of the Metal BTSC Complexes

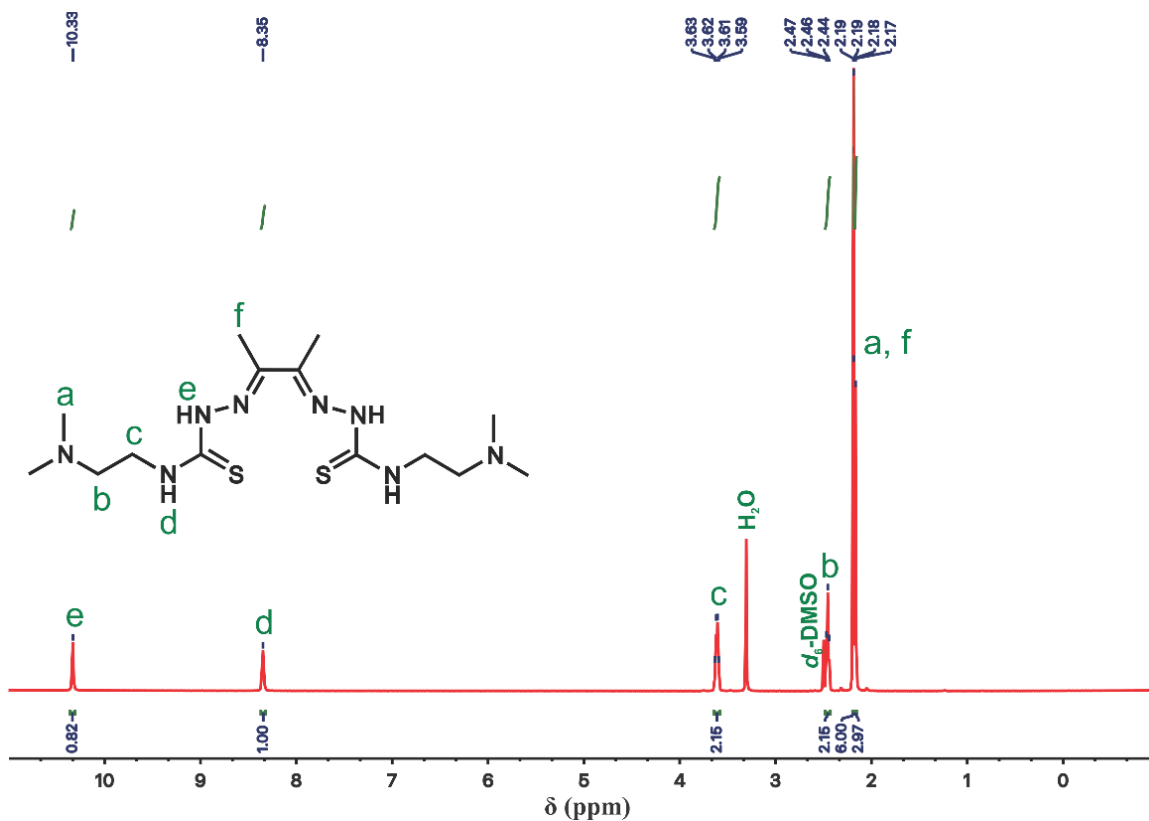


Figure B.1. ¹H NMR (500 MHz, *d*₆-DMSO) of **12**: δ/ppm 10.33 (bs, 1H, -NH-N=C-), 8.35 (t, 1H, J_{HH} = 5.4 Hz, NH-C=S), 3.61 (q, J_{HH} = 5.8 Hz, 6.4 Hz, 2H, -CH₂NH-), 2.45 (t, J_{HH} = 2.5 Hz, 6.4 Hz, 2H, -CH₂N(CH₃)₂), 2.18 (bs, 6H, -N(CH₃)₂), 2.16 (s, 3H, -CH₃).

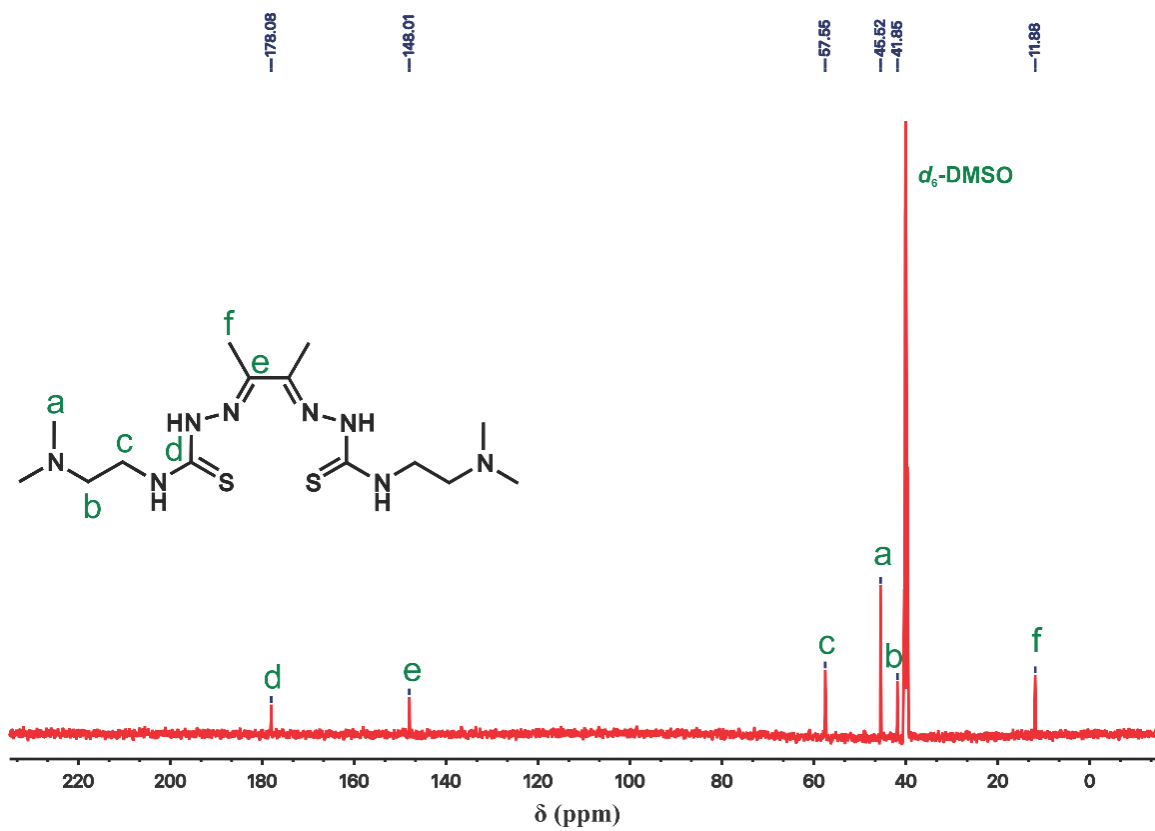


Figure B.2. ¹³C NMR (125 MHz, *d*₆-DMSO) of **12**: δ/ppm 178.1 (C=S), 146.1 (C=N), 57.6(-CH₂NH-), 45.5 (-N(CH₃)₂), 41.9 (-CH₂N(CH₃)₂), 11.9 (CH₃).

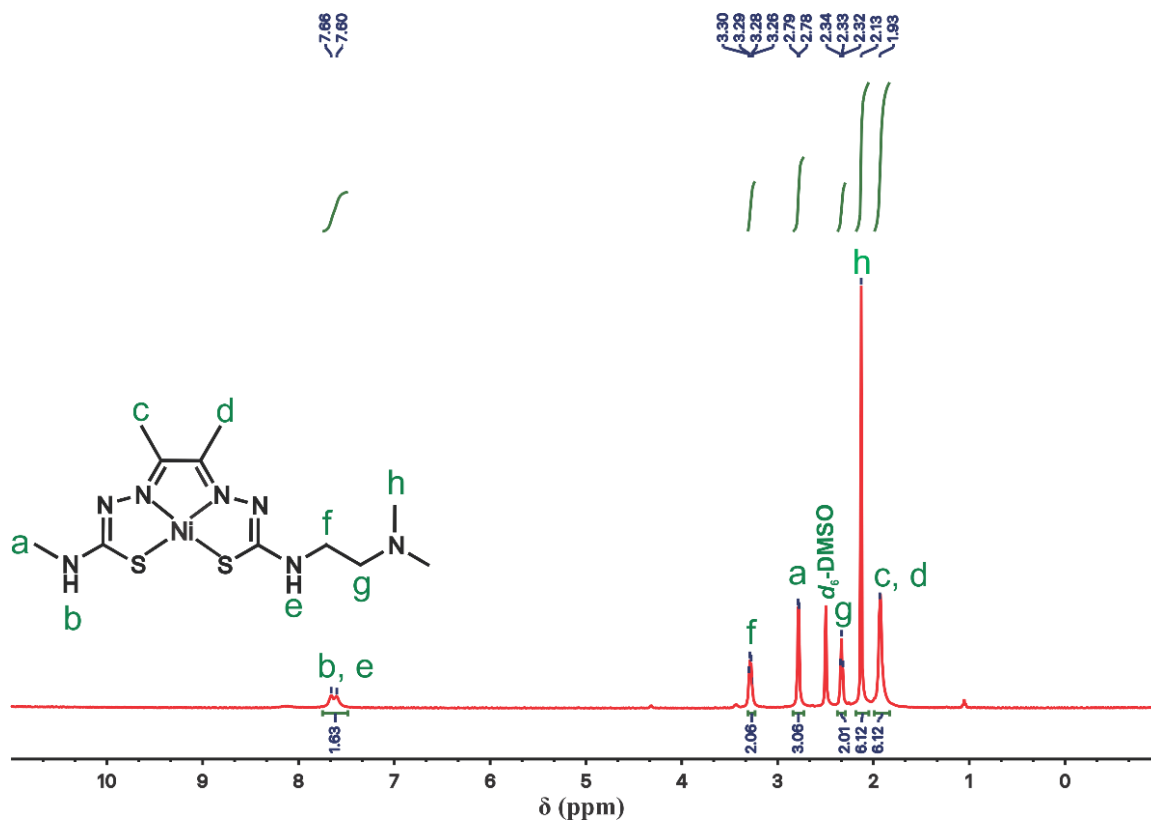


Figure B.3. ^1H NMR (400 MHz, d_6 -DMSO) of Ni-1: δ /ppm 7.66 (bs, 1H, NH-C-S), 7.60 (bs, 1H, NH-C=S), 3.28 (q, $J_{\text{HH}} = 6.0$ Hz, 2H, $-\text{CH}_2\text{NH}-$), 2.78 (d, $J_{\text{HH}} = 4.2$ Hz, 3H, $-\text{CH}_3$), 2.33 ppm (t, $J_{\text{HH}} = 6.7$ Hz, 2H, $\text{CH}_2\text{N}(\text{CH}_3)_2$), 2.13 (bs, 6H, $-\text{N}(\text{CH}_3)_2$), 1.93-1.92 (bs, 6H, 2 x $-\text{CH}_3$).

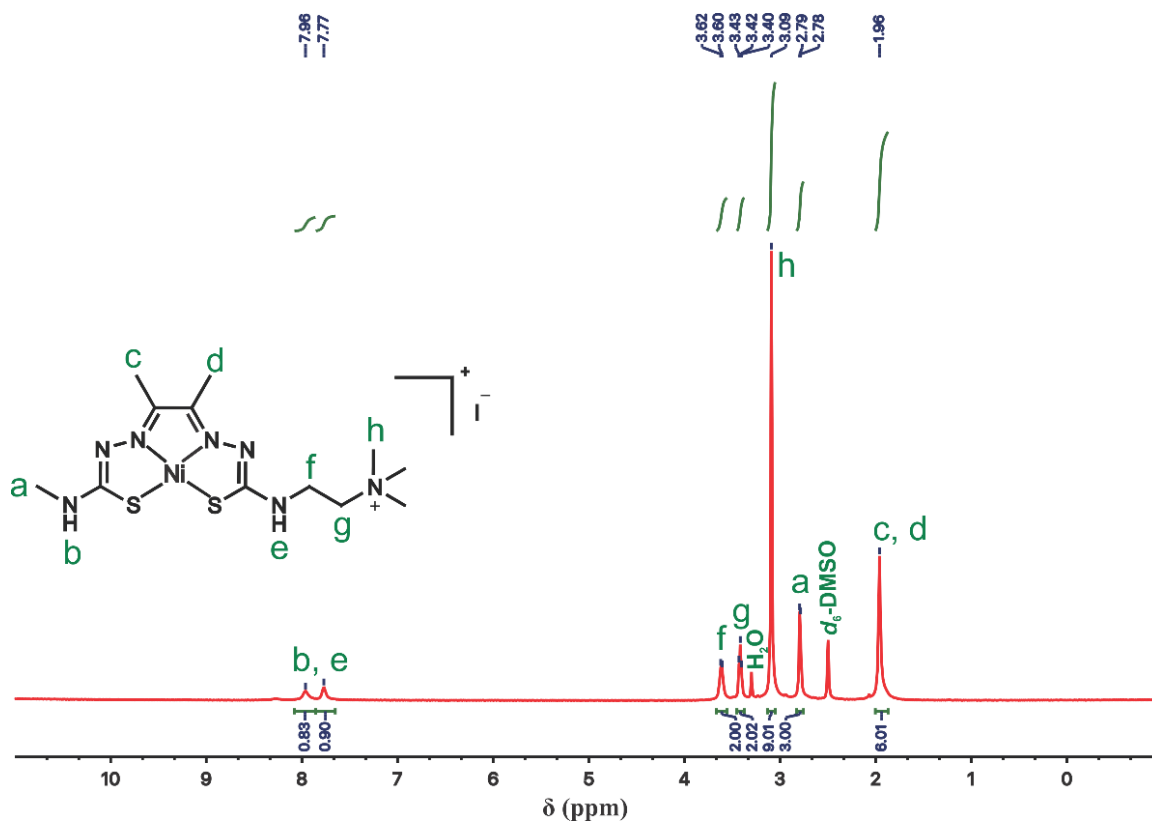


Figure B.4. ¹H NMR (400 MHz, *d*₆-DMSO) of Ni-2: δ/ppm 7.96 (bs, 1H, NH-C=S), 7.77 (bs, 1H, NH-C=S), 3.61 (bs, 2H, -CH₂NH-), 3.42 ppm (t, J_{HH} = 5.9 Hz, 2H, CH₂⁺N(CH₃)₃), 3.09 (bs, 9H, ⁺N(CH₃)₃), 2.79 (d, J_{HH} = 3.5 Hz, 3H, -CH₃), 1.96 (bs, 6H, 2 x -CH₃).

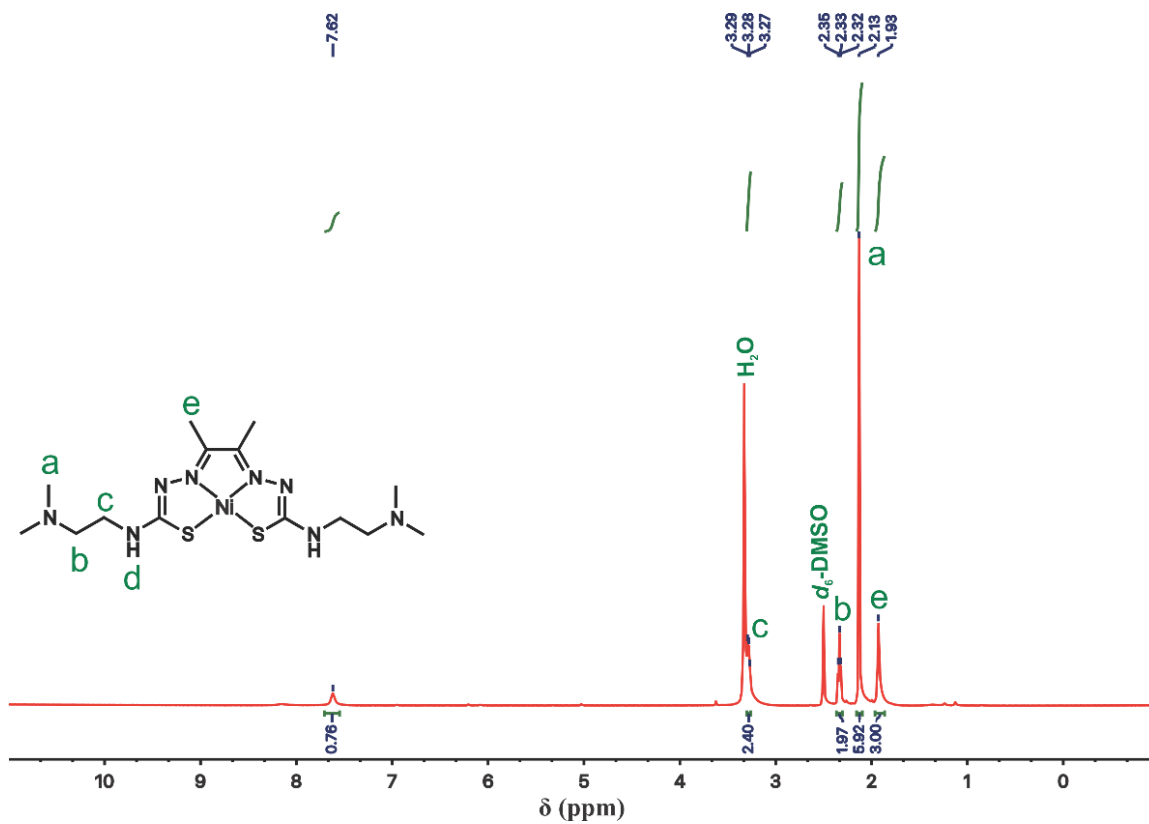


Figure B.5. ¹H NMR (500 MHz, *d*₆-DMSO) of Ni-3: δ /ppm 7.61 (bs, 1H, -NH-C=S), 3.27 (q, $J_{\text{HH}} = 6.2$ Hz, 2H, -CH₂NH-), 2.34 (t, $J_{\text{HH}} = 6.8$ Hz, 2H, -CH₂N(CH₃)₂), 2.13 (bs, 6H, -N(CH₃)₂), 1.92 (bs, 3H, -CH₃).

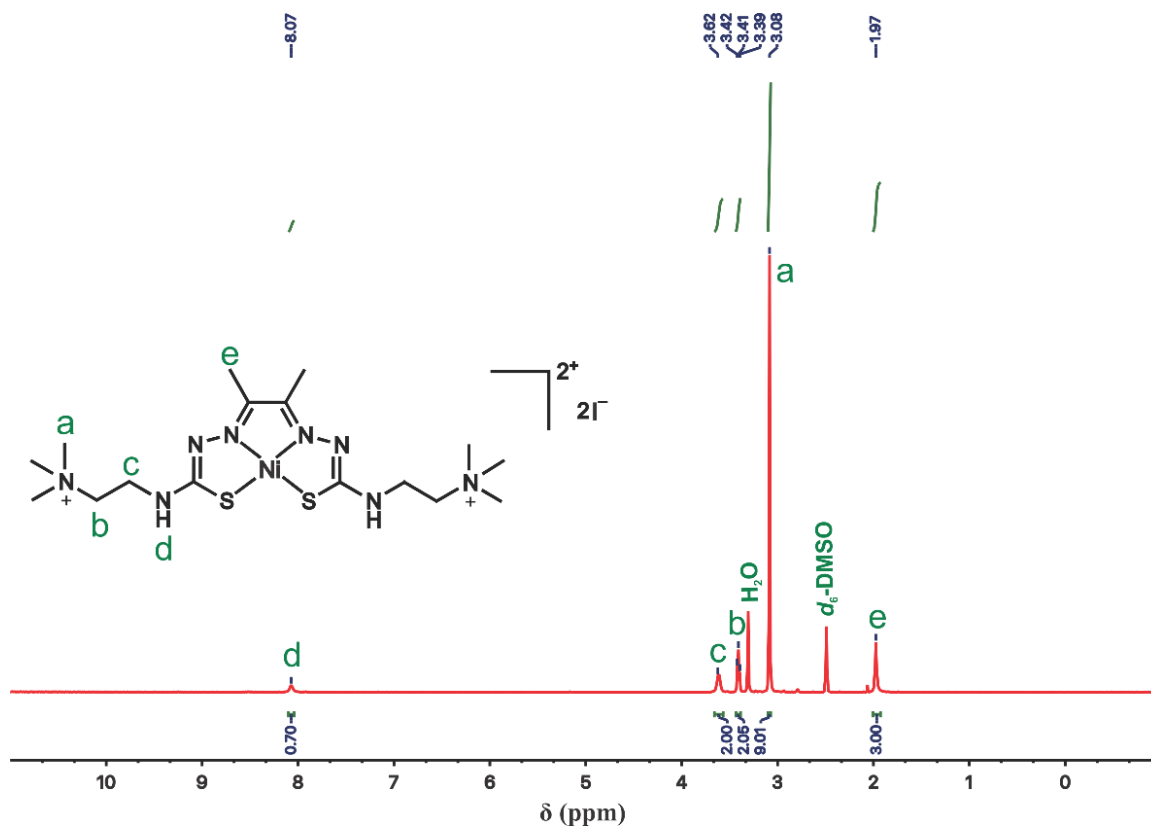


Figure B.6. ¹H NMR (500 MHz, *d*₆-DMSO) of Ni-4: δ/ppm 8.07 (bs, 1H, -NH-C=S), 3.61 (bs, 2H, -CH₂NH-), 3.41 (t, J_{HH} = 6.8, 2H, -CH₂N(CH₃)₃), 3.08 (bs, 9H, -N(CH₃)₃), 1.97 (bs, 3H, -CH₃).

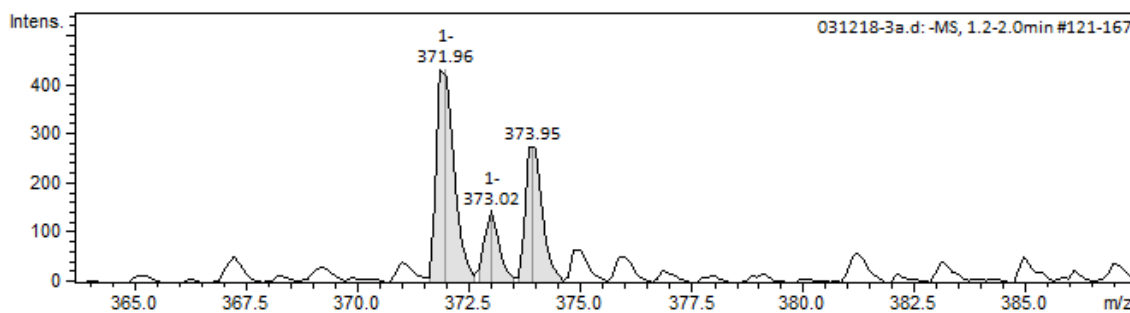


Figure B.7. (-)ESI-MS spectrum of Ni-1 m/z calc. for [M-H]⁻, [C₁₁H₂₁N₇NiS₂]⁻H; 372.07. Found: 371.96.

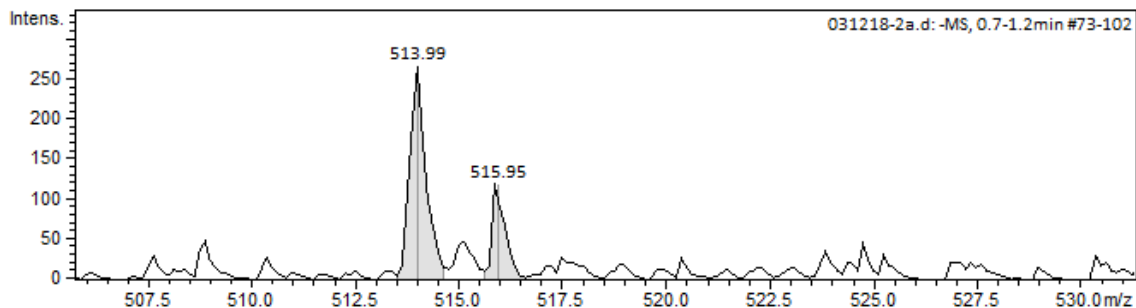


Figure B.8. (-)ESI-MS spectrum of **Ni-2**: m/z calc. for, $[C_{12}H_{24}IN_7NiS_2]-H$; 513.99. Found: 513.99.

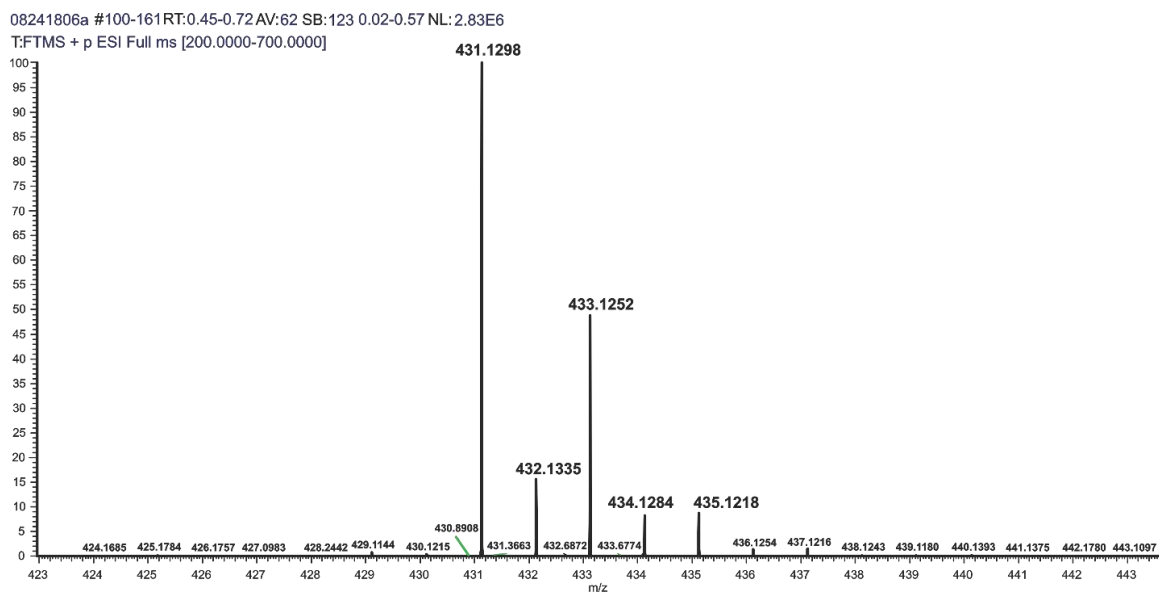


Figure B.9. (+)ESI-MS spectrum of **Ni-3** m/z calc. for $[C_{14}H_{28}N_8NiS_2]+H$: 431.12. Found: 431.1298.

040618-3h #112-170 RT: 0.50-0.70 AM: 50 NI: 0.7150
T: FTMS -p ESI Full ms[100.000]

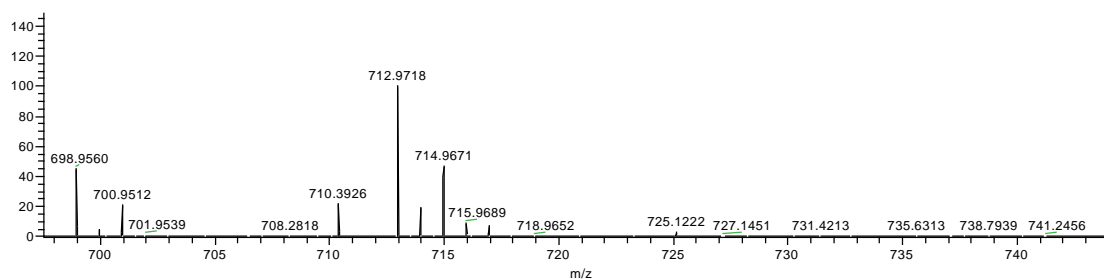


Figure B.10. (-)ESI-MS spectrum of Ni-4 m/z calc. for $[C_{16}H_{34}I_2N_8NiS_2]-H$: 712.98. Found: 712.97.

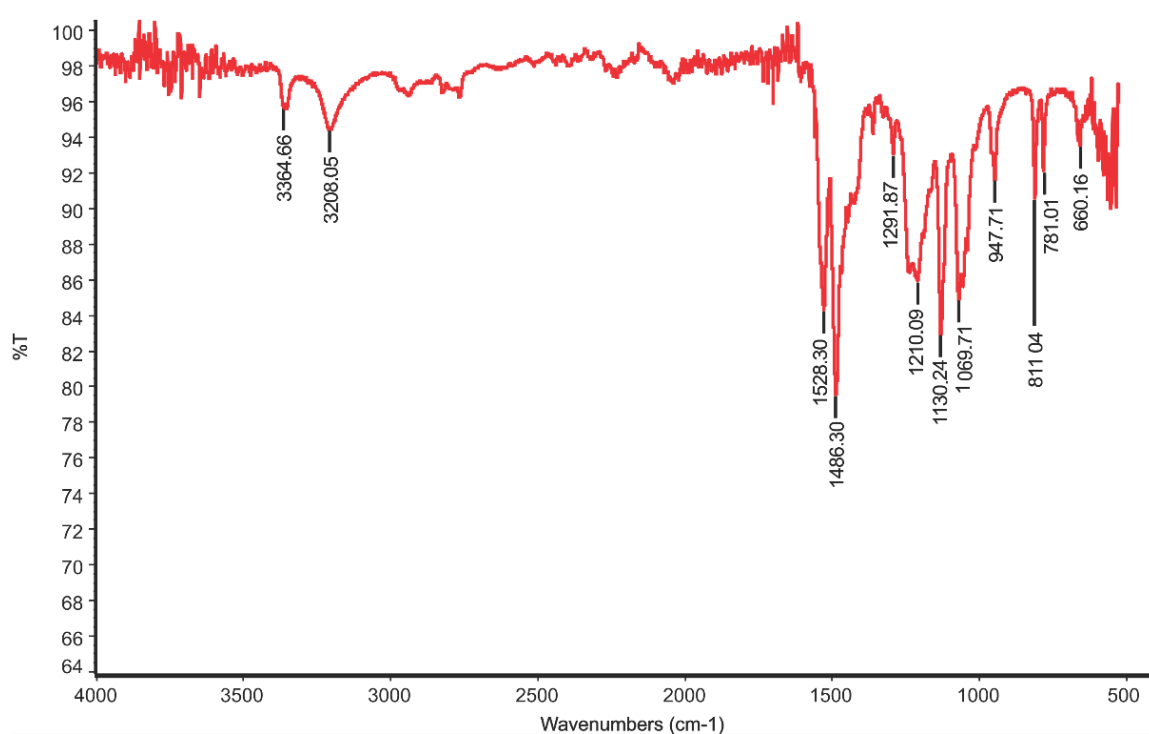


Figure B.11. FT-IR spectrum of **3**.

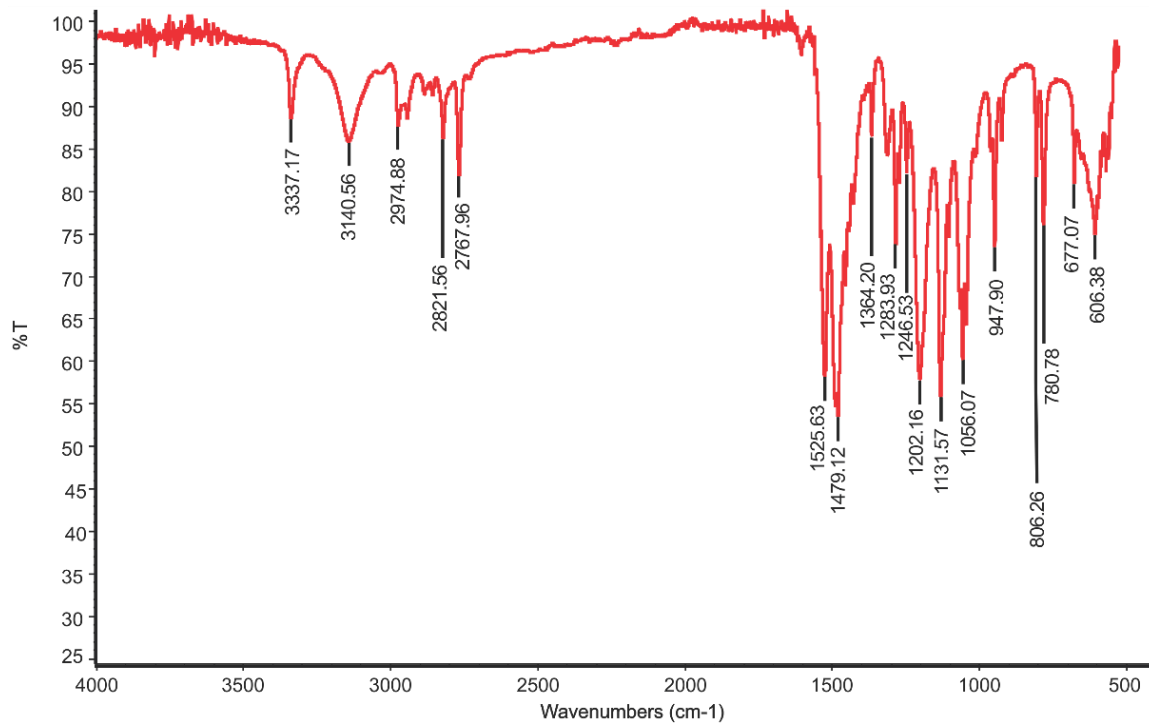


Figure B.12. FT-IR spectrum of 12.

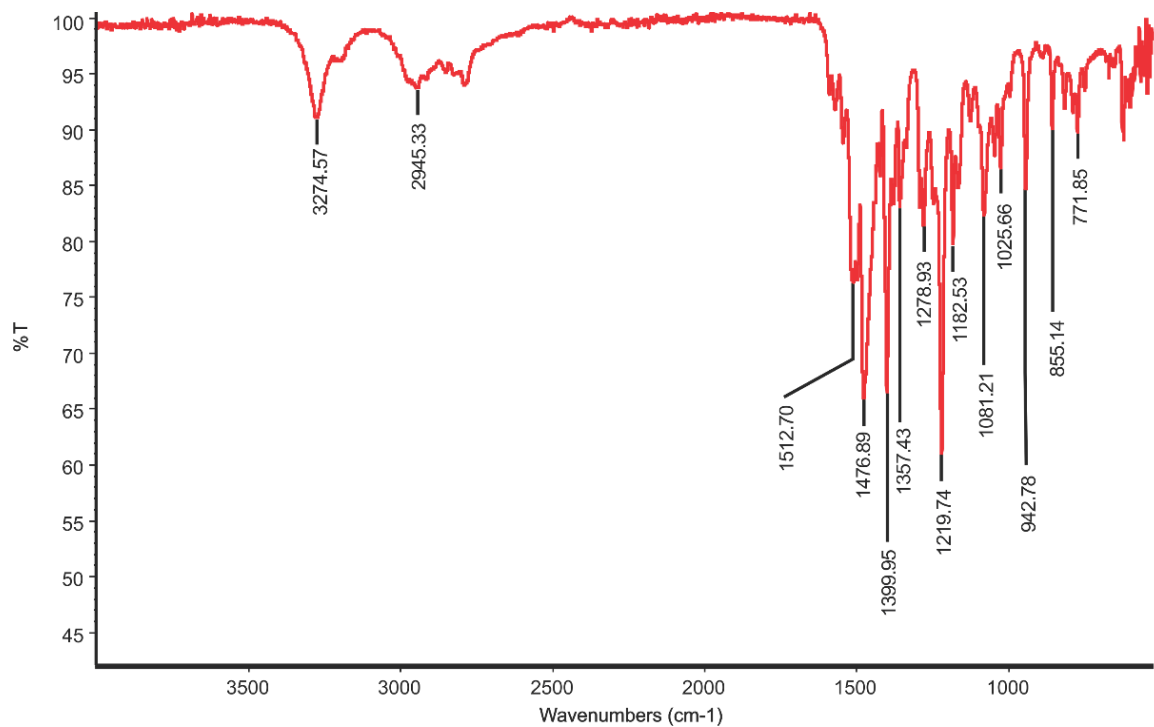


Figure B.13. FT-IR spectrum of Ni-1.

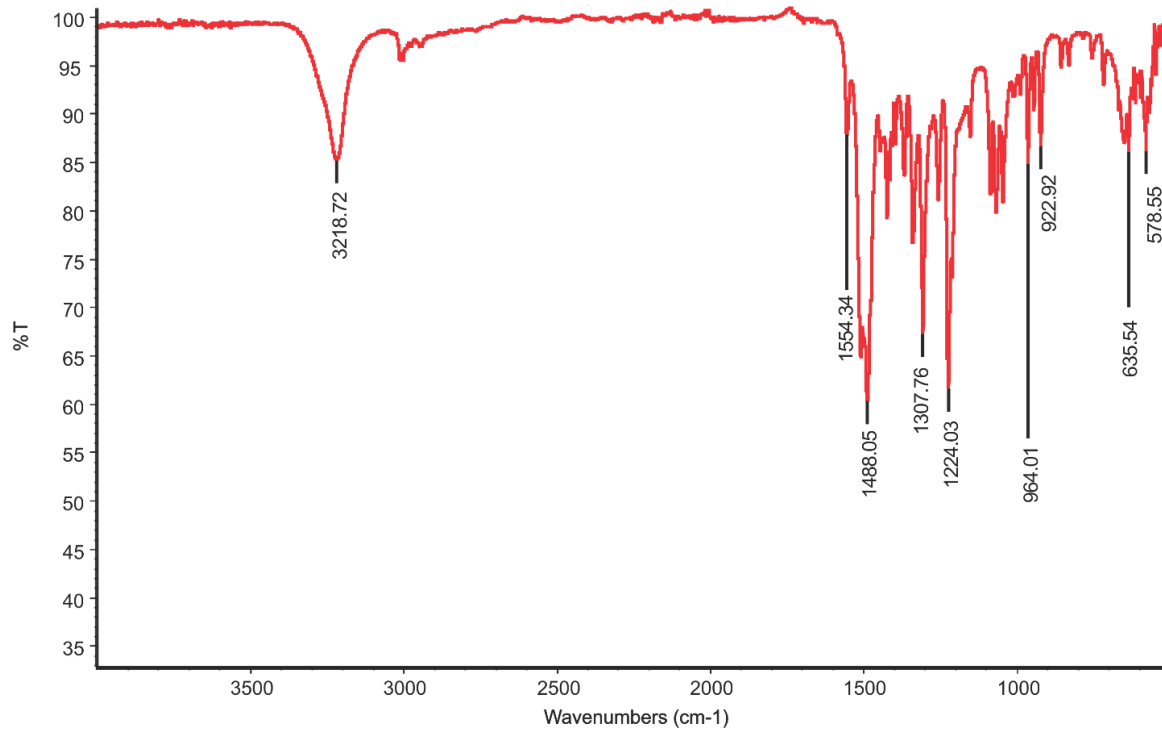


Figure B.14. FT-IR spectrum of Ni-2

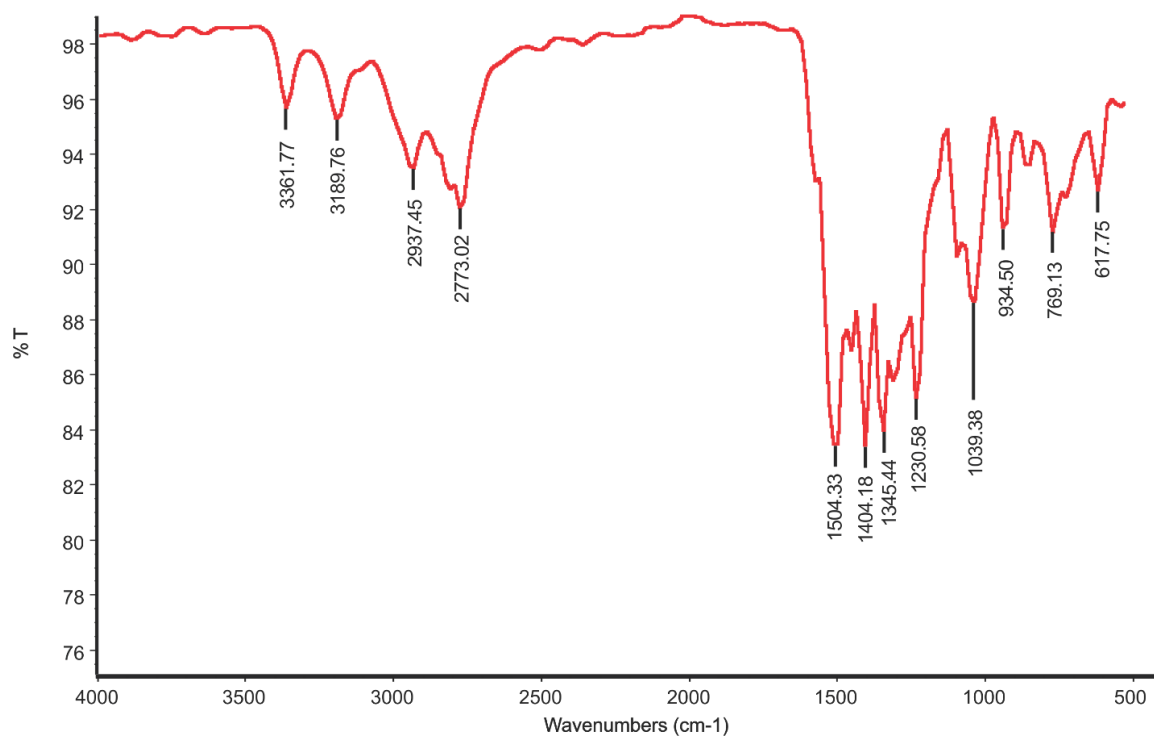


Figure B.15. FT-IR spectrum of Ni-3

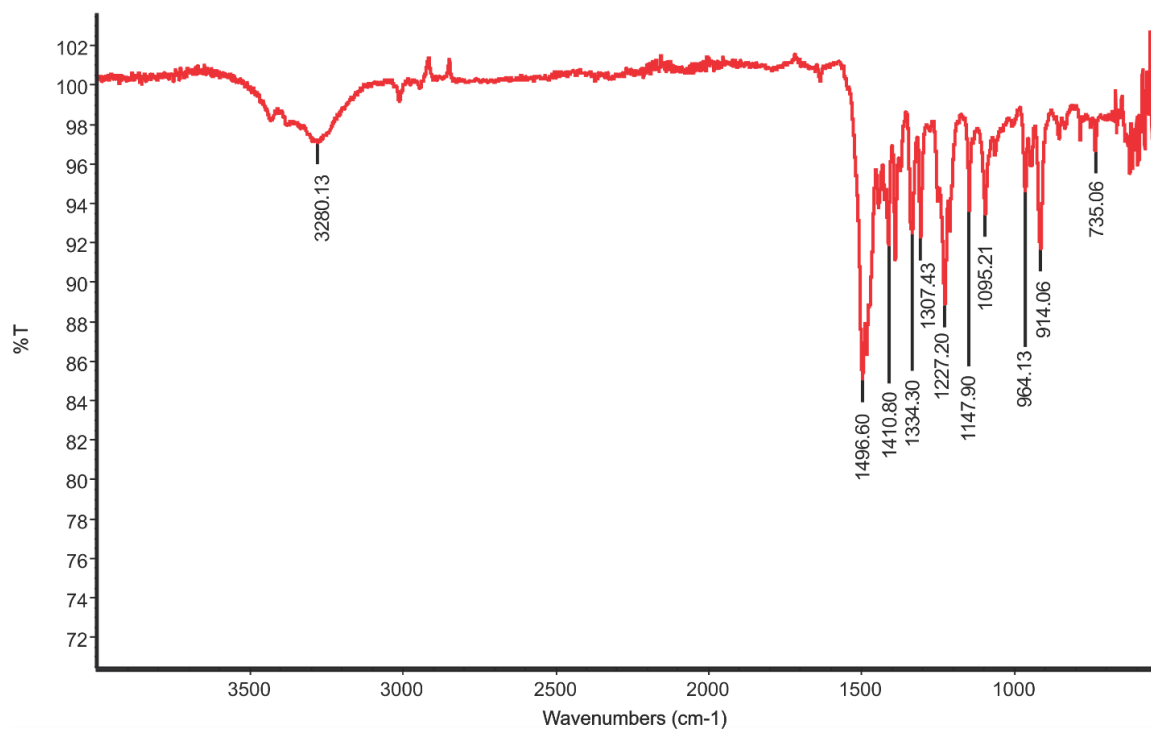


Figure B.16. FT-IR spectrum of Ni-4

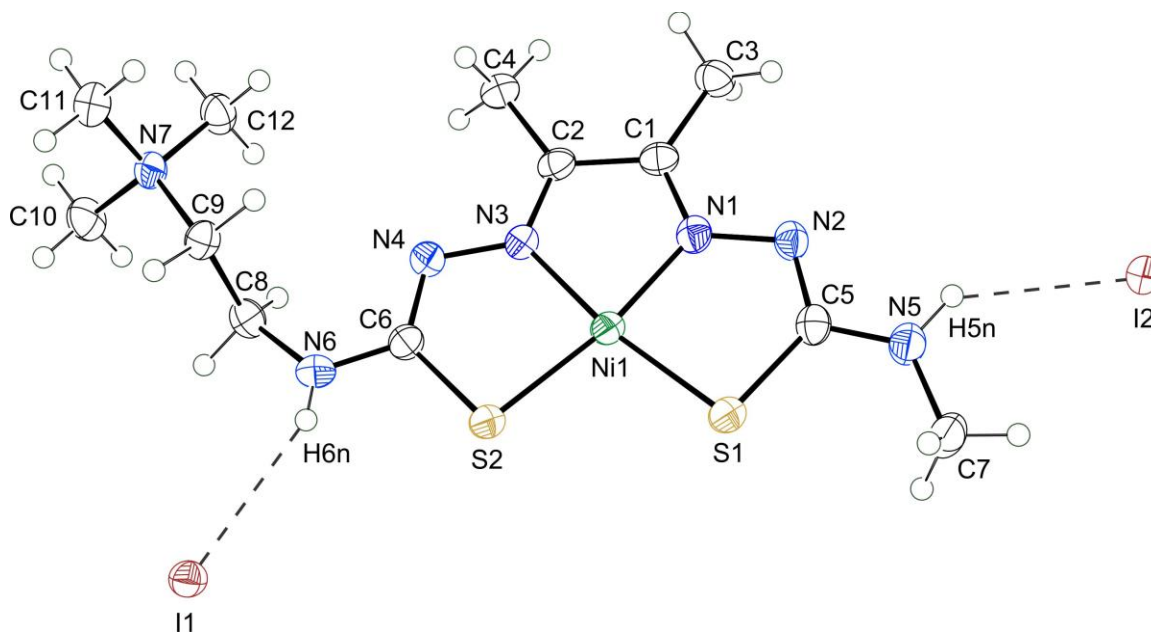


Figure B.17. ORTEP view (50% probability) of Ni-2 showing atom labeling for all non-hydrogen atoms in the asymmetric unit. Both iodide atoms are 50% occupancy.

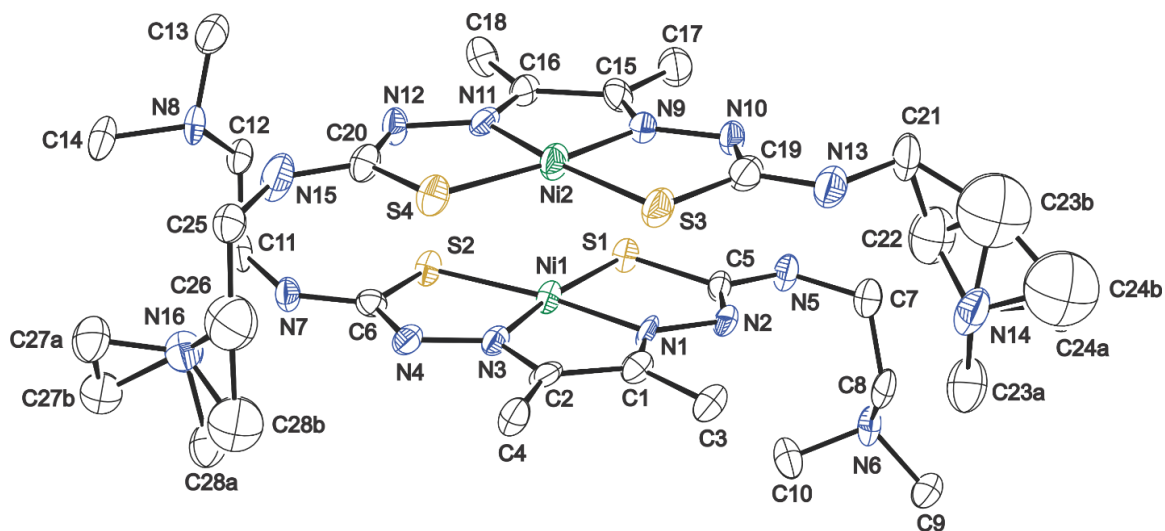


Figure B.18. ORTEP view (50% probability) of **Ni-3** showing atom labeling for all non-hydrogen atoms in the asymmetric unit. All hydrogen atoms are omitted for clarity.

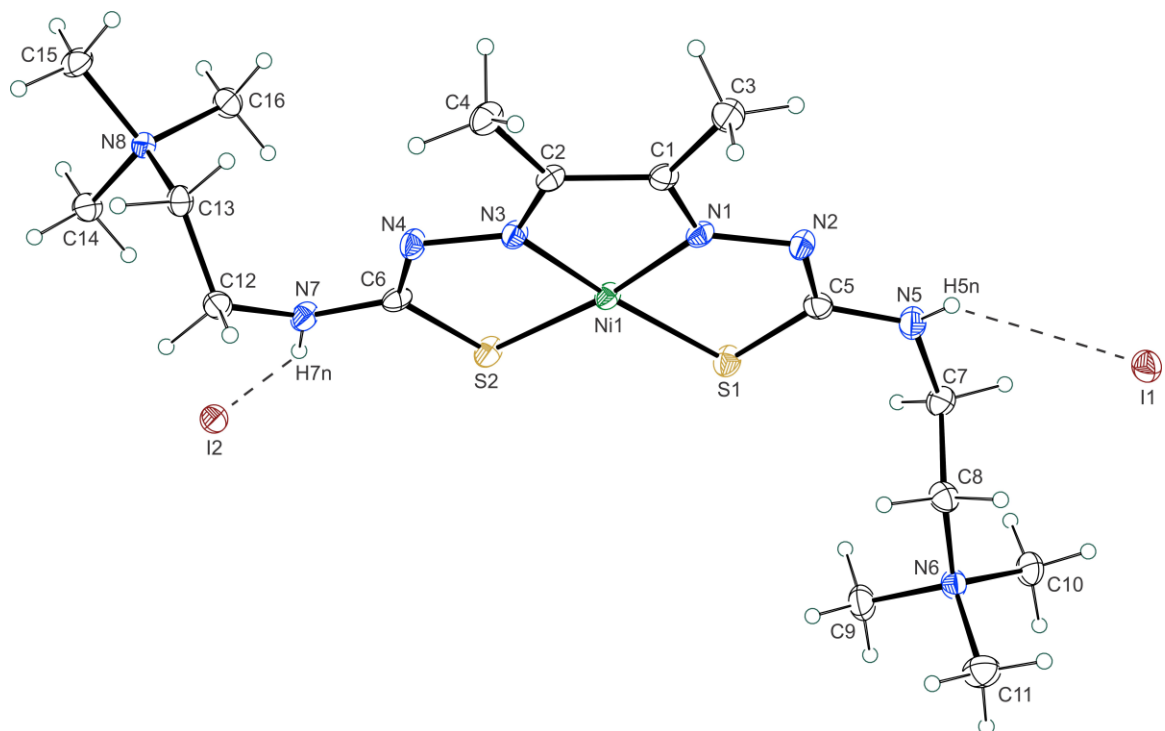


Figure B.19. ORTEP view (50% probability) of **Ni-4** showing atom labeling for all non-hydrogen atoms in the asymmetric unit. Both iodide atoms are of full occupancy.

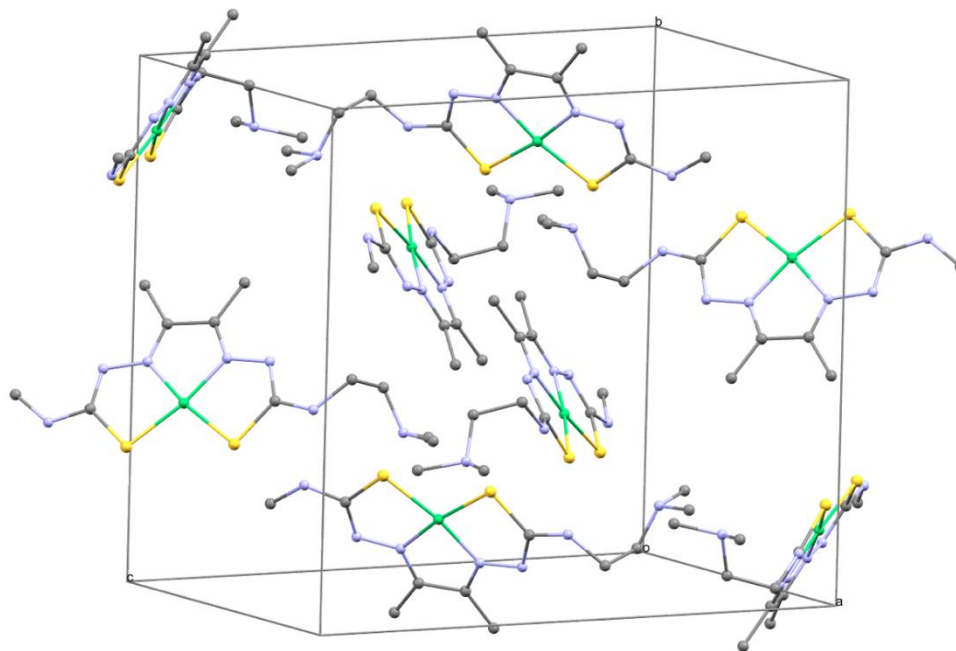


Figure B.20. Unit cell diagram of Ni-1. Hydrogens atoms are omitted for clarity.

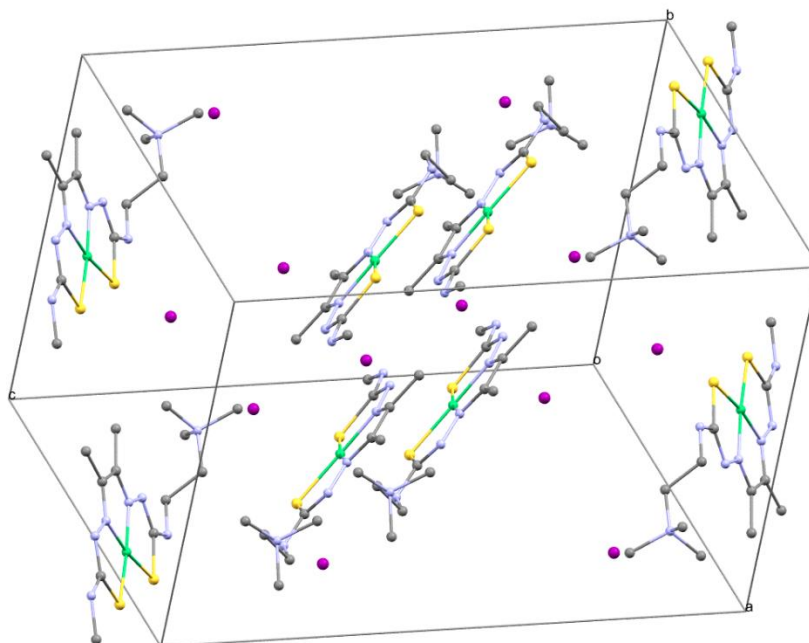


Figure B.21. Unit cell diagram of complex Ni-2. Hydrogens atoms are omitted for clarity.

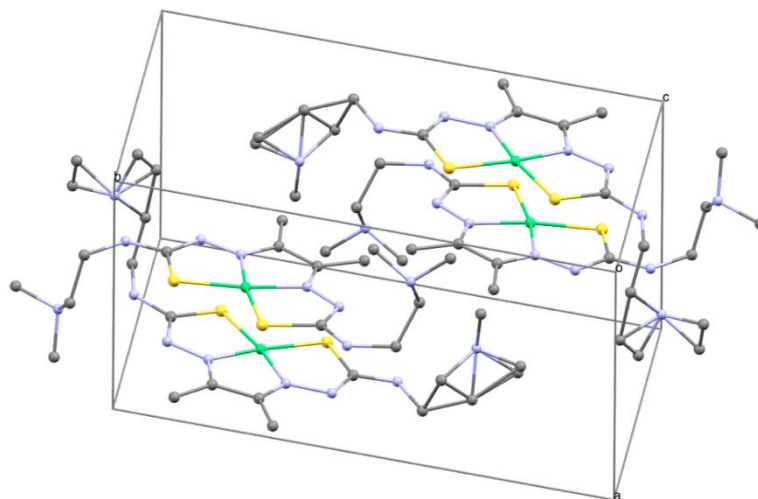


Figure B.22. Unit cell diagram of complex **Ni-3**. Hydrogens atoms are omitted for clarity.

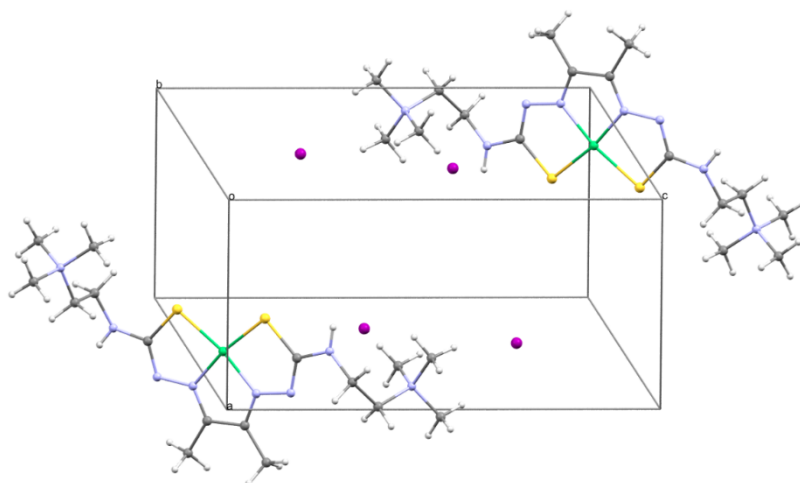


Figure B.23. Unit cell diagram of complex **Ni-4**.

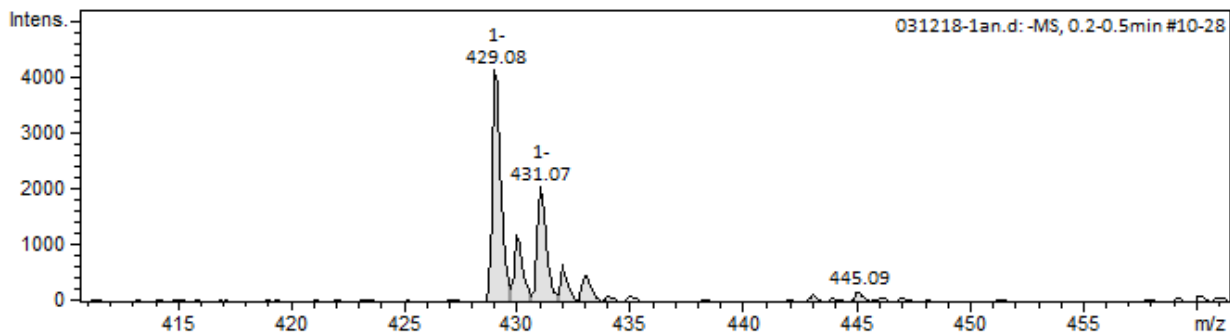


Figure B.24. (-)ESI-MS spectrum of protonated **Ni-3** m/z calc. for $[C_{14}H_{28}N_8NiS_2]\text{-H}$: 429.12. Found: 429.08.

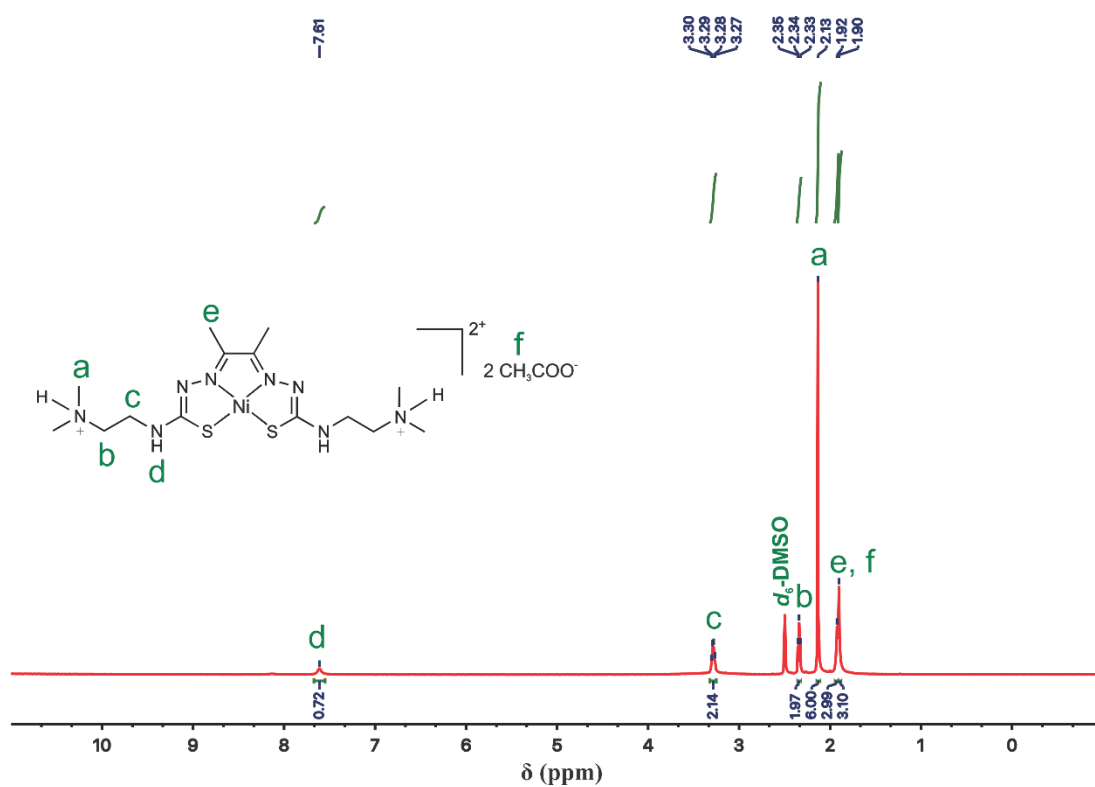


Figure B.25. ^1H NMR (500 MHz, d_6 -DMSO) of protonated **Ni-3**: δ/ppm 7.61 (bs, 1H, -NH-C=S), 3.27 (q, $J_{\text{HH}} = 6.2$ Hz, 2H, $-\text{CH}_2\text{NH}-$), 2.34 (t, $J_{\text{HH}} = 6.8$ Hz, 2H, $-\text{CH}_2\text{N}(\text{CH}_3)_2$), 2.13 (bs, 6H, $-\text{N}(\text{CH}_3)_2$), 1.92 (bs, 3H, $-\text{CH}_3$). The peak at 1.90 is $-\text{CH}_3$ of acetic acid due to nickel(II) acetate being used as the source of nickel. Corresponding $^+\text{N-H}$ peak not observed.

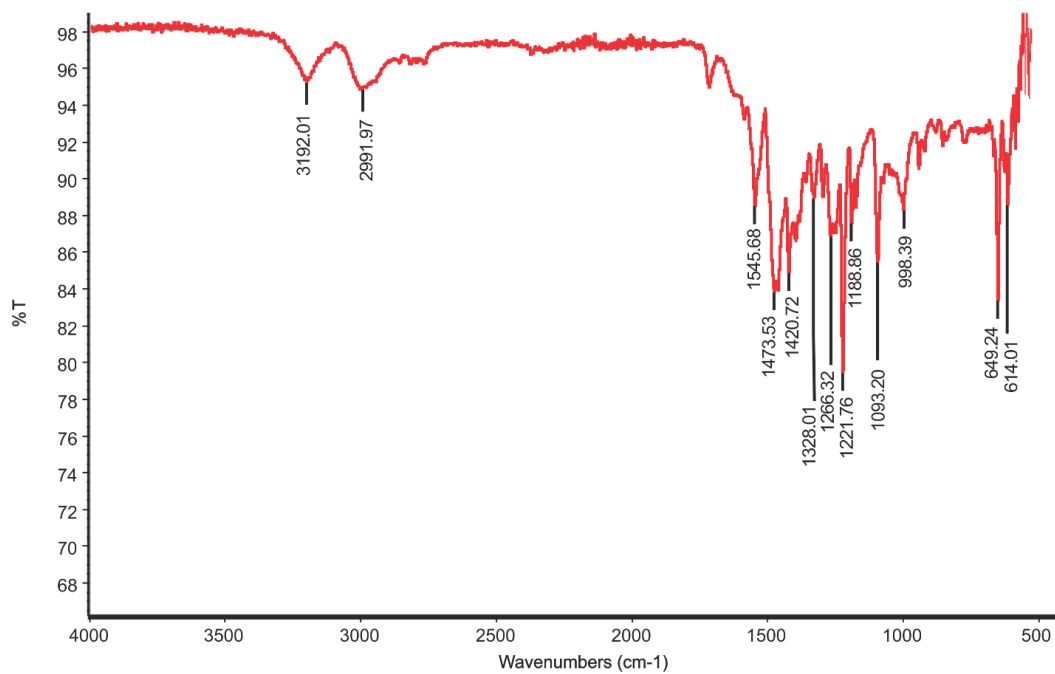


Figure B.26. FT-IR spectrum of protonated Ni-3.

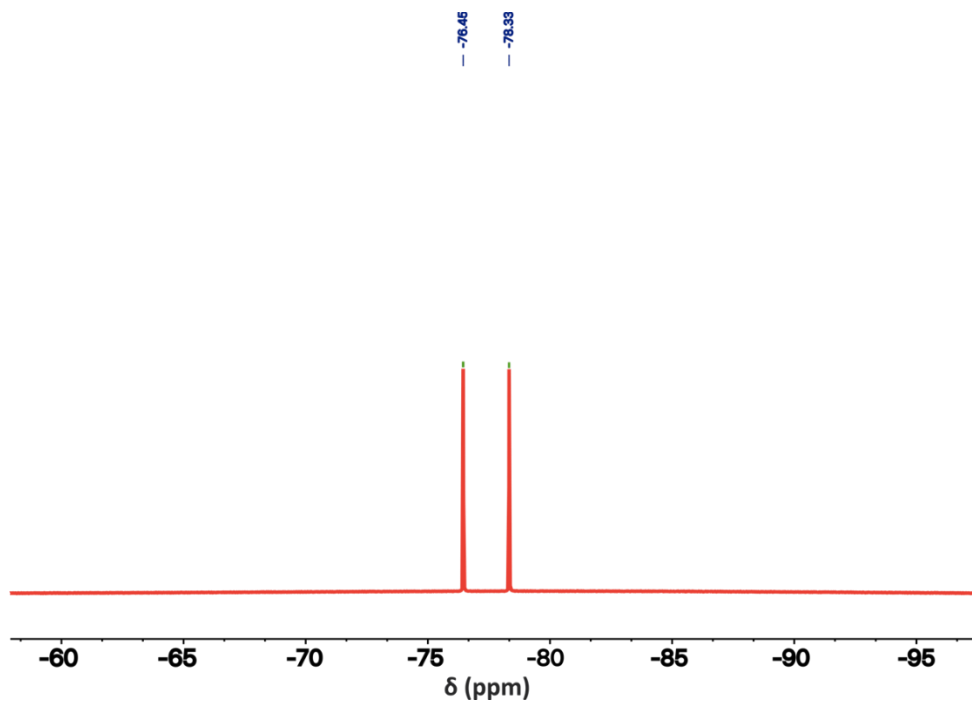


Figure B.27. ^{19}F NMR (376 MHz, $\text{d}_6\text{-DMSO}$) of Cu-2*. δ/ppm -77.39 (d, $J_{\text{FP}} = 706$ Hz)

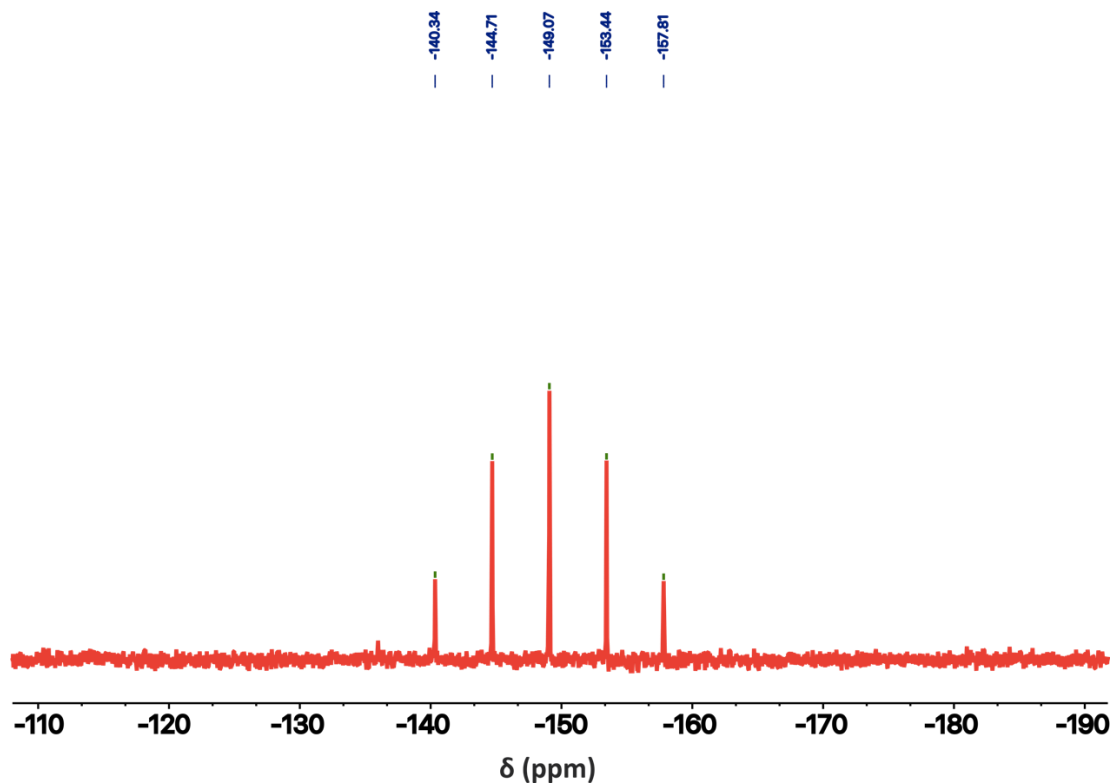


Figure B.28. ^{31}P NMR (162 MHz, $\text{d}_6\text{-DMSO}$) of Cu-2*. δ/ppm -149.07 (h, $J_{\text{PF}} = 706$ Hz)

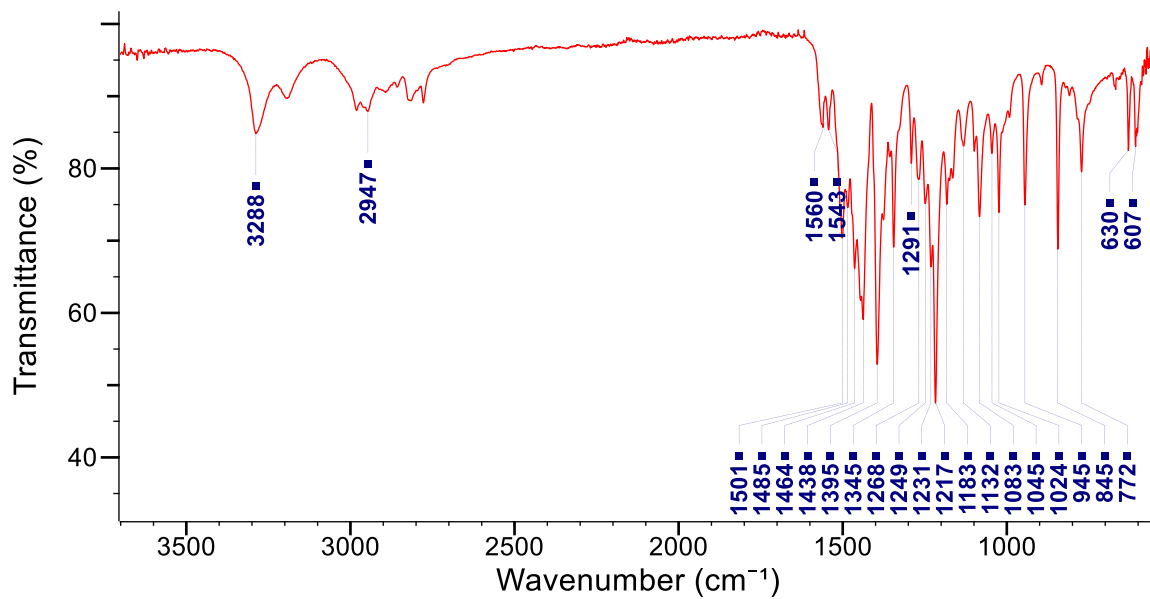


Figure B.29. FT-IR of Cu-1.

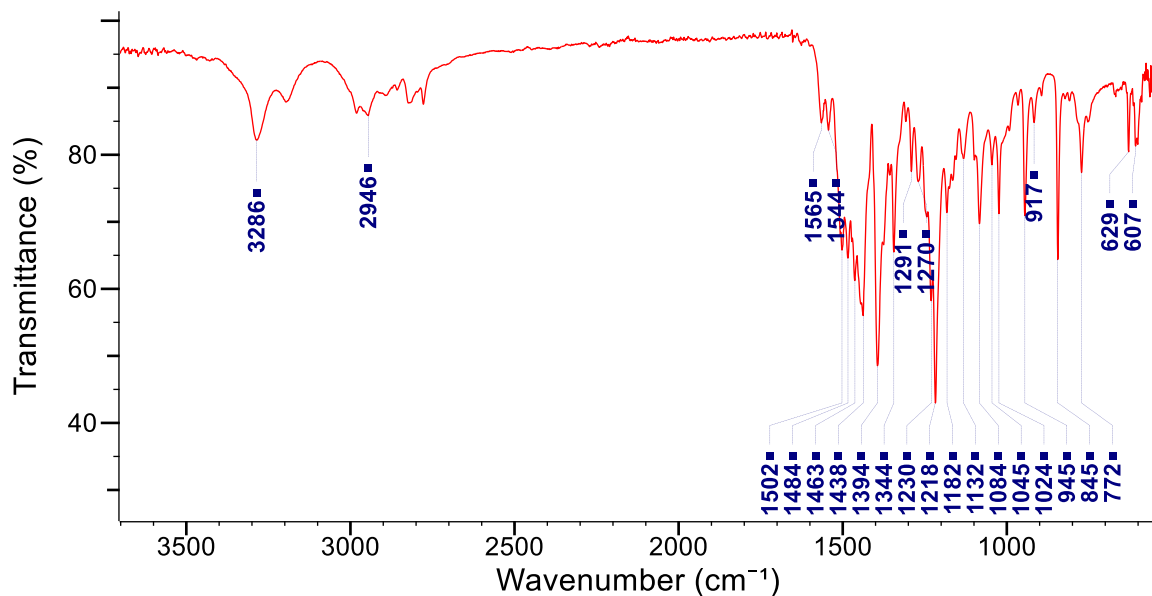


Figure B.30. FT-IR of Cu-2.

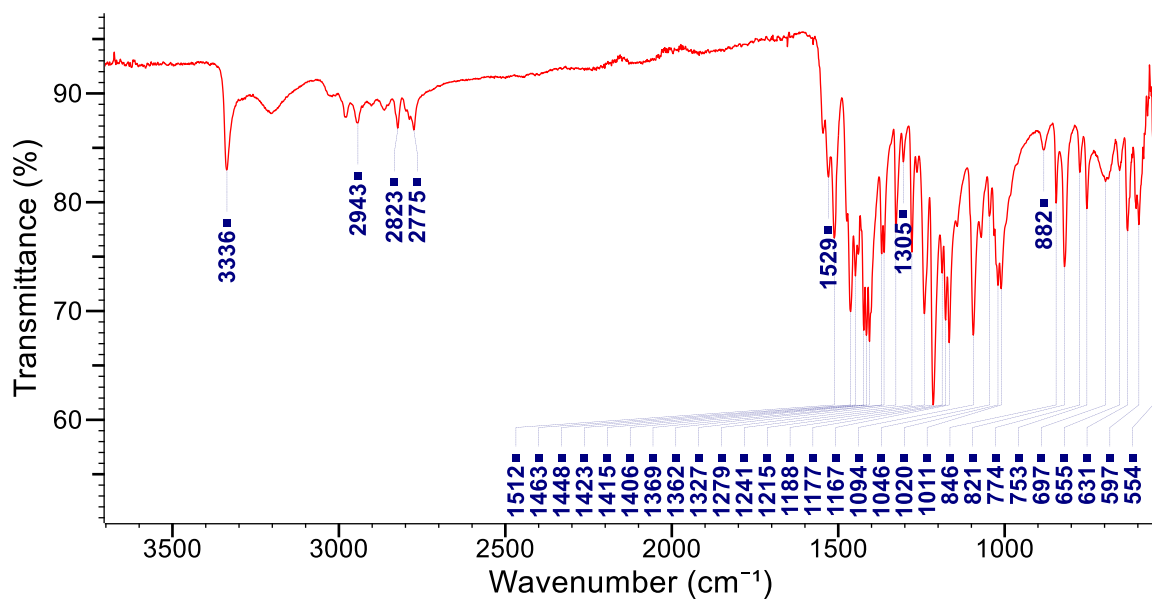


Figure B.31. FT-IR of Cu-3.

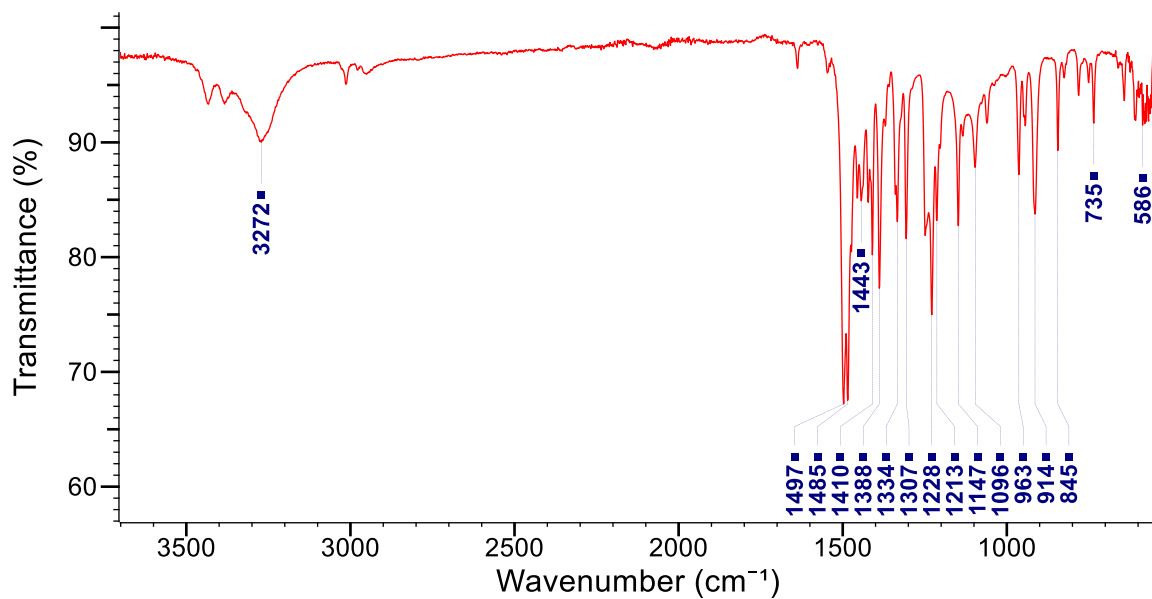


Figure B.32. FT-IR of Cu-4.

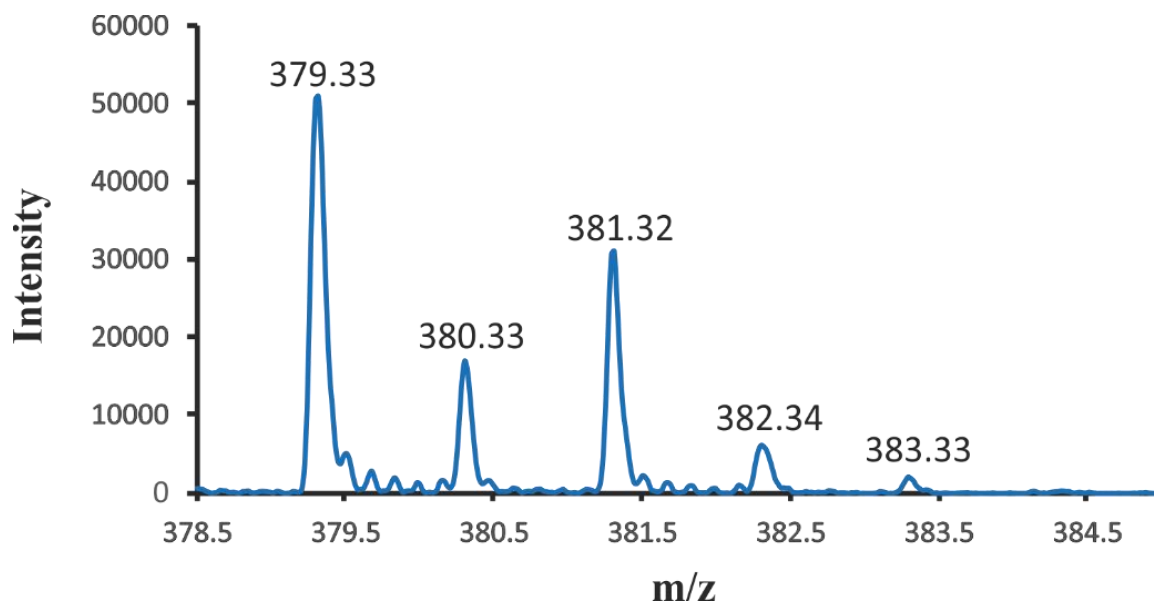


Figure B.33. MALDI-TOF mass spectrum of Cu-1.

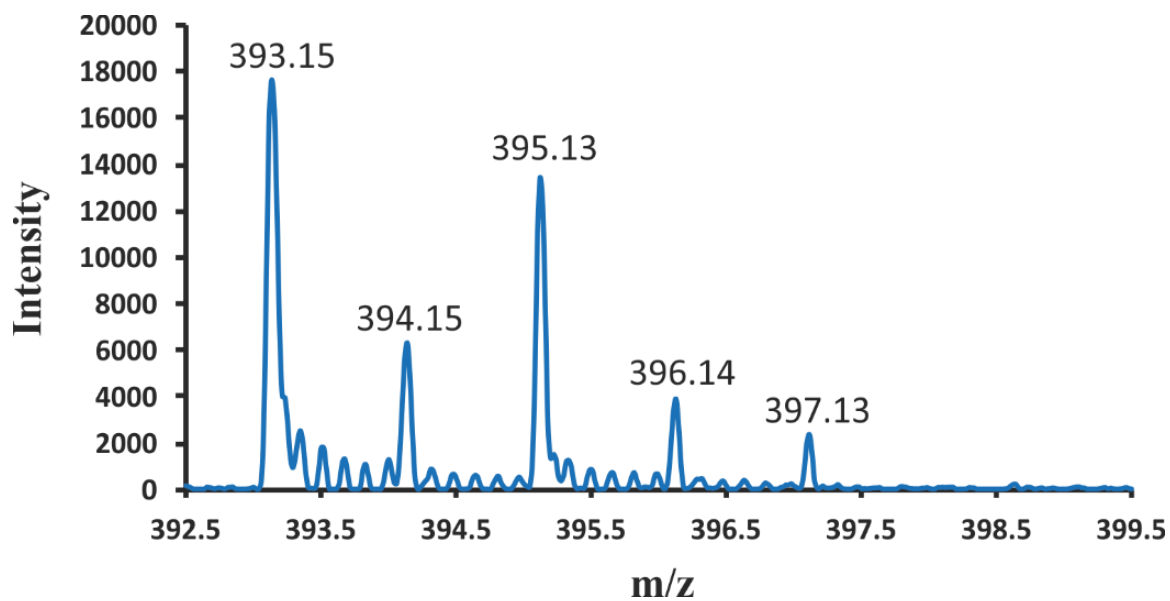


Figure B.34. MALDI-TOF mass spectrum of Cu-2.

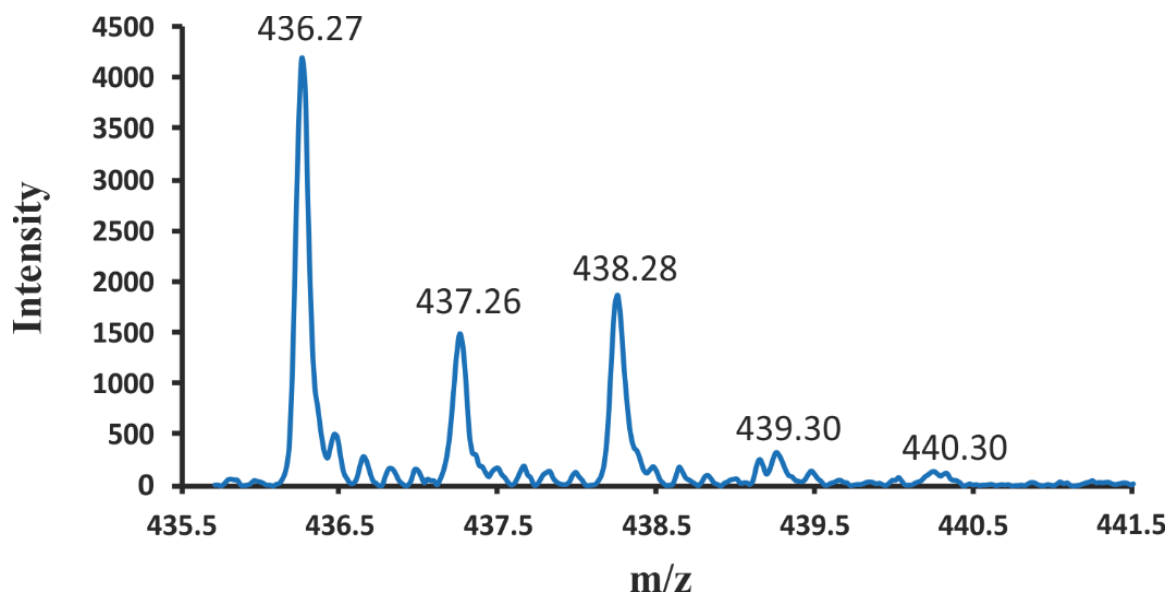


Figure B.35. MALDI-TOF mass spectrum of Cu-3.

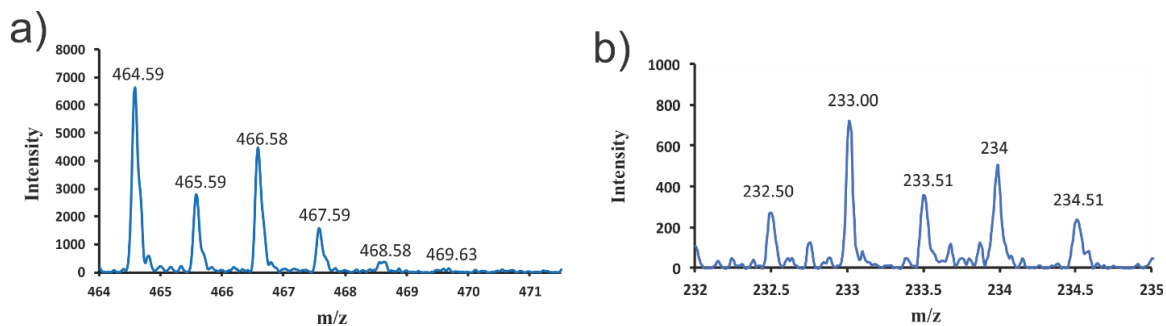


Figure B.36. MALDI-TOF mass spectrum of **Cu-4**. The parent fragment (a) and the $m/2$ fragment (b).

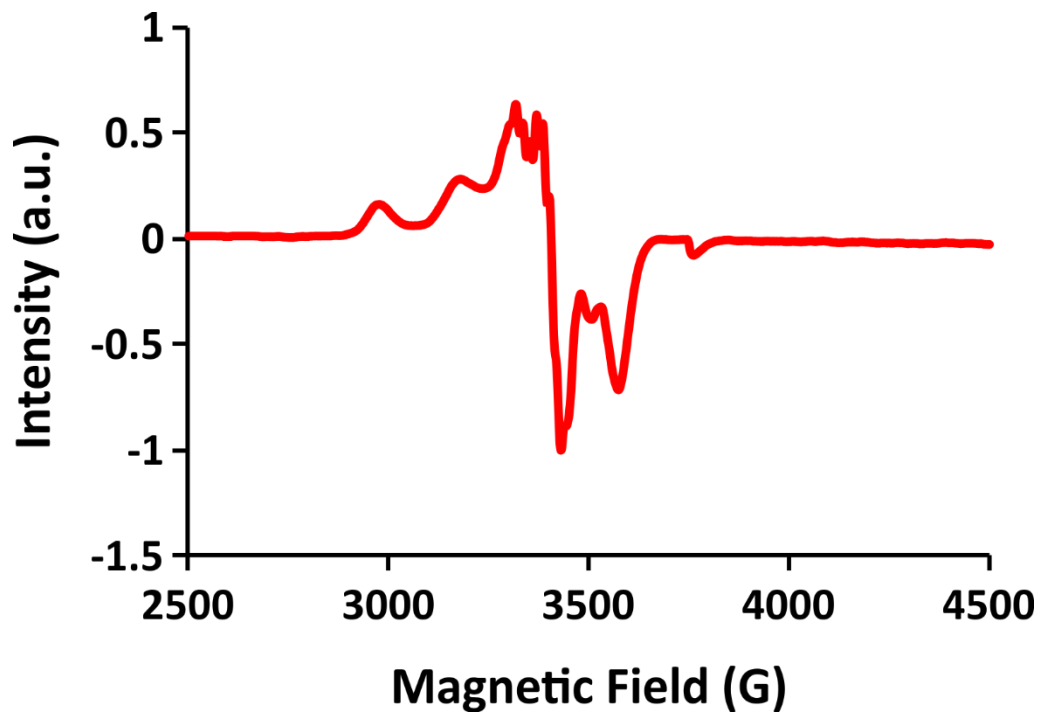


Figure B.37. Low temperature (77 K) EPR spectrum of **Cu-1** in DMF. Microwave frequency = 9.603 MHz, $g_{\parallel} = 2.11$, $g_{\perp} = 2.01$, $A_{\parallel} = 191$ G.

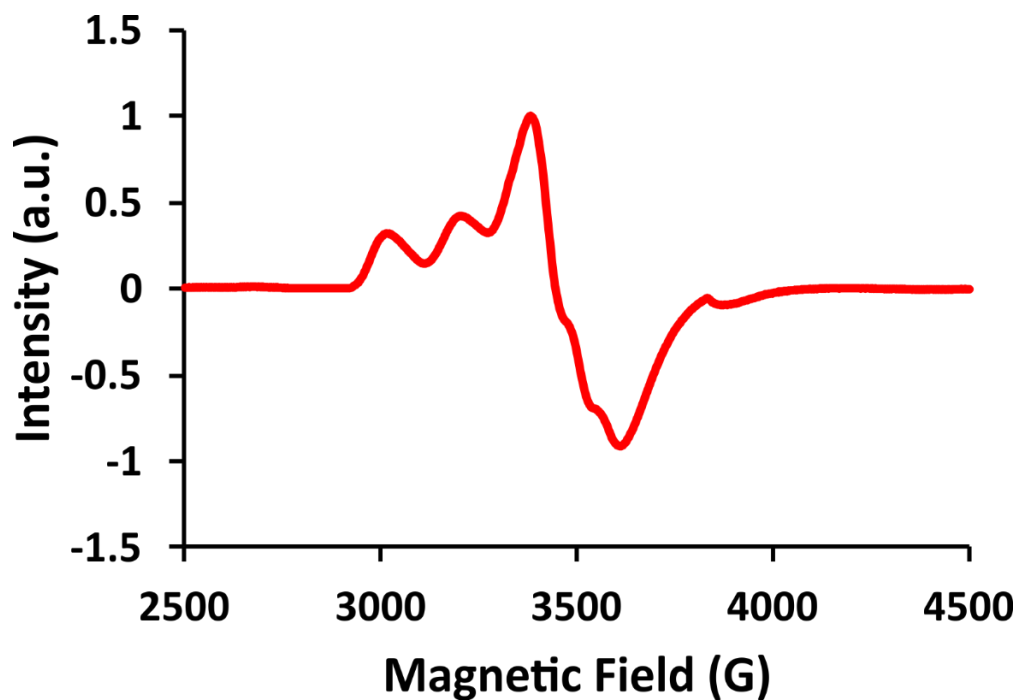


Figure B.38. Low temperature (77 K) EPR spectrum of **Cu-2** in DMF. Microwave frequency = 9.603 MHz, $g_{\parallel} = 2.08$, $g_{\perp} = 2.00$, $A_{\parallel} = 184$ G.

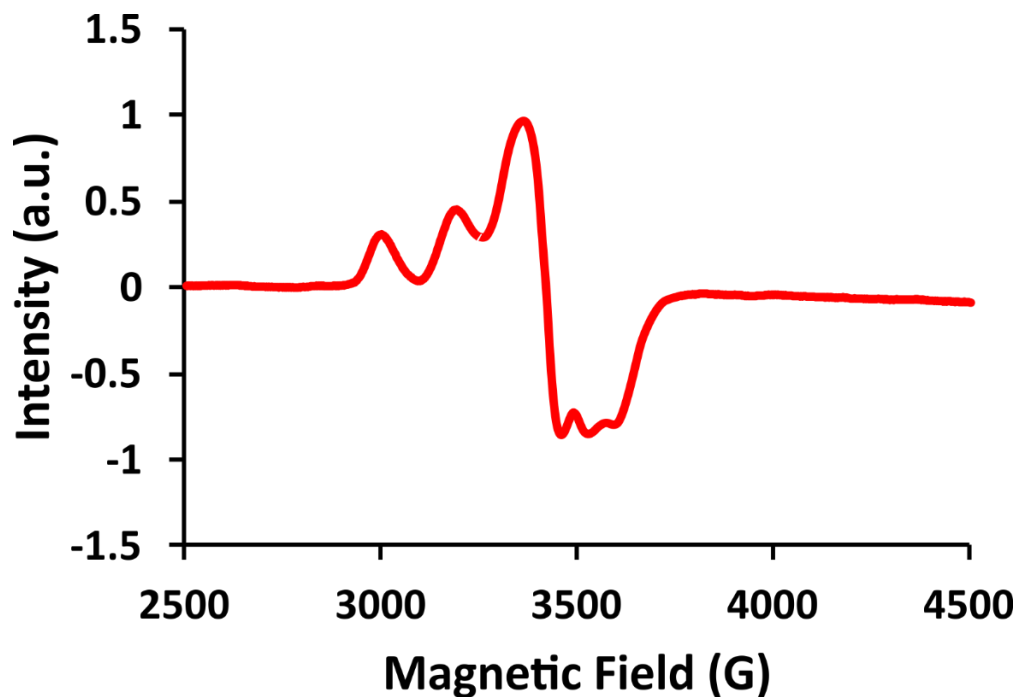


Figure B.39. Low temperature (77 K) EPR spectrum of **Cu-4** in DMF. Microwave frequency = 9.603 MHz, $g_{\parallel} = 2.09$, $g_{\perp} = 2.01$, $A_{\parallel} = 186$ G.

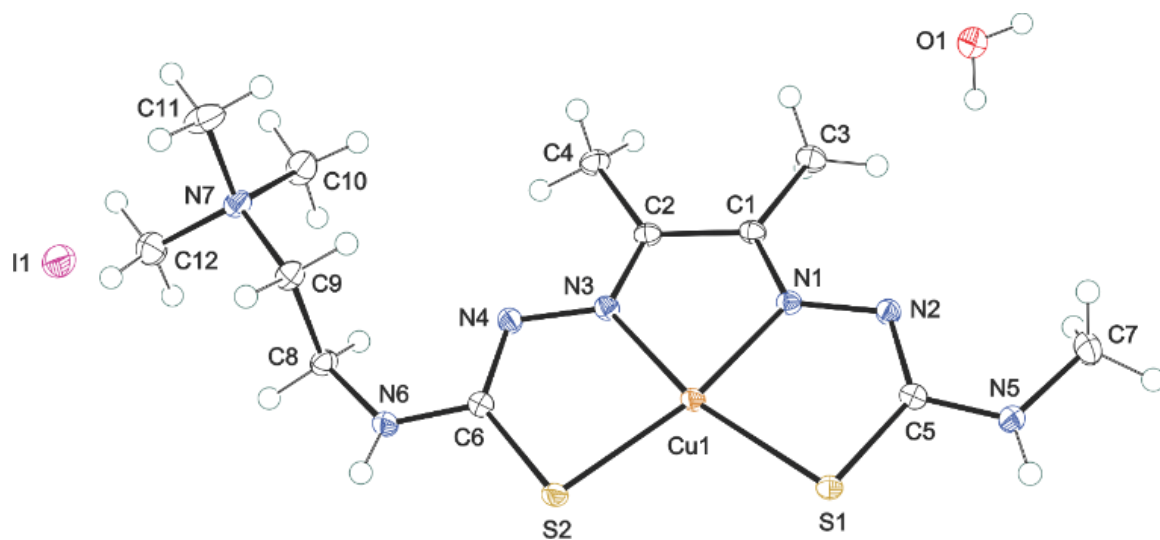


Figure B.40. ORTEP view (50% probability of **Cu-2** showing atom labeling for all non-hydrogen atoms in the asymmetric unit.

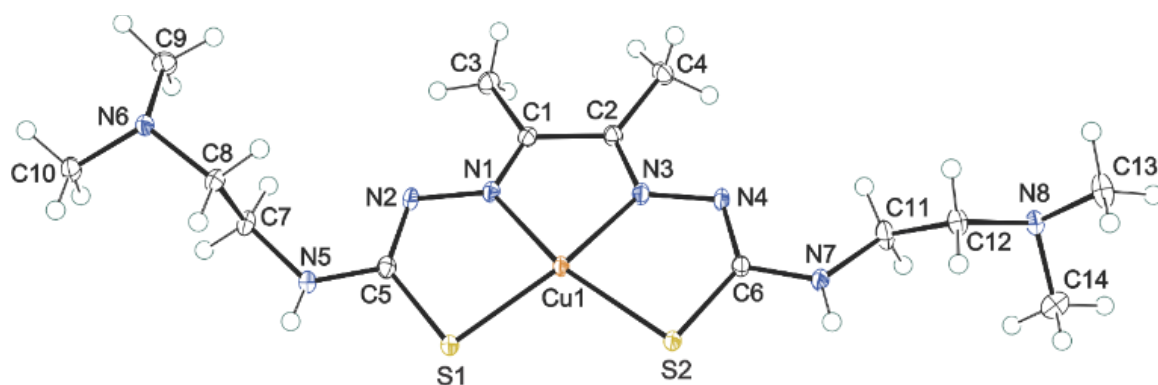


Figure B.41. ORTEP view (50% probability of **Cu-3** showing atom labeling for all non-hydrogen atoms in the asymmetric unit

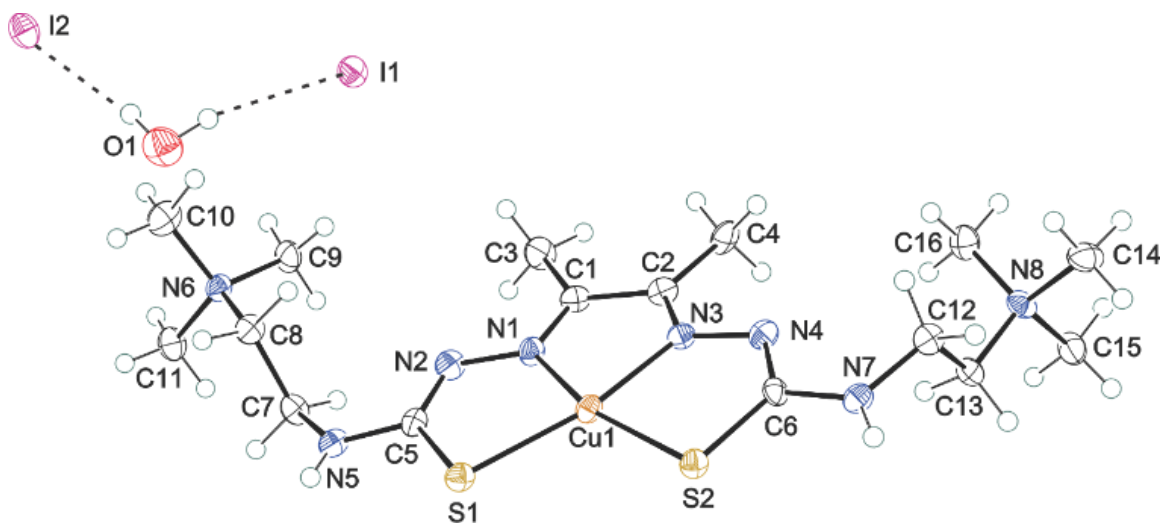


Figure B.42. ORTEP view (50% probability) of **Cu-4** showing atom labeling for all non-hydrogen atoms in the asymmetric unit

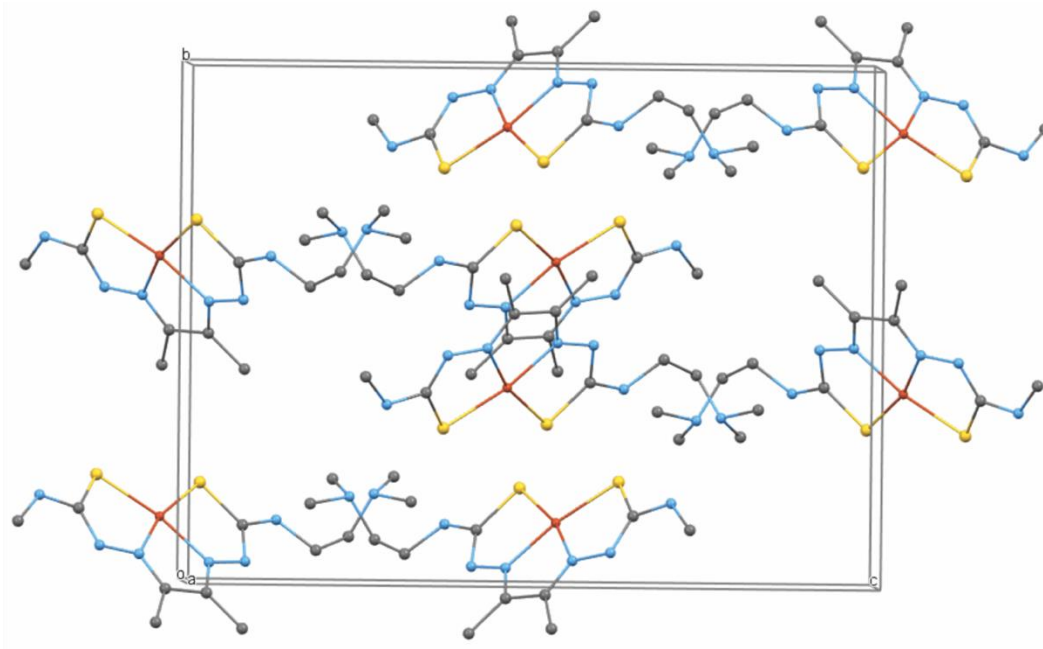


Figure B.43. Unit cell diagram of **Cu-1**. Hydrogens atoms are omitted for clarity.

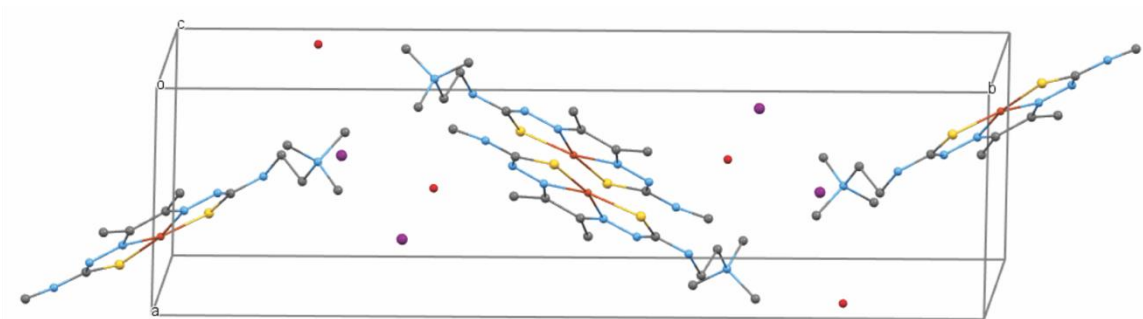


Figure B.44. Unit cell diagram of **Cu-2**. Hydrogens atoms are omitted for clarity.

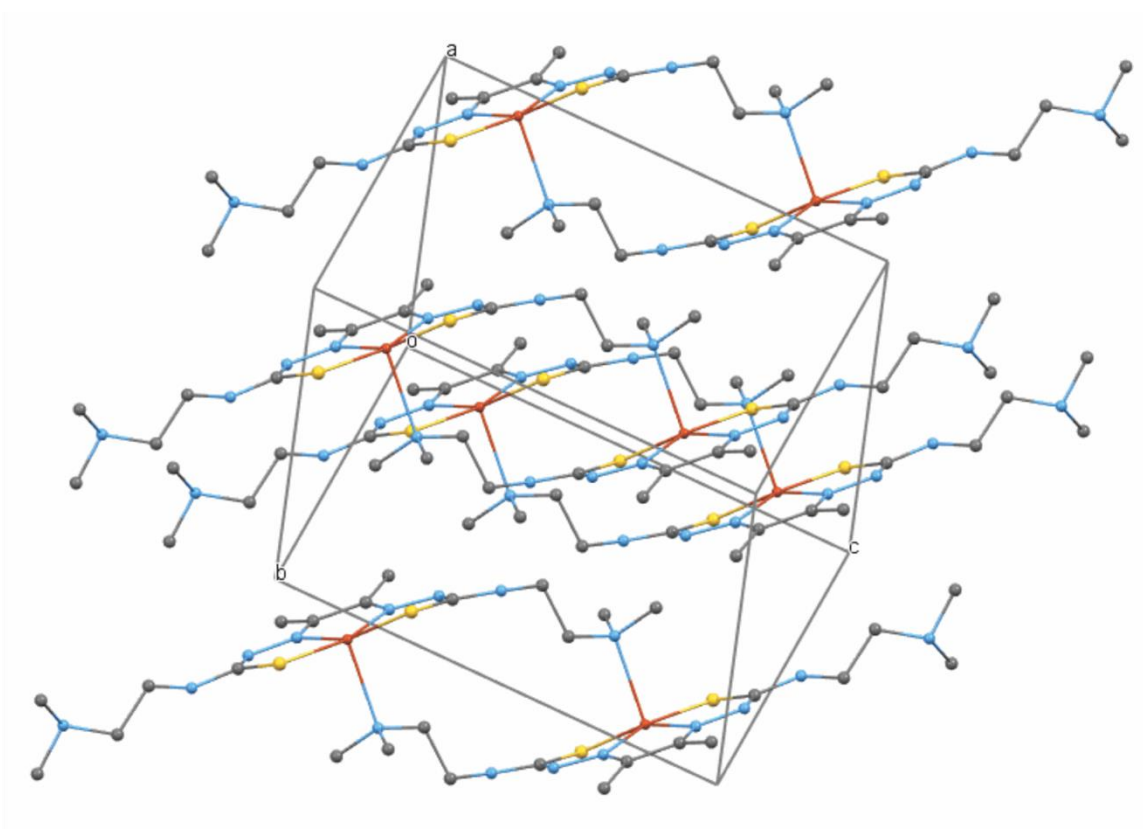


Figure B.45. Unit cell diagram of **Cu-3**. Hydrogens atoms are omitted for clarity.

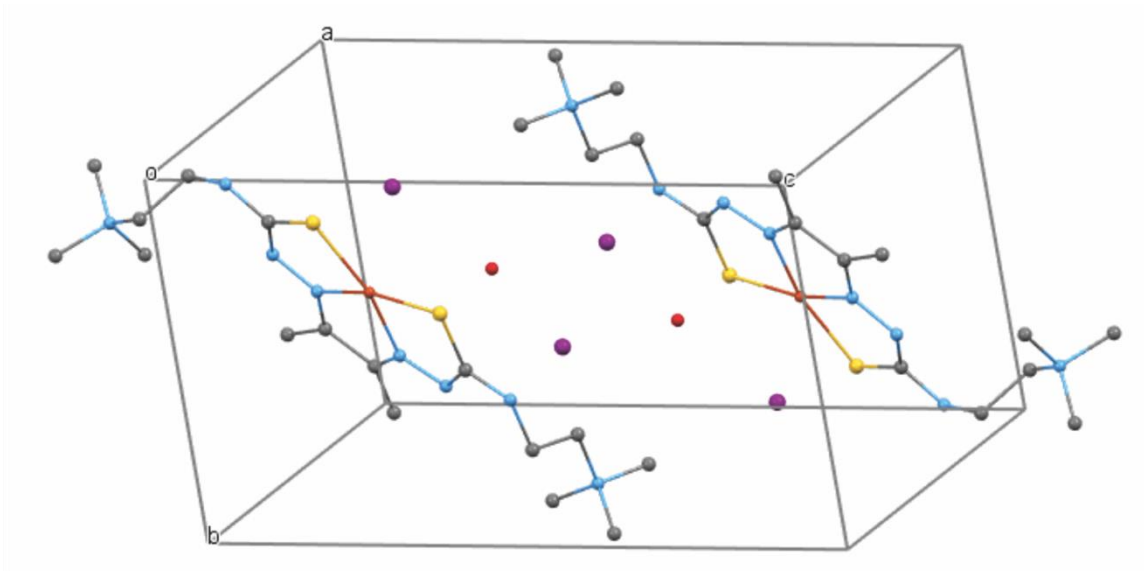


Figure B.46. Unit cell diagram of **Cu-4**. Hydrogens atoms are omitted for clarity.

Table B.1. Crystal Data and Structure Refinement for **Cu-1 – Cu-4**

Identification code	Cu-1	Cu-2	Cu-3	Cu-4
Empirical formula	C ₁₁ H ₂₁ CuN ₇ S ₂	C ₁₂ H ₂₄ CuN ₇ S ₂ .H ₂ O.I	C ₁₄ H ₂₈ CuN ₈ S ₂	C ₁₆ H ₃₄ CuN ₈ S ₂ .H ₂ O.2I
CCDC number	2013250	2013252	2013249	2013251
Formula weight	379.01	538.96	436.1	737.99
Temperature (K)	101.95(10)	102.05(10)	102(3)	101.9(2)
Wavelength (Å)	0.71073	0.71073	0.71073	0.71073
Crystal system	Orthorhombic	Monoclinic	Triclinic	Triclinic
Space group	<i>Pbca</i>	<i>P2₁/n</i>	<i>P</i> 1	<i>P</i> 1
Unit cell dimensions				
<i>a</i> (Å)	10.6564(4)	8.2819(4)	8.8712(3)	9.3519(5)
<i>b</i> (Å)	15.0501(6)	29.944(2)	9.1946(3)	9.7849(4)
<i>c</i> (Å)	20.1476(8)	8.9097(4)	12.8507(3)	15.2845(8)
α (deg)	90	90	95.544(2)	85.659(4)
β (deg)	90	115.093(6)	106.566(3)	73.253(4)
γ (deg)	90	90	107.451(3)	81.935(4)
<i>V</i> (Å ³)	3231.3(2)	2001.03(19)	939.24(5)	1325.16(11)
<i>Z</i>	8	4	2	2
<i>d</i> _{calcd} (Mg/m ³)	1.558	1.789	1.542	1.85
Absorption coefficient (mm ⁻¹)	1.614	2.858	1.401	3.335
F(000)	1576	1076	458	726
Crystal color, habit	orange plate	red-brown plate	red-brown prism	orange needle
Crystal size (mm ³)	0.20 x 0.20 x 0.01	0.42 x 0.20 x 0.05	0.30 x 0.17 x 0.05	0.40 x 0.03 x 0.01
θ range for data collection (deg)	3.38 to 27.22	3.25 to 33.60	3.38 to 30.18	3.30 to 27.34
Index ranges	- 13 ≤ <i>h</i> ≤ 13 - 16 ≤ <i>k</i> ≤ 16 - 25 ≤ <i>l</i> ≤ 25	- 12 ≤ <i>h</i> ≤ 12 - 46 ≤ <i>k</i> ≤ 46 - 13 ≤ <i>l</i> ≤ 13	- 12 ≤ <i>h</i> ≤ 12 - 13 ≤ <i>k</i> ≤ 13 - 18 ≤ <i>l</i> ≤ 18	- 12 ≤ <i>h</i> ≤ 12 - 12 ≤ <i>k</i> ≤ 12 - 19 ≤ <i>l</i> ≤ 19
Reflections collected	16683	33362	27814	11440
Independent reflections	3600 [R(int) = 0.0603]	7885 [R(int) = 0.0348]	5554 [R(int) = 0.0326]	11440 [R(int) = 0.0000]
Completeness to theta max (%)	99.8	99.6	99.9	99.5
Absorption correction	multi-scan	multi-scan	multi-scan	multi-scan
Max. and min transmission	1.000 and 0.928	1.000 and 0.624	1.000 and 0.922	1.000 and 0.796
Refinement method	full-matrix least-squares on F ²	full-matrix least-squares on F ²	full-matrix least-squares on F ²	full-matrix least-squares on F ²
Data/restraints/parameters	3600 / 0 / 274	7885 / 0 / 305	5554 / 0 / 338	11440 / 3 / 293
Goodness of fit on F ²	1.078	1.078	1.05	1.133
Final R indices [<i>I</i> > 2σ(<i>I</i>)] ^{a,b}	R1 = 0.0404, wR2 = 0.0765	R1 = 0.0289, wR2 = 0.0564	R1 = 0.0234, wR2 = 0.0539	R1 = 0.0733, wR2 = 0.1736
<i>R</i> indices (all data) ^{a,b}	R1 = 0.0641, wR2 = 0.0849	R1 = 0.0392, wR2 = 0.0600	R1 = 0.0279, wR2 = 0.0564	R1 = 0.0993, wR2 = 0.1833
Largest diff. peak and hole (e · Å ⁻³)	0.544 and -0.498	1.065 and -0.666	0.449 and -0.317	4.067 and -1.658

[a] R1 = $\Sigma||F_o| - |F_c||/\Sigma|F_o|$. [b] wR2 = $\{\Sigma[w(F_o2 - F_c2)^2]/\Sigma[w(F_o2)^2]\}^{1/2}$, where $w = q/\sigma^2(F_o2) + (qp)^2 + bp$. GOF = $S = \{\Sigma[w(F_o2 - F_c2)^2]/(n - p)\}^{1/2}$, where *n* is the number of reflections and *p* is the number of parameters refined.

Table B.2 Selected Bond Distances (Å) and Angles (deg) for **Cu-1 – Cu-4**.

Bond Distances	Cu-1	Cu-2	Cu-3	Cu-4
Cu1-N1	1.967(2)	1.9732(13)	1.9820(10)	1.966(6)
Cu1-N3	1.960(2)	1.9562(14)	1.9647(11)	1.956(6)
Cu1-S1	2.2394(7)	2.2574(5)	2.2650(3)	2.258(2)
Cu1-S2	2.2392(8)	2.2709(4)	2.2929(3)	2.267(2)
S1-C5	1.766(3)	1.7615(16)	1.7555(13)	1.755(7)
S2-C6	1.753(3)	1.7491(17)	1.7575(12)	1.762(7)
N1-C1	1.294(3)	1.300(2)	1.3007(16)	1.284(10)
N1-N2	1.375(3)	1.3626(19)	1.3701(14)	1.359(9)
N2-C5	1.323(4)	1.326(2)	1.3284(16)	1.304(10)
N3-C2	1.296(3)	1.298(2)	1.2979(16)	1.276(10)
N3-N4	1.368(3)	1.3618(19)	1.3703(14)	1.360(9)
N4-C6	1.336(3)	1.324(2)	1.3199(16)	1.316(10)
C1-C2	1.475(4)	1.474(2)	1.4756(16)	1.474(11)
Bond Angles	Cu-1	Cu-2	Cu-3	Cu-4
N3-Cu1-N1	80.65(9)	80.02(6)	80.22(4)	79.1(3)
N3-Cu1-S1	165.89(7)	163.91(4)	157.97(3)	164.25(19)
N1-Cu1-S1	85.25(7)	84.70(4)	83.65(3)	85.14(19)
N3-Cu1-S2	85.62(7)	85.24(4)	83.70(3)	85.03(19)
N1-Cu1-S2	165.52(7)	164.14(4)	162.39(3)	163.59(19)
S1-Cu1-S2	108.47(3)	109.343(16)	109.740(12)	110.67(8)

Appendix C. Determination of Diffusion Coefficient (D_0) for Ni-1

Using the Randles-Sevcik equation,

$$i_p = 0.4463[cat] \sqrt{FvD/RT} \quad (1)$$

Plotting peak current (i_p) versus the square root of the scan rate (v)^{1/2}

$$\text{Slope} = 0.4463FA [cat] [(FD_0/RT)]^{0.5}$$

$$\text{Slope} \equiv 2.7661E-5 = 0.4463FA [cat] [(FD_0/RT)]^{0.5}$$

$$A = 0.071 \text{ cm}^2, [cat] = 3E-7 \text{ moles/cm}^3, F = 96485 \text{ C/mole } e^-.$$

$$R = \text{ideal gas constant}, T = 298 \text{ K}.$$

$$D_0 = 2.34E-5 \text{ cm}^2/\text{s}.$$

Appendix D. Electrochemical Studies and Catalytic Activity Determination of Metal BTSCs

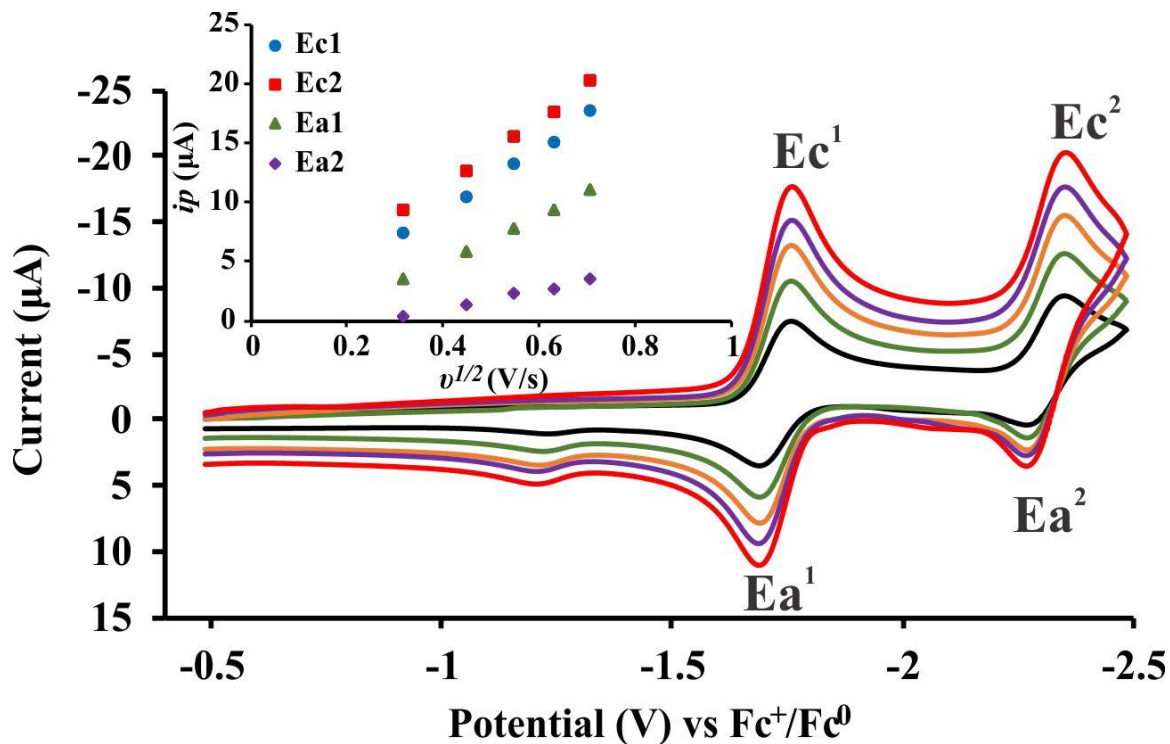


Figure D.1. a) Scan rate dependent CVs of Ni-1 recorded at scan rates of 0.1 (black), 0.2, 0.3, 0.4, and 0.5 V/s (red) in 0.1 M $\text{Bu}_4\text{NPF}_6/\text{MeCN}$ solution. b) Cottrell plot of peak current versus the square root of scan rate.

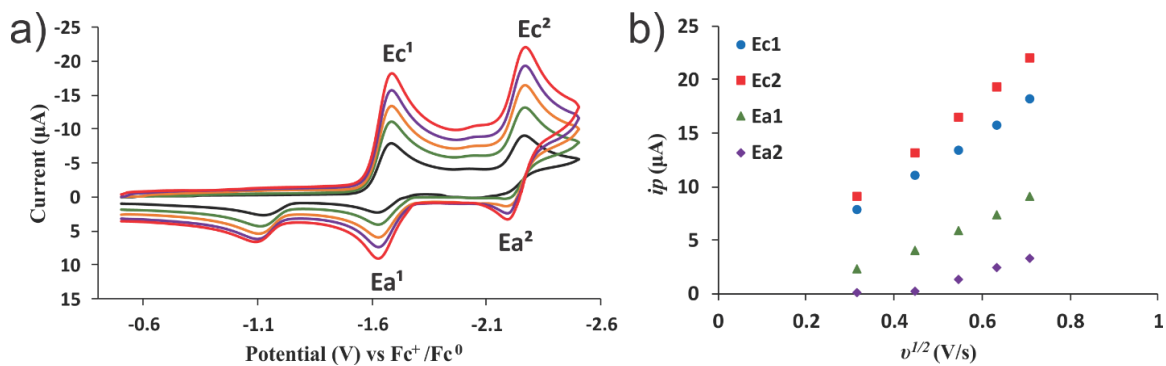


Figure D.2. a) Scan rate dependent CVs of Ni-2 recorded at scan rates of 0.1 (black), 0.2, 0.3, 0.4, and 0.5 V/s (red) in 0.1 M $\text{Bu}_4\text{NPF}_6/\text{MeCN}$ solution. b) Cottrell plot of peak current versus the square root of scan rate.

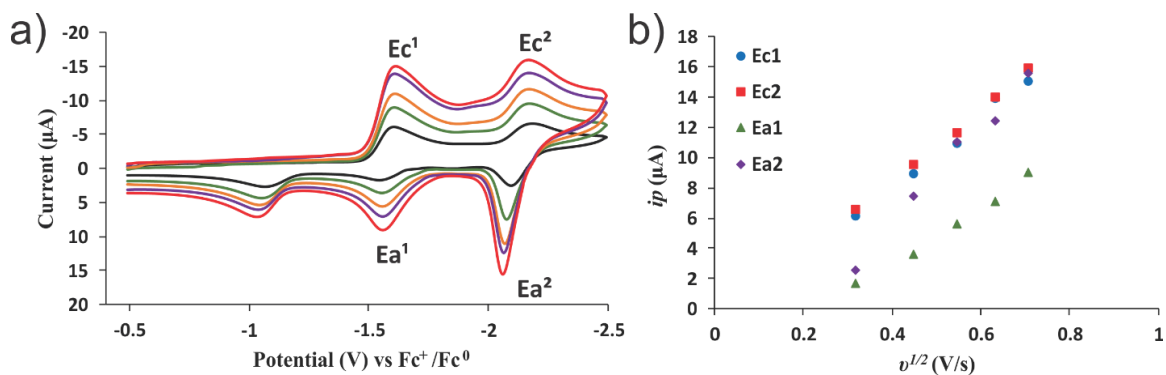


Figure D.3. a) Scan rate dependent CVs of Ni-4 recorded at scan rates of 0.1 (black), 0.2, 0.3, 0.4, and 0.5 V/s (red) in 0.1 M $\text{Bu}_4\text{NPF}_6/\text{MeCN}$ solution. b) Cottrell plot of peak current versus the square root of scan rate.

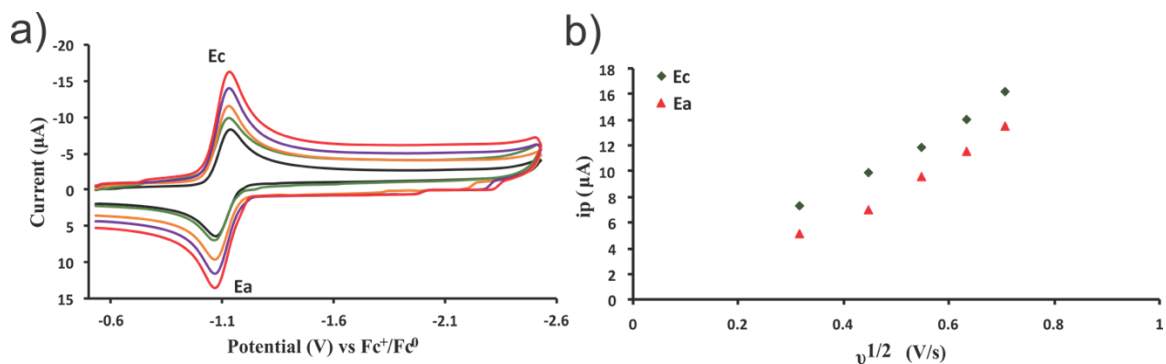


Figure D.4. a) Scan rate dependent CVs of Cu-1 recorded at scan rates of 0.1 (black), 0.2, 0.3, 0.4, and 0.5 V/s (red) in 0.1 M $\text{Bu}_4\text{NPF}_6/\text{MeCN}$ solution. b) Cottrell plot of peak current versus the square root of scan rate (b).

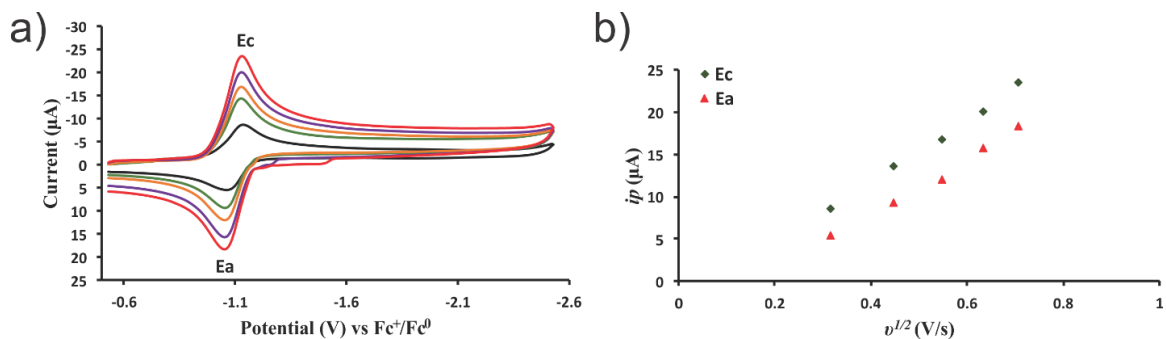


Figure D.5. a) Scan rate dependent CVs of Cu-2 recorded at scan rates of 0.1 (black), 0.2, 0.3, 0.4, and 0.5 V/s (red) in 0.1 M $\text{Bu}_4\text{NPF}_6/\text{MeCN}$ solution. b) Cottrell plot of peak current versus the square root of scan rate.

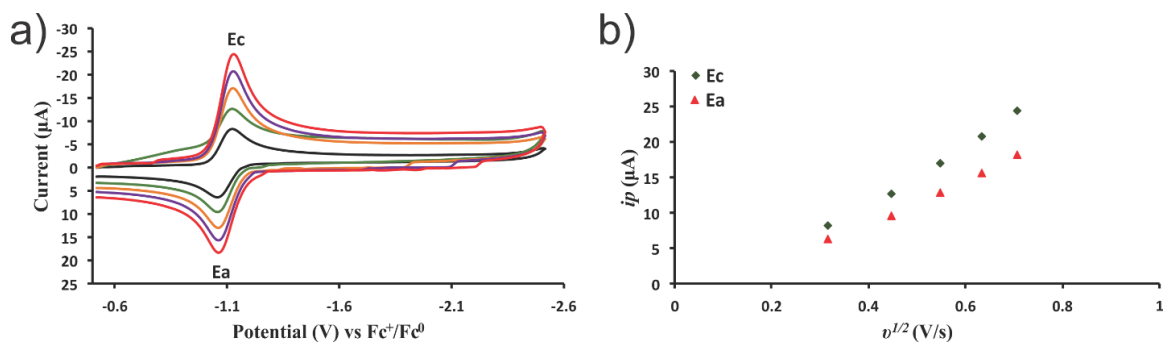


Figure D.6. a) Scan rate dependent CVs of **Cu-3** recorded at scan rates of 0.1 (black), 0.2, 0.3, 0.4, and 0.5 V/s (red) in 0.1 M $\text{Bu}_4\text{NPF}_6/\text{MeCN}$ solution. b) Cottrell plot of peak current versus the square root of scan rate.

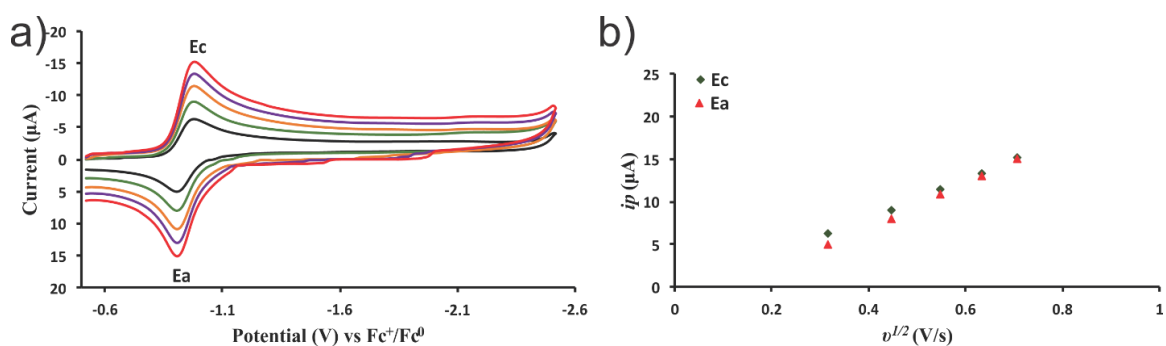


Figure D.7. a) Scan rate dependent CVs of **Cu-4** recorded at scan rates of 0.1 (black), 0.2, 0.3, 0.4, and 0.5 V/s (red) in 0.1 M $\text{Bu}_4\text{NPF}_6/\text{MeCN}$ solution. b) Cottrell plot of peak current versus the square root of scan rate.

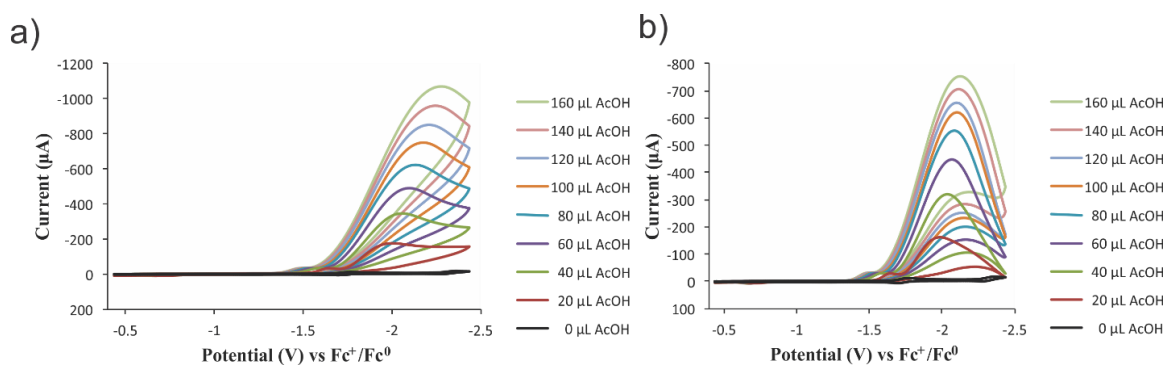


Figure D.8. CVs of 0.3 mM **Ni-1** in MeCN solution with 0.1 M Bu_4NPF_6 collected at scan rate of 200 mV/s with 0, 20, 40, 60, 80, 100, 120, 140, 160 μL CH_3COOH a) without acid blanks subtracted and b) with acid blanks subtracted.

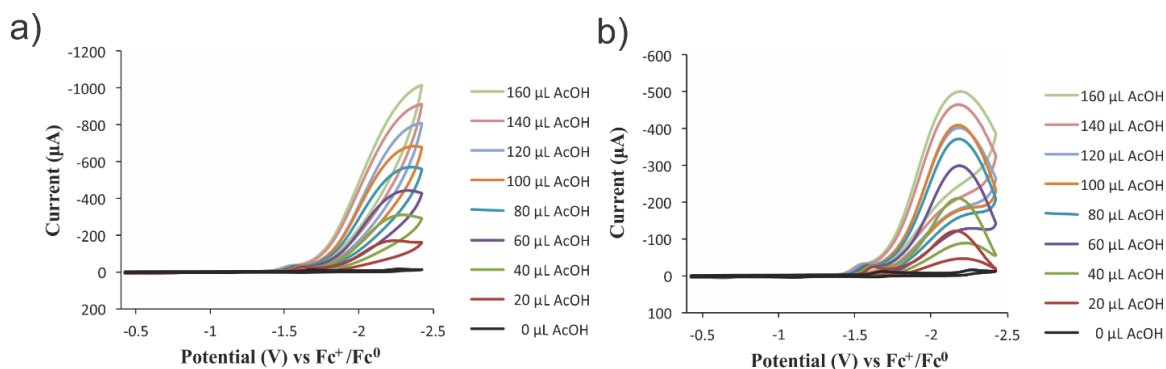


Figure D.9. CVs of 0.3 mM Ni-2 in MeCN solution with 0.1 M Bu₄NPF₆ collected at scan rate of 200 mV/s with 0, 20, 40, 60, 80, 100, 120, 140, 160 µL CH₃COOH a) without acid blanks subtracted and b) with acid blanks subtracted .

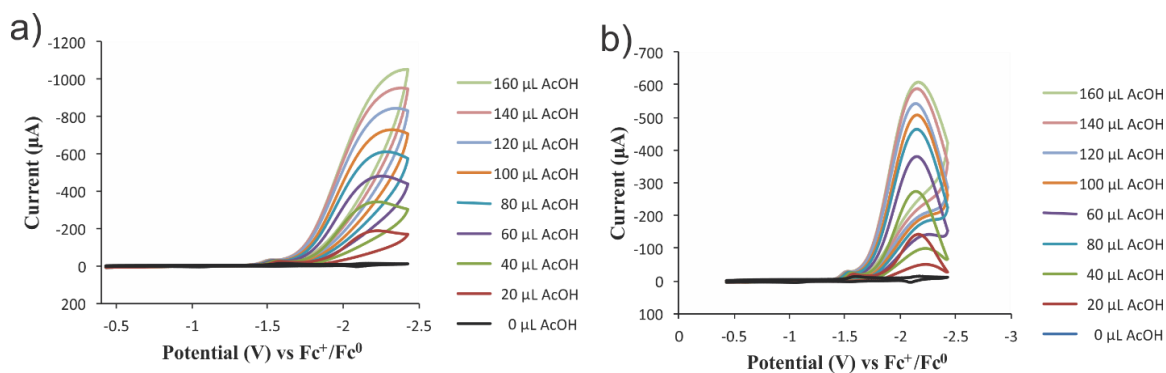


Figure D.10. CVs of 0.3 mM Ni-4 in MeCN solution with 0.1 M Bu₄NPF₆ collected at scan rate of 200 mV/s with 0, 20, 40, 60, 80, 100, 120, 140, 160 µL CH₃COOH a) without acid blanks subtracted and b) with acid blanks subtracted.

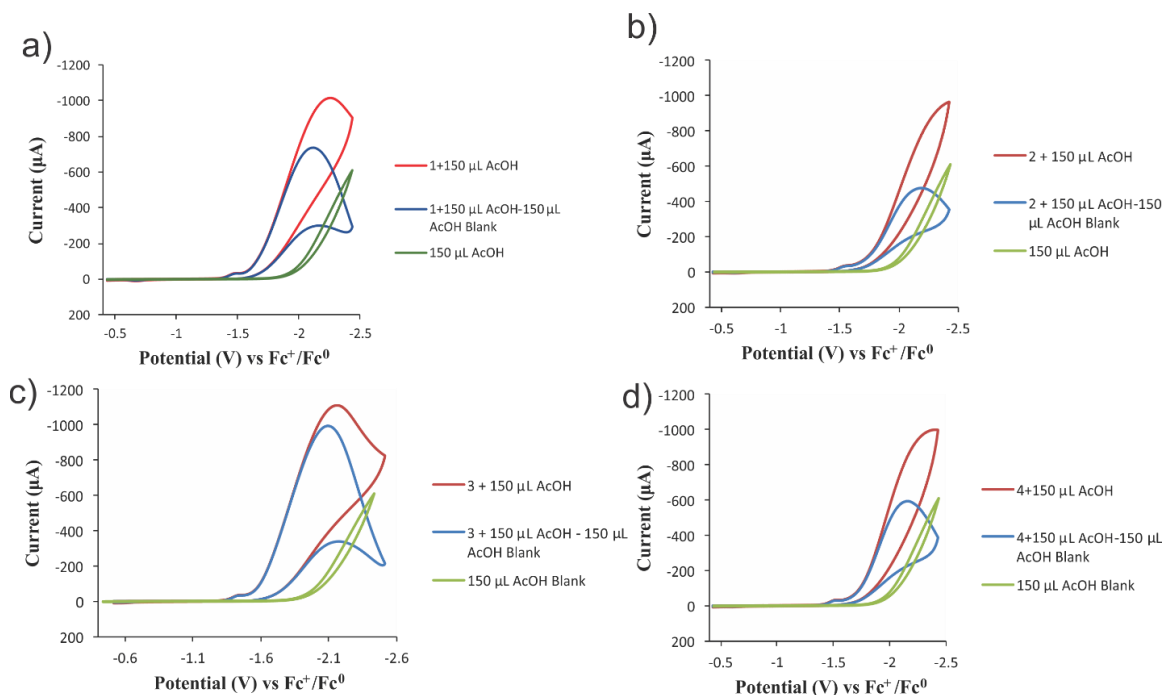


Figure D.11. CVs of 0.3 mM Ni-1 (a), Ni-2 (b), Ni-3 (c), and Ni-4 (d) in MeCN solution with 0.1 M Bu₄NPF₆ collected at scan rate of 200 mV/s with 150 µL CH₃COOH (100 mM) without acid blank subtracted (red), with acid blank subtracted (blue), and 150 µL CH₃COOH blank (green).

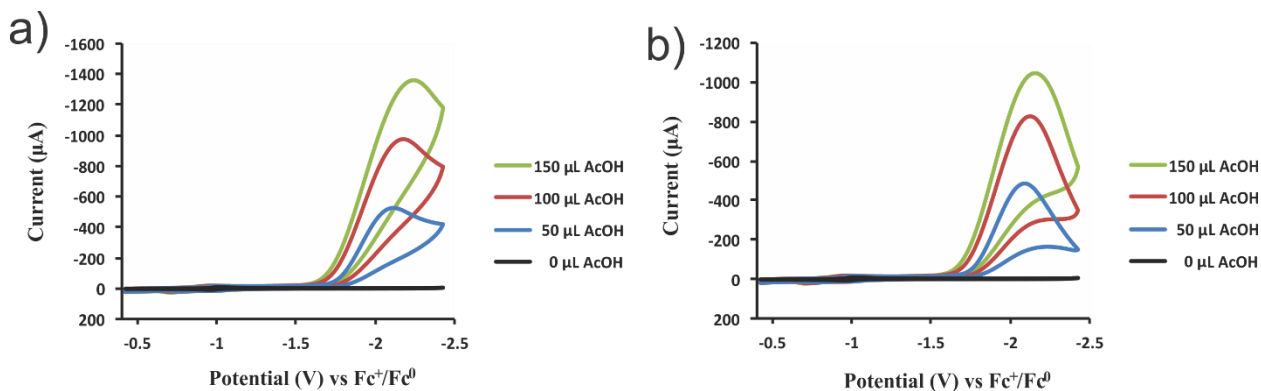


Figure D.12. CVs of 0.3 mM complex Cu-1 in MeCN solution with 0.1 M Bu₄NPF₆ collected at scan rate of 200 mV/s with 0, 50, 100, 150 µL CH₃COOH without acid blanks subtracted (a) and with acid blanks subtracted (b).

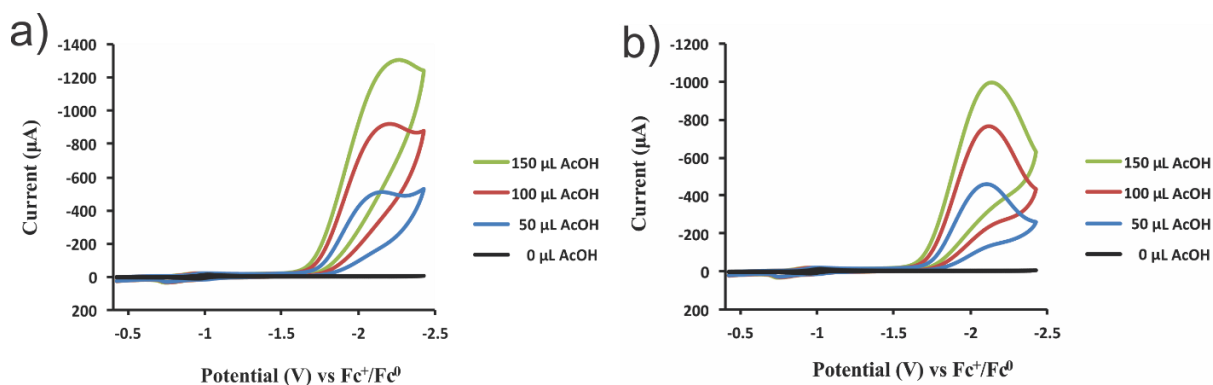


Figure D.13. CVs of 0.3 mM complex **Cu-2** in MeCN solution with 0.1 M Bu_4NPF_6 collected at scan rate of 200 mV/s with 0, 50, 100, 150 μL CH_3COOH without acid blanks subtracted (a) and with acid blanks subtracted (b).

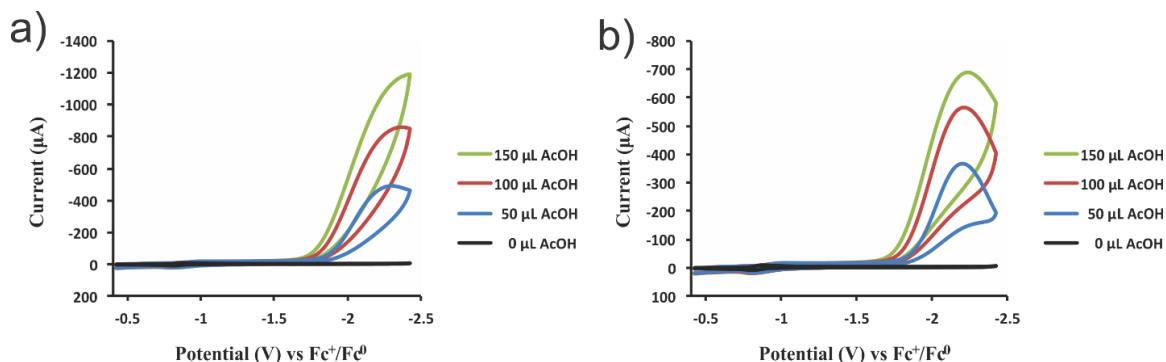


Figure D.14. CVs of 0.3 mM complex **Cu-4** in MeCN solution with 0.1 M Bu_4NPF_6 collected at scan rate of 200 mV/s with 0, 50, 100, 150 μL CH_3COOH without acid blanks subtracted (a) and with acid blanks subtracted (b).

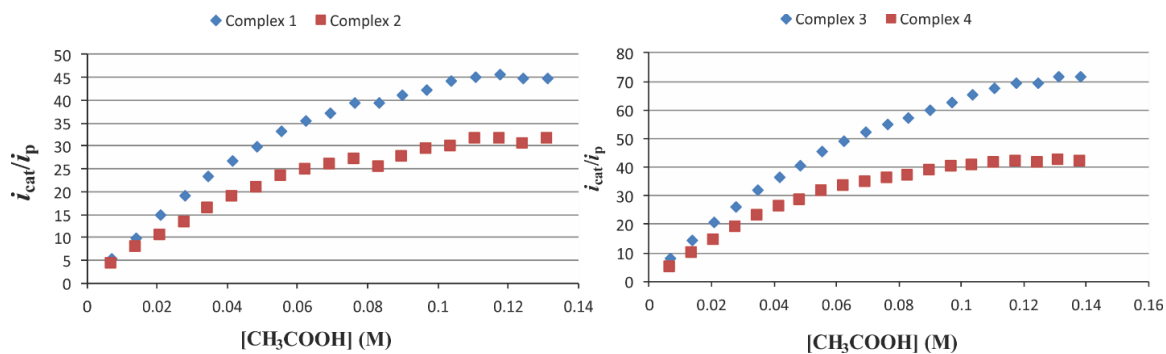


Figure D.15. The catalytic to peak current ratio (i_{cat}/i_p) vs acid concentration for **Ni-1-4**.

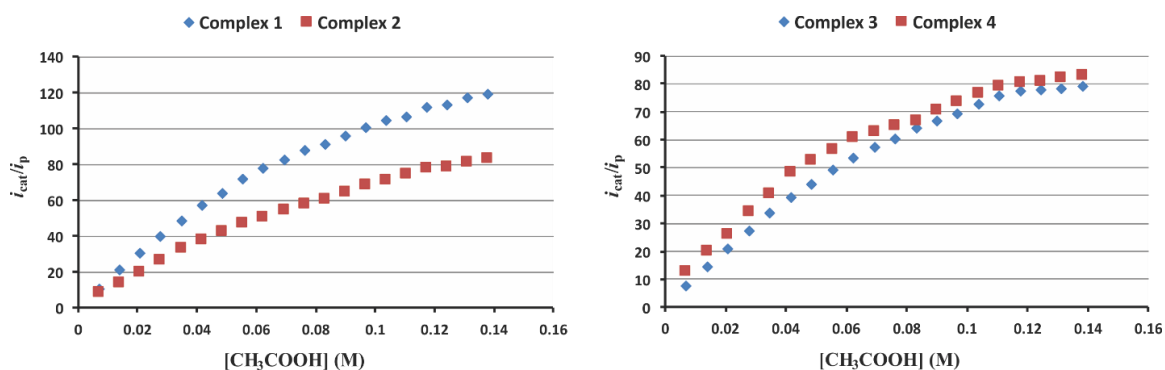


Figure D.16. The catalytic to peak current ratio (i_{cat}/i_p) vs acid concentration for **Cu-1** – **Cu-4**.

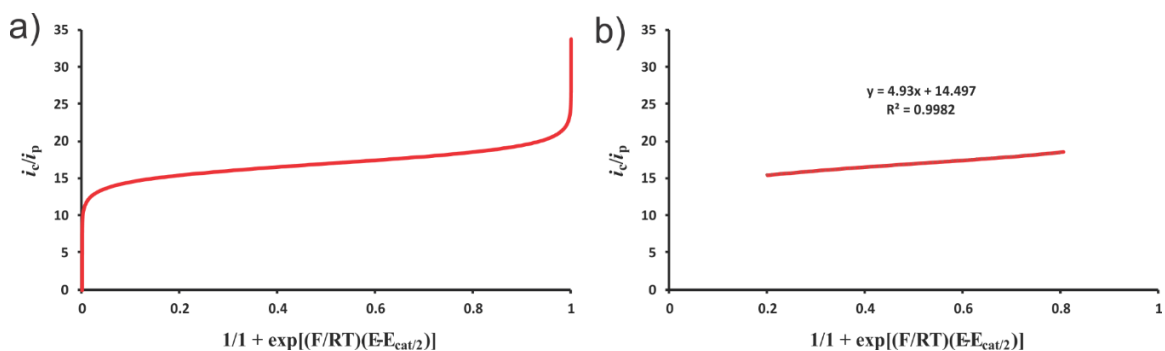


Figure D.17. a) Plot of *foot-of-the-wave analysis* (FOWA) for **Ni-1**. b) Linear region from 0.2 to 0.8 was plotted and slope was calculated.

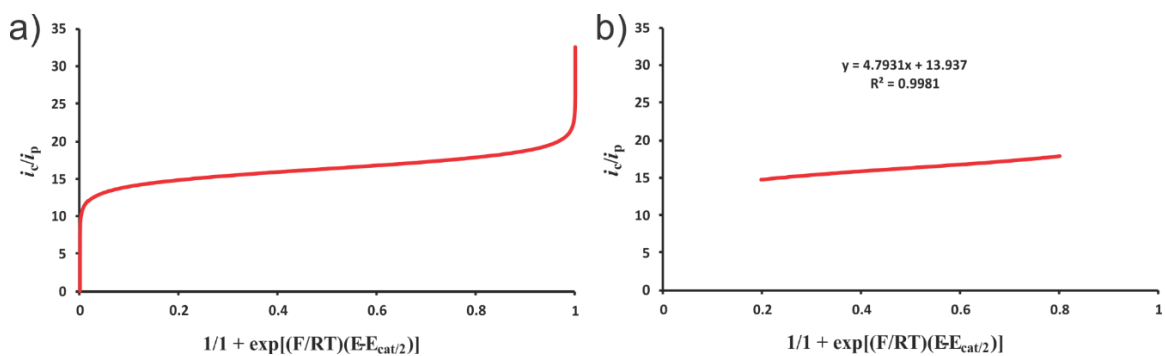


Figure D.18. a) Plot of *foot-of-the-wave analysis* (FOWA) for **Ni-2**. b) Linear region from 0.2 to 0.8 was plotted and slope was calculated.

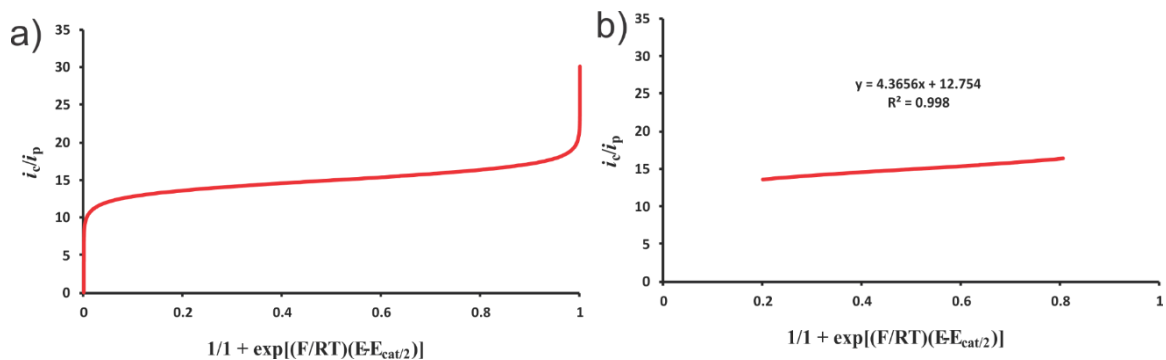


Figure D.19. a) Plot of *foot-of-the-wave analysis* (FOWA) for Ni-3. b) Linear region from 0.2 to 0.8 was plotted and slope was calculated.

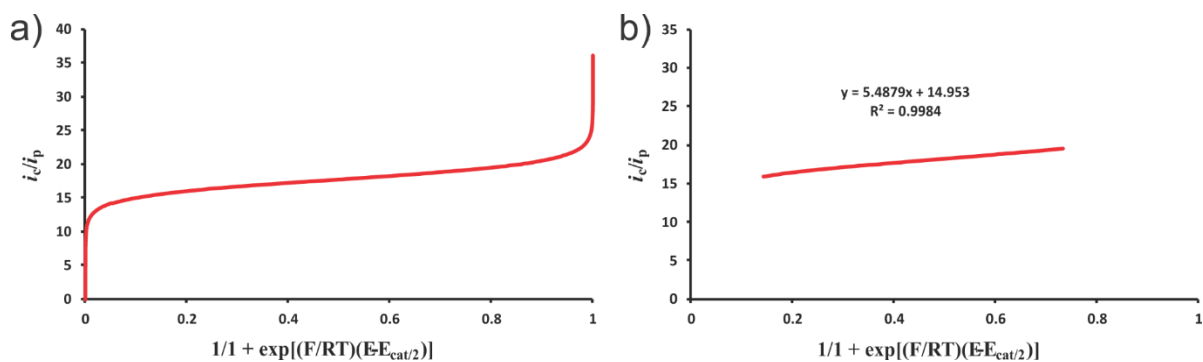


Figure D.20. a) Plot of *foot-of-the-wave analysis* (FOWA) for Ni-4. b) Linear region from 0.2 to 0.8 was plotted and slope was calculated.

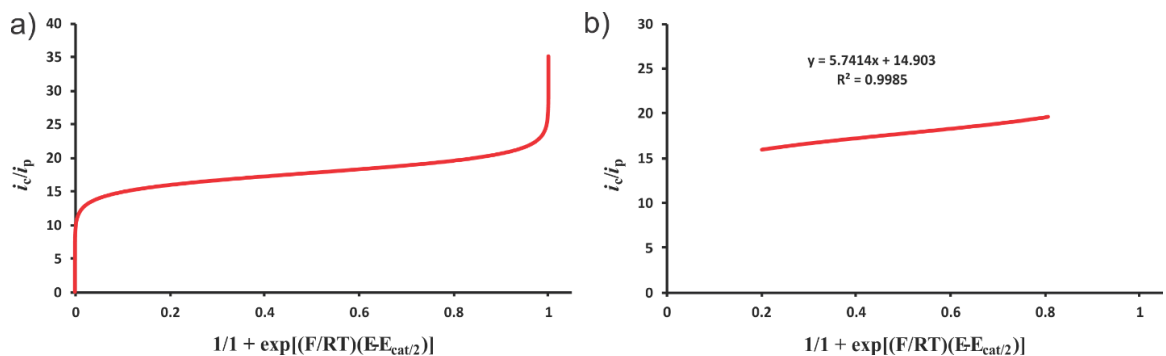


Figure D.21. a) Plot of *foot-of-the-wave analysis* (FOWA) for NiATSM. b) Linear region from 0.2 to 0.8 was plotted and slope was calculated.

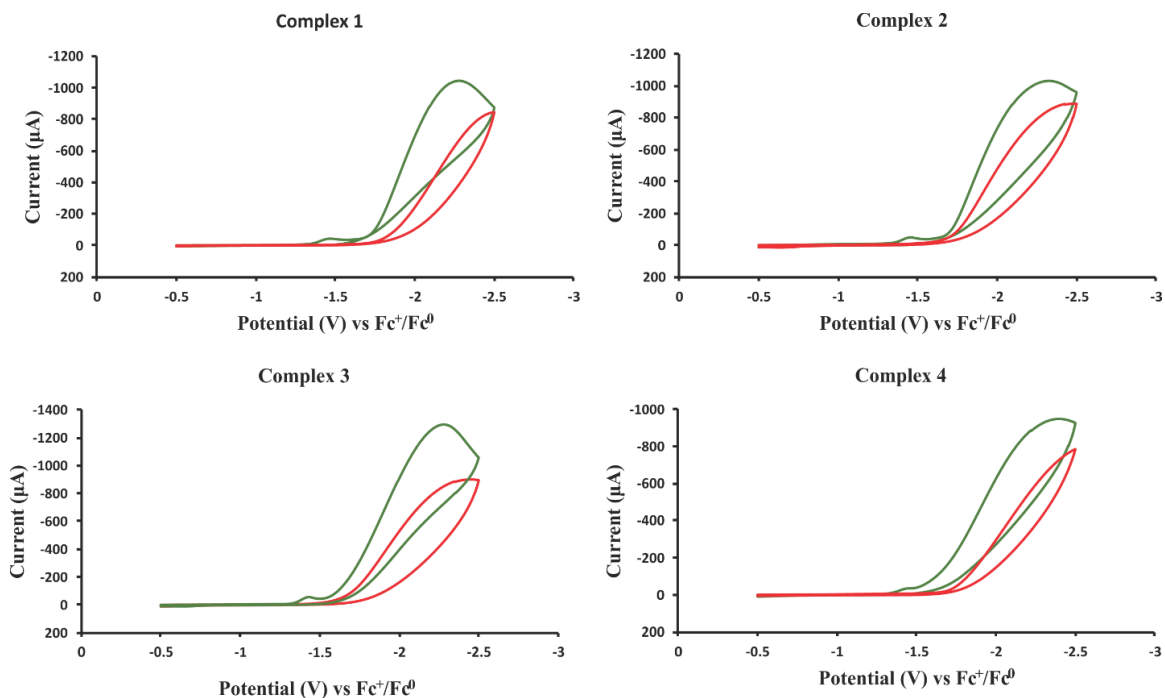


Figure D.22. CVs recorded before the CPC on 0.3 mM of **Ni-1 – Ni-4** in 0.1 M $\text{Bu}_4\text{NPF}_6/\text{CH}_3\text{CN}$ solution (in green) and 100 mM CH_3COOH . CVs recorded after the CPC in 0.1 M $\text{Bu}_4\text{NPF}_6/\text{CH}_3\text{CN}$ solution and 100 mM CH_3COOH (in red).

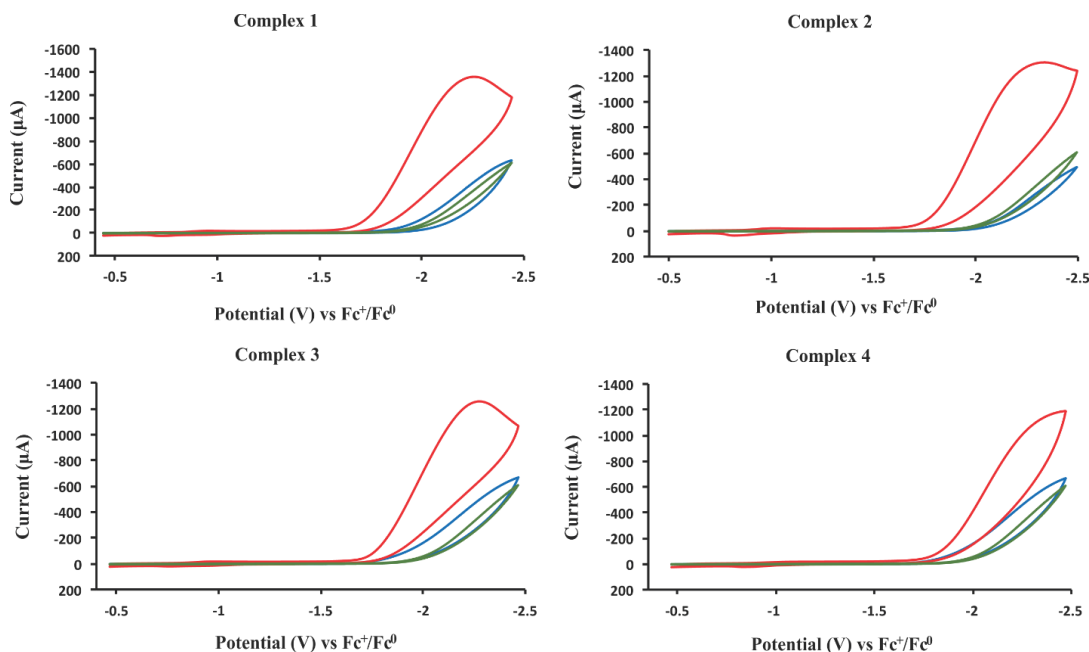


Figure D.23. CVs recorded before the CPC on 0.3 mM of **Cu-1 – Cu-4** in 0.1 M $\text{Bu}_4\text{NPF}_6/\text{CH}_3\text{CN}$ solution and 100 mM CH_3COOH (in red), after the CPC in 0.1 M $\text{Bu}_4\text{NPF}_6/\text{CH}_3\text{CN}$ solution and 100 mM CH_3COOH (in blue), and acid blank 0.1 M $\text{Bu}_4\text{NPF}_6/\text{CH}_3\text{CN}$ solution and 100 mM CH_3COOH (in green).

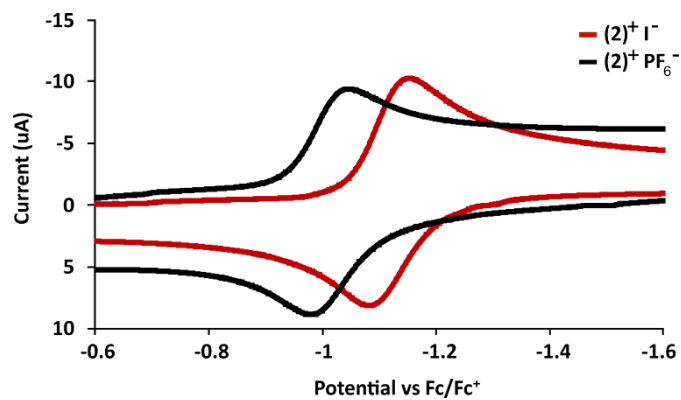


Figure D.24. CVs of **Cu-2** (red) and **Cu-2*** (black) in 0.1 M Bu₄NPF₆/MeCN.

Appendix E. Overpotential Determination

Overpotential (η) values were calculated using the method described by Fourmond et al.⁵⁹ as detailed below. The overpotential is the difference in the catalytic half-wave potential ($E_{cat/2}$) and the reference potential (E_{ref}) for the uncatalyzed reaction (eq. 1).

$$\eta = E_{cat/2} - E_{ref} \quad (1)$$

The value of E_{ref} is dependent on the standard reduction potential of the substrate (E_{H^+/H_2}°), the pK_a , homoconjugation equilibrium constant (K_C), and concentration (C_0) of the acid, the solubility of H_2 ($C_{H_2}^\circ$), and the diffusion of the products with respect to the reactants (ε_D) in the solvent of interest. For the acid saturated conditions (100 mM acetic acid) experiments described in the current manuscript, the relevant values are:

$$\begin{aligned} pK_a &= 2.35^{92} \\ K_C &= 5012^{59} \\ C_0 &= 0.100 \text{ M} \\ C_{H_2}^\circ &= 0.0033 \text{ M}^{59} \\ \varepsilon_D &= 0.040 \text{ V}^{59} \end{aligned}$$

In cases where homoconjugation is non-existent or negligible, E_{ref} is equal to the theoretic half-wave potential ($E_{1/2}^T$) associated with the reduction of the acid AH (eq. 2). The value of $E_{1/2}^T$ can be calculated using equation 3.



$$E_{1/2}^T = E_{H^+/H_2}^\circ - (2.303RT/F)pK_a + \varepsilon_D - (RT/2F)\ln(C_0/C_{H_2}^\circ) \quad (3)$$

For cases where homoconjugation (eq. 4) is substantial, E_{ref} is equal to the theoretic half-wave potential ($E_{1/2(AH/AHA^-)}^T$) associated with equation 5, which is the sum of equations 2 and 4. The value of $E_{1/2(AH/AHA^-)}^T$ can be calculated using equation 6.



$$E_{1/2(AH/AHA^-)}^T = E_{H^+/H_2}^\circ - (2.303RT/F)pK_a + \varepsilon_D + (RT/2F)\ln(2K_C^2 C_0 C_{H_2}^\circ) \quad (6)$$

As stated by Fourmond et al., the correct value of E_{ref} is given by the maximum (least negative) value of $E_{1/2}^T$ and $E_{1/2(AH/AHA^-)}^T$. For the specific conditions noted above, the calculated values are:

$$\begin{aligned} E_{1/2}^T &= -1.46 \text{ V} \\ E_{1/2(AH/AHA^-)}^T &= -1.30 \text{ V} \\ \therefore E_{ref} &= E_{1/2(AH/AHA^-)}^T = -1.30 \text{ V} \end{aligned}$$

Appendix F. Turnover Frequency Determination

Turnover frequency (TOF) values were calculated the peak current method employed by Haddad et al. for Cu(ATSM).⁸ The TOF can be calculated from the peak current of the catalyst in the absence (i_p) and presence of substrate (i_{cat}) as summarized below.

In the absence of substrate, the peak current is dependent on the catalyst concentration ([cat]) and diffusion coefficient (D), the scan rate (v), and the area of the electrode (A) as defined by the Randle-Sevick equation (eq. 1). The factor of 0.4463 is related to the diffusion equations,⁹³ R is the gas constant, and T is temperature in K.

$$i_p = 0.4463FA[cat]\sqrt{\frac{FvD}{RT}} \quad (1)$$

In the presence of substrate, the peak current is also dependent on the concentration of the substrate. Equation 2 details the relationship between the catalytic current i_{cat} , the catalyst concentration [cat], and the acid concentration $[H^+]$ for a catalytic reaction that is second-order in acid and first-order in catalyst.⁹⁴

$$i_{cat} = nFA[cat]\sqrt{Dk[H^+]^2} \quad (2)$$

Thus, the ratio of i_{cat}/i_p (eq. 9) is obtained by dividing equation 3 by equation 2. In this form, the terms A and D are eliminated and do not need to be accurately determined.

$$\frac{i_{cat}}{i_p} = \frac{n}{0.4463} \sqrt{\frac{RTk[H^+]^2}{Fv}} \quad (3)$$

Under pseudo first-order conditions where $k_{obs} = k[H^+]^2$ and equation 3 simplifies to 4.⁹⁵

$$\frac{i_{cat}}{i_p} = \frac{n}{0.4463} \sqrt{\frac{RTk_{obs}}{Fv}} \quad (4)$$

Equation 4 can be simplified further to equation 11 when $n = 2$. When at scan rate independent conditions, equation 11 can be used to estimate the observed rate constant or TOF.

$$TOF = k_{obs} = 1.94 \times v \left[\frac{i_{cat}}{i_p} \right]^2 \quad (5)$$

Equations 1 - 5 are used for TOF estimation for electrocatalysts under “pure kinetic conditions” where plateau current is easily observable as an S-shaped wave that is scan rate independent. Although S-shaped waves are not obtained in this work, the equations do provide an initial assessment of catalytic activity.⁹⁶

The TOF values and relevant parameters for their determination for **Cu-1** to **Cu-4** are provided in table below.

Complex	i_p, mA	i_{cat}, mA	$v, V s^{-1}$	TOF, s^{-1}
(Cu)ATSM	6.2	983	0.2	9500
Cu-1	6.3	1022	0.2	10300
Cu-2	6.4	1007	0.2	9400
Cu-3	5.5	976	0.2	12000
Cu-4	6.4	963	0.2	8700

Appendix G. TON Calculations for Ni-1

$$q_{\text{total}} = q_{\text{cat}} - q_{\text{blank}} = 22.72 \text{ C} - 15.05 \text{ C} = 7.67$$

Theoretical moles of hydrogen produced through q_{total} :

$$7.67 \text{ C} \times (1 \text{ mol e}^- / 96485 \text{ C}) \times (1 \text{ mol H}_2 / 2 \text{ mol e}^-) = 0.0000397$$

$$\text{TON} = \text{Theoretical moles of H}_2 / \text{Moles of catalyst used} = 0.0000397 / 0.000003 = 13$$

Appendix H. Photoelectric Characterization of Metal BTSC Attached to Various Surfaces

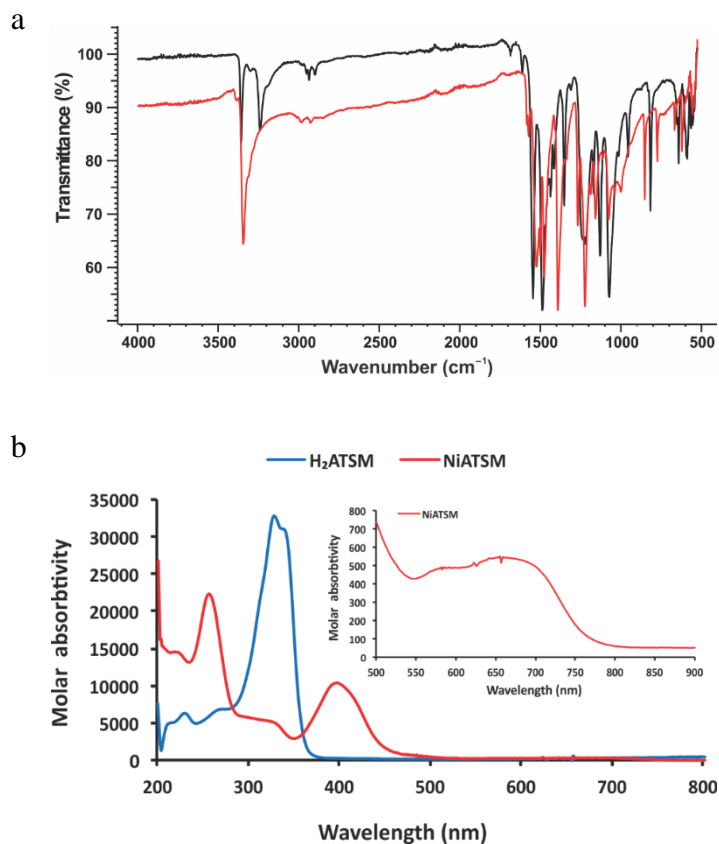


Figure H.1. Spectroscopic characterization of H₂ATSM and NiATSM. a) FT-IR spectra of H₂ATSM (black) and NiATSM (red), b) UV-Vis spectra of H₂ATSM and NiATSM in 1:1 MeCN:MeOH solution. Inset shows the d-d charge transfer region.

CURRICULUM VITAE

Caleb Calvary
Ph.D. Candidate, Department of Chemistry
University of Louisville
Phone: 614-202-0898; E-mail: caleb.calvary@louisville.edu

EDUCATION

- Ph.D. in Chemistry, University of Louisville, Louisville, KY 2018– Present
- Mentors: Prof. Craig Grapperhaus and Prof. Robert Buchanan.
 - Research Focus: Synthesis and electrochemical characterization of metal bis(thiosemicarbazones).
- M.S. in Chemistry, University of Louisville, Louisville, KY 2014 – 2018
- Mentors: Prof. Craig Grapperhaus and Prof. Robert Buchanan.
 - Research Focus: Synthesis and electrochemical characterization of metal bis(thiosemicarbazones).
- B.S in Chemistry, Marshall University, Huntington, WV 2009 – 2014
- Mentor: Prof. Michael Castellani.
 - Research Focus: Synthesis and characterization of air and moisture sensitive *ansa-metallocenes*.

PROFESSIONAL EXPERIENCE

Department of Chemistry, University of Louisville, Louisville, KY

- Teaching Assistant in General Chemistry 2015 – 2017
- Research Mentoring: Trained five undergraduate students: Anna Davis (2016-2019), Alan Weihe (2015), Henry Brun (2018-2019), Eli Thacker (2019), and Ali Costello (2019)

Department of Chemistry, Marshall University, Huntington, WV

- Learning assistant for freshman and organic chemistry

HONORS and FELLOWSHIPS

- Awarded multiple summer fellowships during undergraduate career at Marshall University (SURE and SURF).
- Awarded Student of distinction in Chemistry in 2014 at Marshall University.
- Awarded a chemistry department fellowship upon entry to the University of Louisville.

AFFILIATIONS

- Member of the American Chemical Society, Inorganic Chemistry Division
- Member of the Academy of Sciences of Indiana

EXPERTISE

- Ligand design and synthesis
- Synthesizing coordination complexes
- Air-Free (Schlenk) Technique

SKILLS

Instruments: Experienced in operating the following instruments and interpretation of the corresponding data:

- Varian Inova 400 MHz NMR
- Varian Inova 500 MHz NMR
- Bruker EMX EPR Spectrometer
- Bruker AXS APEX X-Ray Spectrometer
- ThermoNicolet 360 IR
- Agilent 8463 UV-Vis
- PE Biosystems Voyager DE-Pro MALDI-TOF
- Gamry Instruments Interface1000 E Potentiostat
- FEI Nova600 FEG-SEM

Software: Advanced proficiency in: Microsoft Office, Corel draw, ChemOffice, MestreNova, SciFinder, Shelxtl, Mercury, EndNote X9.

PUBLICATIONS

1. **Calvary, C. A.**; Hietsoi, O.; Mashuta, M. S.; Buchanan, R. M.; Grapperhaus, C. A., Synthesis and electrochemical characterization of copper(II) bis(thiosemicarbazone) catalysts for hydrogen evolution reactions. *Eur. J. Inorg. Chem.* **2020**, Submitted,
2. **Calvary, C. A.**; Hietsoi, O.; Strain, J. M.; Mashuta, M. S.; Spurgeon, J. M.; Buchanan, R. M.; Grapperhaus, C. A., Synthesis, characterization, and HER activity of pendant diamine derivatives of NiATSM. *Eur. J. Inorg. Chem.* **2019**, 3782-3790. DOI: (10.1002/ejic.201900721).
3. Gulati, S.; Hietsoi, O.; **Calvary, C. A.**; Strain, J. M.; Pishgar, S.; Brun, H. C.; Grapperhaus, C. A.; Buchanan, R. M.; Spurgeon, J. M., Photocatalytic hydrogen evolution on Si photocathodes modified with bis(thiosemicarbazone)nickel(II)/Nafion. *Chem. Commun.* **2019**, 55, 9440-9443. DOI: (10.1039/c9cc04117f)

PRESENTATIONS

1. **Calvary, C. A.**; Hietsoi, O.; Mashuta, M. S.; Buchanan, R. M.; Grapperhaus, C. A., Synthesis and electrochemical characterization of copper(II) bis(thiosemicarbazone) catalysts for hydrogen evolution reactions. The 2019 ACS Great Lakes Regional Meeting, Lisle, IL, May 1–4, **2019**.
2. **Calvary, C. A.**; Hietsoi, O.; Mashuta, M. S.; Buchanan, R. M.; Grapperhaus, C. A., Synthesis and electrochemical characterization of copper(II) bis(thiosemicarbazone) catalysts for hydrogen evolution reactions. The 134th Annual Academy Meeting. Indianapolis, IN, March 30, **2019**.
3. **Calvary, C. A.**; Hietsoi, O.; Mashuta, M. S.; Buchanan, R. M.; Grapperhaus, C. A. Shifting the potential anodically through alkylation of functionalized nickel(II) bis(thiosemicarbazone) complexes. The *2019 Gordon Research Conference* on Inorganic Reaction Mechanisms, Galveston, TX, March 10 - 15, **2019**.
4. **Calvary, C. A.**; Hietsoi, O.; Mashuta, M. S.; Buchanan, R. M.; Grapperhaus, C. A., Synthesis and electrochemical characterization of copper(II) bis(thiosemicarbazone) catalysts for hydrogen evolution reactions. Grad Student Regional Research Conference, University of Louisville, Louisville, KY, February 28, **2019**.
5. Davis, A. E.; **Calvary, C. A.**; Grapperhaus, C. A.; Buchanan, R. M., Facile and Efficient Synthesis of Thiosemicarbazone Derivatives with Functionalized Pendant Amines. Grad Student Regional Research Conference, University of Louisville, Louisville, KY, February 28, **2019**.
6. **Calvary, C. A.**; Hietsoi, O.; Mashuta, M. S.; Buchanan, R. M.; Grapperhaus, C. A., Synthesis and electrochemical characterization of nickel(II) bis(thiosemicarbazone) catalysts for hydrogen evolution reactions. 2018 Ohio Inorganic Weekend (OIW), The Chemistry & Biochemistry Department at Ohio University, Athens, OH, November 9–10, **2018**.

7. **Calvary, C. A.**; Hietsoi, O.; Grapperhaus, C. A.; Buchanan, R. M.; Mashuta, M. S., Synthesis and electrochemical characterization of NiATSM derivatives with pendant hindered amine bases. The 256th ACS National Meeting, Boston, MA, August 19–23, **2018**, INOR-510510.
8. **Calvary, C. A.**; Hietsoi, O.; Mashuta, M. S.; Grapperhaus, C. A.; Buchanan, R. M., Synthesis and characterization of new bis(thiosemicarbazonato) Ni(II) complexes for electrocatalytic hydrogen evolution. Fourth Annual Society of Postdoctoral Scholars Research Symposium, University of Kentucky, Lexington, KY, June 1st, **2018**.

PATENTS

1. Grapperhaus, C. A.; Buchanan, R. M.; Haddad, A. Z.; **Calvary, C. A.** Compounds, their preparation, related compositions, catalysts, electrochemical cells, fuel cells, and uses thereof. U.S. Pat. Appl. Publ. **2019**, US 20190106385 A1 20190411.
2. Grapperhaus, C. A.; Buchanan, R. M.; Vishnosky, N. S.; Young, J. O. E.; Bates, P. J.; Andres, Sarah A.; **Calvary, C. A.** Preparation of thiosemicarbazone derivatives as anti-cancer agents. PCT Int. Appl., **2018**, WO 2018204564 A1 20181108.